Scalable and Robust Inference of Sparse Brain Signals via Personalized Physiological System Identification

by
Md. Rafiul Amin

A dissertation submitted to the Department of Electrical and Computer Engineering,

Cullen College of Engineering

in partial fulfillment of the requirements for the degree of

Doctor of Philosophy
in Electrical Engineering

Chair of Committee: Rose T. Faghih

Committee Member: Thomas J. Hebert

Committee Member: Saurabh Prasad

Committee Member: Joseph T. Francis

Committee Member: Rohit Reddy

University of Houston
December 2021

DEDICATION/EPIGRAPH

This dissertation is dedicated to,

my parents, my wife, and my siblings for their unconditional love and support.

Md. Rafiul Amin

December 2021

ACKNOWLEDGMENTS

I am very thankful to my advisor Dr. Rose T. Faghih, for allowing me to be a part of the computational medicine lab and providing her supervision to conduct my research during this journey. This dissertation would not have been possible without her clear direction and guidance. Her expertise, enthusiastic encouragement, patience, precious advice, and valuable feedback made it possible to complete this successful research project. I respect her enthusiasm for her work and her extraordinary achievements in the field. She has always been very supportive and a great source of inspiration to be very proactive in my research. She has always appreciated and encouraged my new ideas towards my research problems. Her advising approach has improved my ability of critical thinking towards a research problem. She also provided me opportunities to collaborate with researchers from different backgrounds, further bolstering my growth as a researcher. Not only did she encourage me to do my research, but she also advised me to mentor other junior students. It also helped me possess clear thoughts over different problems and enriched my knowledge in a broader spectrum. I consider myself very fortunate to work under her supervision in my academic life, and I hope to gain even more from her in the future.

I would also like to acknowledge my colleagues Dilranjan Wickramasuriya and Hamid Fekri Azgomi for helping me by reviewing my research outcomes and providing their valuable feedback and perspective. I feel blessed to have such peers for my continuous progress in research. Furthermore, I would like to thank all of my current and former lab mates. It has been a great pleasure having such great friends and colleagues.

I express my gratefulness to my family, who have been extremely encouraging in all aspects of my life. I would especially like to thank my father, Md Ruhul Amin, and my mother, Hosne Ara Begum, for their unconditional love and support. My father has always inspired me to science and mathematics. Without his encouragement, I would not be able to be in engineering. On the other hand, my mother has always been supportive and gave me strength no matter what failure or challenges I faced along the way. Both my parents

encouraged me to be selfless and taught me to think about people around me. My parents have been a constant source of motivation and energy in my life. They have also taught me to be grateful for the opportunities that I received and use them for the greater good of society. I express my love and gratitude to my wife for being by my side during my tough times. I also would like to thank my elder sister for helping and guiding me in my studies. Furthermore, I thank my younger brother, who has always been a source of encouragement and support in my challenging times.

I would like to thank all of my teachers and mentors who have always guided me towards this path. I am very fortunate to have great teachers and mentors who not only taught me my academic syllabus but also helped me to be able to dream a better career goal. I especially would like to thank my undergraduate thesis supervisor Dr. S. M. Mahbubur Rahman, who advised me to pursue higher studies after graduation. Without his encouragement, it would not be possible for me to be in the place where I am now.

Finally, I would like to thank all my friends. I am very fortunate and blessed to have a lot of generous and kind-hearted friends. My friends in Houston have been around me and constantly supported me at all times. They are the ones who made me feel Houston is my hometown. I also would like to thank my friends around the world, with whom I can share anything and everything in life.

ABSTRACT

Electrodermal activities (EDA) are any electrical phenomena observed on the skin. Skin conductance (SC), a measure of EDA, shows fluctuations due to autonomic nervous system (ANS) activation induced sweat secretion. Since it can capture psychological and physiological information, there is a significant rise in the research for tracking mental and physiological health with SC recording. SC signal that is an observation of the EDA dynamics is representative of the class of signals generated by sparse dynamic systems. These signals can be deconvolved to uncover hidden variables. However, the current state-of-the-art of system theoretic deconvolution and consequent investigation has many challenges. The challenges include the need for a framework that incorporates prior physiological knowledge, the absence of a robust inference framework that can reliably fuse multichannel observations, and the non-convexity of the parameter estimation optimization problem. In addition to that, there is a lack of a comprehensive physiologically motivated model, the existing deconvolution method has poor scalability, and there is the presence of motion artifacts. Therefore, firstly, we model the fast varying fluctuations, i.e., the phasic component of SC using a two-dimensional state-space model representing the diffusion and evaporation processes of sweating with a sparse impulsive signal as the input representing ANS activation. We model the slowly varying fluctuation, i.e., the tonic component of SC with several cubic B-spline functions. We formulate an optimization problem with physiological priors on system parameters, a sparsity prior on the neural stimuli, and a smoothness prior on the tonic component. Finally, we employ a generalized cross-validation-based coordinate descent approach to balance the smoothness of the tonic component, the sparsity of the neural stimuli, and the residual. Secondly, we propose a model that combines multichannel SC recording that relates to the impulsive sparse ANS activation. Then we introduce a generalized cross validation-based deconvolution approach utilizing this model. Thirdly, we utilize the continuous system identification technique to reformulate the cost function as a convex one for the deconvolution problem. Fourthly, we propose a comprehensive model for the SC dynamics. The proposed model is a 3D state-space representation of the direct

secretion of sweat via pore opening and diffusion followed by corresponding evaporation and reabsorption. The comprehensive model enables us to derive a scalable fixed interval smoother-based sparse deconvolution approach for scalable ANS activation inference. We incorporate generalized cross-validation to tune the sparsity level. Finally, we propose a motion artifact reduction scheme that leverages multiresolution linear/nonlinear adaptive filters and three-axis accelerometer-based motion reference. We further perform experiments to obtain the motion artifact contaminated data and the corresponding motion reference signal for validating the proposed scheme. For evaluation, we utilize both experimental, publicly available, and simulated datasets to investigate the performance of our proposed schemes. Our results show that our approach is successfully recovering ANS activation from SC recordings by addressing the existing challenges. Furthermore, we validate our approaches for reliability, robustness, and scalability by evaluating their event SC response detection performance. Finally, our results validate that our physiology-motivated state-space model can comprehensively explain the EDA dynamics and outperforms all previous approaches. Our findings introduce a whole new perspective and have a broader impact on the standard practices of EDA analysis and the analysis of similar systems with sparse dynamics.

TABLE OF CONTENTS

LIST OF TABLES

LIST OF FIGURES

1 Introduction

1.1 Motivation and Objective

The human race underwent many difficulties due to epidemics of bacteria-transmitted diseases such as tuberculosis, plague, cholera, etc. [1, 2, 3] until recent times. These diseases have been studied extensively, and treatments have been made available [4]. The present challenges we face are diseases such as heart disease, major depression, anxiety, obesity, and chronic illness. The number of patients diagnosed with such conditions is increasing day by day [5, 6]. Among them, the term 'stress' is considered as the twenty-first century epidemic [7]. Regular tracking of mental health in an unobtrusive way requires systematic and reliable analysis of physiological signals to identify the underlying brain-related variables. In this thesis, we investigate novel methodologies for obtaining the underlying brain activity related to different types of stress from electrodermal activity (EDA).

The phrase EDA was first introduced in 1966 as a common term for variation in electrical properties of the skin [8, 9]. EDA has been widely used in psychophysiology since its discovery as it correlates with autonomic nervous system (ANS) activation. ANS is the part of our body that generally dictates the body's fight-or-flight response mechanism. EDA can be exosomatically recorded by measuring skin conductance (SC). Some authors use the term "galvanic skin response" (GSR) to refer to the SC. In response to emotional stress, the ANS stimulates sweat glands depending on the psychological and physiological demands. Consequently, salty secretions from sweat glands increase the SC. This elevation in SC then gradually decreases in an exponential manner. This is known as SC response (SCR). SC measurements can be analyzed to investigate the corresponding ANS activation, which contains a great deal of information about human emotional arousal [10].

There are a few vital signals in the human body similar to EDA that have the potential to be measured continuously and unobtrusively using very simple instrumentation. The unobtrusive nature of the measuring techniques has led to a new era of wearable technology for

continuous health monitoring. Such signals include cardiac signals (e.g., electrocardiogram (ECG) and photoplethysmogram (PPG)), skin temperature (SKT), EDA, muscle activity (e.g. electromyogram (EMG)), etc. [11, 12]. Among them, PPG and SKT have been widely integrated in consumer wearable technologies along with reliable techniques for decoding useful information. In the past few decades, extensive research has been performed, mainly on PPG signal analysis for wearable implementation, with the goal of continuous health monitoring. The next candidate with the most potential for revolutionizing wearable health monitoring is the EDA [13]. However, the amount of research performed on EDA signals is relatively limited compared to cardiac signals. Although researchers have published many studies to systematically model EDA in the last two decades, there are still many fundamental characteristics of EDA being discovered today. For example, in 2020, Subramaniam *et al.* [14] have shown that the point process characterizes EDA in normal healthy participants. Therefore, further study is required to identify the more accurate system dynamics of EDA so that critical information related to health monitoring can be obtained.

1.2 Prior Studies and Existing Challenges

Macefield *et al.* [15] have shown that areas of the brain related to sympathetic nervous activity can be identified by using functional magnetic resonance imaging (fMRI) of the brain and by recording concurrent microelectrodes readings generated by sympathetic outflow to muscle and skin. They have proposed to extend this idea to examine specific disorders of emotional expression to comprehend underlying neural processes. To collect fMRI data, a clinical setup is necessary which will be convenient for clinical diagnosis. Unfortunately, it is not convenient for daily tracking of neural process related to emotional states. Bomba *et al.* [16] used heart rate variability (HRV) from the ECG signal as a measure of ANS imbalance. However, Soh *et al.* [17] illustrated the underlying challenges and complexity of acquiring ECG data using wearable technology. In another study, Faghih *et*

al. [18] were able to recover the amplitude and timing of ANS activation related to different fear states employing EDA signals with a deconvolution scheme [19, 20]. Utilizing recovered timings and amplitudes, emotional states can be estimated to analyze emotional disorders.

EDA is related to a system that is representative of a class of systems having sparse dynamics. The observations of such systems, such as SC signal, can be deconvolved to obtain hidden variables to gain insight. Many deconvolution schemes have been proposed for such signals including SC data. Benedek *et al.* [21] proposed a non-negative approach to decompose SC data into discrete compact responses and at the same time assessed deviations from the standard SCR shape. However, this decomposition approach detects noise as SCRs. In a later work, Bach *et al.* [22] have implemented a low-pass filter to separate the slow varying tonic components and then utilized a third-order differential equation to model the fast varying component, i.e., phasic component in SC. Nevertheless, the FIR filter-based separation of the slow and fast varying components has limitations as both phasic and tonic component has concentrated energies in overlapping frequency components. Therefore, use of an ordinary FIR low-pass filter to extract tonic component will give rise distorted phasic component with negative values. Greco *et al.* [23] proposed decomposing SC data into tonic and phasic components. They formulated a quadratic programming problem to find sparse solutions for the input stimuli. However, the use of fixed SCR shape parameters and regularization parameters makes it challenging to find an optimal sparse solution. In another work, Gallego *et al.* [24] proposed an approach to obtain a more sparse solution; however, this approach seems to oversparsify the solution. Furthermore, the cubic spline basis function-based model may overfit the data and provide a solution that is not physiologically plausible. In the deconvolution scheme proposed by Faghih *et al.* [25, 18, 19, 20, 26], a two-step coordinate descent approach has been incorporated. In the first step, they used the FOCal Under-determined System Solver (FOCUSS) algorithm [27] to find a sparse solution of the ANS activation. This step is a convex optimization problem to which a global solution can be achieved. In the following

step, their algorithm employs another optimization problem to find the physiological system parameters, which are not convex. Therefore, the solution can stagnate at a local minimum. The authors overcome this utilizing multiple random initializations.

In addition to a non-convexity formulation for parameter estimation, the methods utilized in [23, 24] suggested to use the cubic B-spline and linear trend-based modeling of the tonic part of SC to achieve a reasonable fit to the data. However, the cubic spline basis function based model may overfit to the data and provide a solution that is not physiologically plausible. Especially, the decay time of the physiological parameter has a coupling with the cubic spline coefficient as both jointly define the smoothness of the EDA variation. As a result, there is a potential chance that the solution of the decay component might be out of the physiological boundary while solving for both of them at the same time. Therefore, proper physiological priors should be considered to obtain a tracktable solution. Furthermore, what weight should someone put on the smoothness level of the tonic component has not been explored yet. An automatic scheme that balances between the smoothness level of the tonic component, the sparsity level of the ANS activation, and the model fit is required.

Although the model proposed in [23, 24] can achieve a reasonable fit to the data, it lacks reasonable physiological justification and the corresponding coefficients of the obtained cubic spline functions have no interpretation. There are several hypothesises regarding sweat generation, sweat secretion, evaporation, and re-absorption [28]. All these physiological understanding has not been fully explored to design a comprehensive mathematical model. Lack of a physiology-motivated comprehensive model prevents us from designing scalable approaches. In addition, the lack of a complete state-space model makes it difficult to design scalable fixed interval smoother based inference approaches for recovery of ANS activation.

Furthermore, all previous approaches [29, 21, 23, 22, 30, 24, 18] utilized only single channel information during the inference of ANS activation. Nevertheless, the use of only a single channel can be very unreliable as the data can be corrupted with noise and motion artifacts. As SC recordings from multiple channels are highly correlated and share

common ANS information, utilizing multichannel information for ANS activation inference scheme could lead to more reliable and accurate information. Finally, none of the previous approaches consider a scheme to effectively reduce the amount of noise with the utilization of a reference motion information.

1.3 Thesis Outline

This thesis investigates new methodologies to account for five previous challenges related to sparse deconvolution with applications in EDA. The first part investigates a unified inference scheme utilizing physiological measurements and physiological priors with generalized cross-validation for balancing between the priors and the model fit. In the second part, this thesis provides a combined system modeling and robust optimization formulation for the multichannel deconvolution approach. In the third part, it discusses a convex optimization formulation for the parameter estimation part of the deconvolution problem using continuous system identification techniques. The fourth part of the thesis provides a physiologically motivated comprehensive model for obtaining a scalable and real-time brain activity inference framework from EDA recordings. The last part of the thesis provides an evaluation of multiresolution linear/nonlinear adaptive filters for motion artifact reduction with motion reference.

1.3.1 Identification of Sympathetic Nervous System Activation from Skin Conductance: A Sparse Decomposition Approach with Physiological Priors

Sweat secretions lead to variations in SC signal. The relatively fast variation of SC, called the phasic component, reflects sympathetic nervous system activity. The slow variation related to thermoregulation and general arousal is known as the tonic component. It is challenging to decompose the SC signal into its constituents to decipher the encoded neural information related to emotional arousal. Therefore, in this part we model the phasic

component using a second-order differential equation representing the diffusion and evaporation processes of sweating. We include a sparse impulsive neural signal that stimulates the sweat glands for sweat production. We model the tonic component with several cubic B-spline functions. We formulate an optimization problem with physiological priors on system parameters, a sparsity prior on the neural stimuli, and a smoothness prior on the tonic component. Finally, we employ a generalized cross-validation-based coordinate descent approach to balance among the smoothness of the tonic component, the sparsity of the neural stimuli, and the residual. Furthermore, we illustrate that we can successfully recover the unknowns separating both tonic and phasic components from both experimental and simulated data. Furthermore, we successfully demonstrate our ability to automatically identify the sparsity level for the neural stimuli and the smoothness level for the tonic component.

1.3.2 Robust Inference of Autonomic Nervous System Activation using Skin Conductance Measurements: A Multi-Channel Sparse System Identification Approach

The ANS stimulates various sweat glands for maintaining body temperature as well as in response to various psychological events. Variations in SC measurements due to salty sweat secretion can be used to infer the underlying ANS activity. Recovering both ANS activity and the underlying system from noisy single-channel recordings is challenging. As the same ANS activity drives all sweat glands throughout the skin, the same information is encoded in different SC recordings. We perform system identification and develop a physiological model for multichannel SC recordings relating them to ANS activation events. Using a multirate formulation, we estimate the number, timings, and amplitudes of ANS activity and the unknown model parameters from multichannel SC data. We incorporate a generalized cross-validation-based sparse recovery approach to balance between the sparsity level of the inferred ANS activity and the goodness of fit to the multichannel SC data. In this part, we show our results of successfully deconvolving multichannel experimental auditory

stimulation SC data from human participants. We analyze experimental and simulated data to validate the performance of our concurrent deconvolution algorithm; we illustrate that we can recover the ANS activity due to the underlying auditory stimuli. Furthermore, we estimate the stress using inferred ANS activity based on multichannel deconvolution of SC data collected during different driving conditions and at rest.

1.3.3 Sparse Deconvolution of Electrodermal Activity via Continuous-Time System Identification

One of the challenges with the existing SC deconvolution methods is the non-convexity of the optimization formulations for estimating the parameters given the stimuli. We solve this parameter estimation problem using a continuous-time system identification framework: i) we specifically use the Hartley modulating function (HMF) for parameter estimation so that the optimization formulation for estimating the parameters given the stimuli is convex; ii) we use Kaiser windows with different shape parameters to put more emphasis on the significant spectral components so that there is a balance between filtering out the noise and capturing the data. We apply this algorithm to SC data, a measure of EDA, collected during cognitive stress experiments. Under a sparsity constraint, in the HMF domain, we successfully deconvolve the SC signal. We obtain the number, timings, and amplitude of the underlying neural stimuli along with the system parameters. Moreover, using simulated data, we illustrate that our approach outperforms existing EDA data analysis methods in recovering underlying stimuli.

1.3.4 Physiological Characterization of Electrodermal Activity Enables Scalable Near Real-Time Autonomic Nervous System Activation Inference

The current state-of-the-art lacks a physiologically motivated approach for real-time inference of ANS activation from EDA. Therefore, in this part, we propose a comprehensive model for the SC dynamics. The proposed model is a 3D state-space representation of the

direct secretion of sweat via pore opening and diffusion followed by corresponding evaporation and reabsorption. As the input to the model, we consider a sparse signal representing the ANS activation that causes the sweat glands to produce sweat. In addition to the proposed model, we derive a scalable fixed interval smoother-based sparse recovery approach utilizing the proposed comprehensive model to infer the ANS activation enabling edge computation. We incorporate a generalized cross-validation-based approach to tune the sparsity level. Finally, we propose an expectation-maximization based deconvolution approach for learning the model parameters during the ANS activation inference. For evaluation, we utilize an experimental dataset, and the results show that our comprehensive state-space model can successfully describe the SC variations with high scalability, showing the feasibility of real-time applications. Results validate that our physiology-motivated state-space model can comprehensively explain EDA and outperforms all previous approaches. Our findings introduce a whole new perspective and have a broader impact on the standard practices of EDA analysis.

1.3.5 Evaluation of Adaptive and Bayesian Filters for Artifact Removal from Electrodermal Activity Leveraging Noise Source Reference

EDA shows a significant correlation with ANS activation. Accurate EDA analysis along with the ANS activation inference has a wide range of applications in mental health monitoring. However, the presence of motion artifacts in the SC data collected in ambulatory settings makes the analysis unreliable. In this study, we propose a multirate adaptive filtering scheme to remove motion artifacts from the SC data that utilizes three-axis accelerometer data. We evaluated four types of linear/nonlinear adaptive filters. We utilize the simulated as well as experimental data to evaluate the performance of the adaptive filters. Furthermore, we utilize the respiration signal to identify the probability of respiration-induced SC artifacts. Next, we utilize a Bayesian filter-based *expetation-maximization* approach to identify the activation that is comprised of respiration induced and ANS induced ones.

Finally, we propose a method to isolate two types of activation based on the respiration analysis. Our result shows that linear FIR recursive least-squares filters are performing best compared to other types of adaptive filters. We draw this conclusion by obtaining the receiver operating characteristics of detectability of the event-related SCRs after artifact reduction with different adaptive filters. Moreover, we saw that the recursive least-squares filter has always provided stable results for both simulated and experimental datasets. Finally, our results also show our ability to detect the respiration-induced SC responses and corresponding ANS activation. The evaluation of the adaptive filters shows the potential of utilizing reference signals with effective artifact modeling for successful reduction. Effective artifact reduction will lead to practical implementations of closed-loop wearable machine interface architectures to regulate emotions for mental and physical well-being.

An illustration of the summary of the proposed method is provided in Figure 1. Figure 1-(**A**) illustrates the objective of the proposal, i.e., to accurately infer brain activation from multi-channel recording. Figure 1-(**B**) shows a general overview of the proposed deconvolution approach. Figure 1-(**C**) shows a snippet of the results and comparison with other approaches.

1.4 Scientific Significance

Appropriate EDA analysis has applications in a wide range of fields such as mental disorders, pain, cognitive stress tracking, wakefulness, etc. As different physiological signals, including EDA, contain information about human emotional arousal, they have potential applications in the field of mental health. For example, preventing death from mental disorders with regular tracking could be one potential application as Walker *et al.* [31] reported that a large portion of deaths worldwide are attributable to mental health-related disorders. A meta-analysis shows that mental disorders are a major risk factor for suicide [32]. Suicide is one of the leading causes of death in the United States in the year 2017 [33] and the cost related to suicide alone in the United States were more than $90 billion in

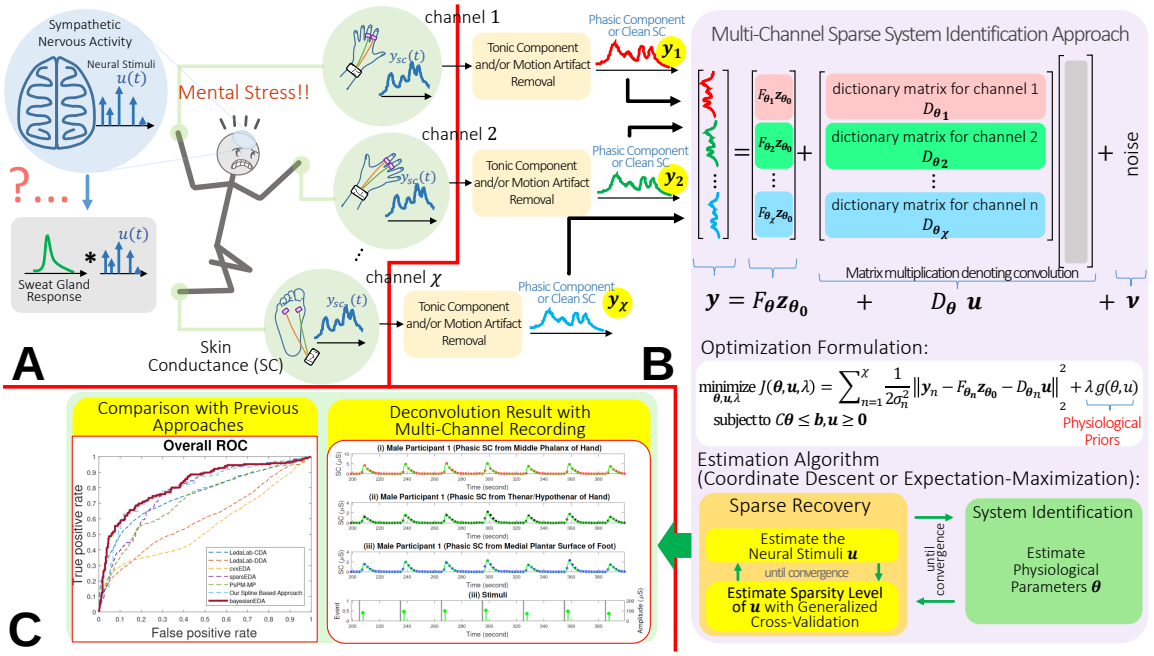

Figure 1: **An General Overview of the Proposed Multi-channel Deconvolution Scheme for Inferring Brain Acrivity from SC.**

2013 [34]. Studies have recommended [34] community-based immediate psychiatric services, including telepsychiatric support for reducing suicide-related costs which require continuous monitoring. Augmenting EDA with other physiological signals for time-to-time monitoring of critical patterns of emotional regulation could potentially help preventing psychiatric disorders [35].

Another possible potential application could be detecting diabetic neuropathy and tracking the efficacy of the treatment in the patient population. Diabetic neuropathy refers to small nerve damage caused by prolonged exposure to high levels of blood glucose concentration [36]. As a result, small nerves along with the sudomotor nerves in the legs, feet, and hands that are responsible for transmitting ANS activation are prone to neuropathy [36]. As confirmed by numerous studies in [37, 38, 39], damages in small nerves including the sudomotor nerves may lead to abnormal EDA variations. Furthermore, it is well known in clinical diagnostics that the development of anomalies in sweat secretions may be attributed to forms of disorders, such as hypohidrosis and anhidrosis [40]. Moreover, such disorders

may indicate diseases like diabetes mellitus [40]. Clinical investigations of abnormalities in the SC recordings can be pivotal for the early detection of such diseases.

2 Identification of Sympathetic Nervous System Activation from Skin Conductance: A Sparse Decomposition Approach with Physiological Priors

2.1 An Overview of Sympathetic Nervous System Activation and Corresponding Skin Conductance Response

Although the skin's electrical activity was first observed in the 1880s, the term "electrodermal activity" (EDA) was first introduced in 1966 as a common phrase for electrical phenomena in the skin [8, 9]. Since its discovery, EDA has been very popular in psychophysiology research as variations in the skin's electrical conductivity correlate with the sympathetic nervous system (SNS) activation. SNS is a part of our body's autonomic nervous system (ANS), which is primarily responsible for the fight-or-flight response mechanism. EDA can be exosomatically recorded by measuring skin conductance (SC). Some authors use the term "galvanic skin response" (GSR) to refer to the SC. In response to emotional stress, ANS stimulates sweat glands depending on the psychological and physiological demands. Consequently, salty secretions from sweat glands increase the SC. SC measurements can be analyzed to investigate the corresponding ANS activation, which contains a great deal of information about human emotional arousal [10].

SC is considered as a composition of two components [9, 42, 29, 21, 23]. The relatively slow varying component, called the tonic component, is generally related to the thermoregulation of the body, ambient temperature, humidity, and the general arousal of a person [9, 43]. Wickramasuriya *et al.* [44] showed that the tonic component can be incorporated

Chapter two was first presented in part at 2019 41st Annual International Conference of the IEEE Engineering in Medicine and Biology Society (EMBC) [8]. Chapter two has been mainly adopted from Amin, Md Rafiul, and Rose T. Faghih. "Identification of Sympathetic Nervous System Activation From Skin Conductance: A Sparse Decomposition Approach With Physiological Priors." IEEE Transactions on Biomedical Engineering 68.5 (2020): 1726-1736 [41].

in an arousal state estimation scheme assuming it contains the general arousal information of a person. Some authors have measured it as SC level (SCL) [9]. On the contrary, the comparatively fast varying component is a reflection of neural stimulation from the SNS. The fast varying component is called the phasic component which is comprised of discrete SC responses (SCRs). Discrete SCRs can be related to various SNS activation events. In summary, SC can be represented as the sum of two convolution operations: (1) between a sparse neural stimuli from SNS and a fast physiological smoothing kernel and (2) between some arbitrary unknown activation function and a slow physiological smoothing kernel. There is a growing interest in identifying such systems as well as the underlying neural stimuli representation SNS activation for a better understanding of physiological phenomena [45, 46].

Appropriate EDA analysis along with SNS activation identification technique has applications in a wide range of fields such as mental disorders, pain, cognitive stress tracking, wakefulness, etc. As different physiological signals, including SC, contain information about someone's emotional arousal, they have potential applications in the field of mental health. For example, preventing deaths from mental disorders with regular tracking could be one potential application as Walker *et al.* [31] reported that a large portion of the deaths worldwide is attributable to mental health-related disorders. A meta-analysis shows that mental disorders are a major risk factor for suicide [32]. Suicide is one of the leading causes of death in the United States in the year 2017, and it has increased by 3.7% from the previous year [33]. Suicide related costs for the United States were $93.5 billion in 2013 alone [34]. Shepard *et al.* [34] emphasized the community based immediate psychiatric services, including telepsychiatric support for reducing suicide-related costs. Regular tracking of problematic patterns of emotional regulation could potentially help prevent psychiatric disorders [35]. Electroencephalogram, electrocardiogram, respiration, functional near-infrared spectroscopy [47], and EDA, could be investigated to identify abnormal patterns of emotional regulation [48]. Day to day tracking and analysis of emotional regulation requires

reliable wearable implementations for suicide-prone patients.

In a different context, studies have also shown that abnormal SC recordings can be attributed to diabetic neuropathy and other diabetic diseases [37, 38, 39]. Diabetic neuropathy refers to the small nerve damages caused by prolonged exposure to high levels of blood glucose concentration [36]. Small nerves in the legs, feet, and hands are more prone to neuropathy [36]. The small nerve fibers also include the sudomotor nerves that are primarily responsible for delivering the SNS activation to the sweat glands for sweat secretion. Abnormal SC variation or asymmetry of SC recordings from different skin regions might be an indication of diabetic neuropathy. According to clinical diagnostics, the development of early stages of sweat formation disorders is related to various forms of illnesses, including hypohidrosis or anhidrosis, which accompany diseases like diabetes mellitus [40]. Systematic analysis of SC recording to identify these asymmetries can be crucial for the early prevention of such illness.

In the early days, most of the SC studies in psychophysiology were performed with only basic statistics. In the last two decades, researchers have come up with systematic analysis tools with a goal of understanding SNS activation patterns [49]. Several popular methods have been widely used for decomposing SC recording into its constituents. Benedek *et al.* [29, 21] proposed two methods within a toolbox named LedaLab to decompose SC signal into several discrete SCRs. However, their methods lead to non-sparse solutions for neural stimuli which may over-fit to the noise. Bach *et al.* [22] have proposed the dynamic causal modeling (DCM) approach for inferring the neural stimuli. They have considered a linear time-invariant system for modeling SCRs. They optimize the model parameters for a large dataset. They later also proposed a matching pursuit (MP) approach for alternative and faster implementation [50]. However, as a pre-processing step, they perform band-pass filtering (between 0.015 and 5 Hz) to remove the tonic component [51]. As both phasic and tonic components are SC measures, they are non-negative and both should have a spectral overlap in the low-frequency region. Therefore, simple band-pass filtering

introduces physiologically impossible negative values in the filtered signal and hence can distort the actual underlying components. Greco *et al.* [23] proposed a decomposition algorithm based on quadratic programming named cvxEDA where they have considered two different dictionaries for modeling tonic and phasic components. They considered the sparsity condition in neural stimuli. Nonetheless, the manual selection of the SCR shape parameters as well as the hyperparameters for imposing the sparsity prior on SNS activity and smoothness prior on the tonic component makes it challenging to find an appropriate solution. Hernando-Gallego *et al.* [24] proposed a fast and sparse decomposition algorithm named sparsEDA, however, it seems to provide an overly sparse solution leading to missing significant SCRs. Studies in [18, 52, 53, 54] proposed coordinate descent deconvolution approaches to account for the individual differences in the SCR shape parameters, but these do not solve for the tonic component.

In the present study, we propose an algorithm to recover the SNS neural stimuli, the underlying SCR shape parameters, and the tonic component from observed SC sampled data. Inspired by the works in [23, 18, 25, 19, 20, 26, 55, 56], we use a second-order differential equation model based on diffusion and evaporation process of sweat to relate SC to the internal unobserved neural stimuli and model the tonic component with a set of cubic basis-spline (B-spline) functions. We formulate an optimization problem based on the proposed model including: 1) Gaussian prior on SCR shape parameters, 2) sparsity prior on neural stimuli (l_1-norm penalization), and 3) smoothness prior on the tonic component (energy penalization, i.e. l_2-norm penalization on the cubic B-spline coefficients). We propose a block coordinate descent approach to recover the unknowns by incorporating sparse recovery for the neural stimuli and the interior-point method for the SCR shape parameters and the tonic component estimation. Moreover, we implement generalized-cross-validation (GCV) to obtain regularization parameters for both the l_1-norm and l_2-norm penalization terms, respectively for the neural stimuli and cubic B-spline coefficients. Finally, we analyze both experimental and simulated SC datasets to show the performance

of our proposed approach.

2.2 Method

2.2.1 Dataset Description

In this study, we analyse the SCRs to loud sounds [57], auditory oddballs [58], pain by electric shocks [59], white noise bursts [60], visual detection tasks [61]. The experiments were designed to investigate and model event-related SCRs [30]. The number of participants, gender, and age information is provided in Table 1. Dataset 1 contains three-channel SC data (SC measurement from the thenar/hypothenar of the non-dominant hand, the middle phalanx of the dominant second and third finger, and the medial plantar surface of the non-dominant foot) of each of the 26 participants. The rest of the datasets collect data only from the thenar/hypothenar of the non-dominant hand. Therefore, we use the SC recordings from the thenar/hypothenar of the non-dominant hand for all the datasets in this study. The experimental details are given in [30]. The total number of participants is 110 based on the experimental details in [30]. However, data for one participant is missing in Dataset 3 in the online repository. Therefore, we performed our analysis on the rest of the 109 available participants. The reported information in Table 1 is based on the downloaded datasets.

Table 1: Summary of Datasets Used In the Study.

Dataset No.	Experiment Type	Number of Participants	Age (years)
1	Loud Sound Stimulation	26 (13 M, 13 F)	24.4+/-4.9
2	Auditory Oddball Task	20 (9 M, 11 F)	21.8+/-3.3
3	Pain by Electric Shocks	19 (9 M, 10 F)	21.8+/-3.3
4	White Noise Stimulation	22 (11 M, 11 F)	24.7+/-4.5
5	Visual Detection Task	22 (11 M, 11 F)	24.7+/-4.5

Here ‘M’ corresponds to male and ‘F’ corresponds to female.

2.2.2 Model Formulation

As previously mentioned, the SC signal can be thought of as the summation of two different components, i.e. the tonic component and the phasic component. We consider a third component in the formulation representing the measurement noise. The SC signal can be represented combining these three components as follows,

$$y(t) = y_p(t) + y_s(t) + \nu(t), \tag{1}$$

where $y(t)$, $y_p(t)$, $y_s(t)$, and $\nu(t)$ represent the SC signal, phasic component, tonic component, and noise, respectively.

Phasic Component. The phasic component can be thought of as the smoothed version of the neural activity from the SNS. The smoothing is performed by the physiological system composed of a collection of sweat glands, epidermis, and other related skin components. We model the physiological system responsible for smoothing operation using the first-order kinetics of diffusion of sweat from the sweat ducts to the strata cornea and the subsequent first-order kinetics of evaporation from the strata cornea [42, 21, 9]. We combine both diffusion and evaporation kinetics to form the following second-order differential equation, and we relate it to the neural stimuli $u(t)$ generated by SNS,

$$\tau_r \tau_d \frac{d^2 y_p(t)}{dt^2} + (\tau_r + \tau_d)\frac{dy_p(t)}{dt} + y_p(t) = u(t), \tag{2}$$

where τ_r and τ_d represent the rise and decay times for each SCR, respectively. We assume that τ_r and τ_d stay constant during the experiment, however, they can be different from person to person. Let SCR shape parameter vector $\boldsymbol{\tau} = [\tau_r \quad \tau_d]^\top$. Similar to [18, 25, 19, 20, 52, 53], we define an abstract definition of $u(t)$ as the summation of N weighted and shifted impulse functions, i.e. $u(t) = \sum_{i=0}^{N-1} u_i \delta(t - \Delta_i)$, where u_i represents the amplitude of the neural stimulus from SNS at time Δ_i. In this study, we define $\Delta_i = iT_u$, where T_u is

the sampling interval of $u(t)$ in discrete model described in 2.2.3. We define N to represent the number of samples in the discrete form of $u(t)$, and we write it as a function of the SC signal duration T_d ($N = \frac{T_d}{T_u}$); u_i is zero if there is no neural impulse and is a positive value if there exists an impulse at time instance iT_u. Since the number of impulses in the neural stimuli is very small compared to the number of samples in the recorded SC signal, we can represent the neural stimuli as a sparse vector in discrete domain for our analysis similar to [52].

We solve the differential equation in (2) assuming the sweat duct is empty at time $t = 0$, similar to [9, 18, 52, 53]. Hence, the solution to the differential equation becomes,

$$y_p(t) = y_p(0)e^{-\frac{t}{\tau_d}} + h_{\boldsymbol{\tau}}(t) * u(t), \tag{3}$$

where $h_{\boldsymbol{\tau}}(t)$ refers to the system impulse response representing an SCR shape and can be represented as a scaled version of the Bateman function. Here, the operator '$*$' represents the convolution operation. $h_{\boldsymbol{\tau}}(t)$ can be written as follows,

$$h_{\boldsymbol{\tau}}(t) = \begin{cases} \frac{1}{\tau_r - \tau_d}(e^{-\frac{t}{\tau_r}} - e^{-\frac{t}{\tau_d}}) & ; \quad \text{if } t \geq 0 \\ 0 & ; \quad \text{otherwise.} \end{cases} \tag{4}$$

Tonic Component. We utilize a summation of several shifted and weighted cubic B-spline functions to model the tonic component as in [62] and represent it with the following convolution operation,

$$y_s(t) = \psi(t) * q(t), \tag{5}$$

where $\psi(t)$ is the cubic B-spline function and $q(t) = \sum_{j=0}^{P-1} q_j \delta(t - (j-1)\Lambda_s)$ is an alternate representation of the cubic B-spline functions coefficients denoting the scaling and shifting operations. Here, P is the number of different shifted and scaled cubic B-spline waves used.

Λ_s is the knot size of the cubic B-spline function, which is an indicator of the smoothness of the tonic component. In this study, we select $\Lambda_s = 6$ seconds, the same as the maximum value of the decay time that we allow. We choose this value assuming a small increase in the tonic component during an SCR [9].

A cubic spline is a piecewise quadratic polynomial function of its dependent variable. A basis function of a cubic spline $\tilde{\psi}_i(t)$ represents the piece wise function within a certain time duration $t_i < t < t_{i+1}$. The set of cubic basis function can be defined by $S_{P,3} = \{\tilde{\psi}_{i,l}(t)|l = 3, i \in \{0, 1, 2, \cdots, P-1\}\}$ where i denotes the knot number or the time location and l denotes these are cubic B-spline functions. P is the total number of basis functions in the set. For a given sequence of t_i, $\forall i \in \{0, 1, 2, \cdots, P\}$, $\tilde{\psi}_{i,l}(t)$ can be calculated using the following recursive definition,

$$\tilde{\psi}_{i,l}(t) = \begin{cases} 1 & \text{if } l = 1 \ \& \ t_i < t < t_{i+1} \\ \frac{t-t_i}{t_{i+l}-t_i}\tilde{\psi}_{i,l-1}(t) + \\ \frac{t_{i+l+1}-t}{t_{i+l+1}-t_{i+1}}\tilde{\psi}_{i+1,l}(t) & \text{if } l > 1 \ \& \ t_i < t < t_{i+1} \\ 0 & \text{otherwise.} \end{cases}$$

In this study we set a fixed knot to knot distance, i.e. knot size, $\Lambda_s = t_{i+1} - t_i$, $\forall i \in \{0, 1, 2, \cdots, P-1\}$. Therefore we have $t_i = i\Lambda_s$. As our optimization problem is non-convex, it is important that the dictionary function is scaled properly before estimation. Again it is necessary to shift the basis function such that it can appropriately define the tonic components at the start and end of the SC recordings. Therefore, we re-define our tonic component basis functions by adding an extra scaling factor and a time shift, $\psi(t - i\Lambda_s) = \alpha\tilde{\psi}_{i,l}(t - \beta)$. In this study, we searched for a reasonable scaling factor α and time shifts β with trial and error. Finally, we chose $\alpha = 10^2$ and $\beta = 6\Lambda_s$ which gives us reasonable initialization while running the proposed approach on the five datasets. The tonic component is very slow, the tonic component for a time instance is dependent on coefficients

q_j of the several other neighboring cubic B-spline functions. Therefore, to model the tonic component at the beginning and the end of the SC recording, we consider an additional five basis functions in the model, i.e. $P = \left\lceil \frac{T_d}{\Lambda_s} \right\rceil + 5$. Figure 2 shows how a smooth tonic SC is modeled with several Cubic B-spline Functions. In Figure 2 the black curve correspond to the modelled tonic component. The colored curves denotes the weighted and shifted tonic basis functions. The back rectangle denotes the signal duration. A few basis functions outside the signal facilitates smooth transition to zero. Figure 2 also shows that the smooth transition from a non zero value to zero at the start and end of the signal is facilitated by a few extra cubic functions outside the signal region. As mentioned earlier, we considered five extra basis functions which are higher than the required number of basis functions to provide a bit of extra flexibility. The l_2-norm regularized penalization on the cubic B-spline coefficients will lead to unnecessary coefficients set to zero or very close to zero. This way the algorithm can decide the necessary number of cubic B-spline functions necessary to approximate a tonic component. We decided to include extra 5 basis functions to allow two or more basis functions before and after the signal measurement duration. However, the method should perform well as long as there is at least one extra basis function use outside the signal duration. The l_2-norm penalization will set any unnecessary coefficients to zero even someone decides to use more than the number of extra coefficients required and the result will not be affected significantly.

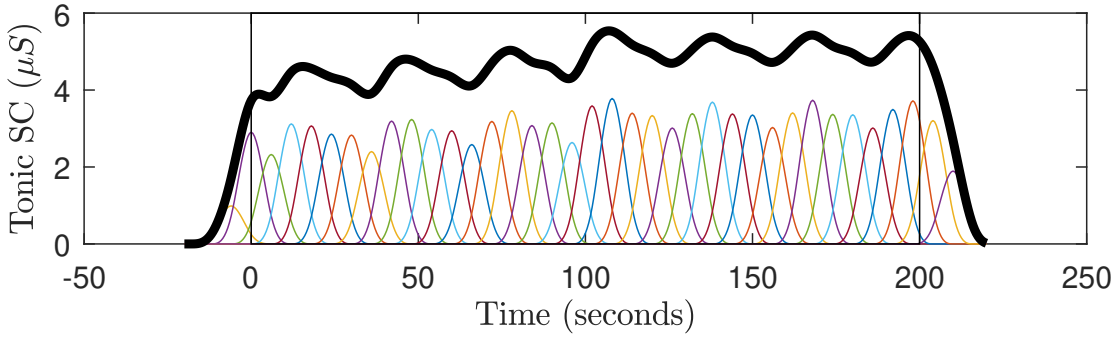

Figure 2: **Tonic Component Modeling with Cubic B-spline Functions.**

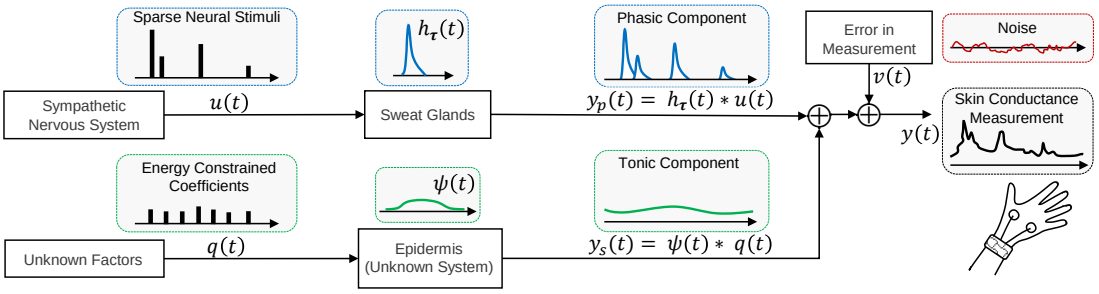

Figure 3: **Model Block Diagram.**

The whole model is illustrated in Figure 3. Figure 3 shows that a single neural stimuli signal $u(t)$ generated by the SNS is responsible for the SCR in a particular skin region of the body. The block diagram in Figure 3 shows the neural stimuli $u(t)$ convolving with sweat glands in a particular region of the skin having a phasic response function $h_{\boldsymbol{\tau}}(t)$ to generate phasic component. The tonic component is represented as a convolution between a signal representing the weights in different time instances for the $q(t)$ and a function $\psi(t)$ denoting the smooth variation. $\nu(t)$ represents the measurement error.

2.2.3 Discrete Model

If SC is periodically sampled with a period of T_y for M measurements, we can write the discrete observation equation as follows,

$$y_k = y_p(kT_y) + y_s(kT_y) + \nu_k, \tag{6}$$

where $k \in \{1, 2, \cdots, M\}$ and ν_k represents the discrete measurement errors. We model ν_k as a zero mean Gaussian random variable. As we are interested in estimating the model unknowns, we write the discrete model for y_k as follows based on (3) and (5),

$$y_k = \underbrace{a_k y_{p_0} + \mathbf{b}_k \mathbf{u}}_{\text{phasic}} + \underbrace{\mathbf{c}_k \mathbf{q}}_{\text{tonic}} + \nu_k, \tag{7}$$

where $a_k = e^{-\frac{kT_y}{\tau_d}}$, $\mathbf{b}_k = \big[h_{\boldsymbol{\tau}}(kT_y)\ h_{\boldsymbol{\tau}}(kT_y - T_u)\ \cdots\ h_{\boldsymbol{\tau}}(T_u)\ \underbrace{0\ \cdots\ 0}_{N-\frac{kT_y}{T_u}}\big]^\top$, $\mathbf{c}_k = \big[\psi(kT_y + \Lambda_s)\ \psi(kT_y)\ \psi(kT_y - \Lambda_s)\ \cdots\ \psi(kT_y - (P-1)\Lambda_s)\big]^\top$; $\mathbf{u} = [u_1\quad u_2\quad \cdots\quad u_N]^\top$ represents a sparse vector containing all the input neural stimuli amplitudes over the entire signal duration and $\mathbf{q} = [q_1\quad q_2\quad \cdots\quad q_N]^\top$ represents all the coefficients of the cubic B-spline basis functions and $y_{p_0} = y_p(0)$. Let $\mathbf{y} = [y_1\quad y_2\quad \cdots\quad y_M]^\top$, $\mathbf{A}_\tau = [a_1\quad a_2\quad \cdots\quad a_M]^\top$, $\mathbf{B}_\tau = [\mathbf{b}_1\quad \mathbf{b}_2\quad \cdots\quad \mathbf{b}_M]^\top$, $\mathbf{C} = [\mathbf{c}_1\quad \mathbf{c}_2\quad \cdots\quad \mathbf{c}_M]^\top$, and $^\circ = [\nu_1\quad \nu_2\quad \cdots\quad \nu_M]^\top$. As y_{p_0} is unknown, we also consider it as an unknown parameter. Therefore, we define a new parameter vector $\theta = [\ \boldsymbol{\tau}^\top\quad y_{p_0}\ ]^\top$, which we plan to estimate. We assume, $T_y = LT_u$, where L is an integer. Now the sampled data vector $\mathbf{y}$ is related to the sparse vector $\mathbf{u}$ representing the neural stimuli through the following equation,

$$\mathbf{y} = \underbrace{\mathbf{A}_\tau y_{p_0} + \mathbf{B}_\tau \mathbf{u}}_{\text{phasic}} + \underbrace{\mathbf{C}\mathbf{q}}_{\text{tonic}} + \boldsymbol{\nu}. \tag{8}$$

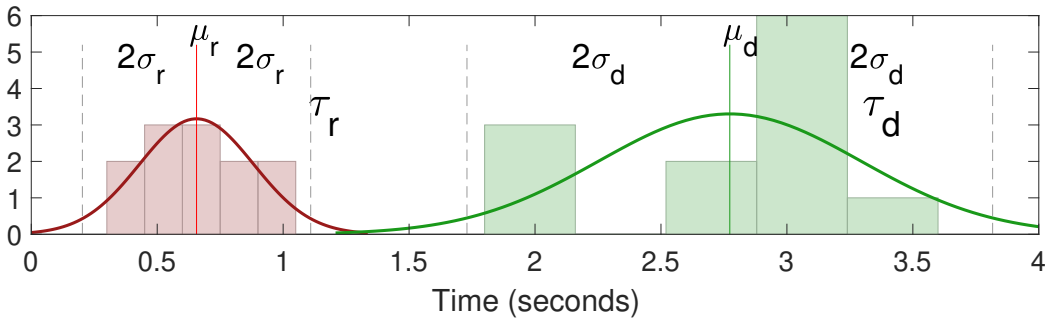

Figure 4: **Histograms of the Estimated SCR Shape Parameters.**

2.2.4 Priors on SCR Shape Parameters

Different SCR shape parameters have been explored for deconvolution in several studies [21, 23]. Previously, prior knowledge on the SCR shapes helped the development of fixed-parameter based approaches [21, 23]. However, the use of fixed SCR shape parameters makes it very difficult to obtain accurate estimation. On the contrary, the manual selection of the

SCR shape parameters can be very cumbersome and time-consuming. Recent advancements of the sparse system identification based approaches iterate between sparse neural stimuli estimation and SCR shape parameters estimation step in a coordinate descent manner [18, 52, 53, 54]. In our previous study in [8], we incorporate tonic component separation along with the estimation of the SCR shape parameters. The approach showed promising results in separating the tonic component along with finding a solution for the neural stimuli and SCR shape parameters. However, this might not hold in a worst-case scenario. In some cases, the minimum might not be achieved inside the physiologically feasible set when the problem has many degrees of freedom, and it might be achieved on the boundaries. Moreover, additional flexibility of estimation SCR shape parameters in the optimization formulation may lead to over-fitting [63]. To avoid such scenarios, we include physiological priors while solving the optimization problem similar to [64]. We assume that the individual SCR shape parameters are Gaussian distributed with some mean and variance. Figure 4 shows the distribution of the estimated parameters in our previous work [54]. In Figure 4, the red and green bar plots correspond to the histogram plots of the estimated rise time τ_r and decay time τ_d in [54], respectively. Furthermore, the red and green curve correspond to the corresponding fitted normal distribution probability distribution function. Finally, the red and green vertical lines correspond to the locations of the means μ_r and μ_d of the corresponding distributions, respectively. σ_r and σ_d denote the stand deviations of the respective distributions. Later, we use this information as a prior in the optimization formulation.

2.2.5 Pre-processing

The SC is recorded with a sampling frequency of 100 Hz. We use the same approach to remove the large discontinuities as in our previous work [54]. As the very first step of the pre-processing, we detect the large discontinuities in the recorded SC data by detecting peaks on the absolute difference of the raw SC signal. We chose a prominence value of 0.1

for peak detection. As the large discontinuities are usually due to the noise and artifacts, we choose the prominence parameter such that it does not capture any SCR as a discontinuity. After detecting a discontinuity, we discard a small patch of 0.5 seconds while keeping the discontinuity in the middle of the patch. We use a cubic B-spline interpolation to fill in the empty space after discarding the patch. We then filter the signal using a low pass filter with a cut-off frequency of 0.5 Hz to discard the high-frequency noise as the SC signal is known to be band-limited to 0.5 Hz [65, 53, 52]. Next, we down-sample the filtered signal to achieve 2 Hz sampling frequency (i.e. $T_y = 0.5$ seconds). We would like to recover $\mathbf{u}$ with 4 Hz sampling frequency (i.e. $T_u = 0.25$ seconds).

2.2.6 Estimation

Optimization Problem Formulation. We use the same approach as in our previous work [54] for pre-processing step which is provided in Section A.1. After pre-processing, we obtain y with 2 Hz sampling frequency (i.e. $T_y = 0.5$ seconds). We would like to recover $\mathbf{u}$ with 4 Hz sampling frequency (i.e. $T_u = 0.25$ seconds). In order to estimate $\mathbf{u}$, $\boldsymbol{\theta}$, and $\mathbf{q}$, using discrete representation in (8), we formulate the following optimization problem while assuming the sparsity constraint on $\mathbf{u}$ and constraining tonic component as always less than or equal to the SC signal (i.e., $\mathbf{Cq} \preccurlyeq \mathbf{y}$):

$$\begin{aligned} &\underset{\boldsymbol{\theta},\mathbf{u},\boldsymbol{q}}{\text{minimize}}\ J(\boldsymbol{\theta},\mathbf{u},\boldsymbol{q}) = \frac{1}{2}||\mathbf{y} - \mathbf{A}_\tau y_{p_0} - \mathbf{B}_\tau \mathbf{u} - \mathbf{Cq}||_2^2 + \lambda_1 ||\mathbf{q}||_2^2 \\ &\text{subject to} \quad \boldsymbol{\tau}^{\min} \preccurlyeq \boldsymbol{\tau} \preccurlyeq \boldsymbol{\tau}^{\max}, 0 \leq y_{p_0} \leq y_1, \\ &\qquad\qquad \mathbf{u} \succcurlyeq 0, ||\mathbf{u}||_0 \ll N, \mathbf{Cq} \preccurlyeq \mathbf{y}, \end{aligned} \tag{9}$$

where $\boldsymbol{\tau}^{\max}$ and $\boldsymbol{\tau}^{\min}$ are the upper and lower bound of the SCR shape parameters. Here, we include the l_2-norm penalization term with regularization parameter λ_1 to avoid over-fitting while solving for the tonic component coefficients $\mathbf{q}$. The above optimization formulation is a sparse recovery problem as $||\mathbf{u}||_0 \ll M < N$, where M is the number of samples in $\mathbf{y}$.

We encourage the sparsity for $\mathbf{u}$ with l_p-norm ($0 < p \leq 2$) regularization as a relaxation to the l_0-norm. We re-write the optimization problem as follows,

$$\begin{aligned} \underset{\boldsymbol{\theta},\mathbf{u},\boldsymbol{q}}{\text{minimize}} \quad & J(\boldsymbol{\theta},\mathbf{u},\boldsymbol{q}) = \frac{1}{2}||\mathbf{y} - \mathbf{A}_\tau y_{p_0} - \mathbf{B}_\tau \mathbf{u} - \mathbf{C}\mathbf{q}||_2^2 \\ & \qquad + \lambda_1 ||\mathbf{q}||_2^2 + \lambda_2 ||\mathbf{u}||_p^p \\ \text{subject to} \quad & \boldsymbol{\tau}^{\min} \preccurlyeq \boldsymbol{\tau} \preccurlyeq \boldsymbol{\tau}^{\max}, 0 \leq y_{p_0} \leq y_1, \\ & \mathbf{u} \succcurlyeq 0,\ \mathbf{C}\mathbf{q} \preccurlyeq \mathbf{y}, \end{aligned} \tag{10}$$

where λ_2 is a regularization parameter which determines the sparsity level for $\mathbf{u}$. We can solve the inverse problem of finding a non-negative $\mathbf{u}$ in (10) with a specific sparsity level using the iterative least squares (IRLS) approach Focal Underdetermined System Solver (FOCUSS+) algorithm [66].

Finally, inspired by the work in [64], we also consider the priors on SCR shape parameters based on the estimations in [54]. We assume that among different individual the rise times τ_r and decay times τ_d are Gaussian distributed with means μ_r and μ_d with corresponding standard deviations σ_r and σ_d, respectively. The optimization formulation with the priors on the SCR shape parameters becomes as follows:

$$\begin{aligned} \underset{\boldsymbol{\theta},\mathbf{u},\boldsymbol{q}}{\text{minimize}} \quad & J(\boldsymbol{\theta},\mathbf{u},\boldsymbol{q}) = \frac{1}{2}||\mathbf{y} - \mathbf{A}_\tau y_{p_0} - \mathbf{B}_\tau \mathbf{u} - \mathbf{C}\mathbf{q}||_2^2 \\ & \qquad + \lambda_1 ||\mathbf{q}||_2^2 + \lambda_2 ||\mathbf{u}||_p^p \\ & + \frac{\lambda_3}{2\sigma_r^2}||\tau_r - \mu_r||_2^2 + \frac{\lambda_4}{2\sigma_d^2}||\tau_d - \mu_d||_2^2 \\ \text{subject to} \quad & \boldsymbol{\tau}^{\min} \preccurlyeq \boldsymbol{\tau} \preccurlyeq \boldsymbol{\tau}^{\max}, 0 \leq y_{p_0} \leq y_1, \mathbf{u} \succcurlyeq 0,\ \mathbf{C}\mathbf{q} \preccurlyeq \mathbf{y}, \end{aligned} \tag{11}$$

where λ_3 and λ_4 are the regularization parameters. In this work, we use $\lambda_3 = \lambda_4 = 1 \times 10^{-1}$. We select $\mu_r = 0.650571$, $\mu_d = 2.77325$, $\sigma_r = 0.212443$ and $\sigma_d = 0.521739$ based on the results in [54].

Generalized Cross-Validation for λ_1 and λ_2. We used the following GCV function to have a valid definition for tall matrix $\mathbf{C}$ for estimating λ_1 [67],

$$\begin{aligned} \underset{\lambda_1}{\text{minimize}}\ G_1(\lambda_1) &= \frac{M||(\mathbf{I}-\mathbf{H}_{\lambda_1})\hat{\boldsymbol{y}}_s||_2^2}{(\text{Trace}(\mathbf{I}-\mathbf{H}_{\lambda_1}))^2} \\ \text{subject to} \qquad & \mathbf{0} \leq \lambda_1 \leq 1\times 10^{-4}, \end{aligned} \tag{12}$$

where $\hat{\boldsymbol{y}}_s = (\mathbf{y} - \mathbf{A}_\tau y_{p_0} - \mathbf{B}_\tau \mathbf{u})$ and $\mathbf{H}_{\lambda_1}$ is the influence matrix. For this case, $\mathbf{H}_{\lambda_1} = \mathbf{C}(\mathbf{C}^\top\mathbf{C} + \lambda_1\mathbf{I})\mathbf{C}^\top$.

FOCUSS+ allows us to obtain a solution for $\mathbf{u}$ such that the number of non-zero elements is predefined. We use FOCUSS+ for the initialization step. Once a reasonable initialization has been obtained, in each iteration of the IRLS algorithm, we use GCV for estimating an appropriate regularization parameter λ_2 similar to [20, 19, 18, 52]. This combination of GCV and FOCUSS+ algorithm is known as GCV-FOCUSS+ [68]. Zdunek *et al.* [68] used the following optimization formulation with singular value decomposition (SVD) for GCV:

$$\begin{aligned} \underset{\lambda_2}{\text{minimize}}\ G_2(\lambda_2) &= \frac{\left[M\sum_{i=1}^{M}\gamma_i^2\left(\frac{\lambda_2}{\sigma_i^2+\lambda_2}\right)^2\right]}{\left[\sum_{i=1}^{M}\left(\frac{\lambda_2}{\sigma_i^2+\lambda_2}\right)^2\right]} \\ \text{subject to} \qquad & \mathbf{0} \leq \lambda_2 \leq 1\times 10^{-4}, \end{aligned} \tag{13}$$

where $\boldsymbol{\gamma} = \mathbf{R}^\top\mathbf{y}_\tau = \begin{bmatrix} \gamma_1 & \gamma_2 & \cdots & \gamma_M \end{bmatrix}^\top$ with $\mathbf{y}_\tau = \mathbf{y} - \mathbf{A}_\tau y_{p_0} - \mathbf{C}\mathbf{q}$, and $\mathbf{B}_\tau\mathbf{P}_{\mathbf{u}}^{\frac{1}{2}} = \mathbf{R}\boldsymbol{\Sigma}\mathbf{Q}^\top$ with $\mathbf{P}_{\mathbf{u}} = \text{diag}(|\text{u}_i|^{2-p})$ and $\boldsymbol{\Sigma} = \text{diag}\{\sigma_i\}$; $\mathbf{R}$ and $\mathbf{Q}$ are unitary matrices and σ_i's are the singular values of $\mathbf{B}_\tau\mathbf{P}_{\mathbf{u}}^{\frac{1}{2}}$. The details of FOCUSS+ and GCV-FOCUSS+ is given below.

2.2.7 FOCUSS+ Algorithm

FOCUSS+ [66] solve for a non-negative $\mathbf{u}$ with n_u non-zero elements while minimizing the following optimization problem,

$$\underset{\mathbf{u}\succcurlyeq 0}{\text{minimize}} \quad \frac{1}{2}||\mathbf{y} - \mathbf{A}_{\boldsymbol{\tau}} y_{p_0} - \mathbf{B}_{\boldsymbol{\tau}}\mathbf{u} - \mathbf{C}\mathbf{q}||_2^2 + \lambda_2 ||\mathbf{u}||_p^p.$$

For $r = 0, 1, 2, \cdots$, FOCUSS+ works as follows:

1. $\mathbf{P}_{\mathbf{u}}^{(r)} = \text{diag}(|\mathbf{u}_i^{(r)}|^{2-p})$

2. $\lambda_2^{(r)} = \left(1 - \frac{||\mathbf{y}-\mathbf{A}_{\boldsymbol{\tau}} y_0 - \mathbf{B}_{\boldsymbol{\tau}}\mathbf{u} - \mathbf{C}\mathbf{q}||_2}{||\mathbf{y}-\mathbf{A}_{\boldsymbol{\tau}} y_0 - \mathbf{C}\mathbf{q}||_2}\right)\lambda_2^{\max}, \quad \lambda_2 > 0$

3. $\mathbf{u}^{(r+1)} = \mathbf{P}_{\mathbf{u}}\mathbf{B}_{\boldsymbol{\tau}}^{\top}(\mathbf{B}_{\boldsymbol{\tau}}\mathbf{P}_{\mathbf{u}}\mathbf{B}_{\boldsymbol{\tau}}^{\top} + \lambda\mathbf{I})^{-1}(\mathbf{y} - \mathbf{A}_{\boldsymbol{\tau}} y_0 - \mathbf{C}\mathbf{q})$

4. $\mathbf{u}_i^{(r+1)} \leq 0 \rightarrow \mathbf{u}_i^{(r+1)} = 0$

5. After iterating for half of the total number of iteration:

   - Detect the impulses having time distances less than the selected minimum peak to peak distance Δ_p. Retain only the largest impulses among the adjacent impulses within Δ_p window.
   - If $||\mathbf{u}^{(r+1)}||_0 > n_{\mathbf{u}}$, select $n_{\mathbf{u}}$ largest values of elements of $\mathbf{u}^{(r+1)}$ and set all other elements to zero.

6. Iterate

In this study, we used $\Delta_p = 1$ second. We select $n_{\mathbf{u}} = (\text{number of peaks in } \mathbf{y}) + 20$.

2.2.8 GCV-FOCUSS+ Algorithm

Similar to the FOCUSS+, GCV-FOCUSS+ also solve for a non-negative $\mathbf{u}$ minimizing the following optimization problem,

$$\underset{\mathbf{u}\succcurlyeq 0}{\text{minimize}} \quad \frac{1}{2}||\mathbf{y} - \mathbf{A}_{\boldsymbol{\tau}} y_{p_0} - \mathbf{B}_{\boldsymbol{\tau}}\mathbf{u} - \mathbf{C}\mathbf{q}||_2^2 + \lambda_2 ||\mathbf{u}||_p^p.$$

However, unlike FOCUSS+, GCV-FOCUSS+ does not solve for $\mathbf{u}$ with a fixed number of non-zero elements. Instead, it utilizes the GCV technique in order to identify a reasonable number of non-zero elements $\mathbf{u}$, i.e., sparsity level. We use the GCV technique for choosing the regularization parameter λ_2 to balance between capturing the noise and the sparsity level of $\mathbf{u}$. Zdunek *et al.* [68] utilized the GCV technique for estimating the value of λ for the FOCUSS+ [66] algorithm with the singular value decomposition as follows:

$$\begin{aligned} &\underset{\lambda_2}{\text{minimize}}\ G_2(\lambda_2) = \frac{\left[M \sum_{i=1}^{M} \gamma_i^2 \left(\frac{\lambda_2}{\sigma_i^2+\lambda_2}\right)^2\right]}{\left[\sum_{i=1}^{M} \left(\frac{\lambda_2}{\sigma_i^2+\lambda_2}\right)^2\right]} \\ &\text{subject to} \qquad \mathbf{0} \leq \lambda_2 \leq 1 \times 10^{-4}, \end{aligned} \tag{14}$$

where $\boldsymbol{\gamma} = \mathbf{R}^\top(\mathbf{y} - \mathbf{A}_\tau y_{p_0} - \mathbf{C}\mathbf{q}) = \begin{bmatrix} \gamma_1 & \gamma_2 & \cdots & \gamma_M \end{bmatrix}^\top$ with $\mathbf{B}_\tau \mathbf{P}_{\mathbf{u}}^{\frac{1}{2}} = \mathbf{R}\boldsymbol{\Sigma}\mathbf{Q}^\top$ with $\mathbf{P}_{\mathbf{u}} = \text{diag}(|\text{u}_i|^{2-p})$ and $\boldsymbol{\Sigma} = \text{diag}\{\sigma_i\}$; $\mathbf{R}$ and $\mathbf{Q}$ are unitary matrices and the σ_i's are the singular values of $\mathbf{B}_\tau \mathbf{P}_{\mathbf{u}}^{\frac{1}{2}}$; M is the total number of data points in $\mathbf{y}$. For $r = 0, 1, 2, \cdots$, GCV-FOCUSS+ works as follows [19]:

1. $\mathbf{P}_{\mathbf{u}}^{(r)} = \text{diag}(|\mathbf{u}_i^{(r)}|^{2-p})$
2. $\mathbf{u}^{(r+1)} = \mathbf{P}_{\mathbf{u}}\mathbf{B}_{\boldsymbol{\tau}}^\top(\mathbf{B}_{\boldsymbol{\tau}}\mathbf{P}_{\mathbf{u}}\mathbf{B}_{\boldsymbol{\tau}}^\top + \lambda_2 \boldsymbol{I})^{-1}\boldsymbol{y}_\theta$
3. $\mathbf{u}_i^{(r+1)} \leq 0 \rightarrow \mathbf{u}_i^{(r+1)} = 0$
4. $\lambda_2^{(r+1)} = \underset{0\leq\lambda_2\leq 1\times 10^{-4}}{\text{argmin}} G_2(\lambda_2)$

5. Iterate until convergence

We use a coordinate descent algorithm similar to our previous work in [8] to solve the optimization problem in (11). The detailed algorithm is provided in Section A.1. We run the algorithm for several random initializations of $\boldsymbol{\theta}$ and take the result that minimizes the least square error between the observed and reconstructed signal.

2.2.9 Coordinate Descent Approach

The optimization formulation for the proposed deconvolution approach is follows:

$$\begin{aligned} \underset{\boldsymbol{\theta},\mathbf{u},\boldsymbol{q}}{\text{minimize}} \quad & J(\boldsymbol{\theta},\mathbf{u},\boldsymbol{q}) = \frac{1}{2}||\mathbf{y}-\mathbf{A}_\tau y_{p_0}-\mathbf{B}_\tau\mathbf{u}-\mathbf{C}\mathbf{q}||_2^2 \\ & \qquad + \lambda_1||\mathbf{q}||_2^2+\lambda_2||\mathbf{u}||_p^p \\ & + \frac{\lambda_3}{2\sigma_r^2}||\tau_r-\mu_r||_2^2+\frac{\lambda_4}{2\sigma_d^2}||\tau_d-\mu_d||_2^2 \qquad (15) \\ \text{subject to} \quad & \boldsymbol{\tau}^{\min} \preccurlyeq \boldsymbol{\tau} \preccurlyeq \boldsymbol{\tau}^{\max}, 0 \le y_{p_0} \le y_1, \mathbf{u} \succcurlyeq 0,\ \mathbf{C}\mathbf{q} \preccurlyeq \mathbf{y}, \end{aligned}$$

We solve the optimization problem using the following coordinate descent algorithm:

We run the algorithm for several random initial values of system parameters. Finally, we choose the estimated values that minimize the least square error $\frac{1}{2}||\mathbf{y}-\mathbf{A}_\tau y_{p_0}-\mathbf{B}_\tau\mathbf{u}-\mathbf{C}\mathbf{q}||_2^2$.

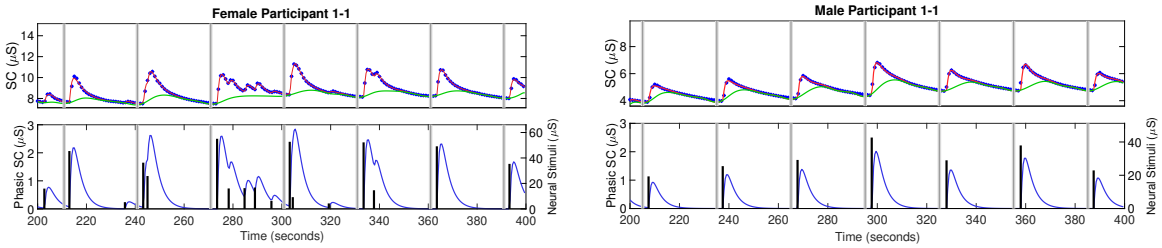

Figure 5: **Estimated Decomposition of the Experimental SC Signals for One Female Participant and One Male Participant.**

.

Algorithm: Generalized-Cross-Validation-Based Block Coordinate Descent

(a) Let $j = 0$. Initialize $\tilde{\boldsymbol{\theta}}^0$ by sampling a uniform random variable on $[0.10, 1.5]$ for $\tilde{\tau}_r^{(0)}$, on $[1.5, 6]$ for $\tilde{\tau}_d^{(0)}$, and on $[0, y_1]$ for y_{p_0}; also initialize $\tilde{\mathbf{q}}^0$ by sampling P number of Gaussian random variables with mean 0.1 and standard deviation of 0.02.

(b) Set $j = j + 1$.

(c) Set $\boldsymbol{\theta} = \tilde{\boldsymbol{\theta}}^{(j-1)}$ and $\mathbf{q} = \tilde{\mathbf{q}}^{(j-1)}$; use FOCUSS+ [66] to solve the inverse problem in (11) to find the stimuli $\tilde{\mathbf{u}}^{(j)}$ by initializing $\tilde{\mathbf{u}}^{(j-1)}$ at a vector of all ones.

(d) Set $\mathbf{u} = \tilde{\mathbf{u}}^{(j)}$ and $\mathbf{q} = \tilde{\mathbf{q}}^{(j-1)}$; use the interior point method to minimize the optimization problem in (11) to solve for $\tilde{\boldsymbol{\theta}}^{(j)}$ by initializing the optimization problem at $\tilde{\boldsymbol{\theta}}^{(j-1)}$.

(e) Set $\boldsymbol{\theta} = \tilde{\boldsymbol{\theta}}^{(j)}$ and $\mathbf{u} = \tilde{\mathbf{u}}^{(j)}$; use the interior point method and minimize the optimization problem in (11) to solve for $\tilde{\mathbf{q}}^{(j)}$ by initializing the optimization problem at $\tilde{\mathbf{q}}^{(j-1)}$.

(f) Repeat between steps (b)-(e) until $j = 30$.

(g) Let $i = 0$. Set $\hat{\boldsymbol{\theta}}^0 = \tilde{\boldsymbol{\theta}}^{(j)}$, $\hat{\mathbf{u}}^0 = \tilde{\mathbf{u}}^{(j)}$, and $\hat{\mathbf{q}}^0 = \tilde{\mathbf{q}}^{(j)}$.

(h) Set $i = i + 1$.

(i) Set $\boldsymbol{\theta} = \hat{\boldsymbol{\theta}}^{(i-1)}$ and $\mathbf{q} = \hat{\mathbf{q}}^{(i-1)}$; use GCV-FOCUSS+ [68] to solve the inverse problem in (11) to find the stimuli $\hat{\mathbf{u}}^{(i)}$ by initializing at $\hat{\mathbf{u}}^{(i-1)}$.

(j) Set $\mathbf{u} = \hat{\mathbf{u}}^{(i)}$ and $\mathbf{q} = \hat{\mathbf{q}}^{(i-1)}$; use the interior point method to minimize the optimization problem in (11) to solve for $\hat{\boldsymbol{\theta}}^{(i)}$ by initializing at $\hat{\boldsymbol{\theta}}^{(i-1)}$.

(k) Set $\boldsymbol{\theta} = \hat{\boldsymbol{\theta}}^{(i-1)}$ and $\mathbf{u} = \hat{\mathbf{u}}^{(i-1)}$; solve (12) to obtain λ_1, and use the interior point method to minimize the optimization problem in (11) to solve for $\hat{\mathbf{q}}^{(i)}$ by initializing at $\hat{\mathbf{q}}^{(i-1)}$.

(l) Iterate between (h)-(k) until convergence.

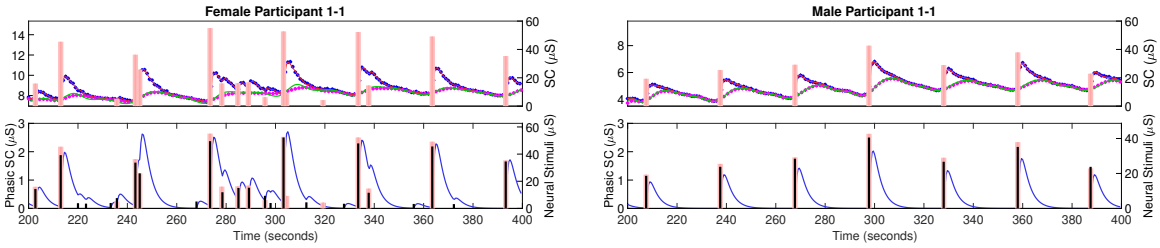

Figure 6: **Estimated Decomposition of the Simulated SC Signals with 25 dB SNR for One Female Participant and One Male Participant.**

.

2.3 Results

2.3.1 Experimental Study

We have applied our approach and decompose the SC measurements recorded from 109 participants from five datasets provided in Table 1 and separate the tonic components $y_s(t)$

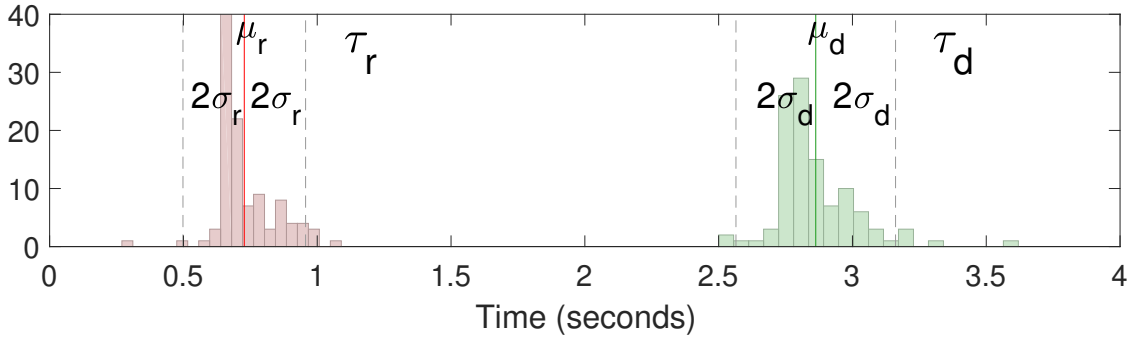

Figure 7: **Histograms of Estimated SCR Shape Parameters using Our Approach.**

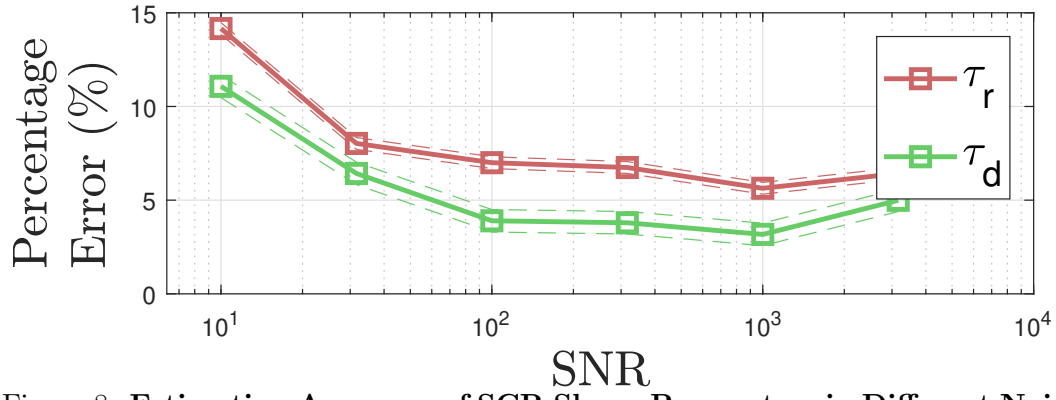

Figure 8: **Estimation Accuracy of SCR Shape Parameters in Different Noise Levels.**

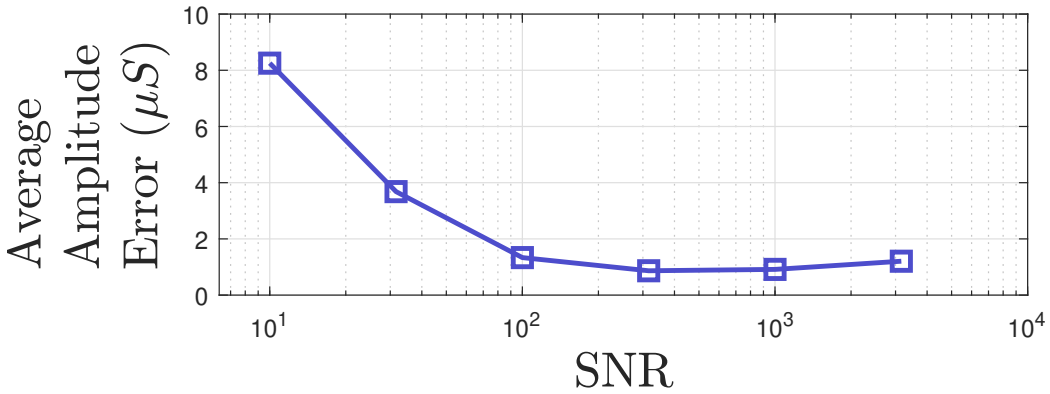

Figure 9: **Average Amplitude Error of Estimated Neural Stimuli in Different Noise Levels.**

and phasic components $y_p(t)$. During each decomposition, we have recovered the underlying neural stimuli $u(t)$, rise time (τ_r), decay time (τ_d), and the initial condition of the phasic component y_{p_0}. We have considered the signal segment from 200 seconds to 400 seconds

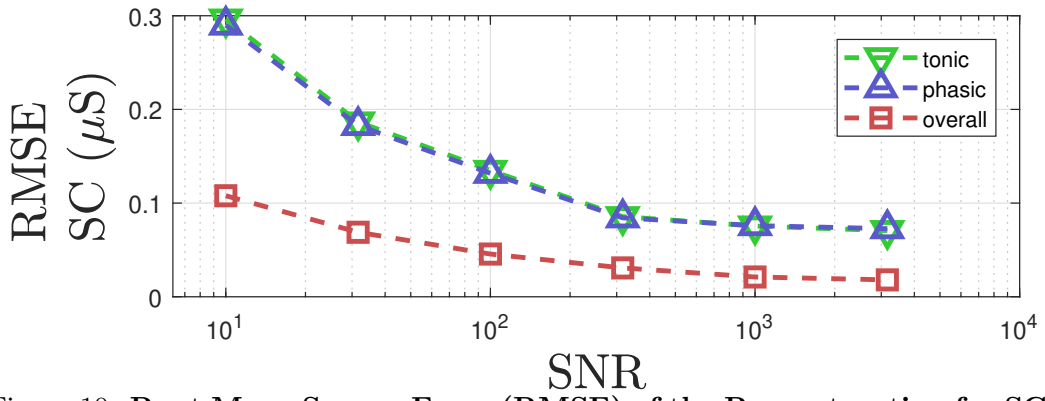

Figure 10: **Root Mean Square Error (RMSE) of the Reconstruction for SC signal and Corresponding Components with Respect to the Ground Truth.**

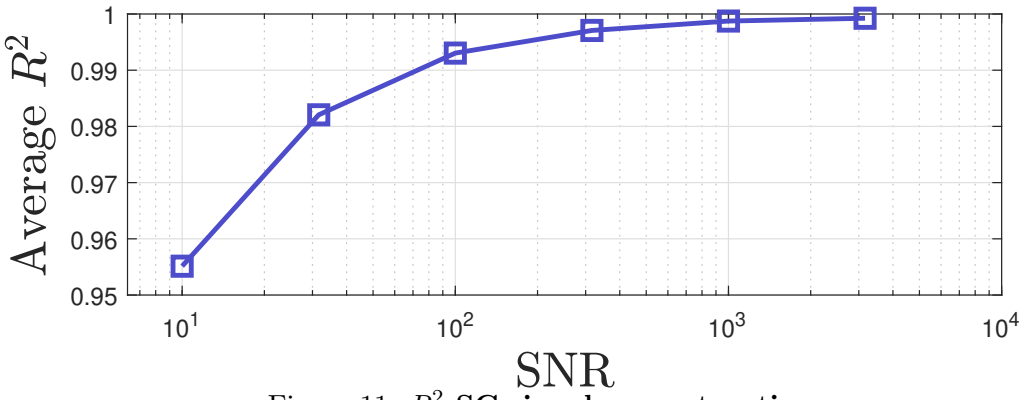

Figure 11: R^2 **SC signal reconstruction.**

for our analysis for Dataset 1, 2, 4, and 5. For Dataset 3, we have considered the signal segment from 100 seconds to 300 seconds for our analysis as the experimental duration for some of the participants is shorter than 400 seconds. Figure 5 shows example results for one female participant and one male participant. In each of the panels in Figure 5: i) the top sub-panel shows the experimental SC signal (blue stars), the reconstructed SC signal (red curve), the estimated tonic component (green curve), and the timings of the auditory stimulations (gray vertical lines); ii) the bottom sub-panel shows the estimated phasic component (blue curve), estimated neural stimuli timings and amplitudes (black vertical lines) due to SNS activation and the timings of the auditory stimuli (gray vertical lines). The number before the hyphen in the participant ID represents the dataset ID based on Table 1. Figure 5 shows that we are successfully able to detect the SNS activation after

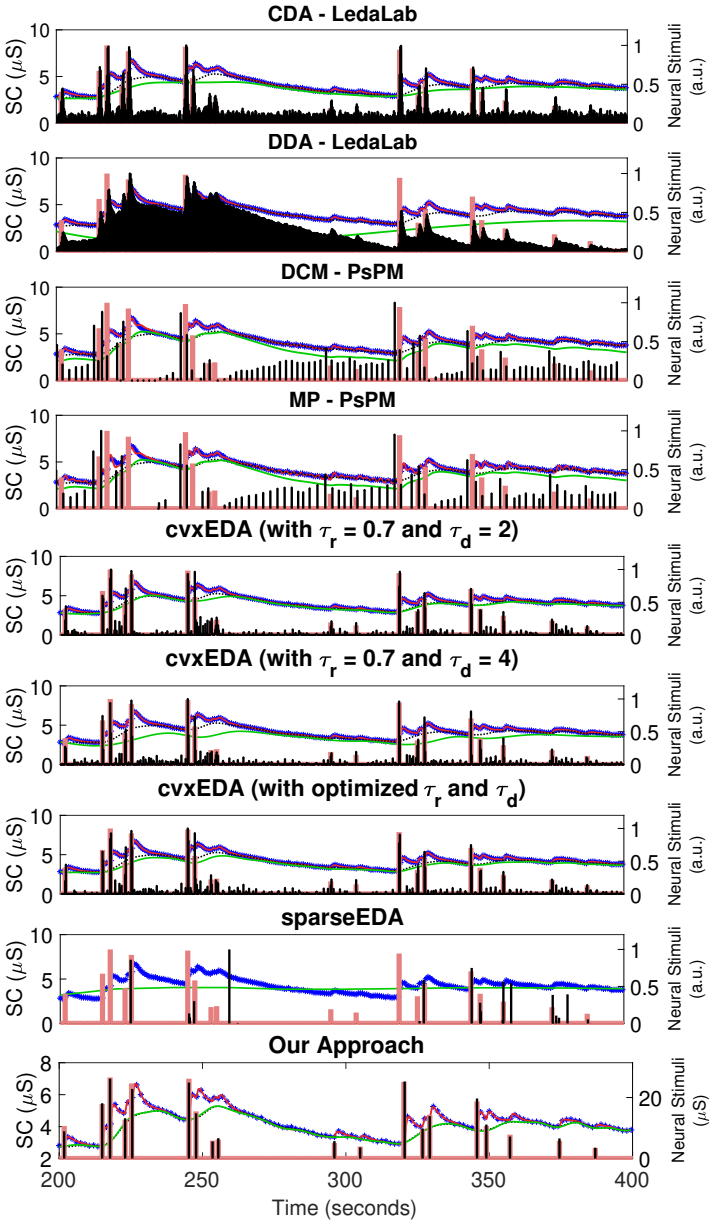

Figure 12: **Performance Comparison of Proposed Approach with Existing Approaches for Simulated Data.**

each auditory stimulation. The rest of the results from experimental data are provided in Section A.1. The estimated rise time (τ_r), decay time, number of pulses ($||\mathbf{u}||_0$), multiple correlation coefficient (R^2), regularization parameters (λ_1 and λ_2), deconvolution run-times are provided in Section A.1 for all 26 participants from Dataset 1.

Figure 7 shows the histogram of the estimated SCR shape parameters from 109 participants. In Figure 7, the red and green bar plots correspond to the histogram plots of the estimated rise time τ_r and decay time τ_d, respectively. Red and green vertical line correspond to the locations of the means μ_r and μ_d of the corresponding histograms, respectively. σ_r and σ_d denote the corresponding standard deviations, respectively. Means of the histograms are estimated to be $\mu_r = 0.7274$ and $\mu_d = 2.8629$ seconds for rise times and decay times, respectively. Corresponding standard deviations are $\sigma_r = 0.1146$ and $\sigma_d = 0.1491$ seconds, respectively. The R^2 values are greater than 0.95 for all participants. The high values of R^2 SC data suggest that our proposed algorithm can successfully decompose the SC recording in its constituent components and separate the tonic and phasic components. The corresponding quantile-quantile plots for the model residuals are also given in Section A.1. The quantile-quantile plots approximately follow a straight line denoting the Gaussian structure in the residuals. Slight deviations from the straight line also suggest that there is a scope of improvement in the system model.

To perform an efficacy analysis of how our algorithm performs in distinguishing between event-related and non-event-related SCRs in Dataset 1, we have derived receiver operating characteristics (ROC) curves [69]. We label all the SCRs that have been detected within 5 seconds after auditory stimuli as the event-related SCRs (positive class). The rest of the detected SCRs are labeled as the non-event-related SCRs (negative class). We consider the amplitudes of the SCRs as the classification scores within the subjects for obtaining the ROC curves [69, 70]. The results show that the ROC curves have the area under the curve (AUC) ranging from 0.5611 to 1 with a median of 0.8636 and a mean of 0.9130. Moreover, we normalized the estimated $\mathbf{u}$ for each participant and combine them to obtain an overall ROC curve. The corresponding overall AUC is 0.864 for Dataset 1. All the ROC curves are provided in Section A.1.

2.3.2 Simulated Study

We simulate data with noise to investigate the efficacy of our approach. We use the results obtained from Dataset 1 to simulate data for 26 participants. In this case, we have ground truths to compare with the estimated unknowns. Our deconvolution approach successfully estimates neural stimuli along with the SCR shape parameters, i.e. the physiological system parameters. Figure 6 shows example deconvolution from simulated data for one female and one male participants with 25 dB SNR with respect to phasic component. In each of the panels in Figure 6, i) the top sub-panel shows the ground truth for SC signal (blue stars), the reconstructed SC signal (red curve), the ground truth for tonic component (red stars), the estimated tonic component (red curve), and ground truth for the neural stimuli (pink vertical lines); ii) the bottom sub-panel shows the estimated phasic component (blue curve), estimated neural stimuli timings and amplitudes (black vertical lines) due to SNS activation and the ground truth for the neural stimuli (gray vertical lines). The number before the hyphen in the participant ID represents the dataset ID based on Table 1.The minimum R^2 for the simulated data with 25 dB noise level is 0.9872. Figures, estimated system parameters ($\hat{\tau}_r$ and $\hat{\tau}_d$), estimated number of pulses ($||\hat{\mathbf{u}}||_0$), estimation errors, and the multiple correlation coefficients (R^2) for the results for all the simulated data with 25 dB SNR are provided in Section A.1.

We also simulate data with different noise levels to see how our approach performs in terms of estimating the unknowns and reconstructed signal. We have used the results obtained from the experimental recordings for all 26 participants to generate 26 signals for each level of noise. We have performed deconvolution to estimate the SCR shape parameters. Afterwards, we have calculated the percentage error for each of the participants. Figure 8 and 9 show how the average estimation error increase as the noise level is increased. In Figure 8, the red and green solid lines denotes the mean percentage error for rise times and decay times from simulated data with different noise levels. The dashed lines corresponds

to the 95% confidence interval. In Figure 9, The blue solid line denotes the average amplitude error of the neural stimuli from estimated data with different noise levels. We have defined the average amplitude error as $|||\tilde{\mathbf{u}}||_1 - ||\mathbf{u}||_1|/||\mathbf{u}||_0$, where $\tilde{\mathbf{u}}$ and $\mathbf{u}$ represent the estimated and the ground truth neural stimuli, respectively. The data is simulated using the obtained results from the all experimental data in Dataset 1. As noise is added to the phasic component prior to addition of tonic component, the SNR is given with respect to the phasic component. Similarly, Figure 10 shows how the reconstruction error decreases and Figure 11 shows how the R^2 value decreases with the increase in the noise level. In Figure 10, the green, blue and red dashed lines denote the RMSE for the reconstructed tonic component, phasic component and overall SC data in different noise levels. The data is simulated using the obtained results from the all experimental data in Dataset 1. As noise is added to the phasic component prior to addition of tonic component, the SNR is given with respect to the phasic component. In Figure 11, the blue solid line denotes the mean R^2 values for the reconstructed SC data with different noise levels. The data is simulated using the obtained results from the all experimental data in Dataset 1. As noise is added to the phasic component prior to addition of tonic component, the SNR is given with respect to the phasic component.

To compare our method with the other existing approaches, we have used synthetic simulated data. We have used the neural stimuli, the SCR shape parameters, and the cubic-spline coefficients obtained from the deconvolution of the experimental recordings of male subject six to simulate the data. We have added Gaussian random noise with 25 dB SNR with respect to the phasic component. We have simulated the data with two different sampling frequencies. We simulated data with 2 Hz sampling frequency for performing deconvolution with our approach. For other methods, we chose a 4 Hz sampling frequency. We specifically do this to show that even with lower sampling frequency, our algorithm performs reasonably well and able to obtain $\mathbf{u}$ with 4Hz resolution while performing in a

compressed sensing regime ($M < N$). Figure 12 shows the decomposition of tonic, phasic component, and recovered neural stimuli using CDA - LedaLab [29], DDA - LedaLab [21], DCM - PsPM [22], MP - PsPM [50], cvxEDA with three different configurations [23], sparsEDA [24], and our proposed approach. Each panel in Figure 12 shows the decomposition performance based on simulated SC signal with 25 dB noise. The panels from top to bottom show the results obtained using CDA - LedaLab [29], DDA - LedaLab [21], DCM - PsPM [22], MP - PsPM [50], cvxEDA with three different configurations [23], sparsEDA [24], and our proposed approach, respectively. In each panel, blue stars represent the simulated data, pink vertical lines represent the ground truth neural stimuli, black vertical lines represent the recovered neural stimuli, the green curve represents the tonic component, the black dotted curve represents the ground truth for the tonic component, and the red curve represents the reconstructed signal. The estimated neural stimuli for all the panels except for the last one are normalized from zero to one to avoid any amplitude scaling originating from different methods and to have a fair comparison. We have used default settings for the parameters for all the approaches except for cvxEDA and sparsEDA. For cvxEDA, we have used the knot size for cubic B-spline functions to be the same as our approach for a fair comparison. Further, we have considered three different configurations for τ_r and τ_d including optimized parameters from our approach for cvxEDA.We perform the comparison with different physiological parameters only with cvxEDA because it considers similar system modeling and optimization formulation as ours. Therefore, this comparison will be fair if carried out against cvxEDA. The results show there are differences in the solution for different selected parameters. In the case of sparsEDA, we have selected the minimum separation between two neural impulses and the threshold for the neural impulse amplitudes to be zero to have the most less sparse solution. DCM - PsPM and MP - PsPM perform linear band-pass filtering for removing the tonic component followed by a DC shift to avoid all the negative value in the phasic. We have performed the adjustments to the obtained results accordingly so that the visual comparison is fair. Qualitatively, the results

show that our algorithm is performing well in terms of capturing the neural stimuli related to the SCRs and discarding small spikes which are comparable to noise spikes. DCM - PsPM and MP - PsPM detects large pulses where there are no pulses mainly because the signal is distorted in the pre-processing step. As observed in Figure 12, other approaches except sparsEDA are providing less sparse solutions compared to the ground truth. Some of the pulses detected by these algorithms are capturing noise. In this case, our proposed approach is performing well in balancing between the sparsity level and discarding noise. On the other hand, sparsEDA is providing an overly sparse solution leading to missing some of the obvious neural impulses captured by all the other algorithms.

In order to perform further comparison between the deconvolution results from different algorithms, we have added noise noise to the raw experimental data. The noise level is selected in a way that the signal SNR is 25 dB for corresponding phasic component estimated during deconvolution. We performed deconvolution on six participants as example. The results are shown in Section A.1.

2.4 Discussions

Decomposition of SC signals into its constituents along with the estimation of the neural stimuli, the rise and decay times of the SCRs is challenging. The challenges includes identification of the sparsity level for the neural stimuli as well as the smoothness of the tonic component. An inaccurate estimation for the smoothness of the tonic component can make the estimation of rise times and decay times inaccurate. As least square formulation has many degrees of freedom, optimization without appropriate physiological constraints may lead to a problem that is not identifiable. The problem becomes much more challenging in the case of under-determined systems, i.e. when the $M < N$. Presence of the smallest amount of noise can lead the system response to a physiologically infeasible solution. We incorporate necessary physiologically plausible constraints to make the optimization problem tractable. Firstly, we consider the sparsity constraint on the neural stimuli. In our previous

works in [8, 53, 54, 52], we constrained the SCR shape parameters within physiologically feasible bounds ($\tau^{\min} = [0.10 \quad 1.5]^\top$ and $\tau^{\max} = [1.5 \quad 6]^\top$). In addition to that, we impose Gaussian priors on τ_r and τ_d. Further, we have chosen the regularization parameters λ_3 and λ_4 such that the solution for τ_r and τ_d do not converge to the boundary. To achieve that, we have first started with a very small value of λ_3 and λ_4 such 1×10^{-5} and ran deconvolution on random selected twelve participants from Dataset 1. However, for some of the participants, the solution for τ_r and τ_d converges to the boundary. Therefore, we gradually increase λ_3 and λ_4 by a factor of 10 until all the stagnation to boundary is avoided. Afterward, we fix the λ_3 and λ_4 for the rest of the 97 participants from all the five datasets. Figure 7 show that none of the estimated parameters are near the boundary constraint. We also impose constraints on the smoothness of the cubic B-spline basis function by including l_2-norm penalization. Finally, we incorporate the GCV technique [67] to have appropriate estimates of λ_1 and λ_2 to achieve a balance between capturing the data and residual error.

As we previously mentioned in [52], although the optimization problem in (11) is convex in terms of $\mathbf{u}$ and $\mathbf{q}$ [23, 8], it is non-convex for $\boldsymbol{\tau}$. During the iterations of coordinate descent, the solution may stagnate at local minima. The stagnation of solution at a local minima leads to an inaccurate separation of tonic and phasic components, some part of the tonic component might be captured in the phasic component. Therefore, we initialize the optimization problem with several random initializations for SCR shape parameters $\boldsymbol{\tau}$. Among all the deconvolution results using these random initializations, we choose the one that minimizes the least square error. The larger number of random initializations means a greater probability of obtaining global minima, i.e. there is a trade-off between the probability of obtaining the optimal solution and the number of random initializations. In this study, we have considered eight random initializations for the system parameters and we ran in the eight CPU cores in parallel. This way we reduce the probability of convergence to a local minimum. Although it is still possible to converge a sub-optimal solution, we have empirically demonstrated on experimental data collected from 109 participants shown

that our algorithm is performing well in terms of modeling the SCR shapes and reducing the number of the unwanted pulse due to incorrect shape parameters. Moreover, based on the simulated study, Figure 8 shows that our approach can reliably estimate the SCR shape parameters with only eight initializations for moderate noise levels.

In this study, we obtain $\mathbf{u}$ with a higher resolution than the recorded signal. For instance, in our study, the sparse vector $\mathbf{u}$ has a length of 800 with 4 Hz sampling frequency while the sampled signal has 400 samples with 2 Hz sampling frequency. We are specifically interested in the accurate timing and amplitude of the SNS activation rather than the phasic component. In contrast, we are more interested in the tonic component itself rather than its cubic B-spline coefficients as the exact cause and appropriate system theoretic modeling of tonic component is unknown. Further, as the body tries to regulate its skin moisture, i.e. the tonic component depending on the cooling demand in the body. Tonic component itself is an indication of the factor related to the thermoregulation rather than its coefficients. Therefore, we use much less number of coefficients in vector $\mathbf{q}$ in order to model the tonic components compared to $\mathbf{u}$. In this study, we have used 39 coefficients to model 200 seconds of SC signal.

Noise can corrupt SC signal, and sometimes small noise spikes can be comparable to the small insignificant SCRs. To avoid such cases, we used an internal threshold in each iteration of GCV-FOCUSS+ part while estimating $\mathbf{u}$. If an estimated non-zero element in $\mathbf{u}$ is smaller than the threshold, that particular value is set to be zero. In this study, we used 3 as the threshold. This threshold works well for almost all the experimental and simulated data. However, our algorithm has detected some small noise spikes as SCRs in simulated data for a few participants. The reason of detecting more spike for these signals is that there are more noise added to these signals compared to the other signals. Although we mentioned we have added noise so that SNR is 25 dB, the SNR value of the simulated data is with respect to phasic component. For these particular simulated signals, the phasic components have more energy compared to the other simulated signals. Because of this

corresponding noise power is also higher. Some noise peak amplitudes are comparable to noise and in few places they have been detected as SCRs. Furthermore, the estimation of tonic component is also slightly inaccurate in places where there is a noise spike that has been detected as an SCR. However, this only happens for a few badly condition cases where noise level is comparable to SCRs.

From our results, we can see the R^2 values are close to 1, denoting that model fits are very good in case of reasonable noise level. Quantile-quantile plots in Section A.1 also follow approximately a straight line. However, there are still slight deviations from the straight line in the quantile-quantile plots for a few experimental data although for simulated data there no such case. This indicates there is a scope of improvement in the system modeling. Specially modeling tonic component with arbitrary cubic B-spline function might not be the most effective way to model the tonic component. Therefore, there is a need for development of tonic component with systematic way based on physiology.

As three unknowns (i.e. $\mathbf{u}$, $\mathbf{q}$, and $\boldsymbol{\theta}$) have been solved in a coordinate descent manner along with the GCV technique to minimize the optimization problem in (11) with appropriate physiologically plausible solution, it takes more time to complete the deconvolution compared to some of the previous methods. The time elapsed for the deconvolution with our approach for Dataset 1 is provided in Section A.1. The deconvolution time required for LedaLab (CDA), LedaLab (DDA), PsPM (DCM), PsPM (MP), cvxEDA, sparsEDA, and our approach for the deconvolution comparison shown in Figure 12 is respectively 1.45 seconds, 8.05 seconds, 153.23 seconds, 0.3162 seconds, 0.211 seconds, 0.1563 seconds, and 89.95 seconds. The other approaches do not concurrently optimize the problem for the SCR shape parameters, the sparsity neural stimuli, and the smoothness level of the tonic component. Although our approach takes more time to deconvolve, our approach outperforms previous approaches in terms of balancing between discarding the noise and capturing significant SCRs.

Perhaps, the most appropriate way of evaluating a method would be to use a dataset that

contains the recording from the nerve endings to the sweat glands and the corresponding SC recording similar to the study in [71]. However, we could not perform such a comparison because of the unavailability of such datasets. Bach *et al.* [72] have suggested evaluating metrics by an algorithm's ability to separating the experimental event vs the non-events or the ability to separate a high-arousal condition. We have performed a similar analysis to show our algorithm's ability to be able to distinguish between separating the experimental event-related vs the non-event-related SCRs obtained corresponding ROC curves. Nevertheless, our algorithm is designed to capture the SCRs for emotional events as well as the spontaneous SCRs which might not be related to an emotional event but originating from the natural physiological control of the body. For example, visually it can be seen that for some participants, there are a lot more spontaneous pulses than the number of auditory stimuli, for some other participants the numbers of SCRs are a lot less than the numbers of provided stimuli. Therefore, there is a limitation in such an evaluation. Distinguishing between event-related and non-event-related SCRs will also heavily depend on how a detection scheme is devised for a specific algorithm and the scheme can be different for different algorithms to obtain the best performance. For example, some algorithms use some sort of thresholding as post-processing before performing the classification [22]. On the other hand, our evaluation does not involve any post-processing. Therefore, we did not perform any comparison based on such evaluation with other algorithms to avoid any unfair comparisons. The objective of the current study is not to show its ability to separate the event-related response but to perform a plausibility assessment with a large dataset of 109 participants and show its ability to capture any phasic response regardless of its reason for the occurrence. We have further demonstrated the performance evaluation of our approach in terms of estimating neural stimuli and the physiological system parameters in simulated data at different noise levels. Further, we qualitatively demonstrate how results from our approach compare with other approaches. The qualitative comparison shows that results are correlated, and our approach is performing better in terms of balancing between noise

reduction and capturing the underlying physiological phenomenon. Apart from the visual demonstration for comparisons with different previous algorithms, we have also included a list of estimated R^2 values and the estimated numbers of neural impulses from the noisy experimental data in Section A.1. The results show that almost the same R^2 is obtained by detecting a greater number of pulses which could be an indication of potential over-fitting for the other algorithms except for sparsEDA, where our algorithm has estimated fewer numbers of impulses but had the same level of model fit. However, the lack of comparative metrics between different algorithms can be considered as a limitation of the study.

3 Robust Inference of Autonomic Nervous System Activation using Skin Conductance Measurements: A Multi-Channel Sparse System Identification Approach

3.1 An Overview of Autonomic Nervous System Inference from Multi-channel Skin Conductance Measurement

Electrodermal activity (EDA) refers to any alteration in the electrical characteristics of the skin caused by salty sweat secretion. Hypothalamic control of sweating is primarily intended for thermoregulation of the human body. Apart from thermoregulation, sweating can also occur due to other physiological events including emotional arousal [53, 73]. Moreover, variations in skin conductance (SC), a measure of EDA, are highly correlated with emotions and can be used for interpreting emotional dysregulation and disturbances [74, 75]. Alterations in SC throughout the different skin regions are regulated by the autonomic nervous system (ANS) [76]. The analysis of SC time series assumed to be modulated by the ANS can potentially be used to track the mental health of an individual in order to prevent mental stress-related problems [77].

Walker *et al.* [31] reported that a large portion of deaths worldwide are attributable to mental health-related disorders. Regular tracking of problematic patterns of emotional regulation could potentially help prevent psychiatric disorders [35]. Physiological signals including electroencephalogram, electrocardiogram, respiration, functional near-infrared spectroscopy [47], and EDA, could be investigated to identify abnormal patterns of emotional regulation [48]. Day-to-day monitoring and tracking of emotional regulation require wearable implementations. However, a reliable, noise-robust monitoring system is challenging

This chapter was first presented in part at the 52nd Asilomar Conference on Signals, Systems, and Computers [53]. Chapter is mainly adopted from Amin, Md Rafiul, and Rose T. Faghih. "Robust inference of autonomic nervous system activation using skin conductance measurements: A multi-channel sparse system identification approach." IEEE Access 7 (2019): 173419-173437. [54].

and yet to be developed. A noise-robust personalized wearable mental health monitoring system could eventually lead to effective monitoring of mental health-related problems [78].

In another context, several recent studies have shown correlations between abnormal SC recordings due to diabetic neuropathy and other different diabetic diseases in different races [37, 38, 39]. Diabetic neuropathy is a type of nerve injury caused by diabetes [36]. Nerves in the legs, feet, and hands are more prone to this type of damages [36]. These nerves include the sudomotor nerves that are responsible for delivering the ANS stimulation to the sweat glands. Diabetic neuropathy may cause abnormal SC in different regions of the body due to nerve damage. Appropriate systematic analysis of SC recordings from different regions may lead to early diagnosis and prevention of diabetes-related complications.

As the SC measurement can be thought of as the convolution of ANS activity with physiological smoothing kernels that consist of sweat glands, sweat secretion, and evaporation dynamics [42], identification of ANS activity is a deconvolution problem. Many research works have been carried out with different methods for the deconvolution of SC recordings to recover the timings and amplitudes of stimulation and to estimate the underlying physiological parameters with the goal of uncovering emotional states using single channel SC data. Benedek *et al.* [29, 21] presented a scheme where a nonnegative deconvolution method is utilized to separate a single SC time series into discrete compact responses. They have also analyzed SC responses to assess the deviations from the standard SC response shape. Nevertheless, their scheme does not consider the sparsity constraint to prevent capturing noise as SC responses. Moreover, they do not consider the individual differences in the modeling of the rise and decay times. They perform their deconvolution for multiple predefined sets of parameters and choose the one that provides the most reasonable fit.

Greco *et al.* [23] proposed a convex optimization formulation to decompose SC time series into tonic and phasic components. Unlike in [21], they considered a the sparsity condition in neural stimuli from the ANS. They use a fixed regularization parameter for imposing the sparsity constraint. However, finding an accurate sparse solution that can handle

inter- and intra-subject variability is challenging with a fixed regularization parameter for automatic processing. In a similar work, Gallego *et al.* [24] proposed a faster decomposition approach to obtain a sparser solution; however, this approach leads to overly sparse solutions compared to the underlying neural stimuli. Faghih *et al.* [25, 19, 26, 18] proposed a two-step coordinate descent deconvolution approach to account for individual differences in the physiological system parameters for SC signals and similar physiological systems. These approaches have been successfully utilized to characterize hormonal dysfunction in fibromyalgia patients [56] as well as a potential neurobiologic substrate for chronic insomnia [79]. However, inference of ANS stimulation along with physiological system parameters using single channel SC recording is challenging in the presence of noise.

A substantial amount of research has been carried out with wearable EDA sensors that can provide better insight into how affect and stress interact with daily life [65, 80, 81]. However, wearable sensors often suffer from poor signal quality as well as motion artifacts. Furthermore, developing algorithms for analyzing EDA data in the presence of artifacts and noise is yet to be undertaken. Fusing multichannel recording with wearable devices to account for the poor signal quality could potentially improve the deconvolution performance. Faghih *et al.* [20] proposed an approach to include multichannel hormone time series using a combined state-space model, and then developed a concurrent deconvolution scheme.

Inspired by the work by Faghih *et al.* [20] for concurrent deconvolution of the multichannel hormone time series, we utilize concurrently collected multichannel SC measurements to robustly infer ANS stimulation. We hypothesize that the changes in SC in different regions of the skin are due to the same ANS stimulation. We implement system identification and propose a state-space model that includes the SC recordings from multiple skin regions. Furthermore, we introduce a multichannel concurrent deconvolution algorithm and analyze SC data using auditory stimulation experimental data. Finally, we use a Bayesian approach [82, 83, 84] to track a cognitive stress level based on the concurrent deconvolution of SC data collected during different stressful driving conditions.

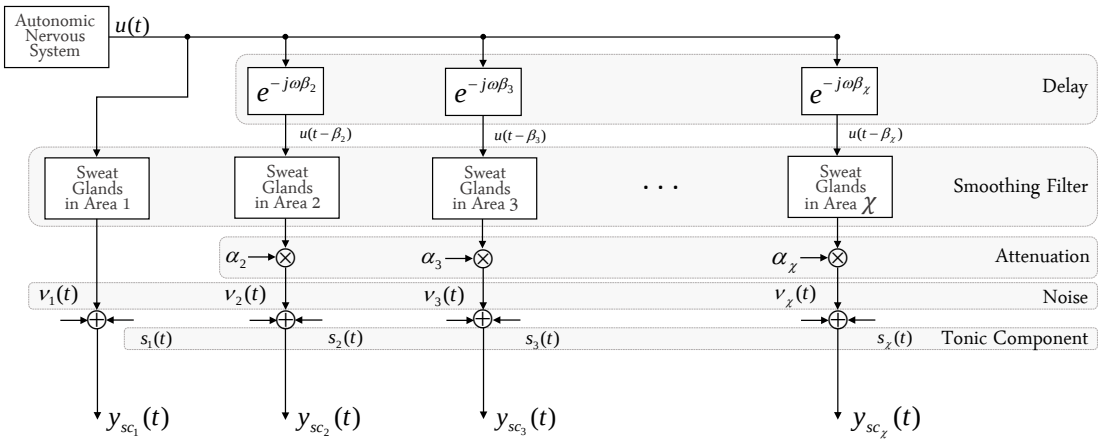

Figure 13: **Model Block Diagram.**

3.2 Methods

3.2.1 Dataset Description

Dataset 1 - Auditory Stimulation. We analyzed the SC responses to loud sounds, simultaneously recorded from palm, fingers and foot data [57]. The experiment was conducted for modeling event-related SC responses. The dataset contains SC data recorded from 26 healthy participants from three different skin locations: the hypothenar of the non-dominant hand, the middle phalanx of second and third finger of the dominant hand, and the medial plantar surface of the non-dominant foot. Each participant was provided 20 auditory stimuli. Each stimulus is single white noise burst of 1s duration. Participants were asked to press a foot operated pedal upon hearing the stimuli. A detailed description of the auditory stimulation experiment is given in [30]. We discard the data contaminated with heavy motion artifacts and the data having very small SC responses from our study.

Dataset 2 - Driver Stress. To assess the performance in tracking stress using deconvolution result, we also analyzed the stress recognition in the automobile drivers dataset [85]. This dataset includes recordings for 17 separate driving sessions on a predefined route with highways, toll roads, and city driving. The driving sessions were all conducted during the mid-morning or mid-afternoon with light traffic. Rest periods were included during

which the drivers sat in the car with their eyes shut. Since annotations of each portion are not publicly available for all the subjects, we could only use one recording whose approximate timings had to be matched with a figure in [85]. We apply the stress tracking algorithm by Wickramasuriya *et al.* [82] on the deconvolution result from the current work and compare the result with the heuristic approach in [82].

3.2.2 Model Formulation for Phasic SC Deconvolution

The variations in SC, caused by salty sweat secretion, are regulated by sudomotor nerve activity (SMNA) in the ANS. SC data can be interpreted as the summation of a fast-varying component and a slow-varying component. The slow-varying component, known as the tonic component, is mainly intended for thermoregulation of the body. The comparatively fast-varying component is termed as the phasic component. The phasic component represents the activity of ANS, which is a reflection of emotional events. The SC signal can be represented as the summation of tonic and phasic components as follows,

$$y_{sc_n}(t) = p_n(t) + s_n(t),$$

where $y_{sc_n}(t)$, $p_n(t)$, and $s_n(t)$ represent the SC signal and its phasic and tonic components for the nth channel, respectively. In the pre-processing stage, we extract the phasic components $p_n(t)$ from the SC data $y_{sc_n}(t)$ using cvxEDA [23]. In this case, we use the default value of the regularization parameter for l_1-norm minimization in cvxEDA [23]. We assume that the extracted phasic components have some Gaussian noise added to them. We consider this as measurement noise. We hypothesize that the same ANS stimulation is responsible for modulating the phasic component of SC data related to different eccrine sweat glands in different regions of skin. We propose a state-space model with n-channel phasic SC data and the single ANS input. Figure 13 shows the complete block diagram of the proposed system model. Figure 13 depicts that a single neural stimuli signal $u(t)$

generated by the ANS is responsible for the phasic response in different regions of the skin throughout the body; the block diagram shows the same neural stimuli $u(t)$ stimulating χ different regions with delay parameters β_n, $\forall n \in \{1, 2, 3, \cdots, \chi\}$; the attenuation term α_n reflects the ratio of the number of sweat glands in the nth region to that of the reference region. We model $p_n(t)$ as a scaled version of a representative internal state $\zeta_n(t)$, which refers to the average amount of sweat in the epidermis associated with the nearest sweat gland. We introduce a scaling factor α_n to account for the number of sweat glands present per unit area where the nth sensor is placed. Relation between $p_n(t)$ and $\zeta_n(t)$ is as,

$$p_n(t) = \alpha_n \zeta_n(t). \tag{16}$$

We describe the system dynamics using the following set of differential equations each denoting the kinetics of sweat secretion and evaporation process in sweat glands [42, 18, 52],

$$\begin{gathered} \tau_r \tau_d \frac{d^2\zeta_1(t)}{dt^2} + (\tau_r + \tau_d)\frac{d\zeta_1(t)}{dt} + \zeta_1(t) = u(t), \\ \tau_r \tau_d \frac{d^2\zeta_2(t)}{dt^2} + (\tau_r + \tau_d)\frac{d\zeta_2(t)}{dt} + \zeta_2(t) = u(t - \beta_2), \\ \vdots \\ \text{and } \tau_r \tau_d \frac{d^2\zeta_\chi(t)}{dt} + (\tau_r + \tau_d)\frac{d\zeta_\chi(t)}{dt} + \zeta_\chi(t) = u(t - \beta_\chi), \end{gathered} \tag{17}$$

where $\zeta_n(t)$ is the internal state which is reflected into $y_n(t)$ from the nth channel, $\forall n \in \{1, 2, \cdots, \chi\}$. The term β_n refers to the delay in the stimuli input for the nth channel. The terms τ_r and τ_d correspond to the rise and decay times of the SC responses, respectively; these parameters are fixed for all channels. β_n can be calculated by taking the cross-correlation of the y_{sc_n} and y_{sc_1} before deconvolution. The location of the maximum value of the cross-correlation is used to calculate the time lag β_n. We assume $\beta_1 = 0$ and $\alpha_1 = 1$ for the reference channel. Under the assumption that the ANS stimuli are sparse as in [18], we represent the input as $u(t) = \sum_{i=1}^{N} q_i \delta(t - \Delta_i)$ where q_i is the amplitude of the impulse in the neural stimuli at time Δ_i.

Let $x_{2n-1}(t)$ and $x_{2n}(t) = \zeta_n(t + \beta_n)$ be the internal states for $\forall n$. Similar to [52, 18], the differential equation in (17) for the nth channel can be re-written in state-space form as follows,

$$\dot{x}_{2n-1}(t) = -\frac{1}{\tau_r} x_{2n-1}(t) + \frac{1}{\tau_r} u(t) \tag{18}$$

$$\text{and } \dot{x}_{2n}(t) = \frac{1}{\tau_d} x_{2n-1}(t) - \frac{1}{\tau_d} x_{2n}(t). \tag{19}$$

The corresponding continuous observation equation can be written as follows,

$$y_n(t) = \alpha_n x_{2n}(t) + \nu_n(t), \tag{20}$$

where $y_n(t)$ is the continuous observation variable and $\nu_n(t)$ refers to the noise process. In matrix form the state-space model can be written as follows,

$$\begin{bmatrix} \dot{x}_{2n-1}(t) \\ \dot{x}_{2n}(t) \end{bmatrix} = \begin{bmatrix} -\frac{1}{\tau_r} & 0 \\ \frac{1}{\tau_d} & -\frac{1}{\tau_d} \end{bmatrix} \begin{bmatrix} x_{2n-1}(t) \\ x_{2n}(t) \end{bmatrix} + \begin{bmatrix} \frac{1}{\tau_r} \\ 0 \end{bmatrix} u(t) \tag{21}$$

$$\text{and } y_n(t) = \begin{bmatrix} 0 & \alpha_n \end{bmatrix} \begin{bmatrix} x_{2n-1}(t) \\ x_{2n}(t) \end{bmatrix} + \nu_n(t). \tag{22}$$

We can write the equations in (21)-(22) in a state-space form, for all channels, as follows,

$$\dot{\boldsymbol{x}}(t) = A_c \boldsymbol{x}(t) + B_c u(t) \tag{23}$$

$$\text{and } \boldsymbol{y}(t) = C_c \boldsymbol{x}(t) + \boldsymbol{\nu}(t), \tag{24}$$

where $\boldsymbol{x}(t) = \begin{bmatrix} x_1(t) \\ x_2(t) \\ \vdots \\ x_{2\chi}(t) \end{bmatrix}_{2\chi\times 1}$, $\boldsymbol{y}(t) = \begin{bmatrix} y_1(t) \\ y_2(t) \\ \vdots \\ y_{\chi}(t) \end{bmatrix}_{\chi\times 1}$, $\boldsymbol{\nu}(t) = \begin{bmatrix} \nu_1(t) \\ \nu_2(t) \\ \vdots \\ \nu_{\chi}(t) \end{bmatrix}_{\chi\times 1}$,

$A_c = \begin{bmatrix} \phi & \mathbf{0} & \cdots & \mathbf{0} \\ \mathbf{0} & \phi & \cdots & \mathbf{0} \\ \vdots & \vdots & \ddots & \vdots \\ \mathbf{0} & \mathbf{0} & \cdots & \phi \end{bmatrix}_{2\chi\times 2\chi}$ with $\phi = \begin{bmatrix} -\frac{1}{\tau_r} & 0 \\ \frac{1}{\tau_d} & -\frac{1}{\tau_d} \end{bmatrix}$,

$B_c = \begin{bmatrix} 1/\tau_r & 0 & 1/\tau_r & 0 & \cdots & 1/\tau_r & 0 \end{bmatrix}^\top_{2\chi\times 1}$,

and $C_c = \begin{bmatrix} 0 & 1 & 0 & 0 & \cdots & 0 & 0 \\ 0 & 0 & 0 & \alpha_2 & \cdots & 0 & 0 \\ \vdots & \vdots & \vdots & \vdots & \ddots & \vdots & \vdots \\ 0 & 0 & 0 & 0 & \cdots & 0 & \alpha_\chi \end{bmatrix}_{2\chi\times 2\chi}$. We define $\boldsymbol{\alpha} = \begin{bmatrix} \alpha_2 & \alpha_3 & \cdots & \alpha_n \end{bmatrix}^\top$.

Discretization: Let T_u be the sampling frequency of the neural stimuli and T_y be the sampling frequency of the phasic SC data for each channel. The timings of the neural impulses can be written as $\Delta_i = iT_u$; q_i is zero if there is no impulse at the ith instance. Let $y_{n,\,k}$ be the observed phasic SC for the nth channel at time instance $t_k = kT_y$. We can write

$$y_{n,\,k} = \alpha_n x_{2n}(t_k) + \nu_{n,\,k}, \tag{25}$$

where $\nu_{n,\,k}$ is the noise associated with the nth channel; $\nu_{n,\,k}$ is modelled as a zero-mean Gaussian random variable. We derive the discrete equivalent of the system, assuming that the input and the states are constant over T_u. The discrete version of the neural stimuli can be written as a vector $\boldsymbol{u} = [q_1 \quad q_2 \quad \cdots \quad q_N]^\top$ that represents the entire neural stimuli over the duration of SC data. Let $\Phi = e^{A_c T_u}$, and $\Gamma = \int_0^{T_u} e^{A_c(T_u-\rho)} B_c d\rho$ to write the

discrete state-space form of (23)-(24) as,

$$\boldsymbol{x}\left[k+1\right]=\Phi\boldsymbol{x}\left[k\right]+\Gamma\boldsymbol{u}[k] \tag{26}$$

$$\text{and } \boldsymbol{y}\left[k\right]=C_c\boldsymbol{x}\left[k\right]+\boldsymbol{\nu}\left[k\right]. \tag{27}$$

As neural stimuli and SC measurement have different sampling frequencies, i.e., $T_y = LT_u$ where L is a positive integer, we let $A_d = \Phi^L$, $B_d = \begin{bmatrix} \Phi^{L-1}\Gamma & \Phi^{L-2}\Gamma & \cdots & \Gamma \end{bmatrix}$, $\boldsymbol{u}_d\left[k\right] = \begin{bmatrix} \boldsymbol{u}\left[Lk\right] & \boldsymbol{u}\left[Lk+1\right] & \cdots & \boldsymbol{u}\left[Lk+L-1\right] \end{bmatrix}^\top$, $\nu_d\left[k\right] = \nu[Lk]$ and $\boldsymbol{z}\left[k\right] = \boldsymbol{x}\left[Lk\right]$; the multi-rate system can be represented as follows,

$$\boldsymbol{z}\left[k+1\right]=A_d\boldsymbol{z}\left[k\right]+B_d\boldsymbol{u}_d\left[k\right] \tag{28}$$

$$\text{and } \boldsymbol{y}[k]=C_c\boldsymbol{z}\left[k\right]+\nu_d\left[k\right], \tag{29}$$

where A_d and B_d are functions of $\boldsymbol{\tau} = \begin{bmatrix} \tau_r & \tau_d \end{bmatrix}^\top$, $\boldsymbol{\alpha}$, T_u, and T_y. Let $\boldsymbol{\theta} = \begin{bmatrix} \boldsymbol{\tau}^\top & \boldsymbol{\alpha}^\top \end{bmatrix}^\top$. As the system is causal, we use (28)-(29) to obtain the observation equation for the kth sample,

$$\boldsymbol{y}\left[k\right]=\mathcal{F}\left[k\right]\boldsymbol{z}\left[0\right]+\mathcal{D}\left[k\right]\boldsymbol{u}+\boldsymbol{\nu}_d\left[k\right],$$

where $\mathcal{F}\left[k\right] = C_cA_d^k$,
$\mathcal{D}\left[k\right] = C_c\begin{bmatrix} A_d^{k-1}B_d & A_d^{k-2}B_d & \cdots & B_d & \underbrace{0 \quad \cdots \quad 0}_{N-kL} \end{bmatrix}$, and $\boldsymbol{u} = \begin{bmatrix} \boldsymbol{u}_d[0] & \boldsymbol{u}_d[1] & \cdots & \boldsymbol{u}_d[k-1] & \cdots & \boldsymbol{u}_d[M-1] \end{bmatrix}^\top_{N\times 1}$.
For the initial condition, we can let $\boldsymbol{z}_{\boldsymbol{\theta}_0} = \boldsymbol{z}\left[0\right] = \begin{bmatrix} 0 & y_1(0) & 0 & \frac{y_2(0)}{\alpha_2} & \cdots & 0 & \frac{y_\chi(0)}{\alpha_\chi} \end{bmatrix}^\top$ similar to the work in [18].

Then, let $\boldsymbol{y} = \begin{bmatrix} \boldsymbol{y}[1]^\top & \boldsymbol{y}[2]^\top & \cdots & \boldsymbol{y}[M]^\top \end{bmatrix}^\top_{\chi M\times 1}$ where $\boldsymbol{y}[k] = \begin{bmatrix} \boldsymbol{y}_{1,k} & \boldsymbol{y}_{2,k} & \cdots & \boldsymbol{y}_{\chi,k} \end{bmatrix}^\top$, $\forall k \in \{1, 2, \cdots, M\}$. Similarly, $\boldsymbol{\nu} = \begin{bmatrix} \nu_d[1] & \nu_d[2] & \cdots & \nu_d[M] \end{bmatrix}^\top_{\chi M\times 1}$ where $\boldsymbol{\nu}_d[k] = \begin{bmatrix} \boldsymbol{\nu}_{1,k} & \boldsymbol{\nu}_{2,k} & \cdots & \boldsymbol{\nu}_{\chi,k} \end{bmatrix}^\top$, $\forall k \in \{1, 2, \cdots, M\}$. Moreover, let $\mathcal{F}_{\boldsymbol{\theta}} = \begin{bmatrix} \mathcal{F}[0] & \mathcal{F}[1] & \cdots & \mathcal{F}[M-1] \end{bmatrix}^\top_{\chi M\times 2\chi}$ and $\mathcal{D}_{\boldsymbol{\theta}} = \begin{bmatrix} \mathcal{D}[0] & \mathcal{D}[1] & \cdots & \mathcal{D}[M-1] \end{bmatrix}^\top_{\chi M\times N}$. Therefore, we can write the solution for the observation equation for all the sampled data as

follows,

$$\boldsymbol{y} = \mathcal{F}_{\boldsymbol{\theta}} \boldsymbol{z}_{\boldsymbol{\theta}_0} + \mathcal{D}_{\boldsymbol{\theta}} \boldsymbol{u} + \boldsymbol{\nu}.$$

Equivalently, we can separately represent the solution for each channel as follows,

$$\begin{aligned} \boldsymbol{y}_1 &= \mathcal{F}_{\boldsymbol{\theta}_1} \boldsymbol{z}_{\boldsymbol{\theta}_0} + \mathcal{D}_{\boldsymbol{\theta}_1} \boldsymbol{u} + \boldsymbol{\nu}_1, \\ \boldsymbol{y}_2 &= \mathcal{F}_{\boldsymbol{\theta}_2} \boldsymbol{z}_{\boldsymbol{\theta}_0} + \mathcal{D}_{\boldsymbol{\theta}_2} \boldsymbol{u} + \boldsymbol{\nu}_2, \\ &\vdots \\ \text{and } \boldsymbol{y}_\chi &= \mathcal{F}_{\boldsymbol{\theta}_\chi} \boldsymbol{z}_{\boldsymbol{\theta}_0} + \mathcal{D}_{\boldsymbol{\theta}_\chi} \boldsymbol{u} + \boldsymbol{\nu}_2. \end{aligned} \tag{30}$$

Here $\boldsymbol{y}_n$, $\mathcal{F}_{\boldsymbol{\theta}_n}$, $\mathcal{D}_{\boldsymbol{\theta}_n}$, and ν_n correspond to the vector and matrices taking the $(\chi(k-1)+n)$th rows from $\boldsymbol{y}$, $\mathcal{F}_{\boldsymbol{\theta}}$, $\mathcal{D}_{\boldsymbol{\theta}}$, and $\boldsymbol{\nu}$, respectively, $\forall k \in \{1, 2, 3, \cdots, M\}$.

Noise Variance Estimation. We assume that the noise term $\nu_{n,k}$ is Gaussian random variable with zero-mean and σ_n^2 variance. Therefore, the energy of the noise is distributed over the whole spectral range of 0 to half of the sampling frequency. To obtain noise variances $\forall n$, we filter the phasic components of the experimental SC signals with a 0.5 Hz high pass filter to remove all the signal components assuming the signals are band-limited to 0.5 Hz. Then, we calculate the variances of the filtered signals to obtain the estimates of the noise variances in the high-frequency region. We interpolate these estimated variances for the whole spectral bandwidth considering the low-frequency region. This enables us to obtain an assessment of the noise variances σ_n^2, $\forall n$.

Model Formulation for Stress Tracking. We assume that the ANS stimulation $\boldsymbol{u}$ for SC responses in SC data is dependent on an internal stress state in the brain. Wickramasuriya *et al.* [82] modeled the evolution of the stress state as a random walk. SC data is modulated by stress and thus the probability p_j of occurrence of a neural stimuli is dependent on the stress state w_j. Given the state process w_j, the observation model defines the probability of observing a neural stimulus. Let the observation variable s_j be a

binary variable where $s_j = 0$ denotes no neural stimulus and $s_j = 1$ denotes a single neural stimulus observed at jth time instance. The probability distribution of s_j can be described using the Bernoulli distribution. State-space model is as follows,

$$w_j = w_{j-1} + \epsilon_j, \qquad \text{(state equation)} \tag{31}$$

$$p_j = \frac{1}{1 + e^{-(\eta + w_j)}}, \qquad \text{(link function)} \tag{32}$$

$$\text{and } P(s_j|q_j) = p_j^{s_j}(1 - p_j)^{1-s_j}, \qquad \text{(observation equation)} \tag{33}$$

where p_j is defined by a logistic equation. The observation model in (33) is defined using the Bernoulli distribution. The parameter η represents the probability of observing a neural stimulus by random chance in a bin at the start of the experiment. We calculate η similarly as in [82]. We use a bin size of 1 second in $\boldsymbol{u}$ to generate $S_{1:J}$. Here J denotes the total number of bins. As the signal sample frequency is also 1 second, number of observation is equal to the number of samples per channel, i.e., $J = M$. With the observation $S_{1:J} = \{s_1, s_2, ..., s_J\}$ indicating the presence or absence of neural stimuli, we estimate $W = \{w_0, w_1, w_2, ..., w_J\}$ and σ_ϵ^2 for in turn estimating $p_j, \ \forall j$ using the Expectation Maximization (EM) algorithm in [82].

3.2.3 Estimation

Preprocessing. We discard all the participants having very heavy motion artifacts in their data for our analysis. The original recorded signal has a sampling frequency of 100 Hz for dataset 1 and 15.5 Hz for dataset 2. We perform all the preprocessing in the original sampling frequency. In the beginning preprocessing step, we find the large discontinuities in the recorded SC data. We take the difference and the negative of the difference of the raw SC data and detect peaks having a prominence of 0.1. We assume these discontinuities are due to the artifacts, and we choose the prominence parameter to detect the artifacts that are much larger than the phasic responses. For a detected discontinuity, we discard

a small patch of 0.5 seconds, while keeping the discontinuity in the middle of the patch. We interpolate the region of the discarded patch in the signal with a spline curve. Then, we perform lowpass filtering on the signal with a 64 order FIR lowpass filter of 3 Hz cut off frequency. As the FIR lowpass filter has linear phase, we also corrected the group delay generated by the FIR filter. Afterward, we apply cvxEDA [23] to separate the tonic component and the phasic component, taking time between knots of the tonic spline function as 6 seconds. All other parameters are kept unchanged from their default value. Next, we calculate the delay parameter β taking cross-correlation between the two phasic components from the first channel and the nth channel for different lags. We take the lag for foot phasic SC data with the maximum correlation. Finally, we resample the signal to 1 Hz sampling frequency.

Deconvolution. The sampling period for phasic SC signal and neural stimuli are $T_y = 1$ seconds and $T_u = 0.25$ seconds, respectively. To estimate the system parameters and the neural stimuli, we use solutions in (30), and formulate the following optimization problem imposing the sparsity constraint on $\boldsymbol{u}$,

$$\begin{aligned} &\underset{\boldsymbol{\theta},\boldsymbol{u},\lambda}{\text{minimize}}\ J(\boldsymbol{\theta},\boldsymbol{u},\lambda) = \frac{1}{2}\sum_{n=1}^{\chi}\frac{1}{\sigma_n^2}||\boldsymbol{y}_n - \mathcal{F}_{\boldsymbol{\theta}_n}\boldsymbol{z}_{\boldsymbol{\theta}_0} - \mathcal{D}_{\boldsymbol{\theta}_n}\boldsymbol{u}||_2^2 + \lambda||\boldsymbol{u}||_p^p \\ &\text{s. t.} \qquad C\boldsymbol{\theta} \leq \boldsymbol{b},\ \boldsymbol{u} \geq \boldsymbol{0}, \end{aligned} \tag{34}$$

where $C = \begin{bmatrix} 1 & -1 & 0 & 0 & \cdots & 0 & 0 \\ 0 & 0 & 1 & -1 & \cdots & 0 & 0 \\ \vdots & \vdots & \vdots & \vdots & \ddots & \vdots & \vdots \\ 0 & 0 & 0 & 0 & \cdots & 1 & -1 \end{bmatrix}^\top$

and $\boldsymbol{b} = \begin{bmatrix} 1.4 & -0.1 & 6 & -1.5 & 100 & -0.01 & \cdots & 100 & -0.01 \end{bmatrix}^\top$. Here $\boldsymbol{\theta} \in \mathbb{R}^{(\chi+1)}$, $C \in \mathbb{R}^{2(\chi+1),(\chi+1)}$, and $\boldsymbol{b} \in \mathbb{R}^{2(\chi+1)}$. The l_p-norm is an approximation of the l_0-norm ($0 < p \leq 2$) [19]. The l_p-norm regularization parameter λ is chosen to maintain a balance between filtering out the noise and the sparsity level of $\boldsymbol{u}$ [19, 20, 52]. We solve the inverse problem of

finding a non-negative $\boldsymbol{u}$ with a specific sparsity level using the Focal Underdetermined System Solver (FOCUSS+) algorithm [66]. Afterwards, we use the generalized cross-validation (GCV) technique to calculate an appropriate value of the l_p-norm regularization parameter λ adaptively similar to the approaches in [20, 19, 18]. In order to estimate λ, we use the singular value decomposition based GCV technique in [68] by minimizing,

$$\underset{0\leq\lambda\leq 0.1}{\operatorname{argmin}}\, G(\lambda|\boldsymbol{\theta},\boldsymbol{u}) = \frac{\left[\mathcal{L}\sum_{i=1}^{\mathcal{L}}\gamma_i^2\left(\frac{\lambda}{\kappa_i^2+\lambda}\right)^2\right]}{\left[\sum_{i=1}^{\mathcal{L}}\left(\frac{\lambda}{\kappa_i^2+\lambda}\right)^2\right]}, \tag{35}$$

where $\boldsymbol{\gamma} = \boldsymbol{R}^\top \boldsymbol{y}_\theta = \begin{bmatrix} \gamma_1 & \gamma_2 & \cdots & \gamma_{\mathcal{L}} \end{bmatrix}^\top$ with $\boldsymbol{y}_\theta = \boldsymbol{y} - \mathcal{F}_{\boldsymbol{\theta}}\boldsymbol{z}_{\boldsymbol{\theta}_0}$, and $\mathcal{D}_{\boldsymbol{\theta}}\boldsymbol{P}_{\boldsymbol{u}}^{\frac{1}{2}} = \boldsymbol{R}\boldsymbol{\Sigma}\boldsymbol{Q}^\top$ with $\boldsymbol{P}_{\boldsymbol{u}} = \text{diag}(|\text{u}_i|^{2-p})$ and $\boldsymbol{\Sigma} = \text{diag}\{\kappa_i\}$; $\boldsymbol{R}$ and $\boldsymbol{Q}$ are unitary matrices and the κ_i's are the singular values of $\mathcal{D}_{\boldsymbol{\theta}}\boldsymbol{P}_{\boldsymbol{u}}^{\frac{1}{2}}$; $\mathcal{L}$ is the total number of data points, i.e., $\mathcal{L} = \chi M$ [68]. In this study, we minimize $G(\lambda)$ for λ within the range of zero to 0.1. For $r = 0, 1, 2, \cdots$, GCV-FOCUSS+ works as follows [19]:

1. $\boldsymbol{P}_{\boldsymbol{u}}^{(r)} = \text{diag}(|\boldsymbol{u}_i^{(r)}|^{2-p})$
2. $\boldsymbol{u}^{(r+1)} = \boldsymbol{P}_{\boldsymbol{u}}\mathcal{D}_{\boldsymbol{\theta}}^\top(\mathcal{D}_{\boldsymbol{\theta}}\boldsymbol{P}_{\boldsymbol{u}}\mathcal{D}_{\boldsymbol{\theta}}^\top + \lambda\boldsymbol{I})^{-1}\boldsymbol{y}_\theta$
3. $\boldsymbol{u}_i^{(r+1)} \leq 0 \rightarrow \boldsymbol{u}_i^{(r+1)} = 0$
4. $\lambda^{(r+1)} = \underset{0\leq\lambda\leq 0.1}{\operatorname{argmin}}\, G(\lambda)$
5. Iterate until convergence

We solve the problem in (34) using the following algorithm:

We run the algorithm with several random initializations of the system parameters τ_r, τ_d and $\alpha_n \forall n$. Finally, we choose the estimate that has the minimum value for the cost function in (34).

Stress Estimation. We follow the Expectation Maximization (EM) approach in [82] to estimate the stress state w_j. In the E-step of their proposed algorithm, a nonlinear recursive

Algorithm: Concurrent Deconvolution

(a) Let i = 0.

Initialization:

(b) Initialize $\tilde{\boldsymbol{\theta}}^0$ by sampling a uniform random variable on [0.10, 1.4] for $\tilde{\tau}_r^{(0)}$, on [1.5, 6] for $\tilde{\tau}_d^{(0)}$, and on [0.01, 1] for $\tilde{\alpha}_n^0$, $\forall n \in \{2, 3, \cdots, \chi\}$; let $j = 1$.

(c) Set $\boldsymbol{\theta} = \tilde{\boldsymbol{\theta}}^{(j-1)}$; use FOCUSS+ to solve the inverse problem in (34) to find the stimuli $\tilde{\boldsymbol{u}}^{(j)}$ by initializing $\tilde{\boldsymbol{u}}^{(0)}$ at a vector with all ones.

(d) Set $\boldsymbol{u} = \tilde{\boldsymbol{u}}^{(j)}$; use the interior point method and minimize the optimization problem in (34) to solve for $\tilde{\boldsymbol{\theta}}^{(j)}$. Let $j = j + 1$.

(e) Repeat between steps (c)-(d) until $j = 30$.

(f) Set $\hat{\boldsymbol{\theta}}^0 = \tilde{\boldsymbol{\theta}}^{(j)}$ and $\hat{\boldsymbol{u}}^0 = \tilde{\boldsymbol{u}}^{(j)}$.

Outer Optimization Problem:

(g) Set $i = i + 1$.

(h) Set $\boldsymbol{\theta} = \hat{\boldsymbol{\theta}}^{(i-1)}$; obtain $\hat{\boldsymbol{u}}^{(i)}$ solving the following steps:

i. Set $m = 0$ and $\hat{\boldsymbol{u}}^{(i)^{(0)}} = \hat{\boldsymbol{u}}^{(i)}$ and $\hat{\lambda}^{(i)^{(0)}} = 2 \times 10^{-3}$.
Inner Optimization Problem:

ii. Set $m = m + 1$.

iii. Set $\lambda = \hat{\lambda}^{(i)^{(m-1)}}$ and $\boldsymbol{\theta} = \hat{\boldsymbol{\theta}}^{(i-1)}$; solve for $\hat{\boldsymbol{u}}^{(i)^{(m)}}$ by initializing the optimization problem in (34) at $\boldsymbol{u} = \hat{\boldsymbol{u}}^{(i)^{(m-1)}}$.

iv. Set $\boldsymbol{u} = \hat{\boldsymbol{u}}^{(i)^{(m-1)}}$ and $\boldsymbol{\theta} = \hat{\boldsymbol{\theta}}^{(i-1)}$; solve for $\lambda^{(i)^{(m)}}$ by initializing the optimization problem in (35) at $\lambda = \hat{\lambda}^{(i)^{(m-1)}}$.

v. repeat (ii)-(iv) until convergence and set $\hat{\boldsymbol{u}}^{(i)} = \hat{\boldsymbol{u}}^{(i)^{(m)}}$.

(i) Set $\boldsymbol{u}$ equal to $\hat{\boldsymbol{u}}^{(i)}$; solve for $\hat{\boldsymbol{\theta}}^{(i)}$ using interior-point method by initializing the optimization problem in (34) at $\hat{\boldsymbol{\theta}}^{(i-1)}$.

(j) Iterate between (g)-(i) until convergence.

---

point process forward filter followed by a backward smoother has been implemented to estimate the stress state of the subject. The forward filter estimates the stress state $w_{j|j}$ in the jth bin, given $S_{1:j}$, i. e., the observations up to the jth bin. The backward smoother estimates the stress state $w_{j|J}$ in the jth bin, given $S_{1:J}$, i. e., all the observations (up to the Jth bin). $p_{j|j}$ denotes the probability of a neural stimuli impulse occurring within the jth bin given the observation $S_{1:j}$, and $p_{j|J}$ the probability of a neural stimuli impulse at jth bin

given all of the data $S_{1:J}$. In this case, the value of parameter σ_ϵ^2 has been determined by maximizing the complete data log-likelihood likelihood estimate at the previous iteration.

3.2.4 Expectation Step

At the $(l+1)$th iteration, the expectation of all the data log likelihood has been calculated in the E-step given $S_{1:J}$, the stress state, $\sigma_\epsilon^{2(l)}$, and $w_0^{(l)}$. The superscript l represents that the values are calculated from the lth iteration. The forward and backward filter methods for E-step are given as follows:

Forward Filter. Given $\sigma_\epsilon^{2(l)}$ and $w_0^{(l)}$, the estimation of $w_{j|j}$ and $\sigma_{j|j}^2$ has been carried out using a recursive nonlinear filter algorithm [82, 86] as follows,

$$w_{j|j-1} = w_{j-1|j-1}, \tag{36}$$

$$\sigma_{j|j-1}^2 = \sigma_{j-1|j-1}^2 + \sigma_\epsilon^{2(l)}, \tag{37}$$

$$w_{j|j} = w_{j|j-1} + \sigma_{j|j-1}^2 \left[s_j - \frac{1}{1+e^{-(\alpha+w_{j|j})}} \right], \tag{38}$$

$$\text{and } \sigma_{j|j}^2 = \left\{ \frac{1}{\sigma_{j|j-1}^2} + \frac{e^{(\eta+w_{j|j})}}{[1+e^{(\eta+w_{j|j})}]^2} \right\}^{-1}, \tag{39}$$

for $w_0 = w_0^{(l)}$, $\sigma_{0|0}^2 = \sigma_\epsilon^{2(l)}$ and $j = 1, 2, ..., J$. As $w_{j|j}$ appears on both sides of Equation (38), it can be solved using Newton's method.

Backward Filter. From Equations (38) and (39), the posterior mode estimate $w_{j|j}$ and its variance $\sigma_{j|j}^2$ can be obtained. Given these estimations, the fixed-interval smoothing algorithm can be applied to compute $w_{j|J}$ and $\sigma_{j|J}^2$. The algorithm is as follows [86],

$$A_j = \frac{\sigma_{j|j}^2}{\sigma_{j+1|j}^2}, \tag{40}$$

$$w_{j|J} = w_{j|j} + A_j \left(w_{j+1|J} - w_{j+1|j} \right), \tag{41}$$

$$\text{and } \sigma^2_{j|J} = \sigma^2_{j|j} + A^2_j \left(\sigma^2_{j+1|J} - \sigma^2_{j+1|j} \right), \tag{42}$$

for $j = J-1, ..., 1$ with initial conditions $w_{J|J}$ and $\sigma^2_{J|J}$.

3.2.5 Maximization Step

At the maximization step, the expected value of the complete data log-likelihood is used to select the model parameters for the next iteration as follows [86],

$$\begin{aligned} \sigma^{2(l+1)}_{\epsilon} = & \frac{2}{J+1} \Bigg[\sum_{j=2}^{J} (\sigma^2_{j|J} + w^2_{j|J}) \\ & - \sum_{j=2}^{J} (A_j \sigma_{j|J} + w_{j|J} w_{j-1|J}) \Bigg] \\ & + \frac{1}{J+1} \left[(2\sigma^2_{1|J} + \frac{3}{2} w^2_{1|J}) - (\sigma^2_{J|J} + w^2_{J|J}) \right] \end{aligned} \tag{43}$$

$$\text{and } w_0^{(l+1)} = \frac{1}{2} w_{1|J}. \tag{44}$$

The EM algorithm repeatedly iterates between the E-step and the M-step until convergence. The estimated state w_j at each time instance is assumed to be Gaussian distributed $w_j \sim N(w_{j|J}, \sigma_{j|J})$ and we define high arousal index (HAI) as $\Pr(w_j > w_T)$ similar to [83]. The threshold w_T is set to subject's mean stress state value across the whole experiment.

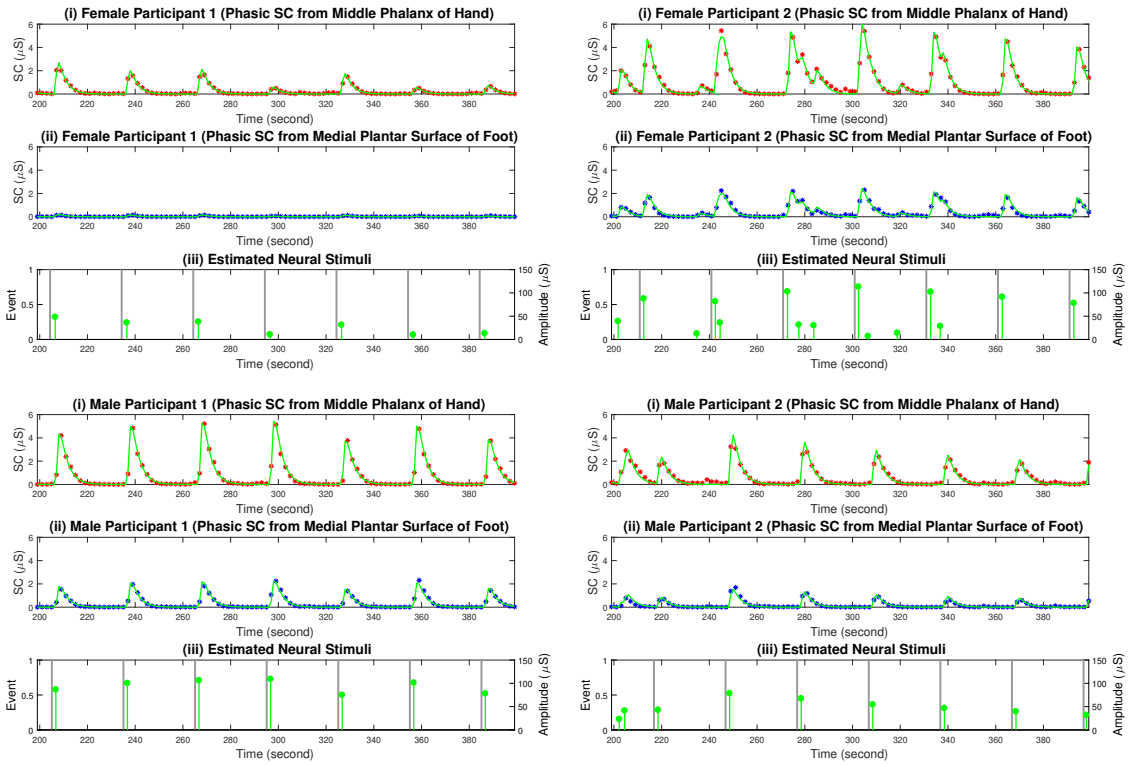

Figure 14: **Estimated Deconvolution of the Experimental Phasic SC Signals Two Female and Two Male Particiapants.**

3.3 Results

3.3.1 Dataset 1

We use the proposed algorithm and concurrently deconvolve SC measurements from the middle phalanx of the hand and the medial plantar surface of the foot collected during an auditory stimulation experiment and recover the underlying stimuli $u(t)$, the corresponding rise time (τ_r) and decay times (τ_d) of SC responses, and the attenuation (α_2) at the medial plantar surface of foot with respect to the middle phalanx of hand. Results in Figure 14 show that the proposed algorithm successfully recovers the timing and amplitudes of neural stimuli and the underlying system parameters, i.e., the rise and decay times for two female participants and two male participants. In each of the panels in Figure 14, i) the top sub-panel shows the experimental (red stars) and the estimated (green curve) phasic component

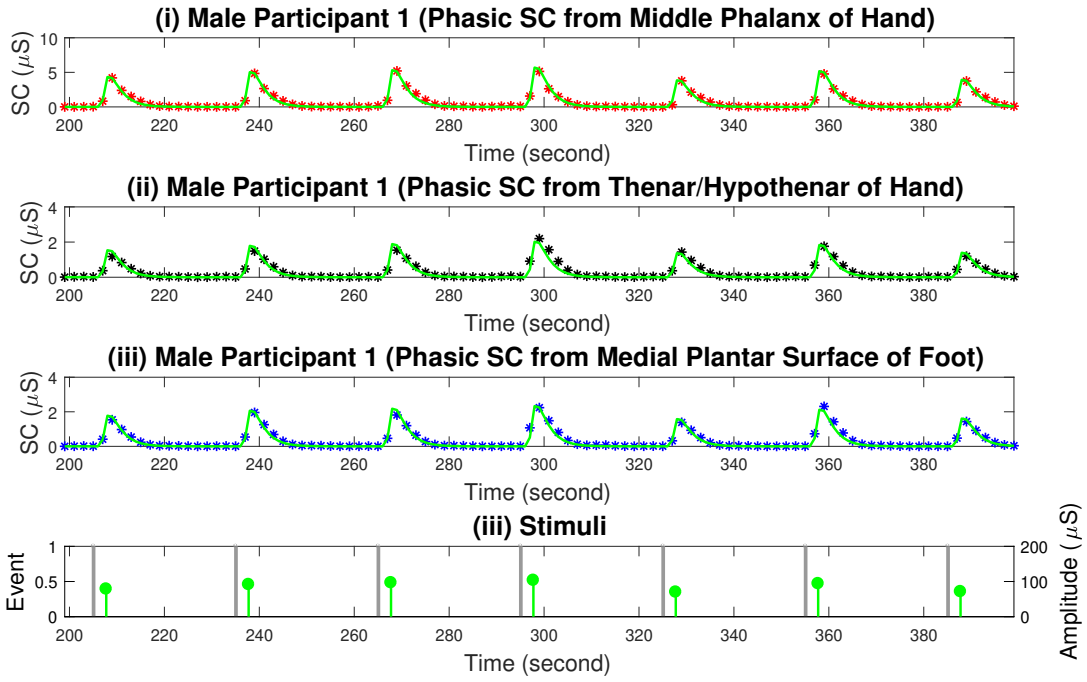

Figure 15: **Three Channel Deconvolution on Experimental Data.**

corresponding to the middle phalanx of hand; ii) middle subpanel shows the experimental (blue stars) and estimated (green curve) phasic component corresponding to the the medial planar surface of foot; and iii) bottom sub-panel shows the timings of the auditory stimuli (gray vertical lines) and the estimated ANS activation timings and amplitudes (green vertical lines). The figures for the deconvolution results for all 12 participants are given in the Appendix. We considered the signal segment from 200 seconds to 400 seconds for our analysis. The multiple correlation coefficient (R^2) has been calculated for all twelve reconstructed signals. The high values of R^2 (found to be greater than 0.95 except for male participant 3 and the explanation is given in Section 3.4) for hand phasic SC data suggest that our proposed algorithm can successfully recover the underlying physiologically plausible ANS stimulation. For foot data, the R^2 values are greater than 0.80 except for the male participant 4 and it is also explained in Section 3.4. In general, the R^2 values from reconstructed foot data are lower compared to the R^2 values from the reconstructed

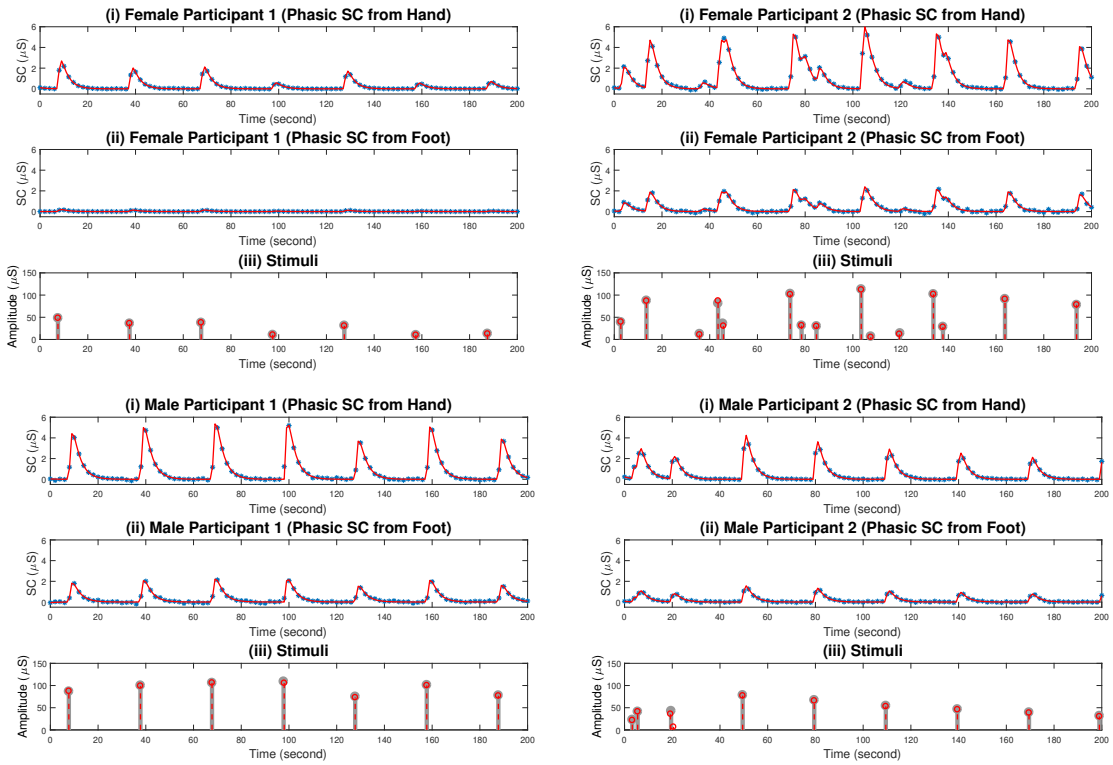

Figure 16: **Estimated Deconvolution of the Simulated Phasic SC Signal.**

hand data. Lower R^2 values for foot data suggest that foot signals are noisier than the hand signals. Table 2 shows all the estimated parameters as well as the R^2 values for all 12 participants. In Table 2, τ_r, τ_d, and α_2 denote the rise time, decay time and the attenuation parameter for the foot SC data; and R_h^2 and R_f^2 correspond to the R^2 for the fits of the hand and foot SC data, respectively. The quantile-quantile plot of the model residuals after deconvolution follows a straight line, suggesting that the residuals are Gaussian distributed. All quantile-quantile plots for 12 are provided in the Appendix.

Figure 15 shows an example of three-channel deconvolution. Here, in each of the panels in Figure 15, i) the first subpanel shows the experimental (red stars) and the estimated (green curve) phasic component corresponding to the middle phalanx of the hand; ii) the next subpanel shows the experimental (black stars) and estimated (green curve) phasic component corresponding to the thenar/hypothenar of hand; iii) the next sub-panel shows the

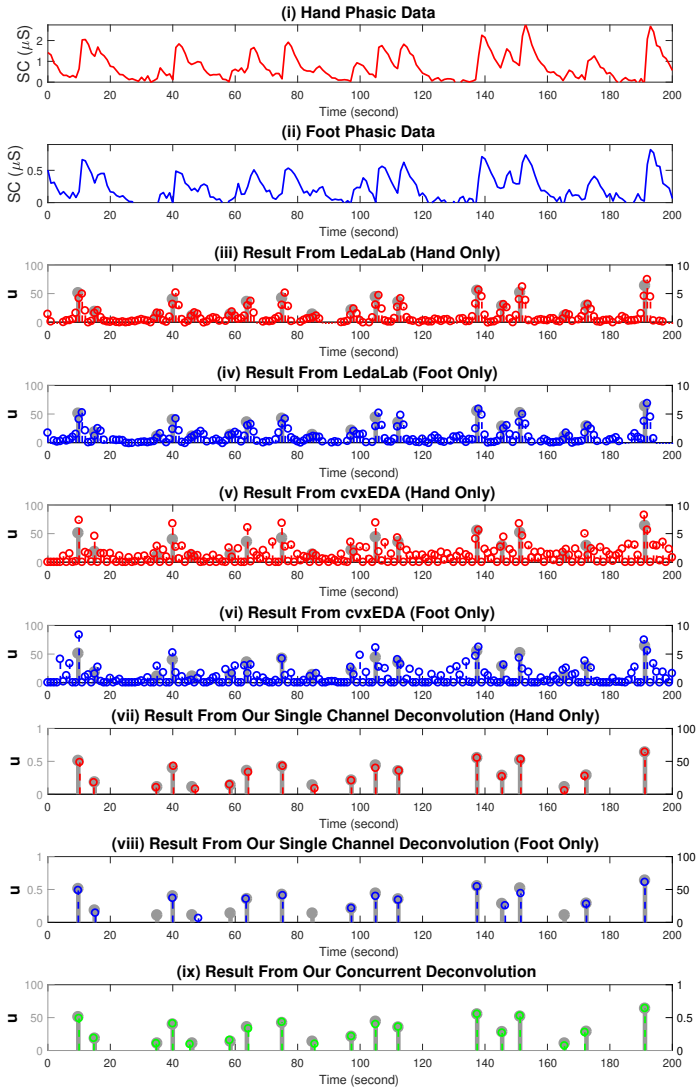

Figure 17: **Performance Comparison of Proposed Concurrent Deconvolution Approach with Existing Approaches.**

experimental (blue stars) and estimated (green curve) phasic component corresponding to the medial planar surface of foot; and iv) bottom sub-panel shows the timings of the auditory stimuli (gray vertical lines) and the estimated ANS activation timings and amplitudes (green vertical lines). Here we include the third recording from the thenar/hypothenar of the hand in the concurrent deconvolution scheme. We are able to successfully deconvolve

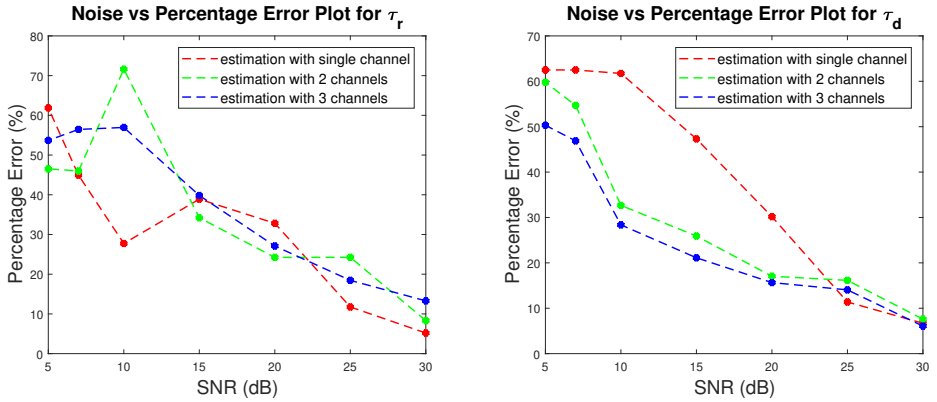

Figure 18: **Noise vs Accuracy Plot for Rise Time and Decay Time.**

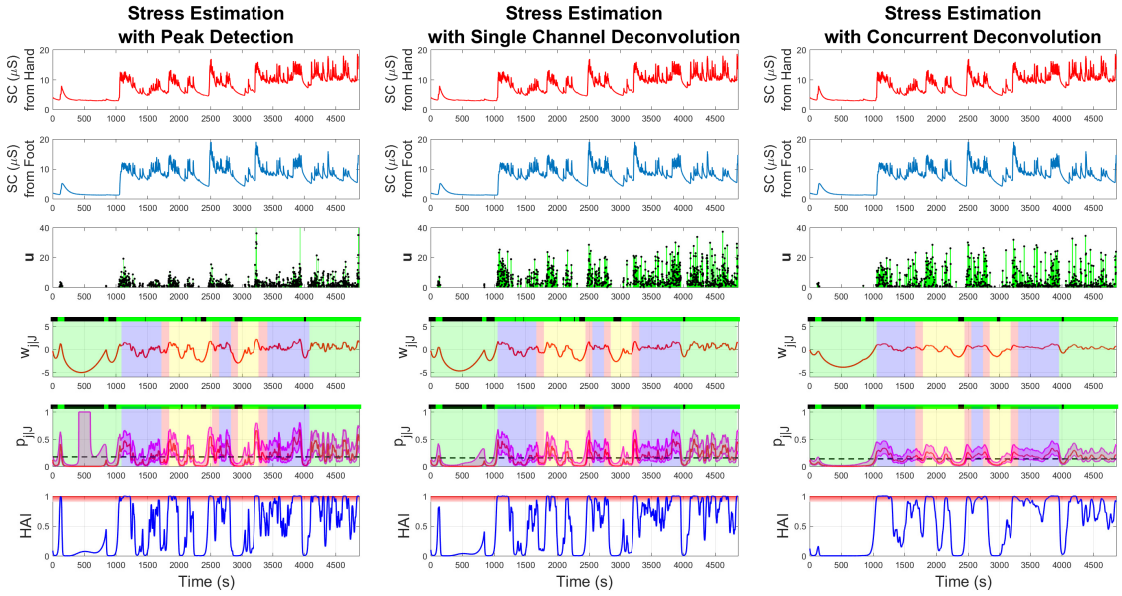

Figure 19: **Stress State Estimation from Drivers Stress Dataset.**

the three-channel SC data and obtain all unknown parameters. The R^2 obtained for all three channels are 0.985, 0.937 and 0.965.

To validate our approach, we simulate data using the results from the deconvolution and the parameters obtained are given in Table 2. To simulate the noisy data, we added zero-mean Gaussian noise with 30 dB and 20 dB signal-to-noise ratio (SNR) to the reconstructed phasic SC data corresponding to both hand and foot channels, respectively. These SNR values are chosen to obtain comparable noise levels as in the experimental data. Thereafter,

Table 2: The Estimated Model Parameters and the Squares of the Multiple Correlation Coefficients (R^2) for the Fits of the Experimental Skin Conductance Time Series.

Female Participant	Subject ID	τ_r (second)	τ_d (second)	α_2	β (second)	λ	R_h^2	R_f^2
1	15	0.562	3.021	0.074	1.470	0.0020	0.989	0.914
2	12	0.794	2.886	0.403	1.120	0.0725	0.986	0.954
3	7	0.499	3.125	0.148	1.010	0.0584	0.984	0.812
4	18	1.026	2.102	0.129	0.720	0.105	0.982	0.931
5	21	0.695	2.909	0.373	1.150	0.0384	0.985	0.947
6	25	0.341	2.684	0.621	0.940	0.1068	0.954	0.894
Male Participant	Subject ID	τ_r (second)	τ_d (second)	α_2	β (second)	λ	R_h^2	R_f^2
1	11	0.772	3.104	0.411	1.150	0.0357	0.994	0.969
2	26	0.519	3.200	0.364	1.430	0.0505	0.980	0.922
3	8	0.715	1.815	0.030	1.710	0.0267	0.787	0.807
4	10	0.310	3.587	0.630	0.760	0.0542	0.955	0.734
5	20	0.640	2.741	0.224	0.970	0.0784	0.968	0.812
6	23	1.001	2.105	0.422	0.860	0.0251	0.984	0.921

Table 3: The Estimated Model Parameters and the Squares of the Multiple Correlation Coefficients (R^2) for the Fits of the Simulated Skin Conductance Time Series.

Female Participant	$\hat{\tau}_r$	$\hat{\tau}_d$	$\hat{\alpha}_2$	$\frac{\lvert\tau_r-\hat{\tau}_r\rvert}{\tau_r}\times 100\%$	$\frac{\lvert\tau_d-\hat{\tau}_d\rvert}{\tau_d}\times 100\%$	$\frac{\lvert\alpha_2-\hat{\alpha}_2\rvert}{\alpha_2}\times 100\%$	$\hat{\lambda}$	R_h^2	R_f^2
1	0.562	3.013	0.074	0.050	0.262	0.553	0.0058	0.999	0.987
2	0.820	2.823	0.401	3.276	2.182	0.483	0.0357	0.998	0.985
3	0.501	3.108	0.150	0.391	0.539	1.312	0.0197	0.998	0.986
4	0.853	2.655	0.129	16.914	26.329	0.230	0.0366	0.994	0.982
5	0.694	2.908	0.373	0.081	0.076	0.119	0.0138	0.999	0.987
6	0.339	2.691	0.628	0.923	1.626	1.327	0.0299	0.998	0.987
Male Participant	$\hat{\tau}_1$	$\hat{\tau}_2$	$\hat{\alpha}_2$	$\frac{\lvert\tau_1-\hat{\tau}_1\rvert}{\tau_1}\times 100\%$	$\frac{\lvert\tau_2-\hat{\tau}_2\rvert}{\tau_2}\times 100\%$	$\frac{\lvert\alpha-\hat{\alpha}_2\rvert}{\alpha_2}\times 100\%$	$\hat{\lambda}$	R_h^2	R_f^2
1	0.734	3.115	0.413	4.893	0.408	0.148	0.0290	0.994	0.985
2	0.527	3.111	0.368	1.674	2.765	1.268	0.0266	0.998	0.984
3	0.851	1.500	0.032	19.078	17.369	5.527	0.0168	0.866	0.860
4	0.322	3.492	0.643	3.759	2.649	2.012	0.0128	0.997	0.983
5	0.654	2.727	0.2272	2.122	0.510	1.420	0.0391	0.991	0.975
6	0.940	2.479	0.430	2.235	4.193	0.164	0.0323	0.998	0.986

we again deconvolve the noisy simulated data to compare the results with the ground truth used to simulate the data. Figure 16 shows results from four simulated data. In Figure 16, the panels show the deconvolution results on the simulated data for two female and two male participants, respectively. In each panel, i) the top subpanel shows the simulated (blue stars) and the estimated (red curve) phasic components corresponding to the middle phalanx of hand; ii) middle panel shows the simulated (blue stars) and estimated (red curve) phasic components corresponding to the the medial planar surface of foot; and iii) bottom sub-panel shows the timings of the simulated ANS activation timings and amplitudes (gray

Table 4: Deconvolution Errors with Our Single Channel and Concurrent Deconvolution using Simulated Data.

Approaches	$\frac{\sum \lvert\Delta_i - \hat{\Delta}_i\rvert}{\lVert\hat{\mathbf{u}}\rVert_0}$	$\frac{\lVert\mathbf{u}-\hat{\mathbf{u}}\rVert}{\lVert\mathbf{u}\rVert_0}$	$\frac{\lvert\tau_r - \hat{\tau}_r\rvert}{\tau_r} \times 100\%$	$\frac{\lvert\tau_d - \hat{\tau}_d\rvert}{\tau_d} \times 100\%$
Only Hand	0.26	0.61	5.80	8.25
Only Foot	0.28	1.22	21.57	6.83
Concurrent	0.18	0.46	1.23	3.26

line) and the estimated ANS activation timings and amplitudes (red dashed line). The deconvolution results for all twelve participants are given in the Appendix A.2. Table 3 shows the estimated parameters, the corresponding estimated errors, and R^2 values. In Table 3, τ_r, τ_d, and α_2 denote the rise time, decay time and the attenuation parameter for the foot SC data; symbols with hat and without hat denote the estimated and the true values of the parameters, respectively; and R_h^2 and R_f^2 correspond to the R^2 for the fits of the hand and foot SC data, respectively.

To further validate our approach, we simulated noisy data using a synthetic input and the model parameters $\tau_r = 0.75$, $\tau_d = 4$, and $\alpha_2 = 0.3$. In this case, we have the ground truth for comparison. To simulate the noisy data, we added zero-mean Gaussian noise with 20 dB and 15 dB SNR to the hand and foot phasic SC data, respectively. These two levels of noise are chosen because of the higher levels of noise in the foot data. Figure 17 shows the simulated data for both channels. In Figure 17, the panels (i) and (ii), respectively, depict the synthetic simulated data with 20 dB and 15 dB noise for the hand and foot. Panels (iii) and (iv) show results with LedaLab [21]. The panels (v) and (vi) show the results with cvxEDA [23]. The panels (vii) and (viii) show the recovered neural stimuli with our single channel deconvolution. Panel (vii) shows the recovered results with our concurrent deconvolution on simulated hand and foot SC data. Gray vertical lines correspond to the ground truth, and the red, blue, and green vertical lines correspond to recovered neural stimuli with hand data, foot data, and concurrent deconvolution. We perform deconvolution on the simulated noisy data. Figure 17 also shows the deconvolution performance of other existing algorithms for comparison, as well as our single channel deconvolution approach.

Results using simulated data show that our concurrent deconvolution scheme outperforms the existing methods. The last three panels in Figure 17 and the corresponding estimation errors in Table 4 also show how our concurrent deconvolution scheme performs better than our single channel deconvolution approach. Moreover, Figure 18 shows how noise effects the estimation accuracy for τ_r and τ_d. In Figure 18, Left and right subpanels show how the percentage error increases with low SNR; each data point corresponds to the average percentage error of eight simulated trials; the model parameters for the simulated data used are $\tau_r = 0.75$ seconds, $\tau_d = 4$ seconds, $\alpha_2 = 0.5$ and $\alpha_3 = 0.3$. Neural stimulus used for the simulation is the same as in Figure 17.

3.3.2 Dataset 2

Figure 19 shows the stress estimates for the estimated neural stimuli using the heuristic peak detection [82], our single channel deconvolution [83], and our concurrent deconvolution. In Figure 19, all three panels from left to right show the estimated stress from the driver stress dataset with heuristic peak detection [82], our single channel deconvolution [83], and our concurrent deconvolution, respectively; the subpanels respectively depict the recorded SC signal from hand, SC signal from foot, inferred autonomic nervous activity $\boldsymbol{u}$, stress state $w_{j|J}$ and probability of $p_{j|J}$ with their confidence intervals. The color-coded backgrounds green, light violet, light red, and yellow correspond to rest period, city driving, toll road, and highway, respectively. Figure 19a shows the stress estimation result using the approach proposed in [82] for the driver using heuristic peak detection scheme for detecting neural stimuli $\boldsymbol{u}$. We perform both multi-channel and single channel deconvolution on a small segment from 1500 seconds to 1700 seconds of the recorded signal. After deconvolving phasic SC segment, we solve the inverse problem of estimating $\boldsymbol{u}$ for entire phasic SC signal using FOCUSS+ and GCV-FOCUSS+ with the $\boldsymbol{\theta}$ estimated from the deconvolution step. Then, we bin the estimated $\boldsymbol{u}$ with a bin size of 1 seconds. We use the same stress estimation approach in [82] with the results obtained using our concurrent deconvolution algorithm.

3.4 Discussion

Figure 13 shows the overall system block diagram, where the system parameters for different regions are assumed to be same and the attenuation terms $0.01 \leq \alpha_2, \alpha_3, \cdots, \alpha_\chi \leq 100$. However, we have also considered other configurations for the system and tried to formulate optimization problems. We investigate different possibilities with two-channel recordings. We have considered the configuration by taking $\boldsymbol{\tau}$ the same for both hand (middle phalanx) and foot (medial plantar surface) regions. In this case, the attenuation $\alpha_2 = 1$ which corresponds to the recording from foot. The R^2 squared fit for the foot is very low and a clear attenuation factor other than $\alpha_2 = 1$ is observed. Then, we formulate the problem with the configuration, which has two different sets of system response parameters (rise time and decay) $\boldsymbol{\tau}$ for both channels while keeping $\alpha_2 = 1$. This time, the solutions for $\boldsymbol{\tau}$ for both hand and foot stagnated at extreme bounds and fit after reconstructions were not good for at least one channel. Next, we have analyzed the data taking $\boldsymbol{\tau}$ different and $0.01 \leq \alpha_2 \leq 100$. In this case, the fits after reconstruction were good for most of the channels but all the solutions for $\boldsymbol{\tau}$ for both hand foot regions stagnated in the upper/lower bounds. This is because the optimization formulation has too many degrees of freedom. Therefore, we remove some degrees of freedom by taking $\boldsymbol{\tau}$ same for both hand and foot regions. In addition to that, we introduced a delay in the input from the foot sweat glands causing a delayed phasic response and successfully concurrently deconvolved phasic SC signals from the hand and foot, and recovered neural stimuli and underlying physiological system parameters.

It is somewhat counterintuitive that the skin conductance system responses (i.e., the corresponding rise times and decay times) in different regions are similar in shape, although there can be dissimilarities in the sweat glands. This is because different rise times and decay times for different skin locations will lead to too many degrees of freedom. It is possible to have many solutions to the system for a given set of observed data. In this work, we assumed the system response does not have much variance in different skin regions.

Moreover, the variability in different skin regions is captured by the tonic component. We remove the tonic component before proceeding with the deconvolution steps. In one of our works [8], we have developed a deconvolution scheme to separate the tonic and phasic components iteratively in a coordinate descent manner. It is possible to develop a similar approach for the multichannel case. In this way, the variability of the phasic SC response in different skin locations can be captured. It might also require additional physiological constraints on the phasic SC response parameters as the assumption of different phasic SC response parameters will result in too many degrees of freedom in the optimization problem leading to infinitely many solutions.

Deconvolution of SC signals is a challenging problem as multiple sets of physiological parameters and neural stimuli exist which closely approximate the observed signal. Besides, the smallest level of noise can perturb the solution to a physiologically infeasible point because of the sensitive nature of the system impulse response with respect to the physiological parameters. The proposed formulation is a nonconvex problem and we solve it using a coordinate descent deconvolution approach until convergence to a local minimum. To account for non-convexity, we use multiple initializations and choose the solution that minimizes the cost function compared to all other solutions that the algorithm finds. To ensure an identifiable solution, we use appropriate physiologically plausible constraints similar to [52, 53] on the unknowns. Figure 17 shows the results from the previous two algorithms: LedaLab [29] and cvxEDA [23]. These two existing methods can solve the inverse problem of finding $\boldsymbol{u}$ using single channel data assuming known physiological parameters. In contrast, the proposed approach can solve for both the physiological system parameters and the inverse problem of finding neural stimuli using multichannel recording.

From our analysis of the auditory stimulation data, we observe a very large phasic response right after a stimulation has been given to the participant. For example, female participant 1, male participant 2, and male participant 3 have significantly distinct phasic SC responses right after the auditory stimuli. Although the phasic SC data from female

participant 2 shows multiple responses after one auditory stimulation, the very first response right after an auditory stimulation is usually very prominent. Other comparatively smaller responses indicate that the participant requires more perspiration to reduce the body temperature increase due to increased metabolism. Our algorithm successfully detected these small responses as well. In general, the distance between two consecutive phasic responses is more than a few seconds. Therefore, we chose a minimum separation of 1 second between two adjacent peaks in the deconvolution algorithm to obtain a physiologically feasible solution.

SC data can be noisy and small noisy peaks are comparable to the small insignificant phasic SC responses. To avoid detecting noise peaks as SC phasic response, we used an internal threshold in each iteration GCV-FOCUSS+. Any detected estimated nonzero element of $\boldsymbol{u}$ that is smaller than the threshold is set to zero. In this study, we used 5 as the threshold. This threshold works well for almost all participants. However, there are cases where participants have very small phasic SC responses that are very comparable to noise and our algorithm might discard them. For instance, male participant 3 has very small phasic SC responses during auditory stimulation for the hand and foot. In this case, the phasic SC responses that are comparable to the noise are discarded. Figure 83 in Appendix A.2 shows that the simulation results from the simulation corresponding to male participant 3 discards one detected pulse that is very close to 5. This is because the addition of noise to the simulated data made the smallest phasic SC response comparable to noise. This also explains the low R^2 values in male participant 3. In our future work, we plan to include participant-dependent threshold selection to enable us to detect phasic SC responses for cases where the participants have very small ANS activation. In the case of male participant 4, one small peak present between 260 seconds and 280 seconds of foot data is not visible in the hand data. This denotes that the peak is due to noise. Our algorithm discards this peak and prevents overfitting to the noise. This is the reason the R^2 value in male participant 4 foot data is small.

Figure 18 shows how noise can deteriorate the estimation accuracy. Figure 18 also shows that with the addition of more channels, the estimation accuracy of decay time τ_d increases. However, the same is not visible for τ_r. This might be because τ_r is smaller than 1 second, which is less than the sampling frequency. It is hard to capture the information of about τ_r with 1 Hz sampling frequency. Nevertheless, with higher sampling frequency, the estimation accuracy for τ_r should also improve with addition to more channels similar to τ_d.

The stress results obtained in Figure 19 for all the cases are consistent. The result in Figure 19c shows much smoother estimation compared to the result in 19b and 19a. Although stress estimation using the results from single-channel deconvolution obtains a smoother estimate compared to the peak detection one, it is not as good as the concurrent deconvolution. In the first rest period, there is an unwanted peak in the estimated stress state in the heuristic approach. The stress estimation using the result from single-channel deconvolution also detected the unwanted stress state spike. In contrast, the result in Figure 19c shows much-improved stress tracking with no significant stress state spike in the first rest period. A similar spike in the HAI can also be seen in the first rest period for 19b and 19a which is very small in 19c. Simple peak detection algorithm might not provide the accurate timings and amplitudes of the neural stimuli. Moreover, small noise peaks can be captured with the peak detection algorithm where they might not represent actual neural stimuli.

4 Sparse Deconvolution of Electrodermal Activity via Continuous-Time System Identification

4.1 An Overview of Continuous-Time System Identification-Based Electrodermal Activity Deconvolution

In general, electrodermal activity (EDA) refers to any changes in the electrical characteristics of the skin due to different physiological activities. Skin conductance response (SCR), which is one of the measures of EDA for physiological analysis, indicates different eccrine sweat gland activities caused by the stimulation of the autonomic nervous system (ANS), mainly by the sudomotor nerve [76]. When sweat secretions occur in response to stimulations from the autonomic nervous system, there is an alteration in the ionic permeability of the cell membranes. This change in permeability increases conductance in skin tissue. Although sweating, controlled by hypothalamic areas, is mostly intended for thermoregulation, it also depends on other physiological events including emotional arousal [73]. Many works attest to the high correlation between sympathetic nervous activity and EDA [74, 75].

Physiological signals like EDA that have a high correlation with sympathetic nervous activity can help to interpret emotional dysfunctions or abnormalities. Emotional dysfunctions influence psychiatric disorders like depression [87]. Many studies have shown the risks of suicidal behavior in patients having psychiatric disorders including depression and posttraumatic stress disorder [88, 89, 90]. Mortality due to mental disorders has been identified as one of the major causes of death worldwide [31]. Moreover, dysregulation in arousal can cause symptoms including insomnia and irritability [91]. Patients with posttraumatic

This chapter has been adopted from Amin, Md Rafiul, and Rose T. Faghih. "Sparse deconvolution of electrodermal activity via continuous-time system identification." IEEE Transactions on Biomedical Engineering 66.9 (2019): 2585-2595 [52].

stress disorder show symptoms of difficulty in falling asleep and excessive irritability [92]. In psychopathology, identifying problematic patterns of emotion and emotional regulation can characterize psychiatric disorders [35, 93]. Several studies have been carried out to detect mental disorders using emotional tracking [15] and from disturbed arousal conditions [94]. Mental disorder-related issues could be significantly reduced if a personalized health monitoring system [78] with a user-friendly daily psychological condition tracking could be devised.

Macefield *et al.* [15] have shown that areas of the brain related to sympathetic nervous activity can be identified by using functional magnetic resonance imaging (fMRI) of the brain and by recording concurrent microelectrodes readings generated by sympathetic outflow to muscle and skin. They have proposed to extend this idea to examine specific disorders of emotional expression to comprehend underlying neural processes. To collect fMRI data, a clinical setup is necessary which will be convenient for clinical diagnosis. Unfortunately, it is not convenient for daily tracking of neural process related to emotional states. Bomba *et al.* [16] used heart rate variability (HRV) from the ECG signal as a measure of ANS imbalance. However, Soh *et al.* [17] illustrated the underlying challenges and complexity of acquiring ECG data using wearable technology. In another study, Faghih *et al.* [18] were able to recover the amplitude and timing of neural stimuli related to different fear states employing EDA signals with a deconvolution scheme [19, 20]. Utilizing recovered timings and amplitudes, emotional states can be estimated to analyze emotional disorders.

Many deconvolution schemes have been proposed for physiological signals including skin conductance (SC) data. Benedek *et al.* [21] proposed a non-negative approach to decompose SC data into discrete compact responses and at the same time assessed deviations from the standard SCR shape. However, this decomposition approach could detect noise as SCR and does not include the individual differences in modeling the fall and rise times. Greco *et al.* [23] proposed decomposing SC data into tonic and phasic components. They formulated a quadratic programming problem to find sparse solutions for the input stimuli. However, the

use of fixed regularization parameter makes it challenging to find an optimal sparse solution. In another work, Gallego *et al.* [24] proposed an approach to obtain a more sparse solution; however, this approach seems to oversparsify the solution. In the deconvolution scheme proposed by Faghih *et al.* [25, 18, 19, 20, 26], a two-step coordinate descent approach has been incorporated. In the first step, they used the FOCal Under-determined System Solver (FOCUSS) algorithm [27] to find a sparse solution of the neural stimuli. This step is a convex optimization problem to which a global solution can be achieved. In the following step, their algorithm employs another optimization problem to find the physiological system parameters, which is not convex. Therefore, it is possible for the solution to stagnate at a local minimum.

In the present study, we propose an algorithm to find neural stimuli and underlying system parameters and use this algorithm to analyze EDA data. Inspired by the work carried out by Faghih *et al.* [25, 18, 19, 20, 26], we use a state-space model to relate SC to the internal unobserved neural stimuli. However, in this work, we re-formulate the optimization problem for model parameter estimation in [25, 18, 19, 20, 26] as a convex problem to avoid the stagnation of the solutions at local minima. In contrast to the model proposed in [18], we only model the phasic component of SC as a state variable in our state-space equations. We separate the phasic component from the SC using the cvxEDA algorithm proposed in [23]. Then, we take a coordinate descent approach to recover the neural stimuli and estimate the system parameters. We use a modified version of FOCUSS [19] to solve the inverse problem of finding neural stimuli from SC data. For system parameters estimation, we employ a continuous-time system identification approach using Hartley Modulating function. This allows for formulating this problem as a convex optimization problem in terms of neural stimuli and physiological system parameters. We also incorporate a data-dependent bandwidth selection approach for more accurate estimation of physiological system parameters. Then, we apply our method to analyze SC data collected during cognitive stress tasks. We successfully recover the underlying stimuli and the physiological parameters.

4.2 Methods

4.2.1 Experiment

Dataset 1. In this study, we analyze a publicly available dataset collected by Quality of Life Laboratory at the University of Texas at Dallas [95]. The data was collected from 20 college students. Fourteen of them were male and six of them were female. Information on subject ID, age, gender, and body mass index (BMI) of each subject are provided in Section A.3. The experiment was carried out to distinguish between physiological signals during different types of stresses ('cognitive stress', 'emotional stress', 'physical stress', and 'relaxing'). A detailed explanation of the experiment is given in [95]. In this study, we analyze EDA data from 3-minute 'counting task' of the 'cognitive stress' portion of the study. In the 'counting task', the subjects have to count backwards by sevens, beginning with 2485 for three minutes. The SC signal was measured with a sampling frequency of 8 Hz. In our study, we downsample the data by a factor of 2 and obtain the 4Hz signal for analysis. Furthermore, we discard all signals that have been corrupted by heavy artifacts. Therefore, we only analyze 6 subjects whose SC signals are not corrupted by heavy motion artifacts. Table 5 shows subject ID, age, gender, and BMI of each participant.

Table 5: Information of Subjects.

Participant No.	Subject ID	Age	Gender	BMI $[\frac{kg}{m^2}]$
1	01	30	M	30.00
2	05	30	M	24.75
3	08	27	M	19.32
4	09	25	M	21.70
5	12	32	F	20.20
6	16	24	M	16.66

Dataset 2. Skin conductance responses to loud sounds, simultaneously recorded from the palm, fingers, and foot [57] datasets were collected for modeling event-related SC responses. Participants were asked to press a foot-operated pedal in response to 20 auditory stimuli. Auditory stimulations are one-second long white noise bursts. The details of the

experiment are in [30]. We use SC recordings from the middle phalanx of the dominant second and third finger for our study. The dataset contains the timing of the auditory stimulations to perform the comparison with the recovered stimuli. We use this dataset to perform the comparison with existing methods. The signals in this dataset have a sampling frequency of 100 Hz. We downsample the data to 4 Hz for our analysis.

4.2.2 Model Formulation

The SC data can be represented as a summation of two different signals [21, 42]. One is a slowly varying signal called tonic component and another is a comparatively fast varying signal called phasic component. We separate the phasic component from SC using the algorithm proposed by Greco *et al.* [23].

The phasic component of the SC can be modeled as a second-order differential equation. We use a second-order differential equation model similar to the models in [18, 42]. This model describes the changes in the phasic SC as a function of the activity of the sudomotor nerve. The model is defined in state-space form as follows,

$$\dot{x}_1(t) = -\frac{1}{\tau_1}x_1(t) + \frac{1}{\tau_1}u(t) \tag{45}$$

$$\text{and } \dot{x}_2(t) = \frac{1}{\tau_2}x_1(t) - \frac{1}{\tau_2}x_2(t), \tag{46}$$

where x_2 is the SC level of the phasic component and x_1 is an internal unobserved state variable. τ_1 and τ_2 are SC time constants in the model corresponding to the rise time and fall time, respectively. This time-invariant system representation can model the phasic responses under the assumption that the time constants τ_1 and τ_2 do not change over the duration of the experiment. We know that a single neural impulse from ANS is responsible for a single phasic SC response [45, 24, 18]. The length of the experimental signals and the average separation of the consecutive phasic SC responses are very high compared to the number of neural stimuli impulses generated by ANS; hence, we can include a sparsity

constraint on the neural stimuli. In contrast to the model proposed in [42], we consider a finite number of stimuli as the model input (similar to [45, 24, 18]). This definition makes it suitable to take the timings and amplitude of the stimuli to quantify emotional states. We define the sparse abstraction of the input stimulation as $u(t) = \sum_{i=1}^{N} q_i \delta(t - \Delta_i)$, where q_i represents the level of stimulation at time Δ_i. q_i of zero implies no stimulation at time Δ_i. N refers to the length of the input; N is a function of the duration of the experiment and the input sampling interval T_u. In this case, we can write $\Delta_i = iT_u$.

Discrete-Time System Identification. Let's say the signal has been sampled with a sampling interval of T_y for M samples. We can define the observed phasic SC data y_{t_k} as follows,

$$y_{t_k} = x_2(t_k) + \nu_{t_k}, \tag{47}$$

where $k = 1, 2, \cdots, M$; $t_k = kT_y$ and ν_{t_k} represents signal noise. We model ν_{t_k} as a Gaussian random variable and use this assumption to implement a least squares approach in our estimation algorithm. Using the phasic SC data y_{t_k}, we would like to estimate τ_1 and τ_2, and also recover the input $u(t)$, i.e., the amplitudes and timings of the stimuli. Assuming that $x_1(0) = 0$, solution for y_{t_k} would be as follows,

$$y_{t_k} = a_{t_k} y_0 + \mathbf{b}_{t_k} \mathbf{u} + \nu_{t_k}, \tag{48}$$

where $a_{t_k} = e^{-\frac{t_k}{\tau_2}}$, $\mathbf{b}_{t_k} = \big[\frac{1}{(\tau_1-\tau_2)}(e^{-\frac{t_k}{\tau_1}} - e^{-\frac{t_k}{\tau_2}}) \quad \frac{1}{(\tau_1-\tau_2)}(e^{-\frac{t_k-T_u}{\tau_1}} - e^{-\frac{t_k-T_u}{\tau_2}}) \quad \frac{1}{(\tau_1-\tau_2)}(e^{-\frac{t_k-2T_u}{\tau_1}} - e^{-\frac{t_k-2T_u}{\tau_2}}) \quad \cdots \quad \frac{1}{(\tau_1-\tau_2)}(e^{-\frac{T_u}{\tau_1}} - e^{-\frac{T_u}{\tau_2}}) \quad \underbrace{0 \quad \cdots \quad 0}_{N-\frac{t_k}{T_u}}\big]$ and vector $\mathbf{u} = [q_1 \quad q_2 \quad \cdots \quad q_N]^\top$ represents the entire input over the entire experiment. Let $\mathbf{y} = [y_{t_1} \quad y_{t_2} \quad \cdots \quad y_{t_M}]^\top$, $\boldsymbol{\tau} = [\tau_1 \quad \tau_2]^\top$, $\mathbf{A}_\tau = [a_{t_1} \quad a_{t_2} \quad \cdots \quad a_{t_M}]^\top$, $\mathbf{B}_\tau = [\mathbf{b}_{t_1} \quad \mathbf{b}_{t_2} \quad \cdots \quad \mathbf{b}_{t_M}]^\top$, $\boldsymbol{\nu} = [\nu_{t_1} \quad \nu_{t_2} \quad \cdots \quad \nu_{t_M}]^\top$ and y_0 is the initial condition of the phasic SC level. Here, T_y

is always an integer multiple of T_u. Now we can represent the system as,

$$\mathbf{y} = \mathbf{A}_\tau y_0 + \mathbf{B}_\tau \mathbf{u} + \boldsymbol{\nu}. \tag{49}$$

Equation (49) shows the representation of the sampled phasic SC data. In this study, we simulate the data using a state-space approach. A detailed description is given in Section A.3. In this study, we are considering $T_u = T_y$ and $N = M$, i.e., we take the resolution of input vector $\mathbf{u}$ as same as $\mathbf{y}$.

Multi-Rate State-Space Formulation. We show another way of discretization in this section. We put Equations (45)-(47) into a state space form and derive the discrete analog of the system. In this formulation, the unknowns include τ_1 and τ_2, q_i and Δ_i (for $i = 1, 2, \cdots, N$).

Let, $x(t) = \begin{bmatrix} x_1 & x_2 \end{bmatrix}^\top$, $\mathcal{A}_c = \begin{bmatrix} -\frac{1}{\tau_1} & 0 \\ \frac{1}{\tau_1} & -\frac{1}{\tau_2} \end{bmatrix}$, $\mathcal{B}_c = \begin{bmatrix} \frac{1}{\tau_1} \\ 0 \end{bmatrix}$ and $\mathcal{C}_c = \begin{bmatrix} 0 & 1 \end{bmatrix}$. Hence, the state space model can be written as,

$$\dot{x}(t) = \mathcal{A}_c x(t) + \mathcal{B}_c u(t)$$

$$\text{and } y(t) = \mathcal{C}_c x(t) + \nu(t),$$

where $y(t)$ is the observed skin conductance (SC) and $\nu(t)$ is the measurement noise at time t. Assuming that the input and the states are constant over T_u, by letting $\Lambda = e^{AT_u}$, and $\Gamma = \int_0^{T_u} e^{A(T_u - \rho)} d\rho$, we can write the discrete state space form as,

$$x\left[k+1\right] = \Lambda x\left[k\right] + \Gamma u[k]$$

$$\text{and } y\left[k\right] = \mathcal{C}_c x\left[k\right] + \nu\left[k\right].$$

This can be extended to a multirate formulation, i.e., for the cases where neural stimuli and SC measurements have different sampling frequencies. We let the SC measurement

sampling frequency $T_y = LT_u$, where L is an integer. We can also represent L as the ratio of number of samples in neural stimuli and SC signal, i.e. $L = \frac{N}{M}$ where M is the number of available data points. By letting $\mathcal{A}_d = \Lambda^L$, $\mathcal{B}_d = \begin{bmatrix} \Lambda^{L-1}\Gamma & \Lambda^{L-2}\Gamma & \cdots & \Gamma \end{bmatrix}$, $u_d[k] = \begin{bmatrix} u[Lk] & u[Lk+1] & \cdots & u[Lk+L-1] \end{bmatrix}^\top$, $\nu_d[k] = \nu[Lk]$ and $x_d[k] = x_d[Lk]$, we can represent the multi-rate system as,

$$x_d[k+1] = \mathcal{A}_d x_d[k] + \mathcal{B}_d u_d[k]$$
$$\text{and} y[k] = \mathcal{C}_c x_d[k] + \nu_d[k],$$

where $\mathcal{A}_d$ and $\mathcal{B}_d$ are functions of $\boldsymbol{\tau} = \begin{bmatrix} \tau_1 & \tau_2 \end{bmatrix}$. Then, using the state transition matrix, and considering that the system is causal, we can write the system equation as,

$$y[k] = \mathcal{F}[k] x_d[0] + \mathcal{D}[k] \mathbf{u} + \nu_d[k],$$

where $\mathcal{F}[k] = \mathcal{C}_c \mathcal{A}_d^k$, $\mathcal{D}[k] = \mathcal{C}_c \begin{bmatrix} \mathcal{A}_d^{k-1}\mathcal{B}_d & \mathcal{A}_d^{k-2}\mathcal{B}_d & \cdots & \mathcal{B}_d & \underbrace{0 \quad \cdots \quad 0}_{N-kL} \end{bmatrix}$, and $\mathbf{u} = \begin{bmatrix} u_d[0] & u_d[1] & \cdots & u_d[k-1] & \cdots & u_d[M-1] \end{bmatrix}^\top$. $\mathbf{u}$ represents the entire input over the duration of the study. Considering the initial condition $x_1(0) = 0$ and $y(0) = x_2(0) = y_0$, we can let $x_d[0] = \begin{bmatrix} 0 & y_0 \end{bmatrix}^\top$. Then, let $\mathbf{y} = \begin{bmatrix} y[1] & y[2] & \cdots & y[M] \end{bmatrix}^\top_{M\times 1}$, where $\mathbf{y}$ represents all the data points. Moreover, let $\mathbf{F}_\tau = \begin{bmatrix} \mathcal{F}[0] & \mathcal{F}[1] & \cdots & \mathcal{F}[M-1] \end{bmatrix}^\top_{M\times 2}$, $\mathbf{D}_\tau = \begin{bmatrix} \mathcal{D}[0] & \mathcal{D}[1] & \cdots & \mathcal{D}[M-1] \end{bmatrix}^\top_{M\times N}$, and $\boldsymbol{\nu} = \begin{bmatrix} \nu[1] & \nu[2] & \cdots & \nu[M] \end{bmatrix}^\top_{M\times 1}$. Hence, we can represent this system as,

$$\mathbf{y} = \mathbf{F}_\tau x_d[0] + \mathbf{D}_\tau \mathbf{u} + \boldsymbol{\nu}.$$

This solution is equivalent to Equation 5 by considering $\mathbf{F}_\tau x_d[0] = \mathbf{A}_\tau y_0$ and $\mathbf{D}_\tau = \mathbf{B}_\tau$.

Discretization of Neural Impulse Train. As both discrete and continuous representation

of neural stimuli has been carried out with impulse functions, a careful conversion between these representations is necessary. $u(t)$ is defined as a summation of weighted delta functions, i.e., $u(t) = \sum_{i=1}^{N} q_i \delta(t - \Delta_i)$ where $\Delta_i = iT_u$ is the arrival time of the corresponding impulse. Each delta function has an area of 1 under the curve. For discretization, we first take an approximation of the Dirac delta function with a rectangular function of width T_u and height $\frac{1}{T_u}$ to have the area of the rectangle 1 where T_u is the sampling interval of neural stimuli. Then, we sample the neural stimuli with the sampling interval T_u. For example, a continuous time neural stimuli $u_i(t) = q_i \delta(t - \Delta_i)$ with only one weighted impulse can be written as a scaled and shifted rectangular $\tilde{u}_i(t) = \frac{q_i}{T_u} \Pi(\frac{t - \Delta_i - T_u/2}{T_u})$. In Figure 20, each

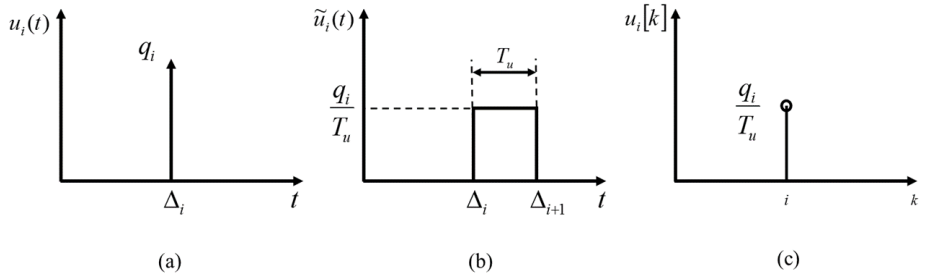

Figure 20: **Discretization of Neural Stimuli.**

panel shows the steps for discretization of the neural stimuli represented with a weighted impulse train: (a) an example of continuous-time neural stimuli $u_i(t)$, represented with with an weighted and shifted Dirac delta function, (b) the approximation to the $u_i(t)$ function with a rectangular function, and (c) the equivalent discrete neural stimuli represented with Kronecker delta function. It has been time scaled to have a bin size equal to the sampling frequency. Amplitude has been scaled with the reciprocal of the sampling frequency to keep the area under the curve same as in $u_i(t)$. Finally, the approximation can be sampled to obtain the discrete sequence $u_i[k]$ (Figure 20 (c)).

Continuous-Time System Identification. In continuous-time system identification technique, we transform the signal into a new domain according to the system model so that the optimization problem for finding system parameters τ_1 and τ_2 becomes convex.

We first write the two first-order coupled differential equations ((45)-(46)) as a second-order differential equation,

$$\alpha_2 \frac{\mathrm{d}^2 y(t)}{\mathrm{d}t^2} + \alpha_1 \frac{\mathrm{d}y(t)}{\mathrm{d}t} + y(t) = u(t), \tag{50}$$

where $y(t)$ is the continuous equivalent of y_{t_k}, $\alpha_1 = \tau_1 + \tau_2$, and $\alpha_2 = \tau_1\tau_2$. If we find α_1 and α_2, then we can solve for τ_1 and τ_2. Let $\boldsymbol{\Theta} = \begin{bmatrix} \alpha_1 & \alpha_2 \end{bmatrix}^\top$, $g_0(\boldsymbol{\Theta}) = (\alpha_2^2 - 4\alpha_1)$. Hence,

$$\boldsymbol{\tau} = \mathbf{g}(\boldsymbol{\Theta}) = \begin{bmatrix} g_1(\Theta) \\ g_2(\Theta) \end{bmatrix} = \begin{bmatrix} \frac{1}{2}\left(\alpha_1 - \sqrt{g_0(\boldsymbol{\Theta})}\right) \\ \frac{1}{2}\left(\alpha_1 + \sqrt{(g_0(\boldsymbol{\Theta})}\right) \end{bmatrix}. \tag{51}$$

The modulating function method for identifying the model parameters begins with multiplying both sides of (50) by the modulating function and integrating over T_d, which is the duration of the sampled signal. The modulating function is given by $\phi_m(t)$ where the integer m refers to the m^{th} spectral component. The length of the modulating function is chosen as same as the sampling duration of the signal. The integration results in

$$\alpha_2 \int_0^{T_d} \phi_m(t) \frac{\mathrm{d}^2 y(t)}{\mathrm{d}t^2} dt + \alpha_1 \int_0^{T_d} \phi_m(t) \frac{\mathrm{d}y(t)}{\mathrm{d}t} dt + \int_0^{T_d} \phi_m(t) y(t) dt = \int_0^{T_d} \phi_m(t) u(t) dt. \tag{52}$$

4.2.3 Estimation

To accomplish our goal, we break down the problem into two subproblems. One is to find the model parameters $\boldsymbol{\tau}$ and another is the inverse problem, i.e., to find the stimuli $\mathbf{u}$. Inspired by the coordinate descent deconvolution scheme by Faghih *et al.* [19], we follow a similar approach. Unlike [19], we use a continuous system identification approach for the parameter estimation. Then, we solve the inverse problem using the FOCUSS algorithm [27]. Using a coordinate descent approach, we iterate between these two steps until convergence. These two steps are described in detail in Sections 4.2.4 and 4.2.6. Then,

the coordinate descent approach is discussed in Section 4.2.10.

4.2.4 System Identification using Hartley Modulating Functions

There are different modulating functions that could be used for continuous-time system identification. One can use any modulating function according to their convenience [96, 97]. Among the two most widely used modulating functions, one option is the Fourier modulating function [97]; however, it involves complex values and is not the best choice for this study. Another one is the Hartley modulating function (HMF) which does not involve complex numbers in spectral components. Apart from having real coefficients, this modulating function also does not depend on the boundary conditions and the computation of all spectral components can be made using fast algorithms for the discrete Hartley transformation [98]. We use the HMF approach as this function and its corresponding spectral components are always real-valued and yet contain all the information that is also contained in the Fourier modulating function [96, 97]. For a κ^{th} order system, the κ^{th} order HMF spectral component has to be calculated. The properties of a κ^{th} order HMF allows us to formulate a convex optimization formulation for model parameter estimation.

Properties of HMF

The κ^{th} order HMF [98] with fixed time interval $[0, T_d]$ is as follows,

$$\phi_m(t) = \sum_{j=0}^{\kappa} (-1)^j \binom{\kappa}{j} \text{cas}((\kappa + m - j)\omega_0 t), \tag{53}$$

where for a variable s, $\text{cas}(s) = \cos(s) + \sin(s)$ and $\frac{\text{dcas}(s)}{\text{d}s} = \text{cas}(-s)$. HMF $\phi_m(t)$ has the following properties:

$$\phi_m(t) \text{ is zero beyond the interval } [0, T_d],$$

$$\text{the } l^{\text{th}} \text{ derivative } \phi_m^{(l)}(t) \text{ exists for all } l = 0, 1, \cdots, \kappa - 1 \text{ and}$$

$$\phi_m^{(m)} = 0 \text{ for } t = 0 \text{ and } t = T_d \tag{54}$$

where $\omega_0 = \dfrac{2\pi}{T_d}$. In this study, the model order is 2. Since we are given the sampled signal, we repeatedly apply integration-by-parts in (52) until all derivatives of the input (or output) signal vanish.

For any signal $\zeta(t)$, the κth order spectral component of lth derivative of the signal can be modified as below [99, 100],

$$\begin{aligned}
&\bar{H}_\zeta^{(l)}(m\omega_0) \\
&= \int_0^{T_d} \phi_m(t) \frac{\mathrm{d}^l \zeta(t)}{\mathrm{d}t^l} dt \\
&= (-1)^l \int_0^{T_d} \zeta(t) \frac{\mathrm{d}^l \phi_m(t)}{\mathrm{d}t^l} dt \\
&= (-1)^l \sum_{j=0}^{\kappa} (-1)^j \binom{\kappa}{j} (\kappa + m - j)^l \omega_0^l (-1)^l \mathrm{cas}(-\frac{l\pi}{2}) \cdot \int_0^{T_d} \zeta(t) \mathrm{cas}((-1)^l(\kappa + m - j)\omega_0 t) dt \\
&= \sum_{j=0}^{k} (-1)^j \binom{\kappa}{j} (\kappa + m - j)^l \omega_0^l \mathrm{cas}(-\frac{l\pi}{2}) \cdot H_\zeta((-1)^l(\kappa + m - j)\omega_0).
\end{aligned} \tag{55}$$

where $\bar{H}_\zeta^{(l)}(m\omega_0)$ is the m^{th} HMF spectral component of l^{th} derivative of the continuous signal $\zeta(t)$, and $H_\zeta(\omega)$ is the Hartley Transform (HT) [101] of $\zeta(t)$ defined by,

$$H_\zeta(\omega) = \int_{-\infty}^{\infty} \zeta(t) \mathrm{cas}(\omega t) dt. \tag{56}$$

Its corresponding transformation of a discrete sequence with N_ζ samples and duration T_d

is given by,

$$\hat{H}_\zeta(m) = \frac{1}{N_\zeta} \sum_{\eta=0}^{M-1} \zeta\left(\frac{\eta T_d}{N_\zeta}\right) \text{cas}\left(\frac{2\pi m\eta}{N_\zeta}\right) dt. \tag{57}$$

Estimation of HMF spectral components can be carried out using the continuous Hartley transform with numeric integration using (56) or direct estimation of Hartley transform using (57). In this study, we use (56) and trapezoidal rule for the numeric integration of Hartley transform. The number of samples N_ζ for signal $y(t)$ and $u(t)$ is equal to M and N, respectively.

Convex Cost Function Formulation with Linear Regression

Using (55), we can rewrite (52) as,

$$\alpha_2 \bar{H}_y^{(2)}(m\omega_0) + \alpha_1 \bar{H}_y^{(1)}(m\omega_0) = -\bar{H}_y^{(0)}(m\omega_0) + \bar{H}_u^{(0)}(m\omega_0). \tag{58}$$

Here,

$$\begin{aligned}
\bar{H}_u^{(0)}(m\omega_0) &= \int_0^{T_d} \phi_m(t)u(t)dt = \int_0^{T_d} \phi_m(t) \sum_{i=1}^{N} q_i \delta(t - \Delta_i)dt \\
&= \sum_{i=1}^{N} \phi_m(\Delta_i) q_i \\
&= \underbrace{\begin{bmatrix} \phi_m(T_u) & \phi_m(2T_u) & \cdots & \phi_m(NT_u) \end{bmatrix}}_{b_\phi^\top(m\omega_0)} \begin{bmatrix} q_1 \\ q_2 \\ \vdots \\ q_N \end{bmatrix} \\
&= b_\phi^\top(m\omega_0)\mathbf{u}.
\end{aligned}$$

We can rewrite (58) as follows,

$$\bar{H}_y^{(0)}(m\omega_0) = -\alpha_2\bar{H}_y^{(2)}(m\omega_0) - \alpha_1\bar{H}_y^{(1)}(m\omega_0) + b_\phi^\top(m\omega_0)\mathbf{u}. \tag{59}$$

Let $Z(m\omega_0) = \bar{H}_y^{(0)}(m\omega_0)$ and let $\varepsilon(m\omega_0)$ model the error in the new domain. Rearranging the (58), it can be rewritten as a linear regression,

$$Z(m\omega_0) = \boldsymbol{\Phi}^\top(m\omega_0)\boldsymbol{\Theta} + b_\phi^\top(m\omega_0)\mathbf{u} + \varepsilon(m\omega_0), \tag{60}$$

where

$$\boldsymbol{\Phi}^\top(m\omega_0) = -\begin{bmatrix} \bar{H}_y^{(2)}(m\omega_0) & \bar{H}_y^{(1)}(m\omega_0) \end{bmatrix}.$$

Taking a sequence of observations for $m = 0, \pm1, \pm2, \cdots, \pm\mathcal{M}$ where $\mathcal{M}$ is the maximum frequency component. Then, (60) can be rewritten as a vector equation. Hence, the following optimization problem can be formulated to find the parameter vector $\boldsymbol{\Theta}$, β and $\mathbf{u}$,

$$\begin{aligned} \underset{\boldsymbol{\Theta},\mathbf{u},\beta}{\text{minimize}} \quad & J(\boldsymbol{\Theta}, \mathbf{u}, \beta) = \frac{1}{2}\boldsymbol{\varepsilon}^\top(\mathcal{M}\omega_0)\mathbf{W}(\beta)\boldsymbol{\varepsilon}(\mathcal{M}\omega_0) \\ \text{subject to} \quad & \\ & G(\boldsymbol{\Theta}) \leq \mathbf{0} \\ & ||\mathbf{u}||_0 \ll N \\ & \mathbf{u} \geq \mathbf{0} \end{aligned} \tag{61}$$

where, $G(\boldsymbol{\Theta}) = \begin{bmatrix} -g_0(\boldsymbol{\Theta}) \\ \tau_1^{min} - g_1(\boldsymbol{\Theta}) \\ g_1(\boldsymbol{\Theta}) - \tau_1^{max} \\ \tau_2^{min} - g_2(\boldsymbol{\Theta}) \\ g_2(\boldsymbol{\Theta}) - \tau_2^{max} \end{bmatrix}$, $\mathbf{W}(\beta)$ is positive-definite symmetric frequency dependent weighting matrix with the shape parameter β, $\boldsymbol{\varepsilon}(\mathcal{M}\omega_0) = \boldsymbol{Z}(\mathcal{M}\omega_0) - \boldsymbol{\Phi}(\mathcal{M}\omega_0)\boldsymbol{\Theta} - \boldsymbol{B}_\phi^\top(\mathcal{M}\omega_0)\mathbf{u}$,

$$\boldsymbol{\Phi}^\top(\mathcal{M}\omega_0) = [\Phi(-\mathcal{M}\omega_0) \quad \cdots \quad \Phi(-\omega_0) \quad \Phi(0) \quad \Phi(\omega_0) \quad \cdots \quad \Phi(\mathcal{M}\omega_0)],$$

$$\boldsymbol{B}_\phi^\top(\mathcal{M}\omega_0) = [b_\phi(-\mathcal{M}\omega_0) \quad \cdots \quad b_\phi(-\omega_0) \quad b_\phi(0) \quad b_\phi(\omega_0) \quad \cdots \quad b_\phi(\mathcal{M}\omega_0)],$$

and

$$\boldsymbol{Z}^\top(\mathcal{M}\omega_0) = [Z(-\mathcal{M}\omega_0) \quad \cdots \quad Z(-\omega_0) \quad Z(0) \quad Z(\omega_0) \quad \cdots \quad Z(\mathcal{M}\omega_0)].$$

(61) is convex in terms of $\mathbf{u}$ and $\boldsymbol{\Theta}$.Given β and $\mathbf{u}$, we can find $\hat{\boldsymbol{\Theta}}$ by minimizing the cost function defined in (61) considering physiological constraints on time constants τ_1 and τ_2 given by $\mathbf{G}(\boldsymbol{\Theta}) \leq \mathbf{0}$. The first constraint restricts the solution of τ_1 and τ_2 to be real valued. In the second and third constraints, we assume rise time τ_1 is within physiological lower and upper bounds τ_1^{min} and τ_1^{max}, respectively. In the fourth and fifth constraints, We also assume fall time τ_2 is within physiological lower and upper bounds τ_2^{min} and τ_2^{max}, respectively. We assume $\mathbf{u}$ is sparse and hence contains a very small number of nonzero elements out of N possibilities ($||\mathbf{u}||_0 \ll N$). As $\mathbf{u}$ refers to the neural stimuli from the brain, all the elements of $\mathbf{u}$ are nonnegative ($\mathbf{u} \geq \mathbf{0}$). We solve this constrained optimization

problem using the interior point method.

Parameter $\mathcal{M}$ Selection for Maximum Frequency Component Inclusion

The Parameter $\mathcal{M}$ has to be selected such that it captures the signal and yet cancels out the noise. Garnier *et al.* [102] recommend choosing $\mathcal{M}\omega_0$ close to the bandwidth of the system to be identified. We calculate the maximum bandwidth $_{max}$ by plugging in the extreme values τ_1^{max} and τ_2^{max} in α_1 and α_2 parameters of (50) to get the transfer function and calculate the corresponding bandwidth. Then, we let $\mathcal{M} = \frac{2_{max}}{\omega_0}$. This choice of $\mathcal{M}$ allows for including all the required frequency components. In order to take the appropriate spectral components of any given data, we propose an adaptive procedure for choosing the weighting matrix $\mathbf{W}$ automatically.

Choosing Weighting Matrix W Many authors have suggested taking all spectral components into account to include the maximum possible frequency component of the system [100, 103]. However, according to our investigation, that does not work well for our deconvolution scheme. Sometimes, it captures noise from the high-frequency region. For successful continuous-time system identification, selecting appropriate weights on the different spectral components is essential [100, 103]. To automate the spectral component selection, we introduce a weighting matrix in which only diagonal elements are non-zero. This weighting matrix $\mathbf{W}$ is chosen such that there is an emphasis on the significant spectral components. Hence, there is a balance between filtering out the noise and capturing the signal. We take all the off-diagonal elements of the weighting matrix as zeros and set all diagonal elements of the matrix using Kaiser windows of appropriate shapes. We specifically use this window function as the shape of the window can be changed only by changing the parameter β. This way, we can select the significant spectral components by optimizing over only one

parameter β. A P point Kaiser window function $w_\beta[j]$ can be defined as follows,

$$w_\beta[j] = \begin{cases} \frac{I_0\left(\beta\sqrt{1-\left(\frac{2j}{P-1}-1\right)^2}\right)}{I_0(\beta)}, & 0 \leq j \leq P-1, \\ 0, & \text{otherwise.} \end{cases} \tag{62}$$

where I_0 is the zeroth-order modified Bessel function of the first kind β determines the shape of the Kaiser window. In this study, we take $P = 2\mathcal{M}+1$. The optimization formulation (61) can be minimized using β values that set matrix $\mathbf{W}(\beta)$ to zero or values close to zero; however, this is not desired. To avoid such situations in estimating β, we write the time domain equivalent of the optimization formulation (61). Let $\hat{\boldsymbol{\Theta}} = \underset{\Theta}{\text{argmin}}\ J(\boldsymbol{\Theta}, \mathbf{u}, \beta) \triangleq f_{\mathbf{u}}(\beta)$. Using (51), $\tau = g(\hat{\boldsymbol{\Theta}}) = g(f_{\mathbf{u}}(\beta)) \triangleq h(\beta)$. Hence, $\mathbf{A}_\tau \triangleq \mathbf{A}_{h(\beta)}$ and $\mathbf{B}_\tau \triangleq \mathbf{B}_{h(\beta)}$. Using (49), the time domain equivalent of the optimization formulation (61) becomes,

$$\begin{aligned} \underset{\boldsymbol{\Theta},\mathbf{u},\beta}{\text{minimize}} \quad & \frac{1}{2}||\mathbf{y} - \mathbf{A}_{h(\beta)}y_0 - \mathbf{B}_{h(\beta)}\mathbf{u}||_2^2 \\ \text{subject to} \quad & \\ & G(\boldsymbol{\Theta}) \leq \mathbf{0}, \\ & ||\mathbf{u}||_0 \ll N, \\ & \mathbf{u} \geq \mathbf{0}. \end{aligned} \tag{63}$$

Given $\hat{\boldsymbol{\Theta}}$ and $\mathbf{u}$, we can find β by the optimization problem in (63).

4.2.5 Choice of HMF Dependent Time Domain Optimization for Estimating β

We can rewrite the cost function in Equation (61) as follows,

$$J(\boldsymbol{\Theta}, \mathbf{u}, \beta) = \frac{1}{2}\sum_{m=-\mathcal{M}}^{-\mathcal{M}} w_\beta[m+M]\varepsilon^2(m\omega_0).$$

Each of the error terms is multiplied by a window coefficient and smaller values of window function coefficients will lead to a smaller value of the cost function. Figure 21 shows how the shape of the window function changes with the value of β. In Figure 21, each curve represents different $w_\beta[j]$ window functions with different shape parameters β; for example, the narrowest window represented with red curve is $w_\beta[j]$ with $\beta = 204.8$ and the widest window represented with blue curve is $w_\beta[j]$ with $\beta = 3.2$.. A higher value of β leads to a very narrow function which minimizes the cost function. However, a higher value of β will discard most of the information in the HMF spectral components. This way of solving the optimization problem in the HMF domain for β tends to discard the signal components along with the noise components. For example, the minimum value for the HMF domain cost function can be found with all zeros in the window function. However, the zero window function clearly discards all information of the signal. To prevent discarding the key information in the HMF spectral components, we can instead solve the time domain equivalent of the optimization formulation in (61), which is presented in the optimization formulation in (63).

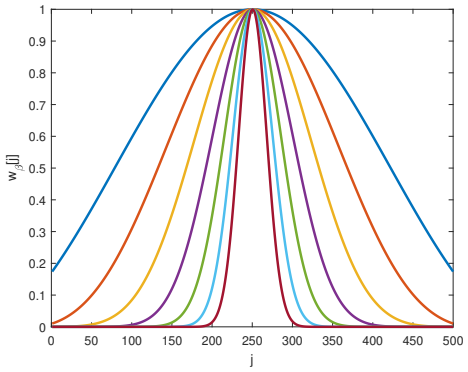

Figure 21: **Kaiser Windows With Different Shape Parameters.**

We solve this optimization problem in (63) using the interior point method. Algorithm 1 summarizes the system identification approach using Hartley modulating functions. The summary is provided as follows:

Algorithm 1. Hartley Modulating Function-Based Continuous System Identification

with Adaptive Band Selection.

Part A:

(a) Calculate the maximum bandwidth ω_{max} of the system using (50) and the τ_1^{max} and τ_2^{max}.

(b) $\mathcal{M} = \frac{2\omega_{max}}{\omega_0}$.

(c) Find all HMF spectral components for $m \in \{-\mathcal{M}, -\mathcal{M}+1, \cdots, -2, -1, 0, 1, 2, \cdots, \mathcal{M}-1, \mathcal{M}\}$.

(d) Initialize $\boldsymbol{\Theta}_{(0)}$ and $\beta_{(0)}$ using the initialization algorithm described in Section A.3.

Part B:

(e) Let $j = 0$.

(f) Set $j = j + 1$.

(g) Set $\mathbf{u}$ and $\boldsymbol{\Theta}$ equal to $\hat{\mathbf{u}}$ and $\boldsymbol{\Theta}_{(j-1)}$, respectively and solve for $\beta_{(j)}$ by initializing optimization formulation in (63) at $\beta_{(j-1)}$.

(h) Set $\mathbf{u}$ and β equal to $\hat{\mathbf{u}}$ and $\beta_{(j)}$, respectively and solve for $\boldsymbol{\Theta}_{(j)}$ by initializing optimization formulation in (61) at $\boldsymbol{\Theta}_{(j-1)}$.

(i) Iterate between (f)-(h) until convergence.

4.2.6 Sparse Inverse Problem in Hartley Modulating Function Domain

The optimization problem in (61) is generally considered as NP-hard. An l_1-norm relaxation can be used to solve this problem using different techniques including basis pursuit, greedy algorithm, iterative thresholding algorithm, or the FOCUSS algorithm and

its extensions [66]. We can cast the optimization problem in (61) as,

$$\begin{aligned} &\underset{\boldsymbol{\Theta},\mathbf{u},\beta}{\text{minimize}} && J(\boldsymbol{\Theta},\mathbf{u},\beta) = \frac{1}{2}\boldsymbol{\varepsilon}^{\top}(\mathcal{M}\omega_0)\mathbf{W}(\beta)\boldsymbol{\varepsilon}(\mathcal{M}\omega_0) + \lambda||\mathbf{u}||_p^p \\ &\text{subject to} && \\ & && G(\boldsymbol{\Theta}) \leq \mathbf{0} \\ & && \mathbf{u} \geq \mathbf{0} \end{aligned} \tag{64}$$

where the l_p-norm is an approximation to the l_0-norm and λ is the regularization parameter which determines the sparsity level of the solution for $\mathbf{u}$. FOCUSS algorithm uses a reweighted norm minimization approach to solve the optimization problem while finding stimuli $\mathbf{u}$. By minimizing the l_2-norm and refining the initial estimate to the final localized energy solution at each iteration, the solution is obtained [27]. By updating λ and $\mathbf{u}$ in every iteration until convergence, we can solve for the sparse vector $\mathbf{u}$. Here, λ balances between the sparsity of $\mathbf{u}$ and the weighted residual error $\sqrt{\boldsymbol{W}}\boldsymbol{\varepsilon}$. By increasing the value of λ, $\mathbf{u}$ becomes more sparse. The matrix $\boldsymbol{B}_{\phi}^{\top}(\mathcal{M}\omega_0)$ is the same in every step and can be calculated only once at the beginning of the algorithm. This makes the algorithm more efficient.

To ensure there is a balance between filtering out the noise and capturing the sparsity of the input, we use the Generalized Cross-Validation (GCV) technique [67] for estimating the regularization parameter. Hence, we use a modified version of the FOCUSS algorithm called GCV-FOCUSS+ [25] algorithm, which is based on the FOCUSS+ [66] and includes a GCV step. Detail descriptions of FOCUSS+ and GCV-FOCUSS+ algorithms are given below.

4.2.7 FOCUSS+ Algorithm

FOCUSS+ [66] solves for nonnegative $\mathbf{u}$ such that $\mathbf{u}$ has a certain maximum sparsity n_u while minimizing the following optimization problem,

$$\underset{\mathbf{u}\geq 0}{\text{minimize}} \quad \frac{1}{2}||\mathbf{y} - \mathbf{A}_{\boldsymbol{\tau}} y_0 - \mathbf{B}_{\boldsymbol{\tau}}\mathbf{u}||_2^2 + \lambda||\mathbf{u}||_p^p.$$

(a) $\mathbf{P}_{\mathbf{u}}^{(r)} = \text{diag}(|\mathbf{u}_i^{(r)}|^{2-p})$

(b) $\lambda^{(r)} = \left(1 - \frac{||\mathbf{y}-\mathbf{A}_{\boldsymbol{\tau}} y_0 - \mathbf{B}_{\boldsymbol{\tau}}\mathbf{u}||_2}{||\mathbf{y}-\mathbf{A}_{\boldsymbol{\tau}} y_0||_2}\right)\lambda_{\max}, \quad \lambda > 0$

(c) $\mathbf{u}^{(r+1)} = \mathbf{P}_{\mathbf{u}}\mathbf{B}_{\boldsymbol{\tau}}^{\top}(\mathbf{B}_{\boldsymbol{\tau}}\mathbf{P}_{\mathbf{u}}\mathbf{B}_{\boldsymbol{\tau}}^{\top} + \lambda\mathbf{I})^{-1}(\mathbf{y} - \mathbf{A}_{\boldsymbol{\tau}} y_0)$

(d) $\mathbf{u}_i^{(r+1)} \leq 0 \rightarrow \mathbf{u}_i^{(r+1)} = 0$

(e) After half of the selected number of iterations, search for the peaks with distances less than the minimum peak to peak distance Δ_{min}. Keep the largest peak among the adjacent peaks within Δ_{min} window.

(f) After about half of the selected number of iterations, if $||\mathbf{u}^{(r+1)}||_0 > n_{\mathbf{u}}$, select $n_{\mathbf{u}}$ the largest values of elements of $\mathbf{u}^{(r+1)}$ and set all other elements to zero.

(g) Iterate

Note that we used $\Delta_{min} = 0.5$ s in this study.

4.2.8 GCV-FOCUSS+ Algorithm

The sparse identification problem in the HMF domain is as follows,

$$\underset{\boldsymbol{\Theta},\mathbf{u},\beta}{\text{minimize}} \qquad J(\boldsymbol{\Theta},\mathbf{u},\beta) = \frac{1}{2}\boldsymbol{\varepsilon}^{\top}(\mathcal{M}\omega_0)\mathbf{W}(\beta)\boldsymbol{\varepsilon}(\mathcal{M}\omega_0) + \lambda||\mathbf{u}||_p^p$$

subject to

$$G(\boldsymbol{\Theta}) \leq \mathbf{0}$$

$$\mathbf{u} \geq \mathbf{0}$$

where $\boldsymbol{\varepsilon}(\mathcal{M}\omega_0) = \boldsymbol{Z}(\mathcal{M}\omega_0) - \boldsymbol{\Phi}(\mathcal{M}\omega_0)\boldsymbol{\Theta} - \boldsymbol{B}_{\phi}^{\top}(\mathcal{M}\omega_0)\mathbf{u}$. Let $\mathbf{Z}_{\boldsymbol{\Theta},\beta} = \sqrt{\mathbf{W}(\beta)}(\mathbf{Z}(\mathcal{M}\omega_0) - \boldsymbol{\Phi}(\mathcal{M}\omega_0)\boldsymbol{\Theta})$ and $\mathbf{B}_{\phi,\beta} = \sqrt{\mathbf{W}(\beta)}\mathbf{B}_{\phi}^{\top}(\mathcal{M}\omega_0)$. Given β and $\boldsymbol{\Theta}$, the optimization problem can be solved for $\mathbf{u}$ using the FOCUSS+ algorithm. We use a GCV based method for choosing a regularization parameter λ that balances between capturing noise and the sparsity level. Zdunek *et al.* [68] used the GCV technique for finding the value of λ for the FOCUSS+ algorithm incorporating singular value decomposition:

$$G(\lambda) = \frac{\mathcal{L}\sum_{i=1}^{\mathcal{L}}\gamma_i^2\left(\frac{\lambda}{\sigma_i^2+\lambda}\right)^2}{\sum_{i=1}^{\mathcal{L}}\left(\frac{\lambda}{\sigma_i^2+\lambda}\right)^2}$$

where $\boldsymbol{\gamma} = \mathbf{R}^{\top}\boldsymbol{Z}_{\boldsymbol{\Theta},\beta} = \begin{bmatrix} \gamma_1 & \gamma_2 & \cdots & \gamma_{\mathcal{L}} \end{bmatrix}^{\top}$ and $\boldsymbol{B}_{\phi,\beta}\mathbf{P}_{\mathbf{u}}^{\frac{1}{2}} = \mathbf{R}\boldsymbol{\Sigma}\mathbf{Q}^{\top}$ with $\boldsymbol{\Sigma} = \text{diag}\{\sigma_i\}$; $\mathbf{R}$ and $\mathbf{Q}$ are unitary matrices and σ_i's are the singular values of $\boldsymbol{B}_{\phi,\beta}\mathbf{P}_{\mathbf{u}}^{\frac{1}{2}}$ [68]. Moreover, $\mathcal{L}$ is the number of data points. In this study, we use a range of zero to 0.1 for λ. For $r = 0, 1, 2, \cdots$, GCV-FOCUSS+ works as follows [19]:

(a) $\mathbf{P}_u^{(r)} = \text{diag}(|\mathbf{u}_i^{(r)}|^{2-p})$

(b) $\mathbf{u}^{(r+1)} = \mathbf{P}_u\boldsymbol{B}_{\phi,\beta}^{\top}(\boldsymbol{B}_{\phi,\beta}\mathbf{P}_u\boldsymbol{B}_{\phi,\beta}^{\top} + \lambda\mathbf{I})^{-1}\boldsymbol{Z}_{\boldsymbol{\Theta},\beta}$

(c) $\mathbf{u}_i^{(r+1)} \leq 0 \rightarrow \mathbf{u}_i^{(r+1)} = 0$

(d) $\lambda^{(r+1)} = \underset{0 \leq \lambda \leq 0.1}{\operatorname{argmin}} G(\lambda)$

(e) Iterate until convergence

4.2.9 Initialization Algorithm

The initialization is performed in the time domain (similar to [19, 18, 20]). A summary of the algorithm to obtain good initial conditions for $\boldsymbol{\tau}$, $\mathbf{u}$ and β is as follows:

(a) Initialize $\tilde{\boldsymbol{\tau}}^0$ by sampling a uniform random variable on $\begin{bmatrix} 0.10 & 1.4 \end{bmatrix}$ for $\tilde{\tau}_1^{(0)}$ and $\begin{bmatrix} 1.5 & 6 \end{bmatrix}$ for $\tilde{\tau}_2^{(0)}$ and let $j = 1$.

(b) Set $\boldsymbol{\tau}$ equal to $\tilde{\boldsymbol{\tau}}^{(j-1)}$ and use FOCUSS+ to solve the inverse problem to find the stimuli $\tilde{\mathbf{u}}^{(j)}$ by initializing $\tilde{\mathbf{u}}^{(0)}$ at a vector with all ones.

(c) Set $\mathbf{u}$ equal to $\tilde{\mathbf{u}}^{(j)}$; use the interior point method and minimize error $||\mathbf{y} - \mathbf{A}_{\boldsymbol{\tau}} y_0 - \mathbf{B}_{\boldsymbol{\tau}} \mathbf{u}||_2$ to solve the time domain system parameter identification problem for obtaining $\tilde{\boldsymbol{\tau}}^{(j)}$.

(d) Repeat between steps (b)-(c) for $j = 1, 2, 3, \cdots, 30$.

(e) We set $\boldsymbol{\tau}^0 = \tilde{\boldsymbol{\tau}}^{(j)}$ and $\mathbf{u}^0 = \tilde{\mathbf{u}}^{(j)}$

(f) We calculate $\boldsymbol{\Theta}^0$ by plugging in $\boldsymbol{\tau}^0$ in $\boldsymbol{\Theta} = \begin{bmatrix} \tau_1 + \tau_2 \\ \\ \tau_1 \tau_2 \end{bmatrix}$.

(g) Using $\mathbf{u}^0$ and $\boldsymbol{\tau}^0$, we first take $\beta_i = 0.1 \times 2^i$ for $i = 0, 1, 2, 3, \cdots, 10$ and set $\beta^0 = \beta_{\min}$ such that $\beta_{\min}$ minimizes $||\mathbf{y} - \mathbf{A}_{h(\beta)} y_0 - \mathbf{B}_{h(\beta)} \mathbf{u}||_2^2$.

4.2.10 Coordinate Descent Deconvolution

In the coordinate descent approach, first, we filter the signal using a 0.5 Hz 64 order FIR lowpass filter [65]. Then, we use the cvxEDA method [23] to separate the phasic component from the filtered SC data. By combining the methods described in Sections

4.2.6 and 4.2.4, a coordinate descent approach can be implemented. Before performing deconvolution, we initialize the algorithm by sampling the system parameters from uniform distributions within the boundary conditions. The detailed description of the initialization algorithm is provided in Section A.3. We propose the following algorithm to recover $\mathbf{u}$ and $\boldsymbol{\Theta}$ from the phasic component.

Algorithm 2: Coordinate Descent in Hartley Modulating Function Domain

(a) Let i = 0

(b) Run Algorithm 1-A.

(c) Set i = i + 1.

(d) Initialize $\hat{\mathbf{u}}^0$ using the initialization algorithm described in Section A.3.

(e) Set $\boldsymbol{\Theta}$ and β equal to $\hat{\boldsymbol{\Theta}}^{(i-1)}$ and $\hat{\beta}^{(i-1)}$; solve for $\hat{\mathbf{u}}^i$ using GCV-FOCUSS+ by initializing the inverse problem in (64) at $\hat{\mathbf{u}}^{(i-1)}$.

(f) Set $\mathbf{u}$ equal to $\hat{\mathbf{u}}^{(i)}$; to solve for $\hat{\boldsymbol{\Theta}}^{(i)}$ and $\hat{\beta}^{(i)}$ using Algorithm 1-B by initializing $\boldsymbol{\Theta}_{(0)}$ and $\beta_{(0)}$ at $\hat{\boldsymbol{\Theta}}^{(i-1)}$ and $\hat{\beta}^{(i-1)}$, respectively.

(g) Iterate between (c)-(f) until convergence.

We run Algorithm 2 for several uniform random initializations of $\boldsymbol{\Theta}$ and take the solution of $\hat{\mathbf{u}}$ and $\hat{\boldsymbol{\Theta}}$ (Setting $\tau = \mathbf{g}(\boldsymbol{\Theta})$) that provides the smallest value of $||\mathbf{y} - \mathbf{A}_\tau y_0 - B_\tau \mathbf{u}||_2^2$. The recovered neural stimuli in the HMF domain can sometimes lead to lower amplitudes for impulses that occur in the beginning or at the end of the neural stimuli vector $\mathbf{u}$. Hence, to ensure this type of behavior does not occur, using the estimated $\hat{\tau}$, in the time domain (similar to [19, 18]), we run the FOCUSS+ algorithm one last time by initializing $\mathbf{u}$ at a vector of all ones and considering a maximum sparsity equal to $||\hat{\mathbf{u}}||_0$.

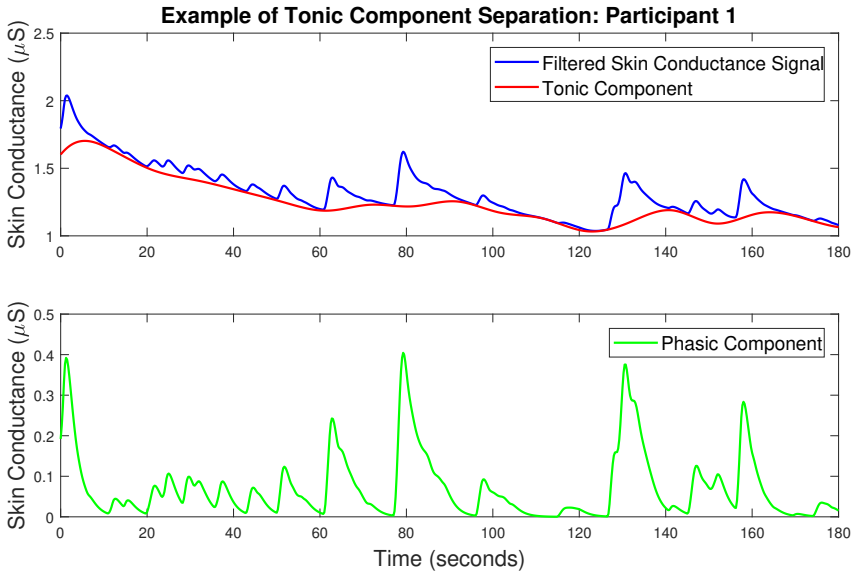

Figure 22: **Tonic Component Separation Example.**

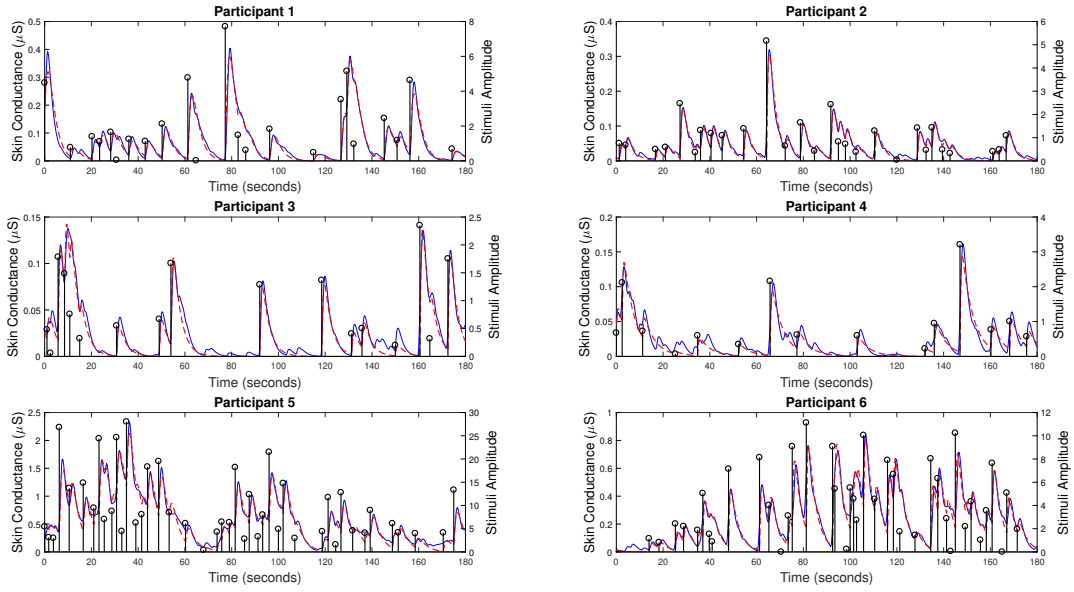

Figure 23: **Estimated Deconvolution of the Experimental Phasic SC Data in 6 Participants from Dataset 1.**

4.2.11 Proof of Convexity of The HMF-based Cost Function in terms of u and $\boldsymbol{\Theta}$

Given β, $\mathbf{W}$ is known and the cost function in HMF domain is as follows,

$$
\begin{aligned}
J(\boldsymbol{\Theta}, \mathbf{u}) &= \frac{1}{2}\boldsymbol{\varepsilon}^{\top}(\mathcal{M}\omega_0)\mathbf{W}\boldsymbol{\varepsilon}(\mathcal{M}\omega_0) \\
&= \frac{1}{2}\left[\boldsymbol{Z}(\mathcal{M}\omega_0) - \boldsymbol{\Phi}(\mathcal{M}\omega_0)\boldsymbol{\Theta} - \boldsymbol{B}_{\phi}(\mathcal{M}\omega_0)\mathbf{u}\right]^{\top} \\
&\cdot \mathbf{W} \cdot \left[\boldsymbol{Z}(\mathcal{M}\omega_0) - \boldsymbol{\Phi}(\mathcal{M}\omega_0)\boldsymbol{\Theta} - \boldsymbol{B}_{\phi}(\mathcal{M}\omega_0)\mathbf{u}\right]. \qquad (65)
\end{aligned}
$$

Then, $J(\boldsymbol{\Theta}, \mathbf{u})$ is convex in $\mathbf{u}$ and Θ. It can be shown that it satisfies the first-order and second-order convexity conditions.

First-order convexity condition.

One should note that $\mathcal{M}$ and ω_0 are known. Let

$$
\chi_i = \begin{bmatrix} \Theta_i^{\top} & \mathbf{u}_i^{\top} \end{bmatrix}^{\top},
$$

$$
A_{\phi} = \begin{bmatrix} \boldsymbol{\Phi}(\mathcal{M}\omega_0) & \boldsymbol{B}_{\phi}(\mathcal{M}\omega_0) \end{bmatrix},
$$

and $\mathfrak{Z} = \mathbf{Z}(\mathcal{M}\omega_0)$. The cost function in (61) can be re-written as,

$$
J(\chi_i) = \frac{1}{2}\left[\mathfrak{Z} - A_{\phi}\chi_i\right]^{\top}\mathbf{W}\left[\mathfrak{Z} - A_{\phi}\chi_i\right].
$$

Here, $J : \mathbb{R}^{N+2} \rightarrow \mathbb{R}$ is convex if and only if $J(\chi_2) - J(\chi_1) - \bigtriangledown J(\chi_1)^{\top}(\chi_2 - \chi_1) \geq 0$ for any χ_1 and χ_2 in **dom** J.

$$
\bigtriangledown J(\chi_1) = -2A_{\phi}^{\top}\mathbf{W}(\zeta - A_{\phi}\chi_1)
$$

Plugging in the values, it can be shown that,

$$J(\chi_2) - J(\chi_1) - \bigtriangledown J(\chi_1)^\top (\chi_2 - \chi_1)$$
$$= (\chi_2 - \chi_1)^\top A_\phi^T \mathbf{W} A_\phi (\chi_2 - \chi_1)$$

The right hand side of the equation is always positive as $\mathbf{W}$ is positive semidefinite. Therefore, J satisfies the first-order condition.

Second-order convexity condition.

Taking the second derivative of J,

$$\bigtriangledown^2 J(\chi) = A_\phi^\top \mathbf{W} A_\phi$$

As $\mathbf{W}$ is a positive semidefinite matrix, $\bigtriangledown^2 J(\chi) \geq 0$. The cost function in HMF domain satisfies the first and second-order conditions of convexity. Therefore, the cost function is convex in Θ and $\mathbf{u}$.

Table 6: Results from Experimental Data.

Participant	τ_1 (seconds)	τ_2 (seconds)	R^2	N_u	λ
1	1.231	2.665	0.973	23	1.10×10^{-3}
2	0.512	2.958	0.966	28	1.80×10^{-3}
3	0.414	3.163	0.963	17	2.90×10^{-3}
4	0.237	4.849	0.916	15	2.60×10^{-3}
5	0.783	3.367	0.971	44	3.62×10^{-2}
6	0.362	3.362	0.927	40	1.00×10^{-3}

Table 7: Results from Simulated Data.

Participant	τ_1 (seconds)	τ_2 (seconds)	$\hat{\tau}_1$	$\hat{\tau}_2$	R^2	$\hat{N}_u$	$\lvert N - \hat{N}_u \rvert$	$\frac{\lvert \tau_1 - \hat{\tau}_1 \rvert}{\tau_1} \times 100$ %	$\frac{\lvert \tau_2 - \hat{\tau}_2 \rvert}{\tau_2} \times 100$ %
1	1.231	2.665	1.167	2.726	0.989	21	2	5.20	2.29
2	0.512	2.958	0.389	3.349	0.977	24	4	24.02	13.22
3	0.414	3.163	0.456	3.074	0.974	14	3	10.14	2.81
4	0.237	4.849	0.182	4.906	0.985	14	1	23.21	1.18
5	0.783	3.367	0.727	3.352	0.987	44	0	7.15	4.09
6	0.362	3.369	0.311	3.345	0.984	36	4	14.09	0.71

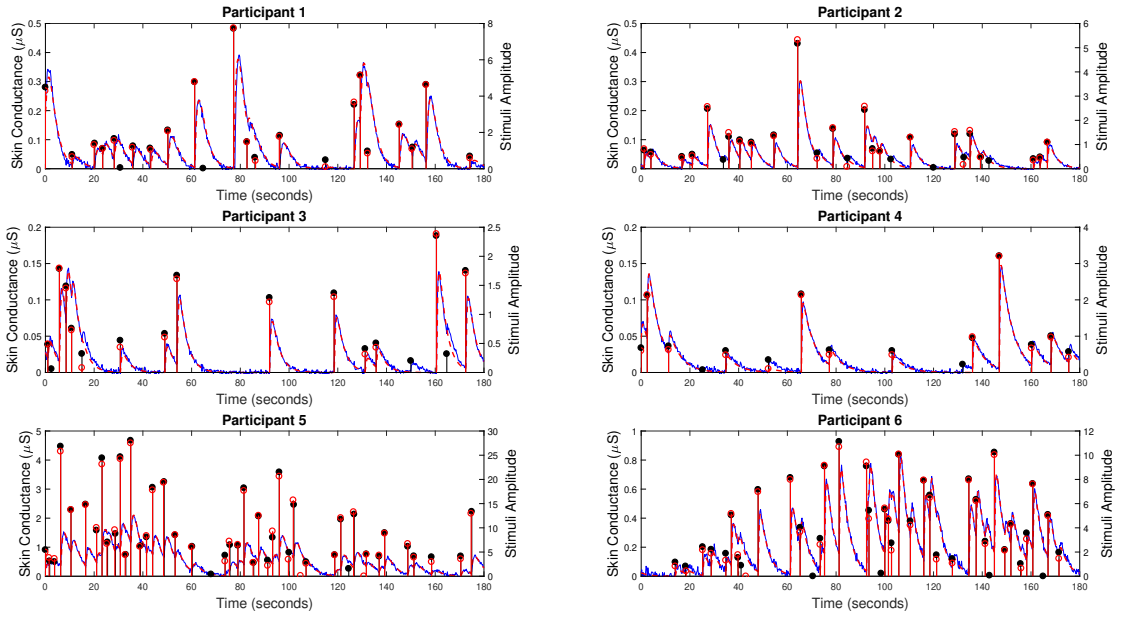

Figure 24: **Estimated Neural Stimuli and Reconstructed Signals of the Simulated Phasic SC Data with 25 dB SNR in 6 Participants from Dataset 1.**

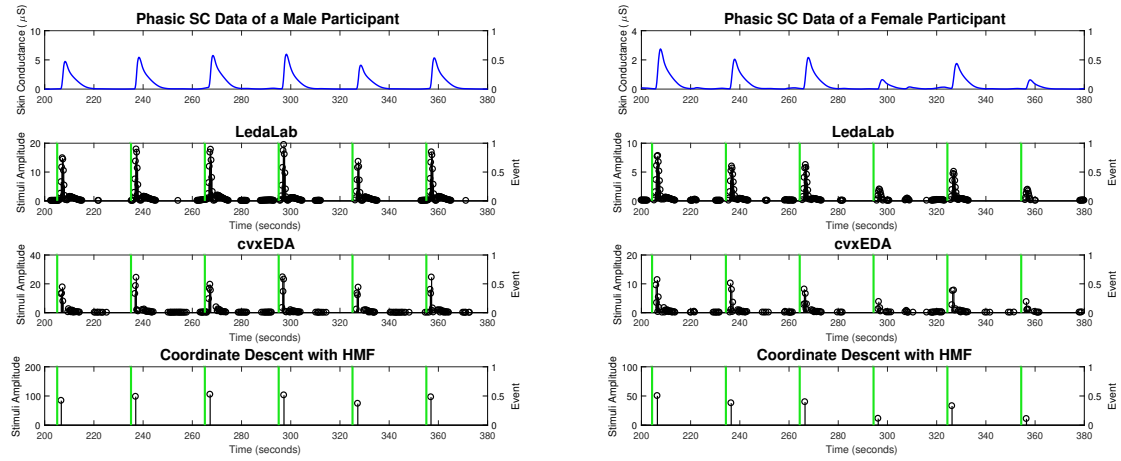

Figure 25: **Estimated Neural Stimuli from the Experimental Phasic SC Data in two Participants from Dataset 2.**

4.3 Results

4.3.1 Experimental Study

Figure 22 shows an example of the tonic component separation with cvxEDA algorithm [23]. In Figure 22, i) the top panel shows the low-pass filtered SC signal (blue curve)

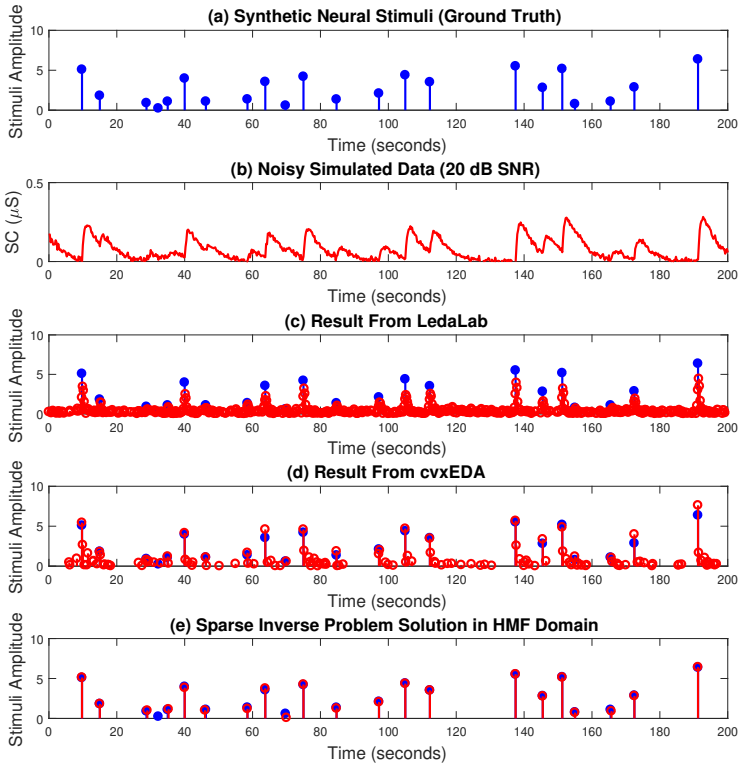

Figure 26: **Comparison of Different Sparse Recovery Algorithms with Simulated Data.**

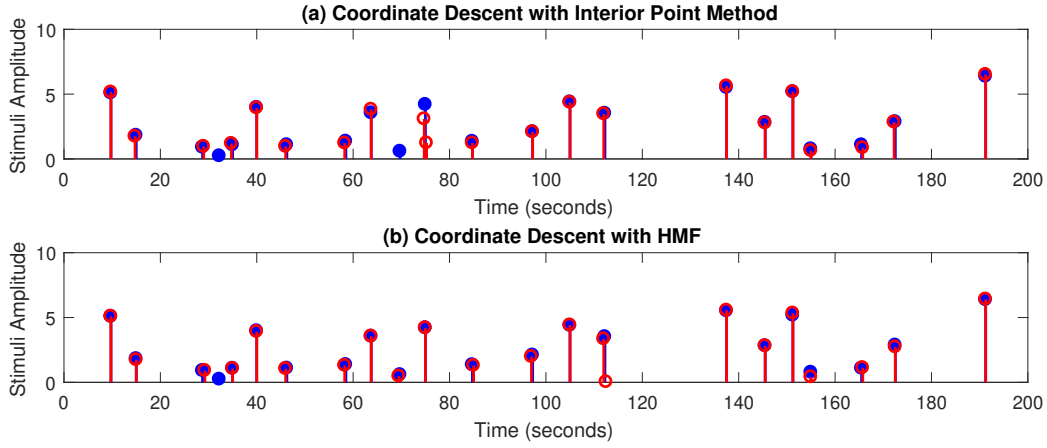

Figure 27: **Comparison of Two Deconvolution Algorithms using Simulated Data.**

and the corresponding estimated tonic part (red curve) with cvxEDA algorithm [23]; ii) the bottom panel shows the extracted phasic component from the corresponding SC signal after subtracting the tonic part. Figure 23 shows the phasic component, recovered neural stimuli, and the reconstructed phasic component of the SC data collected for the participants from Dataset 1. In Figure 23, each panel shows the separated phasic component of the SC data using cvxEDA (blue curve), the estimated reconstructed signal (red dashed), the estimated neural stimuli timings and amplitudes (black vertical lines with the circle on top) for each of the participants. There are several SC peaks present in the data which correspond to the cognitive stress originating from the 'counting task'. Figure 23 also shows the recovered neural stimuli timings and amplitudes that correspond to cognitive stress. Reconstructed signals in Figure 23 were generated using the model defined in (45)-(46). Table 6 shows the corresponding estimated rise time τ_1 and decay time τ_2. In Table 6, the parameters τ_1 and τ_2 are the estimated rise time and fall time of the phasic SC, respectively; N_u is the estimated number of neural stimuli impulses from ANS and R^2 is the square of the multiple correlation coefficient. In Table 7, all the multiple correlation coefficients (R^2) are over 0.915. In Table 7, the parameters $\hat{\tau}_1$ and $\hat{\tau}_2$ are the estimated rise time and decay time of phasic SC, respectively; $\hat{N}_u$ is the estimated number of neural stimuli impulses from ANS and R^2 is the square of the multiple correlation coefficient. Zero mean Gaussian noise has been added to each simulated data point compared to each of the simulated signal. The noise SNR is 25 dB for all of the simulated data. For each participant, the variance of noise is calculated by taking the variance of the residuals after deconvolution on real data. The parameters τ_1 and τ_2 are, respectively, the rise time and decay time of phasic SC used for simulating each dataset. The values of τ_1 and τ_2 are given in Table 6. Table 6 also shows the regularization parameter λ obtained using GCV. All the regularization parameters are less than 3.7×10^{-2} with minimum value of 1×10^{-3}. Quantile-quantile plots of the residuals after reconstruction follows a straight line, which implies the residuals

are zero-mean Gaussian distributed (as assumed in the problem formulation). The quantile-quantile plots are provided in Section A.3. Figures of the SC reconstructed signals with both tonic and phasic components are also provided in Section A.3. The R^2 values for this case are higher than 0.95 for all participants if calculated considering both tonic and phasic components.

We also analyzed SC data from one male participant (subject ID 11) and one female participant (subject ID 15) from Dataset 2. Dataset 2 has auditory stimulation timing information to perform the comparison with the recovered neural stimuli. We expect to see a time delay from the auditory stimulation to the neural stimuli as the neural system should take some time to generate neural stimuli after an auditory stimulation has occurred. Figure 25 shows our approach detects an impulse after every auditory stimulation. In Figure 25 , i) the top subpanels show the separated phasic component of the SC data (blue curve), ii) the second subpanels depict the estimated neural stimuli with ledaLab [21] (black vertical lines), iii) the third subpanels show the estimated neural stimuli with cvxEDA [23] algorithm (black vertical lines), vi) last sub-panels show the estimated neural stimuli with the proposed approach (black vertical lines); green vertical lines represent the timings of the auditory stimulation. The average delays are 2.02 seconds for the male participant and 2.08 seconds for the female participant. The rise time and the decay time for the male participant are 0.34 seconds and 3.41 seconds, respectively. For the female participant, the time constants are 0.59 seconds and 3.32 seconds, respectively. We also compare this performance with other approaches. The LedaLab [21] and the cvxEDA [23] algorithms detect too many pulses compared to our approach.

4.3.2 Simulated Study

We have simulated the noisy phasic SC data using results in Table 6 and Figure 23, and then performed deconvolution on the simulated data to further validate our algorithm. For the simulated data, both the sparse input and the model parameters are known, and we

can compare the deconvolution results with the ground truth. To simulate the noise, we take zero-mean Gaussian random variables with 25 dB signal to noise ratio (SNR) for each participant. Figure 24 shows the recovered amplitudes and timings of the impulses for the simulated phasic SC data. In Figure 24, each panel shows the simulated phasic component of the SC data (blue curve), the estimated reconstructed signal (red dashed), the estimated neural stimuli, timings and amplitudes (red vertical lines with the circle on top) and the ground truth of the neural stimuli timings and amplitudes for each of the simulated data (black lines with the dots on top). Table 7 shows results obtained from the simulated data. The multiple correlation coefficients (R^2) are above 0.97 for noisy simulated data. Blue impulses in Figure 24 are the ground truth impulses used for simulating the data. Figure 24 illustrates that all significant impulses have been detected. However, some of the very small impulses were missed in the presence of noise. The amplitudes and timings of the detected neural stimuli are very close to the ground truth.

Table 7 shows the detected rise and fall times along with the percentage errors. All percentage errors are below 25%. The maximum error in detecting the number of impulses in the neural stimuli is 4. For the simulated data based on participants 2 and 6, the algorithm has missed 4 of the impulses that are insignificant and comparable to the level of added noise. However, the algorithm has detected all significant impulses.

To further compare the performance of our algorithm with the existing algorithms, we used a synthetic $u(t)$ to simulate data using the model in (45)-(46) with model parameters $\boldsymbol{\tau} = \begin{bmatrix} 0.7 & 4.0 \end{bmatrix}$ and noise level of 20 dB signal SNR. In Figure 26, each sub-panel shows (a) the synthetic neural stimuli (ground truth), (b) simulated data with $\tau_1 = 0.7$ seconds, $\tau_2 = 4$ seconds and synthetic neural stimuli $u(t)$ with added noise of 20 dB SNR, (c) the solutions from LedaLab [21], (d) the solution from cvxEDA [23] and (e) the sparse inverse problem solution in HMF domain [19]; blue line, red line, and red curve correspond to the ground truth, estimated stimuli and simulated data, respectively. We then apply different algorithms to compare the performance. Figure 26 shows the performances of different

algorithms. In this case, we assume τ_1 and τ_2 are known because the existing algorithms only solve the inverse problem and do not perform deonvolution. Figure 26 (c) shows that LedaLab [21] detects too many impulses compared to the ground truth. Figure 26 (d) shows that cvxEDA [23] detects a more sparse solution compared to Ledalab; however, it still detects too many impulses compared to the ground truth. As observed, our result in Figure 26 (e) outperforms the existing algorithms.

We also compare the performance of our algorithm with the deconvolution algorithm proposed in [19, 18]. Figure 27 shows the results obtained from the simulated data using the coordinate descent approach for estimating unknowns τ_1, τ_2 and $\mathbf{u}$. Figure 27 (a) shows the result with interior point method as in [19, 18] and Figure 27 (b) shows the result with the proposed HMF domain method. The result is obtained from the simulated data in Figure 26 (a). The estimated rise time and fall time using the proposed method are 0.7054 seconds and 3.9726 seconds, respectively. For both of them, the estimation error is less than 1%. Whereas, the estimated rise time and fall time using the time domain interior point-based coordinate algorithm are 0.5562 seconds and 4.2501 seconds, respectively. In this case, errors are 20.5408% and 6.2514%, receptively. The proposed algorithm has outperformed the time domain approach. In this study, we used 16 random initializations for both algorithms.

4.4 Discussions

Finding the neural stimuli and physiological system parameters related to SC is a challenging problem. Firstly, there can exist multiple sets of physiological parameters and stimuli that closely approximate the observed signal. Secondly, the smallest level of noise can perturb the solution to a physiologically infeasible point due to the sensitive nature of the biexponential function. To overcome these challenges, proper boundary conditions and constraints have to be applied in the optimization problem. Alexander *et al.* [42], use the values of $\tau_1 = 0.75$ seconds and $\tau_2 = 2$ seconds for all datasets they have analyzed. Greco *et al.* [23] set $\tau_1 = 0.75$ and use fixed τ_2 values that vary between 2 and 4. We

assume that the rise times lie between 0.10 to 1.40 seconds to have more flexibility to the subject-specific variations. We also assume decay times are between 1.5 and 6 seconds, respectively. To impose the constraints on $\boldsymbol{\tau}$ during continuous system identification using Hartley modulating function, we used 5 nonlinear physiological constraints on α_1 and α_2 to ensure identifiability. Table 6 shows the corresponding estimated rise time τ_1 and decay times τ_2 which lie within the boundary. The boundary constraints have been chosen such that the system is identifiable and the model parameters do not stagnate at the boundaries.

A good separation of the tonic component depends on an appropriate choice of smoothness of the tonic component which is enforced by the selection of the basis for the tonic component and the l_2 -norm penalization parameter of the spline coefficients in cvxEDA [23]. In this study, we follow cvxEDA [23] for obtaining the tonic component. While cvxEDA [23] has good performance in separating the tonic component from the signal, it can overfit the noise in the phasic component. Moreover, instead of including the subject-specific rise and decay times, it assumes these values are fixed. Taking the phasic component, we use our deconvolution approach to estimate the rise and decay times as well as the stimuli while filtering out the noise. To obtain the phasic component in this study, we used the default parameters in cvxEDA [23]. The value of these parameters is crucial for good separation of the tonic and phasic components.

An inappropriate choice of the input sparsity level ($\mathbf{u}$) and minimum separation constraint between the input impulses (arrival time in $\mathbf{u}$) can lead to an incorrect solution. While the higher number of impulses can lead to overfitting (i.e., capturing the noise as impulse), a higher sparsity level may fail to recover the underlying process. In the initialization step, we choose a minimum separation of 0.5 seconds for the arrival time of the impulses in the FOCUSS+ algorithm. In the coordinate descent step, GCV-FOCUSS+ provides a balance in the sparsity of the stimuli such that it captures the process yet filters out most of the noise.

Table 6 shows the regularization parameters of the GCV-FOCUSS+ part of the algorithm. We constrained λ between 0 and 0.1. The choice of the regularization parameter λ depends on the subject-specific magnitude of the SC signal. The results from the simulated data based on participants 3, 4, and 6 show that in some cases, if there are many small adjacent impulses present in the stimuli in the presence of high levels of noise, some of these small impulses in the stimuli might be missed by the proposed deconvolution algorithm. In this case, the GCV-FOCUSS+ part of the algorithm considers these small spikes as noise. As a consequence, the estimation of rise time could become inaccurate. The decay times are larger in magnitude and are less affected. The deconvolution algorithm always recovers the significant impulses in the stimuli successfully.

The optimization step for finding the stimuli in 4.2.6 is a convex problem [66]. In this study, we formulate an optimization problem that is convex in terms of system parameters and neural stimuli. However, one should note that in implementing the GCV-FOCUSS+ algorithm, if an impulse goes to zero, it never becomes nonzero in the subsequent iterations of the coordinate descent approach. Hence, sometimes the algorithm might not reach the global minimum depending on the initial condition. Moreover, the optimization problem formulation is not convex in terms of β. As a result, it is still possible to stagnate at a local minimum using this approach. We used several random initializations within the boundary conditions to account for this.

Wickramasuriya et al. [82] used the dataset in [95] (discussed in 4.2.1) and recovered the stimuli using cvxEDA [23]. Then, they used a heuristic approach to obtain more sparse neural stimuli. Then, they used these sparse neural stimuli for tracking stress [82]. Our proposed algorithm provides an appropriate sparsity level and can be used directly to track stress using the approach in [82].

5 Physiological Characterization of Electrodermal Activity Enables Scalable Near Real-Time Autonomic Nervous System Activation Inference

5.1 An Overview of Physiological Characterization of Electrodermal Activity for Scalable Autonomic Nervous System Activation Inference.

The term "electrodermal activity" (EDA) refers to any electrical phenomenon in human skin [9]. EDA was discovered in the late 19th century, and since then, it has been widely used in psychophysiology as the EDA fluctuations have high correlations with the autonomic nervous system (ANS) activation. One of the most popular measures of EDA is continuous exosomatic recording of skin conductance (SC). ANS excites sweat glands based on the psychophysiological requirements, and the corresponding salty discharges increase the SC. Examination of SC measurements enables us to investigate the ANS activation related to emotional arousal. [10].

There are a few vital signals in the human body similar to EDA that have the potential to be measured continuously and unobtrusively using very simple instrumentation. The unobtrusive nature of the measuring techniques has led to a new era of wearable technology for continuous health monitoring. Such signals include cardiac signals (e.g. electrocardiogram (ECG) and photoplethysmogram (PPG)), skin temperature (SKT), EDA, muscle activity (e.g. electromyogram (EMG)) etc. [11, 12]. Among them, PPG and SKT have been widely integrated in consumer wearable technologies along with reliable techniques for decoding useful information. In the past few decades, extensive research has been performed, mainly on PPG signal analysis for wearable implementation, with the goal of continuous health monitoring. The next candidate with the most potential for revolutionizing wearable health monitoring is the EDA [13]. However, the amount of research performed on EDA signals is relatively limited compared to cardiac signals. Although researchers have

published many studies to systematically model EDA in the last two decades, there are still many fundamental characteristics of EDA being discovered today. For example, in 2020, Subramaniam *et al.* [14] have shown that the point process characterizes EDA in normal healthy participants. Therefore, further study is required to identify the more accurate system dynamics of EDA so that critical information related to health monitoring can be obtained.

Appropriate EDA analysis has applications in a wide range of fields such as mental disorders, pain, cognitive stress tracking, wakefulness, etc. As different physiological signals, including EDA, contain information about human emotional arousal, they have potential applications in the field of mental health. For example, preventing death from mental disorders with regular tracking could be one potential application as Walker *et al.* [31] reported that a large portion of deaths worldwide are attributable to mental health-related disorders. A meta-analysis shows that mental disorders are a major risk factor for suicide [32]. Suicide is one of the leading causes of death in the United States in the year 2017 [33] and the cost related to suicide alone in the United States were more than $90 billion in 2013 [34]. Studies have recommended [34] community-based immediate psychiatric services, including telepsychiatric support for reducing suicide-related costs which require continuous monitoring. Augmenting EDA with other physiological signals for time-to-time monitoring of critical patterns of emotional regulation could potentially help preventing psychiatric disorders [35].

Another possible potential application is in treating diabetic neuropathy. Diabetic neuropathy refers to small nerve damage caused by prolonged exposure to high levels of blood glucose concentration [36]. As a result, small nerves along with the sudomotor nerves in the legs, feet, and hands that are responsible for transmitting ANS activation are prone to neuropathy [36]. As confirmed by numerous studies in [37, 38, 39], damages in small nerves including the sudomotor nerves may lead to abnormal EDA variations. Furthermore, it is well known in clinical diagnostics that the development of anomalies in sweat secretions

may be attributed to forms of disorders, such as hypohidrosis and anhidrosis [40]. Moreover, such disorders may indicate diseases like diabetes mellitus [40]. Clinical investigations of abnormalities in the SC recordings can be pivotal for the early detection of such diseases.

Because of its wide range of applicability, accurate modeling of system theoretic understanding is a prerequisite. In 1997, Lim et al. [104] proposed a heuristic sigmoid-exponential model to represent the rise and decay characteristics of the SCR shape. Instead of a general approach, they had to consider four different configurations of the proposed model for four different cases. Later in 2005, Alexander et al. [42] proposed a second-order differential equation for defining the SC fluctuations, the solution of which is a bi-exponential function representing the rise and decay of the SCR shape. They assumed that SC is single-phasic, and more specifically, that all fluctuations can be defined with the second-order differential equation. However, eventually, researchers have realized the bi-phasic nature of EDA fluctuations, meaning there are two different components in EDA that vary in two different rates [29, 22, 23, 18, 52, 41]. Benedek *et al.* [29, 29] have suggested bi-exponential functions, namely Bateman functions, to describe the slow varying components with large decay time and the fast varying component with smaller decay times. However, this model cannot not explain both components together. On the other hand, Bach *et al.* [22] have used a low-pass filter to separate the slow varying components and then utilized a third-order differential equation to model the fast varying component. Nevertheless, the FIR filter-based separation of the slow and fast varying components has limitations as pointed out in our previous work [41].

In our previous studies [52, 53, 54, 8, 41], we have developed deconvolution approaches where we investigated the previously known mathematical models for EDA dynamics. In these studies, we have utilized the SC modeling approach in [23], where the authors have modeled the slow varying component of EDA with a linear combination of a few arbitrary cubic spline basis functions. Although such a model can provide a good fit to the data,

it lacks reasonable physiological justification and the corresponding coefficients of the obtained cubic spline functions have no interpretation. Furthermore, the cubic spline basis function based model may overfit to the data and provide a solution that is not physiologically plausible. In addition, the lack of a complete state-space model makes it difficult to design scalable fixed interval smoother (FIS) based inference approaches for recovery of ANS activation. Although similar approaches have been developed for calcium oscillation deconvolution and EEG sleep spindle detection [105], it is difficult to develop such an approach for EDA with the models currently available. During our development of deconvolution approaches, we realized that there is a need for a potential improvement in the current mathematical models for describing EDA dynamics as well as the current deconvolution practices to obtain a systematic and reliable approach with the feasibility of real-time application.

Therefore, in this study, we propose a unified and comprehensive state-space model to describe both the slow and fast varying components of EDA. We first start with a more general and physiologically interpretable nonlinear model and then derive a simpler linear state-space one. Additionally, our proposed model enables us to derive an FIS based novel scalable sparse deconvolution approach which was not previously possible because of the absence of a comprehensive state-space model for the potential of real-time inference. For obtaining our novel approach, we extended the scalable sparse deconvolution approach for calcium and EEG sleep spindle deconvolution proposed by Kazemipour et al. [105], which was developed for a subset of state-space equations considering the input matrix as an identity matrix. We generalized this for the state-space models with any input matrix and apply it for our proposed SC model. Moreover, for estimating the state-space model parameters, we utilize the previously known physiological priors similar to [41]. Furthermore, we employ generalized-cross-validation for balancing between the sparsity level of the ANS activation and the model fit for systematic reduction of the measurement noise. We compare the performance of our approach with previous deconvolution approaches. Furthermore, we

show the scalability of our approach, illustrating the feasibility of devising real-time edge computation with our approach.

5.2 Materials and Methods

5.2.1 Dataset Description

In this study, we analyze the SC recordings where participants experience multiple auditory stimuli (loud sounds) during the experiment [57]. The experiment was designed to investigate event-related SC responses (SCRs) [30]. Each participants received multiple auditory stimuli. Each auditory stimulus is a single white noise burst of 1s length with a 10 ms ramp and 85 dB power. The participants were instructed to press a foot pedal upon hearing a stimulus. The dataset contains recordings from thirteen female and thirteen male participants. For each of the 26 participants, the datasets include three channels of SC recordings from three different locations. We use the SC recordings from the thenar/hypothenar of the nondominant hand for all datasets in this study. The details regarding the experiment are provided in [30]. We pre-process all recordings with an approach similar to [54] and resample the SC recordings to 4 Hz for our analysis.

5.2.2 Proposed Physiological Model

We propose our model based on the *poral valve model* by Edelberg [28]. Initially, we assume the sweat ducts are empty and in response to the received impulsive ANS activation, secretions from the sweat glands start to fill the sweat ducts. As the amount of sweat in the ducts increases, there is an increase in the hydraulic pressure inside. The pressure build-up gives rise to the increasing diffusion into the corneum and the deeper corneum area. This results in a slight rise in the SC level. If the pressure exceeds a certain threshold, the pores of the sweat ducts open for sweat secretion. This way, a fraction of the sweat secreted directly by the pore opening. The secreted sweat and the connected sweat content in the ducts both contributes to the conductance. Therefore, there is a sharp rise in the SC level.

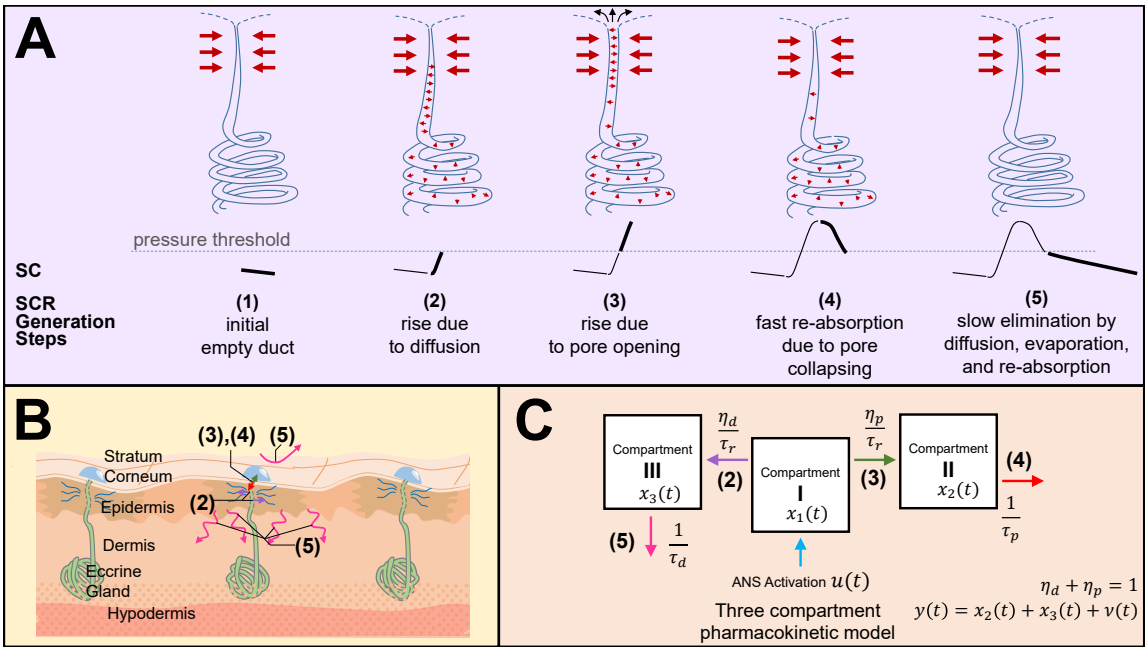

Figure 28: **An overview of the physiology and corresponding proposed model.**

As the direct secretion and the diffusion reduces the hydraulic pressure and the pressure goes below a certain threshold, the pore collapse separates the sweat contents in the ducts and prevents them to contribute to the conductance. Consequently, a faster decay in SC level is observed. We define it as the faster re-absorption resulting in the faster decay time in SC. The remaining secreted fraction of the sweat in the corneum is diffused into the deeper dermis and cleared away from the periductal area by a slow re-absorption process. Along with re-absorption, a fraction in the reduction of SC is because of the evaporation from the surface. These steps will lead to SC level to decay slowly decay. Figure 28 shows: (A) a step by step illustration of the *poral valve model* proposed by Edelberg [28]; (B) an illustration of the cross section of the skin segment and corresponding different regions contributing to the SCR generation process based on *poral valve model*; (C) a three compartment pharmacokinetic realization of the *poral valve model*. With these speculations, we propose the following nonlinear state-space model:

$$\dot{x}_1(t) = -\frac{1}{\tau_r}x_1(t) + u(t), \qquad \text{(sweat production)} \tag{66}$$

$$\dot{x}_2(t) = \frac{\eta_p(x_1(t))}{\tau_r}x_1(t) - \frac{1}{\tau_p}x_2(t), \qquad \text{(pore collapse)} \tag{67}$$

$$\text{and } \dot{x}_3(t) = \frac{\eta_d(x_1(t))}{\tau_r}x_1(t) - \frac{1}{\tau_d}x_3(t), \qquad \text{(slow re-absorption)} \tag{68}$$

where $x_1(t)$, $x_2(t)$, and $x_3(t)$ denote the states corresponding to the amount of sweat in the sweat ducts, in the ducts but electrically conducted to the surface due to the pore opening (contributing to the SC level), and diffused in the corneum. The states $x_2(t)$ and $x_3(t)$ are contributing to the rise in the SC level. τ_p denotes the faster decay time due to fast re-absorption (related to the pore collapse). τ_d represents the slow decay time related to the elimination from corneum partially by re-absorption, diffusion in the deeper corneum, and evaporation. τ_r denotes the rise time or the clearance rate of the sweat from the ducts. The system input $u(t)$ represents the ANS activation. To keep the definition simple, we assume that the ANS activation occurs during the integer multiple of the sampling period. Let T_s be the sampling period. With sparsity assumption as in [18], we represent the ANS activation as $u(t) = \sum_{k=1}^{K} u_k \delta(t - kT_s)$ where u_k is the amplitude of the impulse during the ANS activation at time kT_s. u_k is zero if there is no impulse in the stimuli. Moreover, $\eta_p(x_1(t))$ and $\eta_d(x_1(t))$ are two functions that determine the fraction of sweat that are secreted by direct pore opening and diffusion, respectively. We assume $\eta_p(x_1(t))$ and $\eta_p(x_1(t))$ denote the nonlinearity in the pore opening operation. The nonlinearity of the pore opening is similar to the switching operation and analogous to how a neuron work, i.e., in integrate-and-fire manner as pointed out in [14]. Therefore, we propose to model these nonlinearities

with sigmoid functions similar to the artificial neurons as follows,

$$\eta_p(x_1(t)) = S(\alpha x_1(t) + \beta)$$
$$\text{and } \eta_d(x_1(t)) = 1 - S(\alpha x_1(t) + \beta),$$

where $S(x) = (1 + e^{-x})^{-1}$ represents the sigmoid function. Although we assume it as an integrate-and-fire operation, there is a difference, i.e., even if the pores do not open, the sweat secretion will still be carried out by the diffusion process. We assume that both the amount of absorbed sweat in the corneum and epidermis $x_3(t)$ due to diffusion process and the sweat content in the ducts and electrically conducted to the surface due to the pore opening $x_2(t)$ contribute to the SC level. Therefore, the observation equation is as follows,

$$y(t) = x_2(t) + x_3(t) + \nu(t),$$

where $\nu(t)$ represent the noise signal.

Apparently, the proposed model is highly nonlinear and it is very difficult to derive a practical deconvolution approach that runs in edge devices with this model. For the simplification, we assume that the fraction of sweat secretion that happens via pore opening is always constant. Therefore, the simplified linear version of the model is obtained by the assumption that η_p and η_d is constant w.r.t $x_1(t)$ ($\alpha = 0$) s.t. $\eta_d = 1 - \eta_p = \eta$. Here, η is a constant and it represents the fraction of sweat that is secreted by diffusion process, i.e., $\eta \in [0, 1]$. This simplification makes the model linear and more suitable for scalable edge computation. Now, the simplified model can be thought of as a three compartment pharmacokinetic model as shown in Figure 28-(C). To represent it in vector matrix form we define $\boldsymbol{x}(t) = \begin{bmatrix} x_1(t) & x_2(t) & x_3(t) \end{bmatrix}^\top$, $\boldsymbol{A}_c = \begin{bmatrix} -\frac{1}{\tau_r} & 0 & 0 \\ +\frac{\eta_p}{\tau_r} & -\frac{1}{\tau_p} & 0 \\ +\frac{\eta_d}{\tau_r} & 0 & -\frac{1}{\tau_d} \end{bmatrix}$, $\boldsymbol{B}_c = \begin{bmatrix} 1 \\ 0 \\ 0 \end{bmatrix}$, $\boldsymbol{C}_c =$

$\begin{bmatrix} 0 & 1 & 1 \end{bmatrix}$. Therefore, the continuous state-space model in matrix form is as follows,

$$\dot{\boldsymbol{x}}(t) = \boldsymbol{A}_c\boldsymbol{x}(t) + \boldsymbol{B}_c u(t),$$
$$y(t) = \boldsymbol{C}_c\boldsymbol{x}(t) + \nu(t).$$

Discretization. Let y_k be the observed SC at time instance kT_s. We can write,

$$y_k = \boldsymbol{C}_c\boldsymbol{y}(kT_s) + \nu_k, \tag{69}$$

where $\nu_k\ \forall k$ represent the noise and are modelled as independent and identically distributed (i.i.d) zero mean Gaussian random variable, i.e., $\nu_k \sim \mathcal{N}(0, \sigma_\nu^2)$. We derive the discrete equivalent of the system, assuming that the input and the states are constant over T_s. The discrete version of the neural stimuli can be written as a vector $\boldsymbol{u} = [u_1 \quad u_2 \quad \cdots \quad u_K]^\top$ that represents the entire neural stimuli over the duration of SC data. Let $\boldsymbol{A} = e^{\boldsymbol{A}_c T_s}$, $\boldsymbol{B} = \int_0^{T_s} e^{\boldsymbol{A}_c(T_s-\rho)} B_c d\rho$, and $\boldsymbol{C} = \boldsymbol{C}_c$ to write the discrete state-space form as,

$$\boldsymbol{x}_k = \boldsymbol{A}\boldsymbol{x}_{k-1} + \boldsymbol{B}u_k \quad \text{and} \quad y_k = \boldsymbol{C}\boldsymbol{x}_k + \nu_k, \tag{70}$$

where $\boldsymbol{x}_k \in \mathbb{R}^3$, $y_k \in \mathbb{R}$, u_k, ν_k denote the state vector, the observation, ANS activation, and the measurement error in discrete domain.

5.2.3 Physiological Priors

The proposed model has many unknown parameters, and the number of measurements is relatively small. Therefore, the problem has many degrees of freedom. It is customary to enforce appropriate physiologically motivated priors on the model parameters. Otherwise, in the worst cases scenarios, the solution may not stay within the physiological boundaries and may lead to over-fitting [63]. Therefore, we incorporated physiologically motivated priors on the system model similar to [64, 41]. We assume that the individual model

parameters are Gaussian distributed with some mean and variance similar to [41]. We use this information as a prior in the estimation step. Further, we also consider equality and inequality constraints on the system parameters. First of all, we constraint all the physiological parameters are non-negative. We select a lower bound for τ_r of 0.2 seconds based on the result distribution obtained in our previous study in based on the [41]. Further, we set $\tau_p > \beta_1 \tau_r$ and $\tau_d > \beta_2 \tau_p$. Later, we select the values of β_1 and β_2 by manually by investigating the results by trials and errors such that the fits looks physiologically feasible.

5.2.4 Estimation

We wish to estimate the parameter vector

$$\boldsymbol{\theta} = [\ \theta_1 \quad \theta_2 \quad \theta_3 \quad \theta_4 \quad \theta_5\ ]^\top = [\ \tau_r \quad \tau_p \quad \tau_d \quad \eta_p \quad \eta_d\ ]^\top$$

and unknown ANS activation u_k given the SC measurements $y_k \, \forall k \in \{0, 1, \cdots, K-1\}$. One straighforward way is solve the following optimization problem,

$$\min_{x_k, \forall k, \theta_j, \forall J} \lambda \sum_{k=0}^{K-1} ||\boldsymbol{x}_k - A\boldsymbol{x}_{k-1}||_1 + \sum_{k=0}^{K-1} \frac{||y_k - \boldsymbol{C}\boldsymbol{x}_k||_2^2}{2\sigma_\nu^2} + \sum_{j=0}^{j=J-1} \rho_j \frac{(\theta_j - \bar{\theta}_j)^2}{2\sigma_{\theta_j}^2}, \tag{71}$$

where $(\boldsymbol{x}_k - A\boldsymbol{x}_{k-1}) = \boldsymbol{B}u_k$. If we consider the first term in Equation 71, i.e., the l_1-norm of $(\boldsymbol{x}_k - A\boldsymbol{x}_{k-1})$ as the negative log-likelihood, taking the exponential of the negative of the gives us the Laplace distribution of $\boldsymbol{B}u_k = (\boldsymbol{x}_k - A\boldsymbol{x}_{k-1})$ with parameter $\lambda\mathbb{I}$. The second term in Equation 71 represents the least square error between the observation y_k and the prediction $C\boldsymbol{x}_k$ with a Gaussian observation error assumption. The final term represents the negative loglikelihood of the Gaussian priors on the system parameters with ρ_j, $\bar{\theta}_j$, and σ_{θ_j} represents the regularization parameters, the mean, and variance for the Gaussian priors, respectively $\forall j \in \{0, 1, 2, \cdots, J-1\}$. In this case, $J = 3$. Therefore, Equation 71 can be

considered as the maximum *a posterior* (MAP) estimator as pointed out in [105]. In general, the problem formulation in Equation 71 is solved for u_k by taking derivative of Equation 71 with respect u_k and set it zero. This is particularly done using iteratively re-weighted least square (IRLS) approach. The sparse recovery with the direct analytical solution of the state-space model requires a matrix inversion of a $K \times K$ matrix as shown in our previous works [53, 52, 41]. This step work as the bottle neck of the approach. In this study, we solve the very same problem with iterative re-weighted lease square approach implemented using FIS. The states $\boldsymbol{x}_k$, the ANS activation u_k and the matrices describing system dynamics $\boldsymbol{A}$ and $\boldsymbol{B}$ can be estimated in an expectation-maximization (EM) approach.

Given the probabilistic model that generates a set of observed data $Y = \{y_k\}\,\forall k \in 0, 1, \cdots, K-1$ and a vector of unknown parameters $\boldsymbol{\theta}$, we can write, $p(Y, \theta) = p(Y|\theta)p(\theta)$. The following maximum log-likelihood estimation problem can be solved in order to estimate the θ,

$$\max_{\theta} \ \log p(Y; \theta).$$

Now lets introduce a set of hidden unknown states $X = \{\boldsymbol{x}_k,\, u_k\}\,\forall k$ having a joint probability distribution $p(Y, X; \theta)$. We can re-write the maximum likelihood estimation as the following marginal likelihood function of $p(Y, X; \theta)$,

$$\max_{\theta} \ \log p(Y; \theta) = \max_{\theta} \ \log \int_X p(Y, X; \theta) dX. \tag{72}$$

We defined the joint log-likelihood function for Y, X, and $\boldsymbol{\theta}$ as follows,

$$\begin{aligned}
&\log p(Y, X; \theta) = \log \left(p(Y|X, \boldsymbol{\theta}) p(X|\boldsymbol{\theta}) p(\boldsymbol{\theta}) \right) \\
&= \log p(Y|X, \boldsymbol{\theta}) + \log p(X|\boldsymbol{\theta}) + \log(\boldsymbol{\theta}) \qquad (73) \\
&= \sum_{k=0}^{K-1} \log(p_{\nu_k}(y_k - \boldsymbol{C}\boldsymbol{x}_k)) + \sum_{k=0}^{K-1} \log(p_{\boldsymbol{B}u_k}(\boldsymbol{x}_k - A\boldsymbol{x}_{k-1})) \\
&\qquad\qquad + \log(p(\theta)), \qquad (74)
\end{aligned}$$

where the p_{ν_k} and $p_{\boldsymbol{B}u_k}$ denotes the probability density functions corresponding to $\nu_k = y_k - \boldsymbol{C}\boldsymbol{x}_k$ and $\boldsymbol{B}u_k = \boldsymbol{x}_k - A\boldsymbol{x}_{k-1}$, respectively. Here, only the term $p_{\boldsymbol{B}u_k}(\boldsymbol{x}_k - A\boldsymbol{x}_{k-1})$ depends on θ.

Expectation-Maximization (EM). Obtaining the marginal likelihood by the integration operation in Equation 72 is difficult, especially with edge computation on wearable devices or smart-phones. This problem is usually modified as follows,

$$\begin{aligned}
&\max_{\theta} \log \int_X p(Y, X; \theta) dX = \max_{\theta} \log \left(\int_X \frac{p(Y, X; \theta)}{q(X)} q(X) dX \right) \\
&\geq \max_{\theta} \int_X q(X) \log \left(\frac{p(Y, X; \theta)}{q(X)} \right) dX \quad \text{[Jensen's inequality]} \\
&= \underbrace{\max_{\theta} \int_X q(X) \log \left(p(Y, X; \theta) \right) dX}_{\text{function of } \theta} - \underbrace{\int_X q(X) \log \left(q(X) \right) dX}_{\text{constant}},
\end{aligned}$$

where $q(X)$ is any probability density function. Therefore, the original problem is defined as the following expectation maximization (EM) approach,

$$\max_{\theta} \log p(Y; \theta) = \max_{\theta} \mathbb{E}_{X \sim q(X)} \{ \log p(Y, X; \theta) \}. \qquad (75)$$

As it is expressed in Equation 75, the unknowns can be estimated by iteratively maximizing the expection of the joint log-likelihood in Equation 74.

E-step (Sparse Recovery). Let's assume that we know the current estimate of model

parameters $\boldsymbol{\theta}^{(i-1)}$ from the $(i-1)^{\text{th}}$ iteration of EM. We calculate the corresponding state matrices $\boldsymbol{A}^{(i-1)}$ and $\boldsymbol{B}^{(i-1)}$. At i^{th} iteration of EM, given the sequence of observations $y_k \in Y$ and given probability distribution $q(X) = p(X|Y, \boldsymbol{\theta}^{(i-1)})$, we wish to estimate the expectation of $\boldsymbol{x}_k^{(i)}$ and $u_k^{(i)}$. We choose the probability distribution for u_k such that it enforces sparsity. Kazempour et al. [105] proposed to use Laplace distributed with parameter for sparsity of the innovation terms in the state transition equations. In this study, we consider a broader family of distributions, namely, generalized Gaussian distribution for u_k so that distribution parameters can be selected to obtain a range of distributions such as Gaussian and Laplace distribution. In contrast to [105] where the input matrix is considered as an identity one, we assume that $u_k^{(i)}$ denote the scalar (or column vector) ANS activation and $\boldsymbol{B}^{(i-1)}$ works as a direction vector (or matrix) of innovation in the state transition equation. We consider $u_k^{(i)}$ is generalized Gaussian distributed, i.e.,

$$p(u_k^{(i)}|\gamma^{(i)}, p) = \frac{p\gamma^{(i)}}{4\gamma^{(i)}(1/p)} \exp\left(-\frac{\gamma^{(i)}}{2}|u_k^{(i)}|^p\right),$$

where $\gamma^{(i)}$ and p defines the shape of the generalized Gaussian distribution. $p(u_k|\gamma^{(i)}, p)$ can also be written in terms of $\boldsymbol{x}_k$ with multi-variate generalized Gaussian distribution as follows,

$$\begin{aligned} p(u_k^{(i)}|\gamma^{(i)}, p) = p(\boldsymbol{B}u_k^{(i)}|\lambda^{(i)}, p) &= \exp\left(-\frac{\lambda^{(i)}}{2}||\boldsymbol{B}^{(i-1)}u_k^{(i)}||_p^p\right) \\ &= \exp\left(-\frac{\lambda^{(i)}}{2}||\boldsymbol{x}_k^{(i)} - A^{(i-1)}\boldsymbol{x}_{k-1}^{(i)}||_p^p\right), \end{aligned}$$

where $\lambda^{(i)}$ represents the new parameter related to the new random variable to obtain the equivalent pdf ($\lambda^{(i)}||\boldsymbol{B}^{(i-1)}||_p^p = \gamma^{(i)}$). The sparsity constrain is imposed on $u_k^{(i)}$ for $0 < p < 2$. However, the closed form equations for FIS do not exist for generalized Gaussian distribution where $p \neq 2$, although they are the prerequisite for scalable edge computation of the sparse recovery. Therefore, we approximate the generalized Gaussian distribution with

iterative re-weighted Gaussian distributions for the closed form derivation of the forward filter and backward smoother equations. For example, if $p = 1$, the generalized Gaussian distribution becomes Laplace distribution as shown in [105]. Therefore, we approximate the Laplace distribution of $u_k^{(i)}$ with iterative re-weighted Gaussian distributions, i.e., if at r^{th} re-weighting step the state estimation is $\boldsymbol{x}_k^{(i,r)}$, the Laplace pdf can be approximated with Gaussian pdf as follows,

$$\begin{aligned} p_{\boldsymbol{x}_k} &= \frac{\lambda^{(i,r)}}{2} \exp\left\{ \left(-\frac{\lambda^{(i,r)}}{2} ||\boldsymbol{x}_k^{(i,r)} - A^{(i-1)} \boldsymbol{x}_{k-1}^{(i,r)}||_1 \right) \right\} \\ &\approx \frac{\lambda^{(i,r)}}{2} \exp\left\{ \left(-\frac{1}{2} (\boldsymbol{x}_k^{(i,r)} - A^{(i-1)} \boldsymbol{x}_{k-1}^{(i,r)})^\top \left(Q_{k,}^{(i,r-1)} \right)^{-1} (\boldsymbol{x}_k^{(i,r)} - A^{(i-1)} \boldsymbol{x}_{k-1}^{(i,r)}) \right) \right\}, \end{aligned}$$

where $\lambda^{(i,r)}$ is the regularization at r^{th} re-weighting step. $Q_k^{(i,r)}$ is the co-variance matrix at r^{th} re-weighting step at k^{th} time point and we define it defined as follows,

$$\begin{aligned} Q_k^{(i,r)} &= (\lambda^{(i,r)})^{-1} (\mathbb{E}\{(\boldsymbol{x}_k^{(i,r)} - A^{(i-1)} \boldsymbol{x}_{k-1}^{(i,r)})(\boldsymbol{x}_k^{(i,r)} - A^{(i-1)} \boldsymbol{x}_{k-1}^{(i,r)})^\top\} + \epsilon^2 \mathbb{I})^{\frac{1}{2}} \\ &= (\lambda^{(i,r)})^{-1} ((\boldsymbol{B}^{(i-1)} (u_k^{(i,r)})^2 \boldsymbol{B}^{(i-1)^\top}) + \epsilon^2 \mathbb{I})^{\frac{1}{2}}. \end{aligned}$$

Here, ϵ is a value close to zero for the matrix perturbation to achieve numerical stability. We select $\epsilon = 10^{-5}$ for the numerical stability. The perturbations enable us to obtain feasible inverse during FIS prediction and update equations as $\boldsymbol{B}^{(i-1)} (u_k^{(i,r)})^2 \left(\boldsymbol{B}^{(i-1)} \right)^\top$ is always singular. The generalized approximation is performed by implementing ℓ_p-norm with Gaussian distribution approximation of generalized Gaussian family as follows where $0 < p < 2$,

$$Q_k^{(i,r)} = (\lambda^{(i,r)})^{-1} ((\boldsymbol{B}^{(i-1)} (u_k^{(i,r)})^2 \left(\boldsymbol{B}^{(i-1)} \right)^\top) + \epsilon^2 \mathbb{I})^{\frac{2-p}{2}}. \tag{76}$$

With this approximation, we perform Kalman filtering and backward smoothing to obtain the expectation of the state variables $\mathbb{E}\{\boldsymbol{x}_k^{(i,r)}\}$'s and corresponding covariance matrices.

Constraining the corresponding innovation in the state equation to be along the direction of the vector $\boldsymbol{B}$, we define the expected u_k is given as follows at r^{th} re-weighting step,

$$u_k^{(i,r)} = \underset{u \geq u_{\text{th}}}{\operatorname{argmin}} \frac{1}{2} ||\mathbb{E}\{\boldsymbol{x}_{k+1}^{(i,r)}\} - \boldsymbol{A}^{(i-1)}\mathbb{E}\{\boldsymbol{x}_k^{(i,r)}\} - \boldsymbol{B}^{(i-1)}u||_2^2, \tag{77}$$

where u_{th} is the selected minimum amplitude for ANS activation. This enables us to obtain a constrained solution of u_k without implementing actual constrained Kalman filtering and backward smoothing. As $u_k^{(i,r)}$ is scalar in the above optimization formulation, the solution can be written directly as follows,

$$u_k^{(i,r)} = \max(u_{\text{th}}, ({\boldsymbol{B}^{(i-1)}}^\top \boldsymbol{B}^{(i-1)})^{-1}(\boldsymbol{B}^{(i-1)})^\top(\boldsymbol{x}_{k+1}^{(i,r)} - \boldsymbol{A}^{(i-1)}\boldsymbol{x}_k^{(i,r)})), \tag{78}$$

This allows us to project the error vector along the direction of $\boldsymbol{B}^{(i-1)}$ vector based on least square error with a minimum threshold. In this study, we select $p = 0.5$ for l_p-norm similar to our previous studies in [41, 8, 54, 52, 53].

Adjust Sparsity Level by Choosing γ. In the initialization phase, we choose a scheme for selecting λ similar to IRLS algorithm $FOCUSS+$ algorithm in [66]. At r^{th} re-weighting iteration of E-step, the heuristic estimation of λ works as follows,

$$\gamma^{(i,r)} = \left(1 - \sum_{k=0}^{K-1} ||y_k - \boldsymbol{C}\boldsymbol{x}_k^{(i,r-1)}||_2^2 / \sum_{k=0}^{K-1} ||y_k||_2^2\right)\gamma^{\max}, \quad \gamma > 0. \tag{79}$$

Then, we set $\lambda_n^{(i,r)} = \gamma_n^{(i,r)}/||\boldsymbol{B}^{(i-1)}||_p^p$. Similarly, in the main EM phase, we use generalized-cross-validation (GCV) technique similar to the GCV-FOCUSS+ technique [68]. We modified the GCV technique to obtain scalability. To achieve this, we segment our observations with a window size of M_{gcv} samples and apply GCV to obtain a λ for each window. For n^{th} segment, the discretized vector form solution can be provided as, $\tilde{\boldsymbol{y}}_n = \boldsymbol{F}_n\tilde{\boldsymbol{x}}_{n,0} + \boldsymbol{D}_n\tilde{\boldsymbol{u}}_n$, where $\tilde{\boldsymbol{y}}_n$, $\boldsymbol{x}_{n+1}$, $\tilde{\boldsymbol{u}}_n$ represents the observation vector, the first state and the ANS activation

in the n^{th} segment, respectively. $\boldsymbol{F}_n$ and $\boldsymbol{D}_n$ are the matrices for the complete decretized vector solution for n^{th} block and can be defined as, $\boldsymbol{F}_n = \begin{bmatrix} \boldsymbol{F}_{n,0} & \boldsymbol{F}_{n,1} & \cdots & \boldsymbol{F}_{n,(M_{gcv}-1)} \end{bmatrix}^\top_{M_{gcv}\times 3}$ and $\boldsymbol{D}_{\boldsymbol{\theta}} = \begin{bmatrix} \boldsymbol{D}_{n,0} & \boldsymbol{D}_{n,1} & \cdots & \boldsymbol{D}_{n,(M_{gcv}-1)} \end{bmatrix}^\top_{M_{gcv}\times M_{gcv}}$, where $\boldsymbol{F}_{n,k} = \boldsymbol{C}\boldsymbol{A}^k$ and $\boldsymbol{D}_{n,k} = \boldsymbol{C}\begin{bmatrix} \boldsymbol{A}^{k-1}\boldsymbol{B} & \boldsymbol{A}^{k-2}\boldsymbol{B} & \cdots & \boldsymbol{B} & \underbrace{0 \quad \cdots \quad 0}_{M_{gcv}-k} \end{bmatrix}$. $M_{gcv} = 100$ worked well for our study.

For n^{th} segment, we obtain λ_n using the following optimization formulation based on singular value decomposition (SVD) for GCV proposed in [68],

$$\begin{aligned} \min_{\lambda_n} G_n(\gamma_n) &= \frac{\left[M_{gcv} \sum_{n'=1}^{M_{gcv}} \hat{y}_{n,n'}^2 \left(\frac{\gamma_n}{\kappa_{n,n'}^2 + \gamma_n} \right)^2 \right]}{\left[\sum_{n'=1}^{M_{gcv}} \left(\frac{\gamma_n}{\kappa_{n,n'}^2 + \gamma_n} \right)^2 \right]} \\ \text{s.t.} \quad & \mathbf{0} \leq \gamma_n \leq 1 \times 10^{-4}, \end{aligned} \tag{80}$$

where $\hat{\boldsymbol{y}} = \boldsymbol{U}^\top \hat{\boldsymbol{y}}_{n,\tau} = \begin{bmatrix} \hat{y}_{n,1} & \hat{y}_{n,2} & \cdots & \hat{y}_{n,M_{gcv}} \end{bmatrix}^\top$ with $\hat{\boldsymbol{y}}_{n,\tau} = \tilde{\boldsymbol{y}}_n - \boldsymbol{F}_n \tilde{\boldsymbol{x}}_n$, and $\boldsymbol{D}_n \boldsymbol{P}_{\tilde{\boldsymbol{u}}}^{\frac{1}{2}} = \boldsymbol{U}\boldsymbol{\Sigma}\boldsymbol{V}^\top$ with $\boldsymbol{P}_{\tilde{\boldsymbol{u}}} = \text{diag}(|\tilde{\boldsymbol{u}}_{n,n'}|^{2-p})$ and $\boldsymbol{\Sigma} = \text{diag}\{\kappa_j\}$; $\boldsymbol{U}$ and $\boldsymbol{V}$ are unitary matrices and κ_i's are the singular values of $\boldsymbol{D}_n \boldsymbol{P}_{\tilde{\boldsymbol{u}}}^{\frac{1}{2}}$. We estimate $\gamma_n \ \ \forall n$ and take the median. Finally, we set $\lambda_n^{(i,r)} = \gamma_n^{(i,r)} / ||\boldsymbol{B}^{(i-1)}||_p^p$.

Usually, the re-weighting in E-step converges within a very small number of iterations. We perform the re-weighting in E-step for $r = 0, 1, 2, \cdots, 5$. After finishing all the re-weighting iterations in the E-step, we obtain the following estimations: $\boldsymbol{x}_k^{(i)}, u_k^{(i)}$, $\boldsymbol{P}_{k|k}^{(i)}$, and $\boldsymbol{P}_{k|k-1}^{(i)} \forall k$. Here, $\boldsymbol{P}_{k|k}^{(i)}$ and $\boldsymbol{P}_{k|k-1}^{(i)}$ represents the estimates of $\mathbb{E}\{\boldsymbol{x}_k^{(i)} \boldsymbol{x}_k^{(i)\top}\}$ and $\mathbb{E}\{\boldsymbol{x}_k^{(i)} \boldsymbol{x}_{k-1}^{(i)\top}\}$, respectively. Here, we drop r to represent the final E-step estimations.

M-step (Physiological Parameter Estimation). The M-step at i^{th} iteration can be defined as the following simplified constrained optimization problem utilizing Equation

71 and 75,

$$\min_{\theta_j, \forall j} \mathbb{E}\{\lambda^{(i)} \sum_{k=0}^{K-1} ||\boldsymbol{x}_k^{(i)} - A\boldsymbol{x}_{k-1}^{(i)}||_1 + \sum_{k=0}^{K-1} \frac{||y_k - \boldsymbol{C}\boldsymbol{x}_k^{(i)}||_2^2}{2\sigma_\nu^2} + \sum_{j=0}^{j=J} \rho_j \frac{(\theta_j - \bar{\theta}_j)^2}{2\sigma_{\theta_j}^2}\}, \tag{81}$$

$$\text{s.t.} \quad \boldsymbol{R}\theta \leq s, \quad \boldsymbol{R}_e\theta = s_e,$$

where $\boldsymbol{R} = \begin{bmatrix} -1 & 0 & 0 & 0 & 0; \\ 0 & -1 & 0 & 0 & 0 \\ 0 & 0 & -1 & 0 & 0 \\ \beta_1 & -1 & 0 & 0 & 0 \\ 0 & \beta_2 & -1 & 0 & 0 \end{bmatrix}$, $\boldsymbol{s} = \begin{bmatrix} s_1 \\ s_2 \\ s_3 \\ 0 \\ 0 \end{bmatrix}$,

$\boldsymbol{R}_e = \begin{bmatrix} 0 & 0 & 0 & 1 & 0 \\ 0 & 0 & 0 & 0 & 1 \end{bmatrix}$, and $\boldsymbol{s}_e = \begin{bmatrix} 1-\eta \\ \eta \end{bmatrix}$ determines the constraints on θ. The equality constraints ensures the sum of η_p and η_d are equal to 1. To incorporate estimated $u_k^{(i)}$ from the E-step, we re-write the Equation 81. The modified optimization formulation is as follows,

$$\min_{\theta_j, \forall j} \mathbb{E}\{\frac{\gamma^{(i)}}{2} \sum_{k=0}^{K-1} |u_k^{(i)}|^p + \sum_{k=0}^{K-1} \frac{||y_k - \boldsymbol{C}(\boldsymbol{A}\boldsymbol{x}_{k-1}^{(i)} + \boldsymbol{B}u_k^{(i)})||_2^2}{2\sigma_\nu^2} + \sum_{j=0}^{j=J} \rho_j \frac{(\theta_j - \bar{\theta}_j)^2}{2\sigma_{\theta_j}^2}\} \tag{82}$$

$$\text{s.t.} \quad \boldsymbol{R}\theta \leq s, \quad \boldsymbol{R}_e\theta = s_e.$$

After some algebraic manipulation and assumption that $x_{k-1}^{(i)}$ and $u_k^{(i)}$ are statistically independent $\forall k$, we obtain the following optimization formulation by removing the constant

terms with respect to $\boldsymbol{\theta}$.

$$\begin{aligned}\min_{\theta_j,\forall j} \quad & \frac{1}{2}||\boldsymbol{y}||^2 + \frac{1}{2}Tr(\boldsymbol{A}((\boldsymbol{x}_{k-1}^{(i)}(\boldsymbol{x}_{k-1}^{(i)})^\top + \boldsymbol{P}_{k-1}^{(i)}))\boldsymbol{A}^\top) \\ & - Tr(\boldsymbol{A}(\sum_{k=0}^{K-1} y_k^\top \boldsymbol{C}\boldsymbol{x}_k^{(i)})) - Tr(\boldsymbol{B}(\sum_{k=0}^{K-1} y_k^\top \boldsymbol{C}u_k^{(i)})) \\ & + Tr(\boldsymbol{B}\sum_{k=0}^{K-1}((u_k^{(i)})^2)\boldsymbol{B}^\top) + Tr(\boldsymbol{A}\boldsymbol{x}_{k-1}^{(i)}(u_{k-1}^{(i)})^\top \boldsymbol{B}^\top)) \\ & + \sigma_v^2 \sum_{j=0}^{j=J} \rho_j \frac{(\theta_j - \bar{\theta}_j)^2}{2\sigma_{\theta_j}^2}, \qquad (83) \\ \text{s.t.} \quad & \boldsymbol{R}\theta \leq s, \quad \boldsymbol{R}_e\theta = s_e.\end{aligned}$$

The overall approach can be divided into two phases. In the first phase, we perform initialization with a fixed $u_k^{(i,0)} = \alpha\,\forall k$ at each iteration and with heuristic update of $\lambda^{(i,r)}$. $\alpha = 1$ worked well for our study. In the main EM-phase, we update $u_k^{(i,0)} = u_k^{(i-1,5)}$, i.e. with the values obtained in the previous re-weighting iteration. In E-steps of both phases, we perform a heuristic refinement of u_k. After finishing all re-weighting iterations in the E-step, we obtain the following estimations: $\boldsymbol{x}_k^{(i)}, u_k^{(i)}$, $\boldsymbol{P}_{k|k}^{(i)}$, and $\boldsymbol{P}_{k|k-1}^{(i)}\forall k$. The expected values are plugged into the M-step optimization formulation in 83. The constrained optimization problem in 83 is solved using the interior-point method. The overall algorithm for the initialization and the main EM-phase is provided in Algorithm 1.

5.3 Results

5.3.1 Experimental Study

We use the proposed approach to deconvolve the SC measurements from 26 participants. The deconvolution approach provides the estimates of the underlying ANS activation $u(t)$, rise time (τ_r), faster decay time (τ_p), and slow decay time (τ_d). We have considered the signal segment from 150 seconds to 350 seconds for the analysis on the experimental data. The figures from the deconvolution results for all 13 female and 13 male participants are provided

Input : $y_k \; \forall k$
Output: $u_k \; \forall k$ and θ

Initialization Phase:
Initialize $\tilde{\boldsymbol{\theta}}^0 \sim \mathcal{U}(\boldsymbol{b}_l, \boldsymbol{b}_u)$.
for $i = 1, 2, 3, \cdots, 30$ **do**
  Set $u_k^{(i,0)} = \alpha \; \forall k$
  E-Step: With $\boldsymbol{\theta} = \tilde{\boldsymbol{\theta}}^{(i-1)}$, calculate $\boldsymbol{A}^{(i-1)}$ and $\boldsymbol{B}^{(i-1)}$
  Iterative re-weighting:
  for $r = 1, 2, 3, \cdots, 10$ **do**
    Estimate $\lambda^{(i,r)}$ using 79
    Perform heuristic refinement of $u_k^{(i,r-1)}$
    Set $Q_k^{(i,r-1)} = (\lambda^{(i,r)})^{-1}((\boldsymbol{B}^{(i-1)}(u_k^{(i,r-1)})^2 \left(\boldsymbol{B}^{(i-1)}\right)^\top) + \epsilon^2 \mathbb{I})^{\frac{2-p}{2}}$
    Estimate $\boldsymbol{x}_k^{(i,r)}$, $\boldsymbol{P}_{k|k}^{(i,r)}$ and $\boldsymbol{P}_{k|k-1}^{(i,r)}$ using FIS
    Set $u_k^{(i,r)} = \max(u_{\text{th}}, (\boldsymbol{B}^{(i-1)^\top}\boldsymbol{B}^{(i-1)})^{-1}\boldsymbol{B}^{(i-1)^\top}(\boldsymbol{x}_k^{(i,r)} - A\boldsymbol{x}_{k-1}^{(i,r)}))$.
  end
  M-Step: Set $\boldsymbol{x}_k^{(i)} = \boldsymbol{x}_k^{(i,r)}$, $u_k^{(i)} = u_k^{(i,r)}$, $\boldsymbol{P}_{k|k}^{(i)} = \boldsymbol{P}_{k|k}^{(i,r)}$ and $\boldsymbol{P}_{k|k-1}^{(i)} = \boldsymbol{P}_{k|k-1}^{(i,r)}$, and
  Solve the optimization problem in Eq. 83 to obtain obtain $\boldsymbol{\theta}^{(i)}$
end

Main EM Phase: **while** *until convergence* **do**
  Set $i = i + 1$
  Set $u_k = u_k^{(i-1,r)} \; \forall k$
  E-Step:
  With $\boldsymbol{\theta} = \tilde{\boldsymbol{\theta}}^{(i-1)}$, calculate $\boldsymbol{A}^{(i-1)}$ and $\boldsymbol{B}^{(i-1)}$
  Iterative re-weighting:
  for $r = 1, 2, 3, \cdots, 10$ **do**
    Estimate $\lambda^{(i,r)}$ using the modified GCV technique
    Perform heuristic refinement of $u_k^{(i,r-1)}$
    Set $Q_k^{(i,r-1)} = (\lambda^{(i,r)})^{-1}((\boldsymbol{B}^{(i-1)}(u_k^{(i,r-1)})^2 \left(\boldsymbol{B}^{(i-1)}\right)^\top) + \epsilon^2 \mathbb{I})^{\frac{2-p}{2}}$
    Estimate $\boldsymbol{x}_k^{(i,r)}$, $\boldsymbol{P}_{k|k}^{(i,r)}$ and $\boldsymbol{P}_{k|k-1}^{(i,r)}$ using FIS
    Set $u_k^{(i,r)} = \max(u_{\text{th}}, (\boldsymbol{B}^{(i-1)^\top}\boldsymbol{B}^{(i-1)})^{-1}\boldsymbol{B}^{(i-1)^\top}(\boldsymbol{x}_k^{(i,r)} - A\boldsymbol{x}_{k-1}^{(i,r)}))$.
  end
  M-Step: Set $\boldsymbol{x}_k^{(i)} = \boldsymbol{x}_k^{(i,r)}$, $u_k^{(i)} = u_k^{(i,r)}$, $\boldsymbol{P}_{k|k}^{(i)} = \boldsymbol{P}_{k|k}^{(i,r)}$ and $\boldsymbol{P}_{k|k-1}^{(i)} = \boldsymbol{P}_{k|k-1}^{(i,r)}$, and
  solve the optimization problem in Eq. 83 to obtain obtain $\tilde{\boldsymbol{\theta}}^{(i)}$
end

Algorithm 1: bayesianEDA

in Figure 29-32. Here in each panels, i) the top sub-panel shows the experimental SC signal (blue stars), the reconstructed SC signal (red curve), the estimated tonic component (green curve), and the timings of the auditory stimulations (gray vertical lines); ii) the bottom

sub-panel shows the estimated phasic component (blue curve), estimated ANS activation timings and amplitudes (black vertical lines) and the timings of the auditory stimuli (gray vertical lines). These figures depict the successful estimation of the sparse ANS activation due to auditory stimulation.

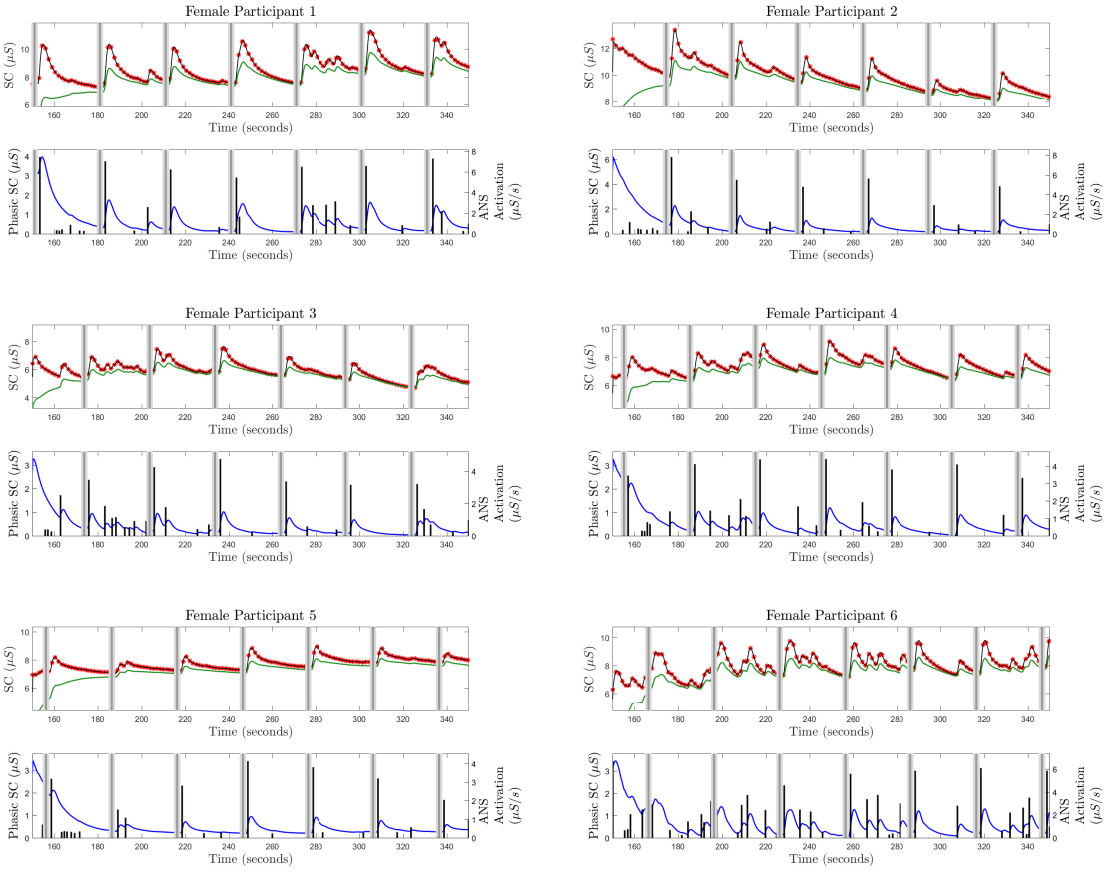

Figure 29: **Estimated Decomposition of the Experimental SC Signals for Female Participant 1 to 6.**

The estimated rise time (τ_r), fast decay time τ_p, slow decay time τ_d, number of pulses ($||\mathbf{u}||_0$), and multiple correlation coefficient (R^2) are provided in Table 8. Figure 33 shows the histogram of the estimated state-space model parameters from all 26 participants. In

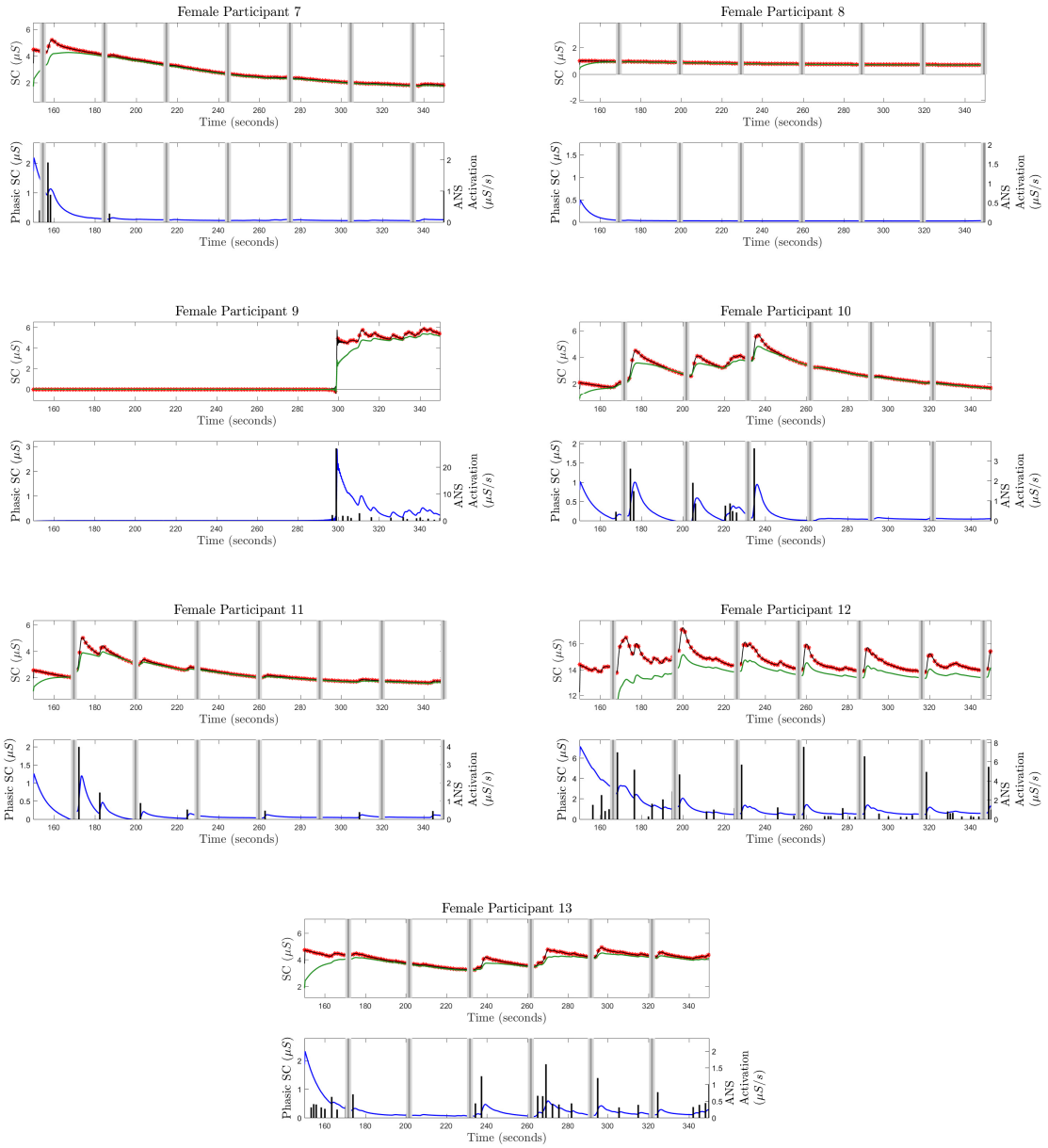

Figure 30: **Estimated Decomposition of the Experimental SC Signals for Female Participant 8 to 13.**

top sub-panel in Figure 33, the red and green bar plots correspond to the histogram plots of the estimated rise time τ_r and decay time τ_d, respectively; the red, green and blue vertical lines correspond to the locations of the means μ_r, μ_p and μ_d of the corresponding histograms, respectively. The estimated means of the parameters among the 26 participants

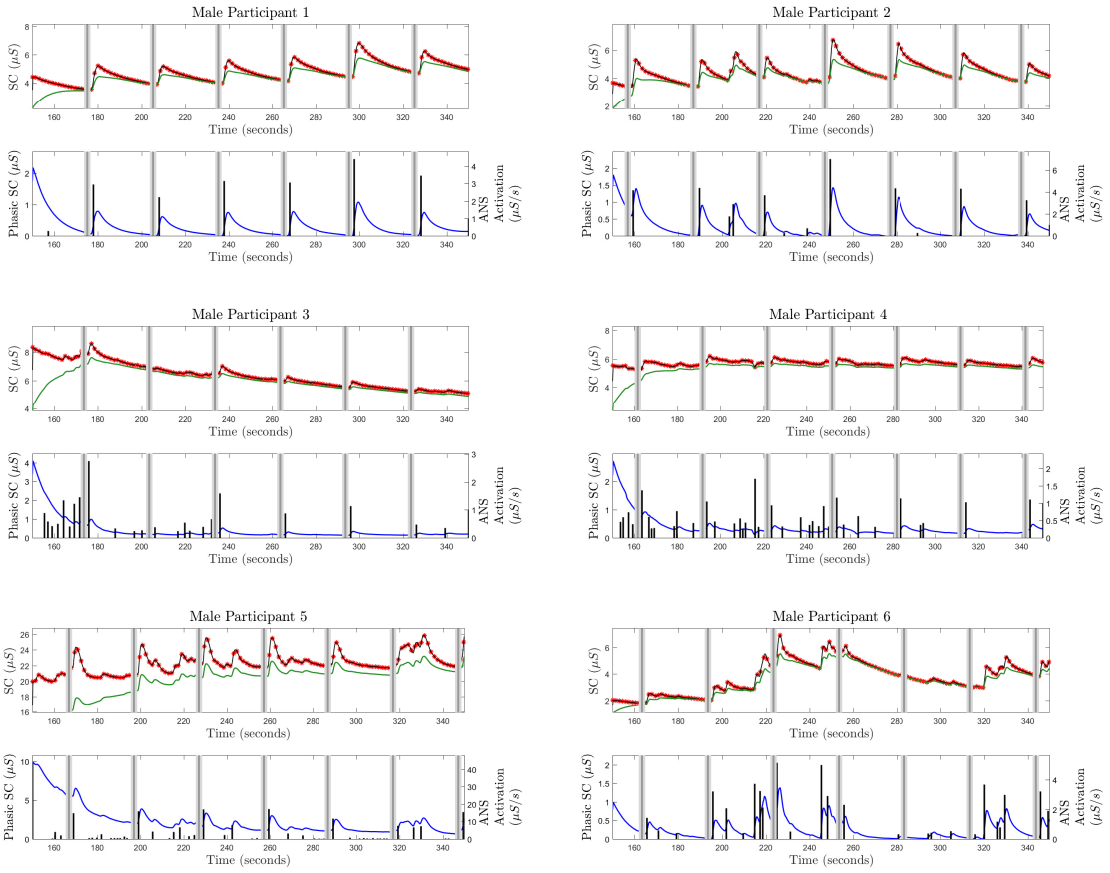

Figure 31: **Estimated Decomposition of the Experimental SC Signals for Male Participants 1 to 6.**

are $\mu_r = 2.0040$, $\mu_p = 5.4545$, and $\mu_d = 81.8175$ seconds for rise times, fast decay time, and slow decay times, respectively. Corresponding standard deviations are $\sigma_r = 0.8675$, $\sigma_p = 1.9258$, and $\sigma_d = 28.8874$ seconds, respectively. The calculated multiple correlation coefficients (R^2) are greater than 0.98 for all participants except for Male Participant 12 (R^2 for Male Participant 12 is 0.8352). This suggests that the proposed model can successfully explain the variations in SC recording.

We utilize the estimated ANS activation $u(t)$ in distinguishing between SCRs that are related to and not related to loud sound events. We label all the impulses in estimated $\boldsymbol{u}$

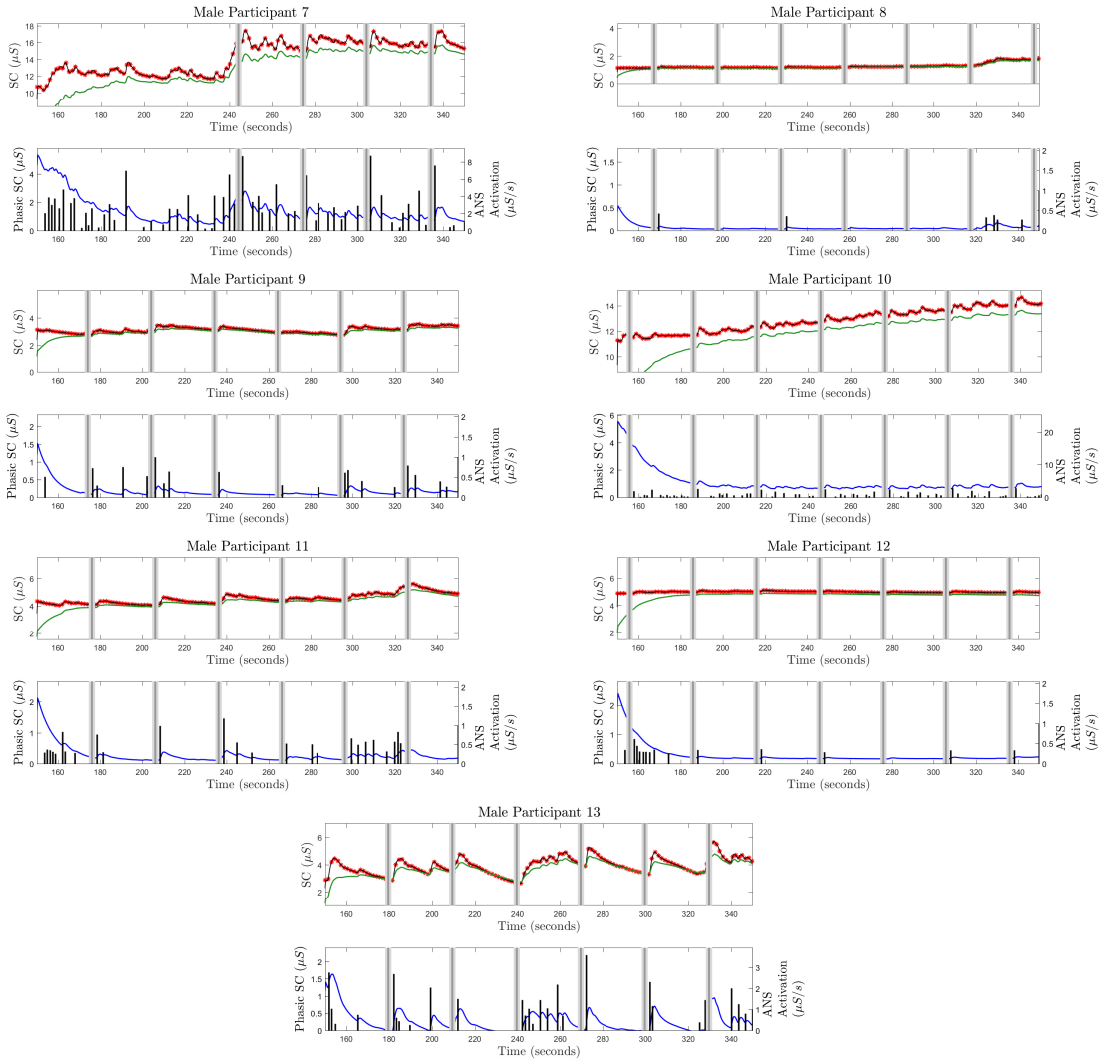

Figure 32: **Estimated Decomposition of the Experimental SC Signals for Male Participant 7 to 13.**

that have been detected within 5 seconds after a loud sound event as the positive class and other impulses as the negative class. We consider the amplitudes of the impulses as the classification scores within the subjects for obtaining the receiver operating characteristic (ROC) curves [69, 70]. The estimated area under the ROC curves (AUC) for all participants ranges from 0.6600 to 1 with a median of 0.9380 and a mean of 0.8960. We individually normalized the estimated $\boldsymbol{u}$ for all participant and combined all $\boldsymbol{u}$ in one vector to obtain an overall ROC. The estimated overall AUC is 0.8196. We compare our proposed bayesianEDA

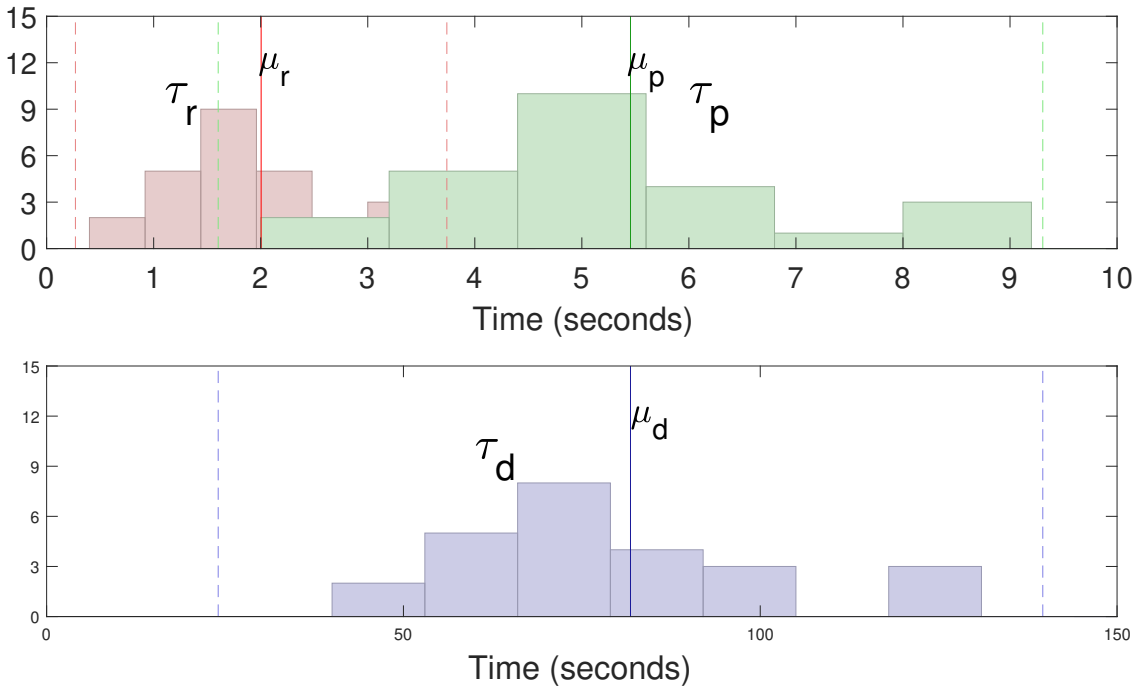

Figure 33: **Histograms of Estimated SCR Shape Parameters using Our Approach.**

approach with LedaLab-CDA [29], LedaLab-DDA [21], cvxEDA [23], sparsEDA [24], PsPM-MP [50], and our spline based approach [41]. Figure 34 shows: (A) the overall ROC curve related to the discrimination power between event-related vs non-event-related SCRs combining all the normalized **u** from each of the individual participants; (B) corresponding AUC of the ROC curves, and (C) total number of the undetected auditory stimulation impulses within 26 participants.

5.3.2 Simulated Study

To further, investigate the efficacy of our approach, we use the reconstructed signal from our experimental study and add Gaussian noise to simulate data for all 26 participants similar to the previous works in [19, 20, 52, 54, 41]. We consider the results from the experimental study as the ground truths to compare with the estimation from the simulated study. The proposed approach successfully estimates the ANS activation along with the

Table 8: The Estimated Model Parameters and the Squares of the Multiple Correlation Coefficients (R^2) for the Fits of the Experimental SC Data

Female Participant	ID	τ_r	τ_p	τ_d	$\|\|\boldsymbol{u}\|\|_0$	R^2
1	12	2.4575	6.4373	96.5591	25	0.9980
2	15	2.6889	6.9542	104.3135	24	0.9936
3	7	1.9565	5.3131	79.6968	28	0.9961
4	18	2.2324	5.9467	89.2004	25	0.9944
5	21	2.2948	6.0929	91.394	24	0.9893
6	25	2.3572	6.2167	93.2508	39	0.9990
7	1	1.3424	3.9588	59.3823	6	0.9986
8	2	0.7779	2.9288	43.9323	1	0.9883
9	5	1.2355	3.7123	55.6841	16	1
10	6	1.3411	3.9759	59.6391	11	0.9997
11	14	1.2101	3.6983	55.4741	9	0.9991
12	16	3.4221	8.6496	129.7442	41	0.9871
13	19	1.5775	4.4758	67.1366	25	0.9928
Male Participant	ID	τ_r	τ_p	τ_d	$\|\|\boldsymbol{u}\|\|_0$	R^2
1	11	1.7215	4.7976	71.9641	8	0.9991
2	26	1.6574	4.6498	69.7463	13	0.9991
3	8	2.0524	5.5199	82.7989	24	0.9987
4	10	1.9070	5.2164	78.2453	40	0.9836
5	20	4.5170	11.0786	166.1788	59	0.9909
6	23	1.5451	4.4054	66.0803	27	0.9998
7	3	3.4100	8.6018	129.0276	58	0.9986
8	4	0.8936	3.1084	46.6253	8	0.9993
9	9	1.3561	4.0062	60.0935	20	0.9963
10	13	3.1618	8.066	120.9899	75	0.9954
11	17	1.6731	4.6962	70.4425	30	0.9976
12	22	1.7625	4.8939	73.4078	16	0.8352
13	24	1.5518	4.4164	66.2467	29	0.9992

physiological model parameters. All the multiple correlation coefficients (R^2) are greater than 0.98 for simulated data with 25 dB noise level is 0.9872. Estimated system parameters ($\hat{\tau}_r$, $\hat{\tau}_p$ and $\hat{\tau}_d$), estimation errors, and the multiple correlation coefficients (R^2) for the results for all the simulated data with 25 dB SNR are provided in Table 9. In Table 9, $\hat{\tau}_r$, $\hat{\tau}_p$ and $\hat{\tau}_d$ denote the estimated rise time, fast decay time, and slow decay time for the simulated SC data. The SC signal is simulated with 25 dB Gaussian noise. Further, also perform

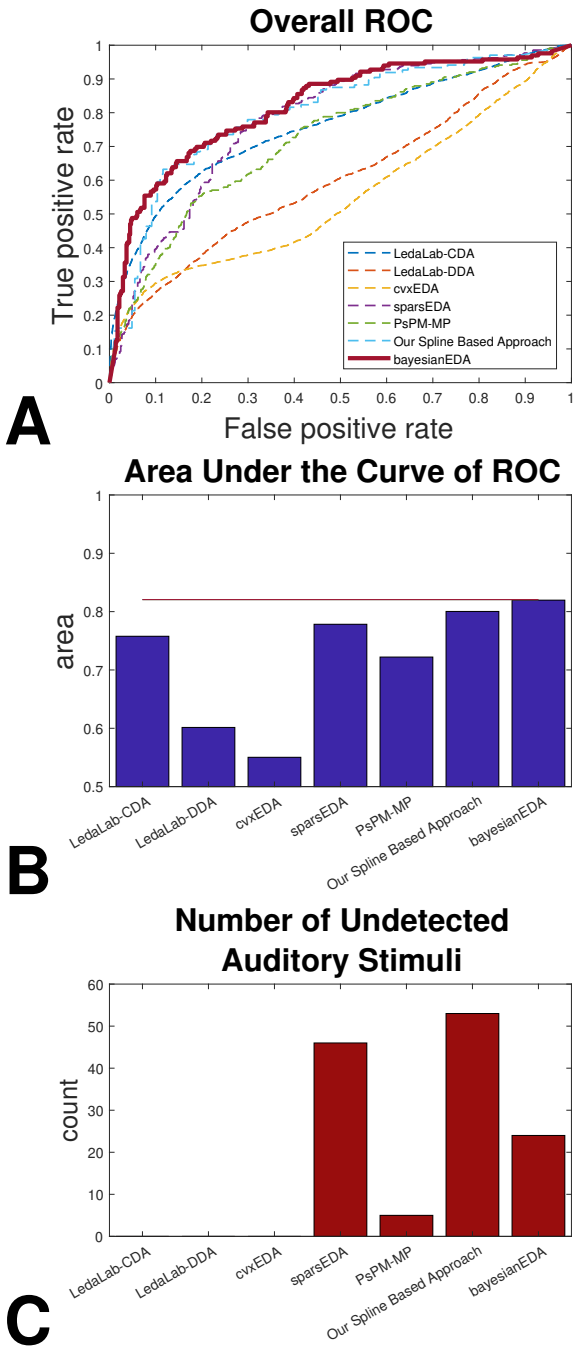

Figure 34: **Event Related SCR Detection Performance Comparison.**

the same analysis for 35 dB SNR noise level. The deconvolution result figures related to both 25 dB abd 35 dB SNR noise level are also provided in Figure 35-42. In each of the panels of these figures, i) the top sub-panel shows the ground truth for SC signal (red stars),

the reconstructed SC signal (black solid curve), the estimated tonic component (green solid curve), and ground truth for the ANS activation (gray vertical lines); ii) the bottom subpanel shows the estimated phasic component (blue solid curve), estimated ANS activation timings and amplitudes (black vertical lines) and the ground truth ANS activation (gray vertical lines).

Table 9: The Estimated Model Parameters, Estimation Errors, and the Squares of the Multiple Correlation Coefficients (R^2) for the Fits of the Simulated SC Data

Female Participant	ID	τ_r	τ_p	τ_d	$\frac{\lvert\tau_r-\hat{\tau}_r\rvert}{\tau_r}\times 100\%$	$\frac{\lvert\tau_p-\hat{\tau}_p\rvert}{\tau_p}\times 100\%$	$\frac{\lvert\tau_d-\hat{\tau}_d\rvert}{\tau_d}\times 100\%$	R^2	run time
1	12	2.4604	6.4389	96.5830	0.1210	0.0247	0.0247	0.99794	31.6575
2	15	2.6990	6.9523	104.2847	0.3778	0.0276	0.0276	0.99755	317
3	7	1.9586	5.3138	79.7069	0.1071	0.0126	0.0126	0.99755	29.5756
4	18	2.2347	5.9467	89.2011	0.1044	0.0008	0.0008	0.99688	30.5766
5	21	2.3006	6.0931	91.3963	0.2512	0.0025	0.0025	0.99363	28.2613
6	25	2.3588	6.2170	93.2545	0.0693	0.0040	0.0040	0.99789	30.4497
7	1	1.3436	3.9595	59.3931	0.0900	0.0182	0.0182	0.99970	26.1312
8	2	0.7779	2.9288	43.9316	0.0018	0.0016	0.0016	0.99830	21.3974
9	5	1.2366	3.7137	55.7056	0.0907	0.0388	0.0388	0.99888	21.5944
10	6	1.3411	3.9762	59.6431	0.0036	0.0067	0.0067	0.99985	24.9445
11	14	1.2102	3.6981	55.4716	0.0079	0.0045	0.0044	0.99976	28.5442
12	16	3.4366	8.6424	129.6358	0.4253	0.0836	0.0836	0.98704	34.1906
13	19	1.5792	4.4764	67.1456	0.1075	0.0133	0.0133	0.99814	26.3280
Male Participant	ID	τ_r	τ_p	τ_d	$\frac{\lvert\tau_r-\hat{\tau}_r\rvert}{\tau_r}\times 100\%$	$\frac{\lvert\tau_p-\hat{\tau}_p\rvert}{\tau_p}\times 100\%$	$\frac{\lvert\tau_d-\hat{\tau}_d\rvert}{\tau_d}\times 100\%$	R^2	run time
1	11	1.7232	4.7982	71.9732	0.0995	0.0126	0.0126	0.99906	25.9000
2	26	1.6579	4.6494	69.7406	0.0312	0.0082	0.0082	0.99911	29.7408
3	8	2.0574	5.5219	82.8286	0.2476	0.0358	0.0358	0.99864	30.1971
4	10	1.9103	5.2170	78.2550	0.1727	0.0125	0.0125	0.98358	28.9428
5	20	4.5459	11.0648	165.9723	0.6384	0.1242	0.1242	0.99098	32.0364
6	23	1.5452	4.4053	66.0799	0.0042	0.0006	0.0006	0.99983	29.6168
7	3	3.4207	8.5952	128.9286	0.3125	0.0767	0.0767	0.99864	32.2376
8	4	0.8937	3.1084	46.6255	0.0026	0.0004	0.0004	0.99938	23.1102
9	9	1.3568	4.0064	60.0960	0.0571	0.0042	0.0042	0.99632	26.4126
10	13	3.1736	8.0676	121.0135	0.3727	0.0195	0.0195	0.99549	31.7452
11	17	1.6754	4.6976	70.4639	0.1386	0.0304	0.0304	0.99762	26.2041
12	22	1.7660	4.8959	73.4382	0.1990	0.0414	0.0414	0.83526	24.6898
13	24	1.5524	4.4157	66.2352	0.0409	0.0174	0.0174	0.99922	28.8487

We add noise with different noise power to investigate how the proposed approach performs in terms of estimating the unknowns and reconstructed signal. We add the Gaussian

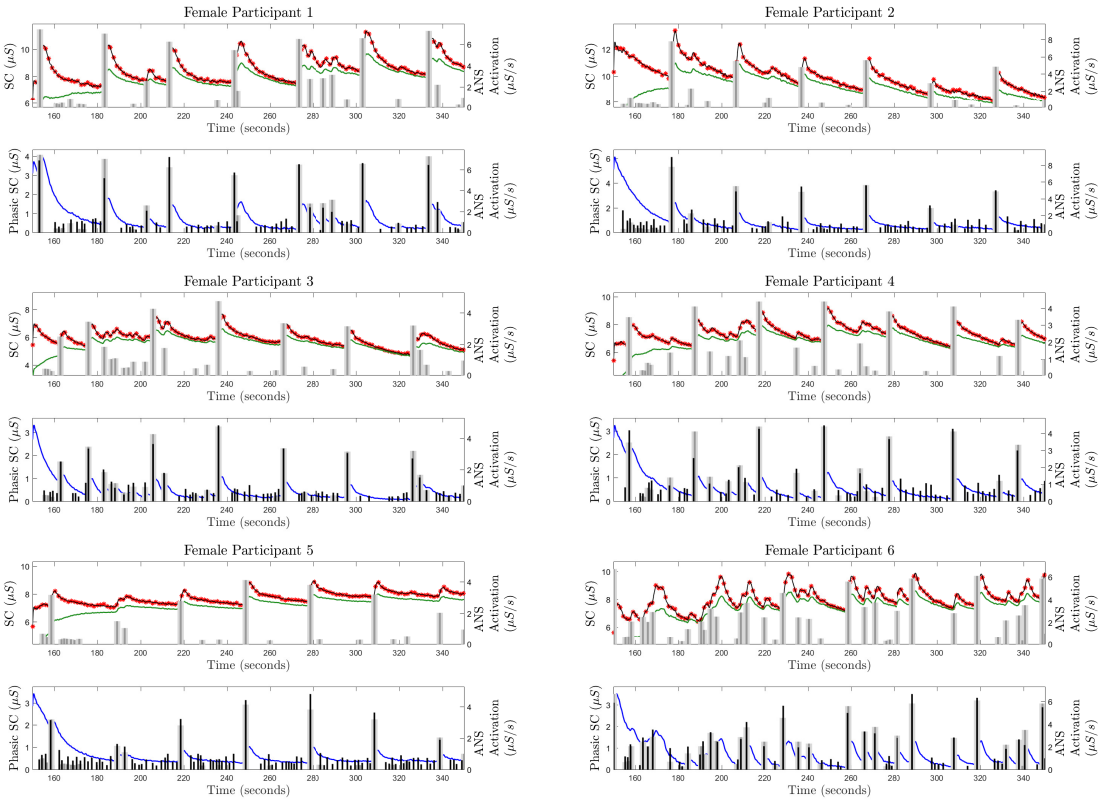

Figure 35: **Deconvolution Results From the Simulated SC Signals with 25 dB SNR for Female Participant 1 to 6.**

.

noise with different energy level to the reconstructed SC signals from the experimental study for all 26 participants and perform deconvolution to estimate the unknowns with the proposed approach. We calculate the average estimation errors of the unknowns for all participants in different noise levels. Figure 43 and 44 show how the average estimation error changes as the noise level is increased. In Figure 43, red squares, green pentagram, and blue triangles connected with solid lines denote the average percentage errors for the estimated rise times, fast decay times, and slow decay time from simulated data with SNR levels. The SNR is provided with respect to the phasic component. In Figure 44, black diamonds with the dashed lines denotes the average amplitude error of the neural stimuli from estimated data with different noise levels. We have defined the average amplitude error as $|||\tilde{\boldsymbol{u}}||_1 - ||\boldsymbol{u}||_1|/||\boldsymbol{u}||_0$, where $\tilde{\boldsymbol{u}}$ and $\boldsymbol{u}$ represent the estimated and the ground truth

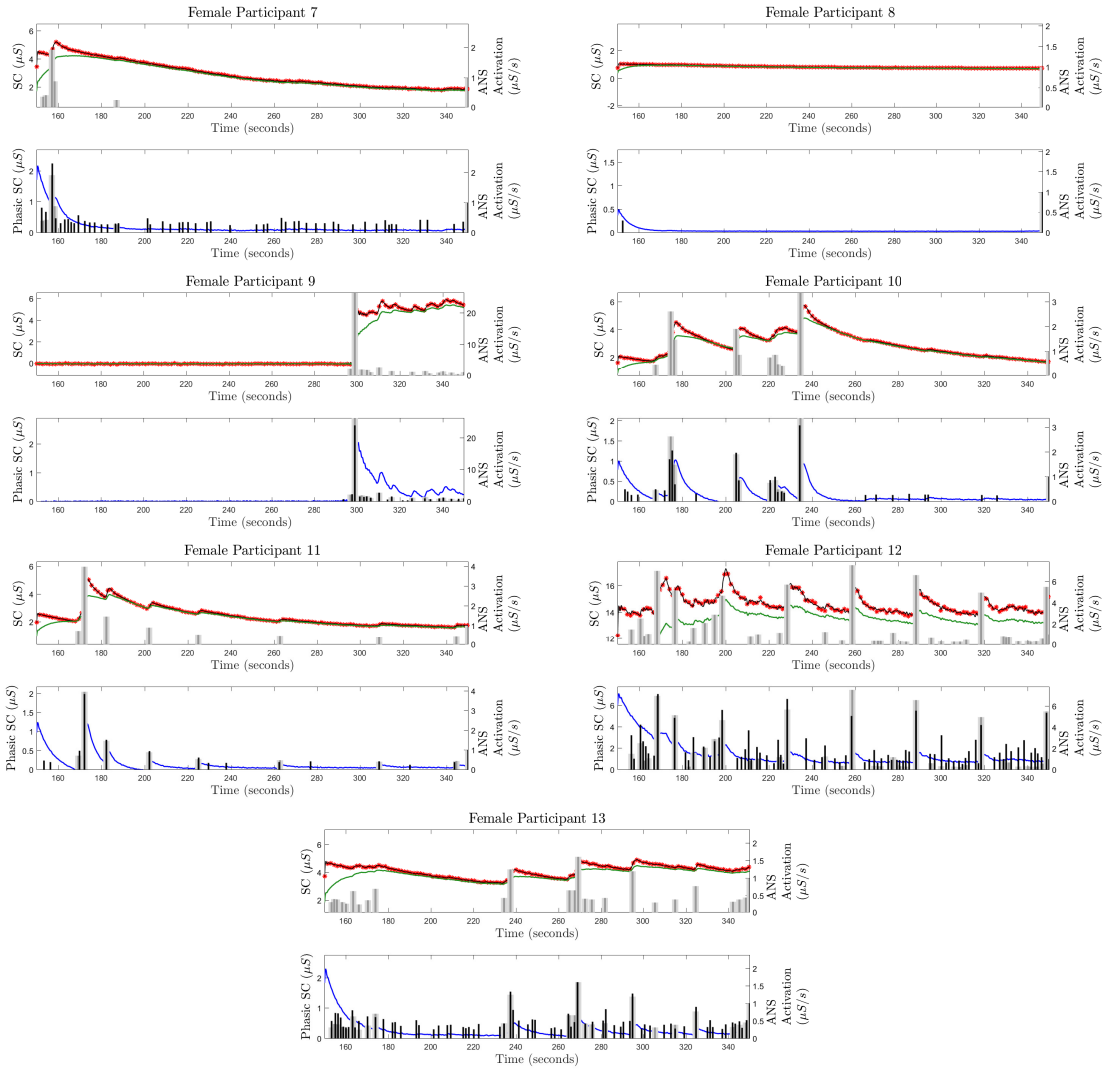

Figure 36: **Deconvolution Results From the Simulated SC Signals with 25 dB SNR for Female Participant 7 to 13.**

neural stimuli, respectively. The data is simulated using the obtained results from the all experimental data in Dataset 1. The SNR is given with respect to the phasic component. Similarly, Figure 45 shows how the reconstruction errors change in different noise levels. In Figure 45, green, blue and red dashed lines denote the RMSE for the reconstructed tonic component, phasic component and overall SC data in different noise levels. Here, the data is simulated using the obtained results from the all experimental data in Dataset 1. As noise is added to the phasic component prior to addition of tonic component, the SNR is

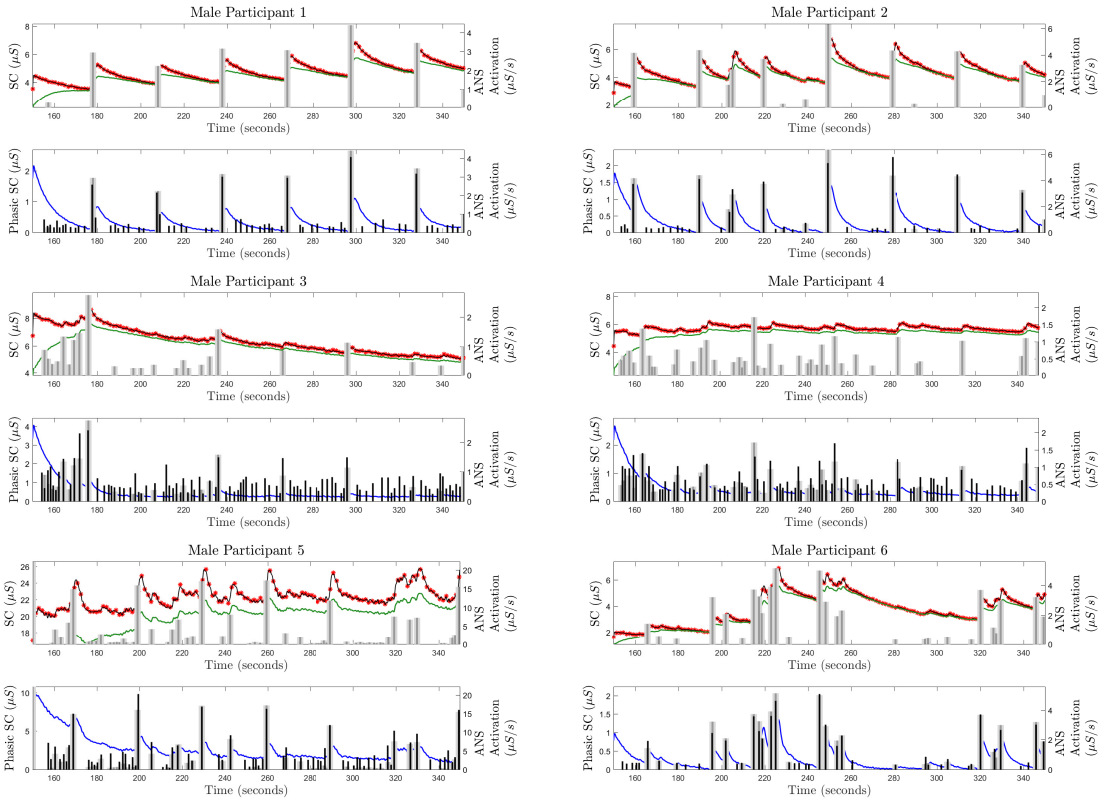

Figure 37: **Deconvolution Results From the Simulated SC Signals with 25 dB SNR for Male Participant 1 to 6.**

given with respect to the phasic component.

To empirically investigate the time complexity of the approach, we utilize the experimental data with different duration and perform deconvolution using our approach. We measure the run-time for each of the deconvolution. Figure 46 shows the distributions of the run-times in different signal lengths. According to the Figure 46, the medians of the run-times increase linearly with the increase in the signal length showing the scalability of the approach. Figure 46 shows boxplots of the run-times of the proposed approach with different signal lengths: the black dots with blue circle in the middle of each boxplot denote median, the bottom and top of each blue box are the 25th and 75th percentiles of the sample, respectively, the red markers denote a few outliers.

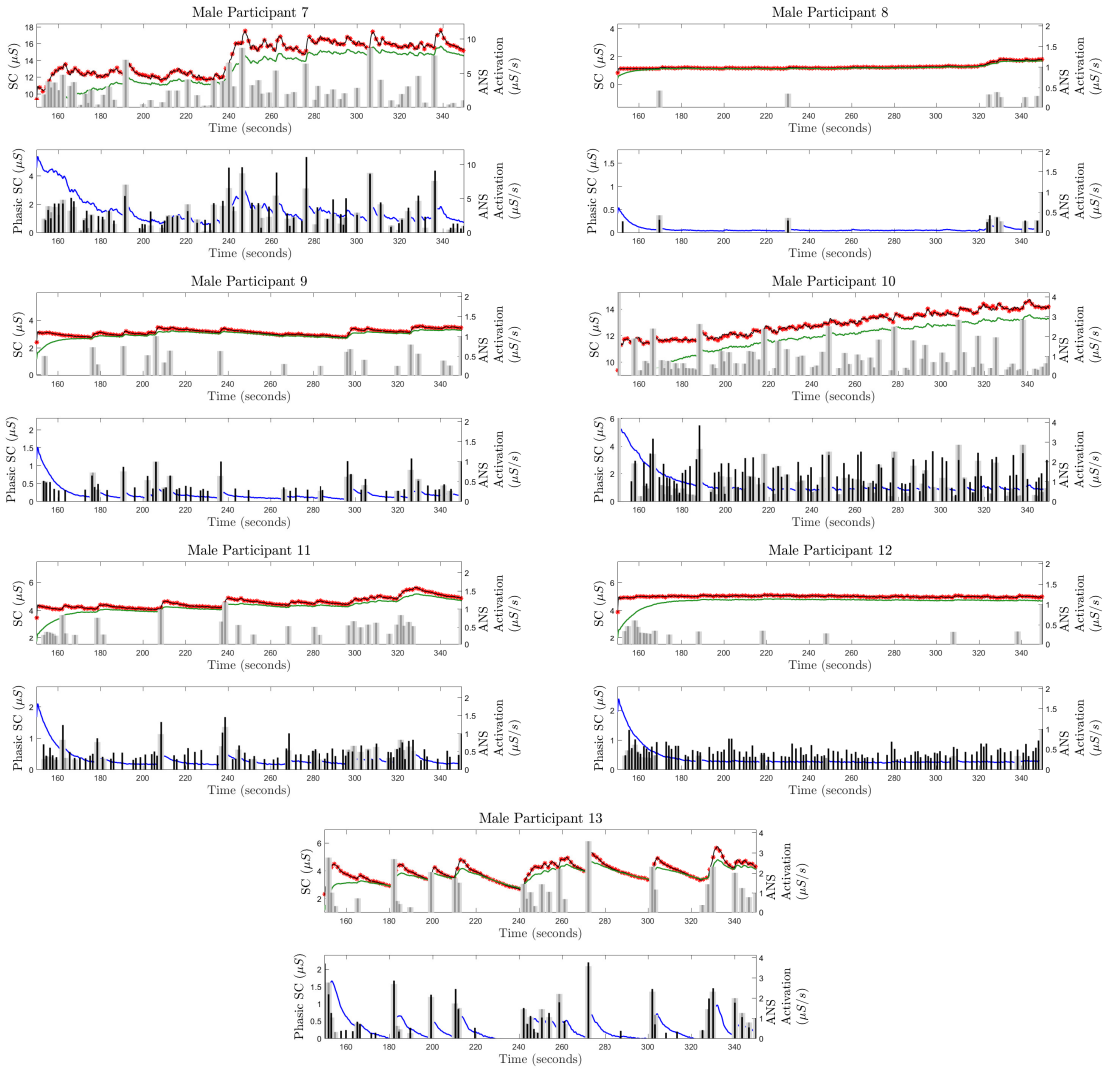

Figure 38: **Deconvolution Results From the Simulated SC Signals with 25 dB SNR for Male Participant 7 to 13.**

5.4 Discussion

Inference of the ANS activation from the SC recordings is challenging given that the underlying physiological system parameters are unknown. The derived EM approach maximizes the complete data log-likelihood. The complete data log-likelihood has many degrees of freedom, i.e., the constraints on variables to be optimized is lower than the number of

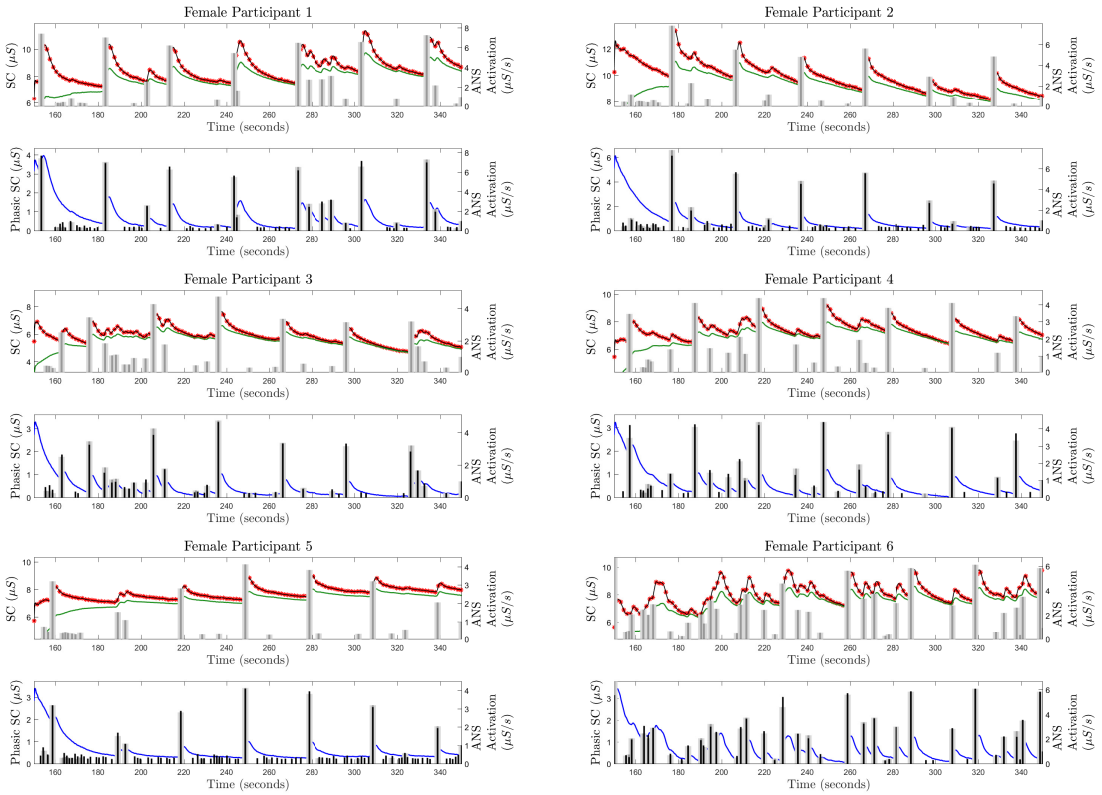

Figure 39: **Deconvolution Results From the Simulated SC Signals with 35 dB SNR Female Participant 1 to 6.**

variables. In other words, there exist many solutions for the unknowns that can closely approximate the sampled signal. The use of a comprehensive state-space model and the removal of cubic spline function based model reduces the number of unknown variables in the optimization. For example, the number of cubic spline functions needed to model slow varying component of 200 seconds is 39, as pointed out in our previous work [41]. On the other hand, the proposed comprehensive model requires only one parameter instead of multiple cubic spline function parameters to model the slow varying component. Furthermore, we consider probabilistic sparsity priors motivated by physiology on the ANS activation along with the Gaussian priors on the physiological system parameters. Last but not the least, we also enforce inequality and equality constrains on the state-space model parameters by trial and error. The constrains $\tau_p > 2\tau_r$, $\tau_d > 15\tau_p$, and $\eta = 0.5$ worked best for us for the

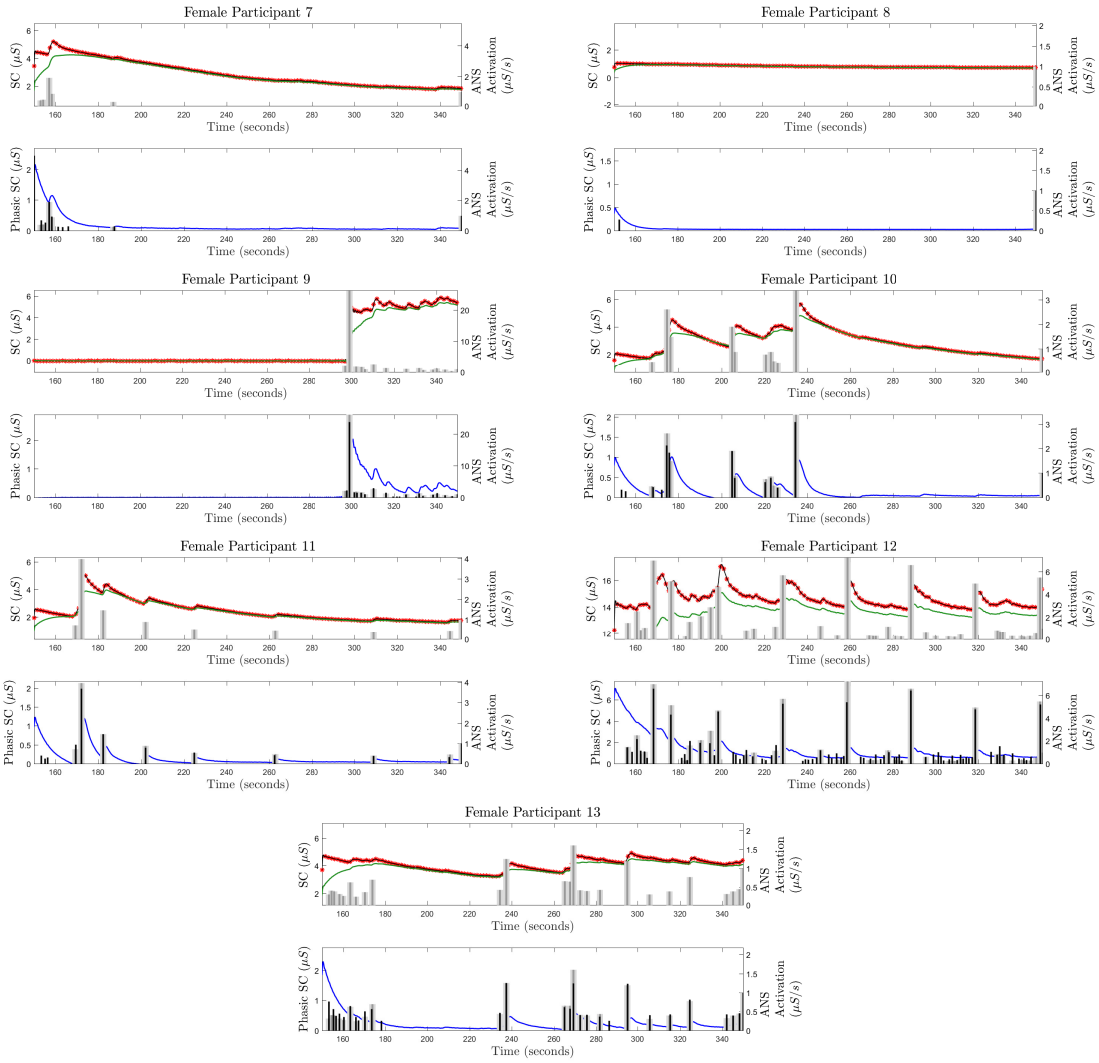

Figure 40: **Deconvolution Results From the Simulated SC Signals with 35 dB SNR for Female Participant 7 to 13.**

dataset we have analyzed.

The complete data log-likelihood that is optimized by the EM approach might suffer from non-convexity and there is a potential risk that the solution may end up in different locations for different initial values. To test that, we run our EM approach for multiple random initializations of the physiological system parameters. Based on the simulated and the experimental datasets we have analyzed, we have observed that the solution for a given SC signal always converge to one location no matter what initial value has been

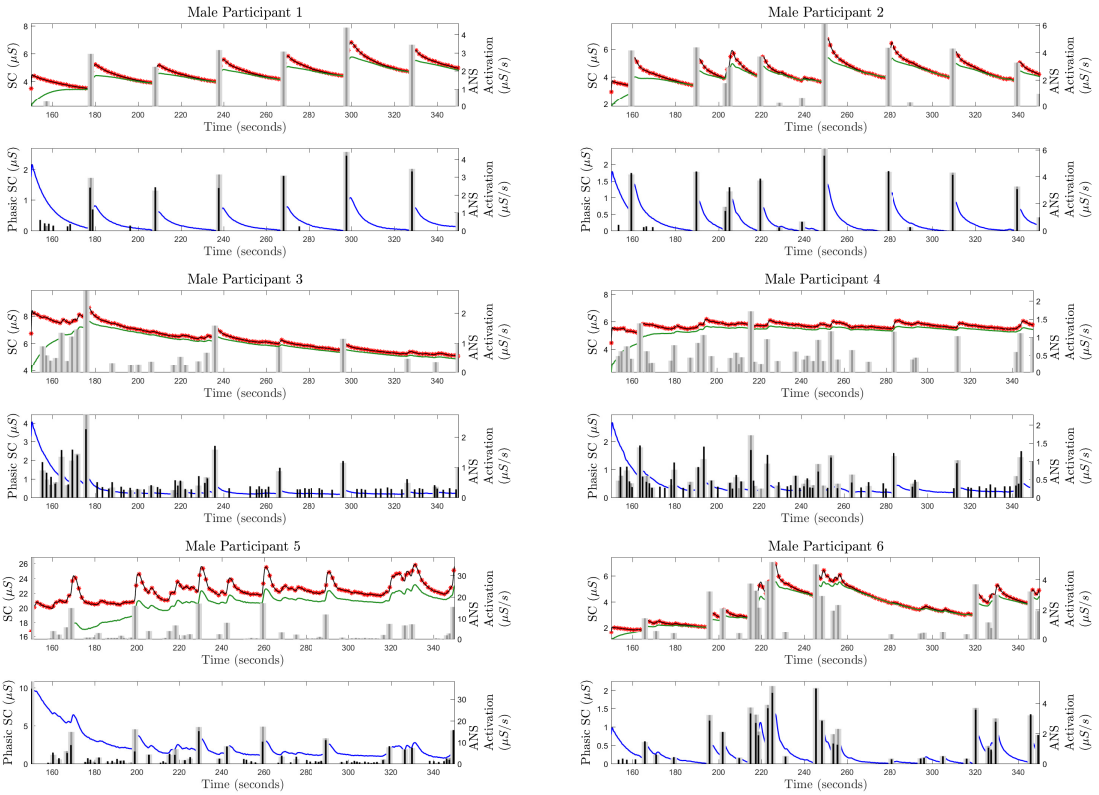

Figure 41: **Deconvolution Results From the Simulated SC Signals with 35 dB SNR for Male Participants 1 to 6.**

selected. Therefore, we decided to only run our approach for one random initialization of the physiological system parameters in this study, unlike our previous approaches where we have used multiple random initializations and selected the solution that satisfies the selection criteria [52, 54, 41].

Figure 29-32 show that the estimations of the initial states as well as the states for about 20-30 seconds can be erroneous. After 20-30 seconds, the state-estimation visually seems reasonable. This erroneous estimation happens because the Kalman filter in the FIS needs a few samples to begin to follow the signal. Therefore, the estimations during the initial few samples can be erroneous. Because of this erroneous estimation of the initial state, the R^2 estimation for male participant 12 became very low compared to other participants.One straightforward way to deal with this is to consider 20-30 seconds of measured

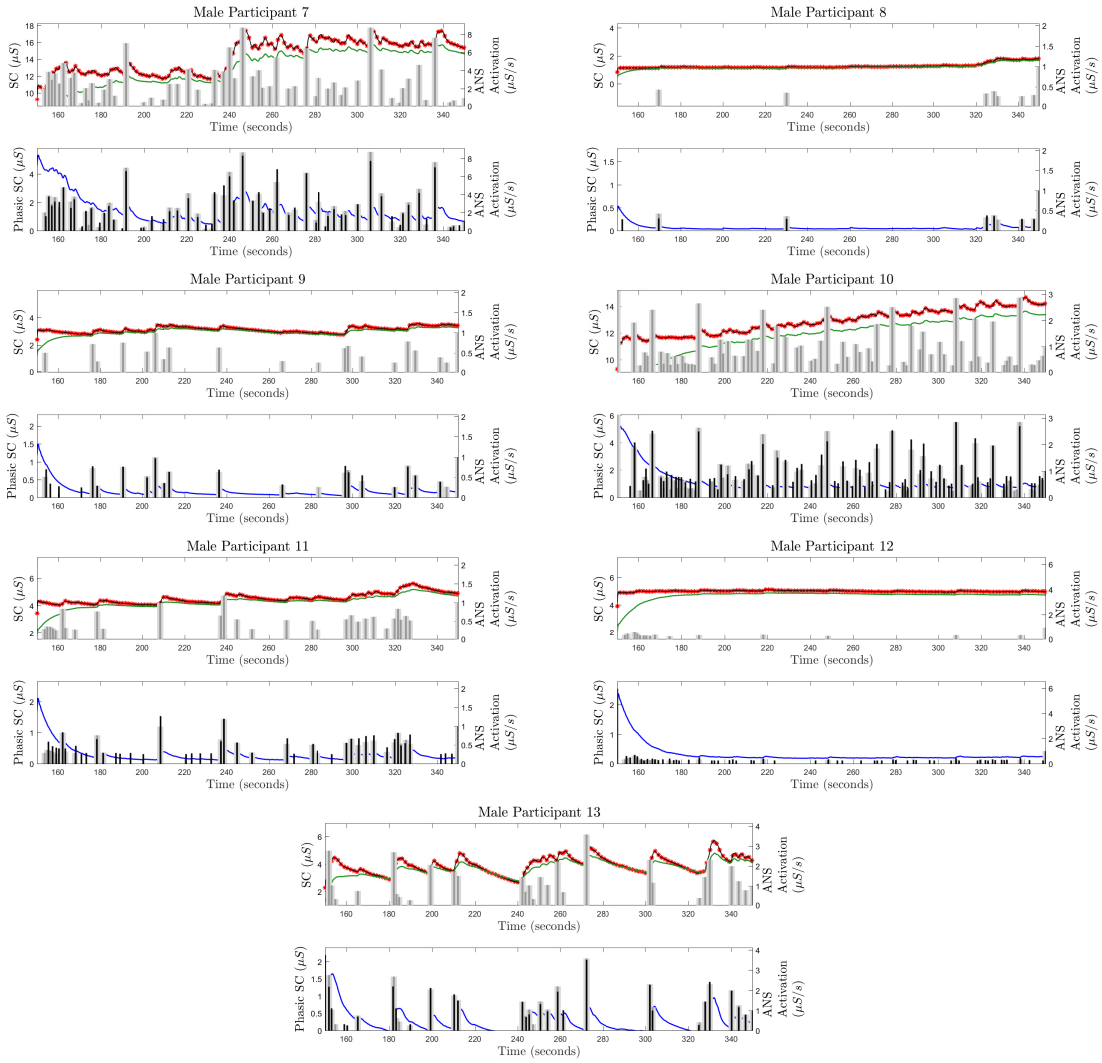

Figure 42: **Deconvolution Results From the Simulated SC Signals with 35 dB SNR for Male Participant 7 to 13.**

signal padded in the beginning. After performing deconvolution in the padded signal, results corresponding to the initial 20-30 seconds can be removed.

Figure 34-A shows that our bayesianEDA has the best ROC curve than all the previous approaches including our previously proposed spline based approach [41]. Figure 34-B shows that our bayesianEDA has the maximum AUC value corresponding ROC curves. Next best ones are our spline based approach (AUC = 0.8003) and sparsEDA (AUC = 0.7783). The ROC curves and AUC values are generated based on only the classification

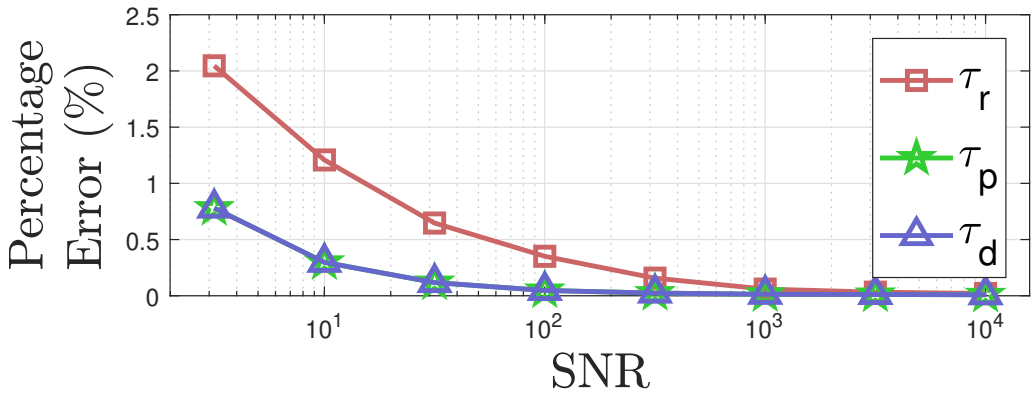

Figure 43: **Noise Levels vs. Estimation Accuracy of The Model Parameters.**

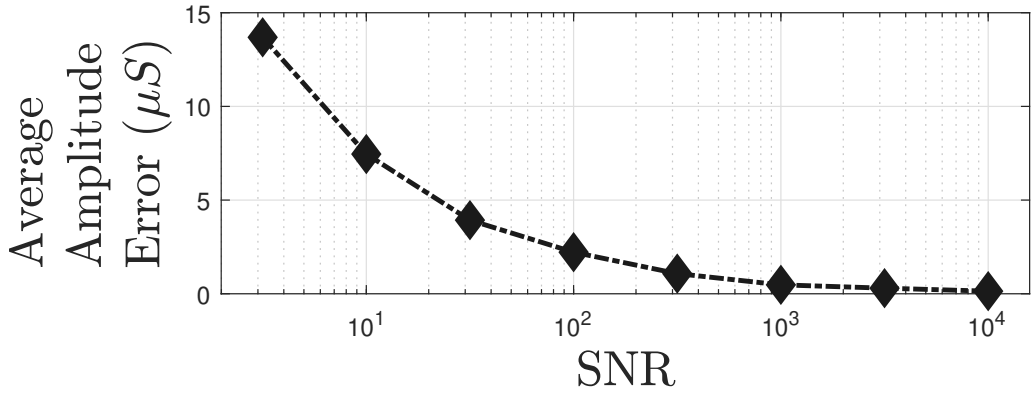

Figure 44: **Average Amplitude Error of Estimated ANS Activation in Different Noise Levels.**

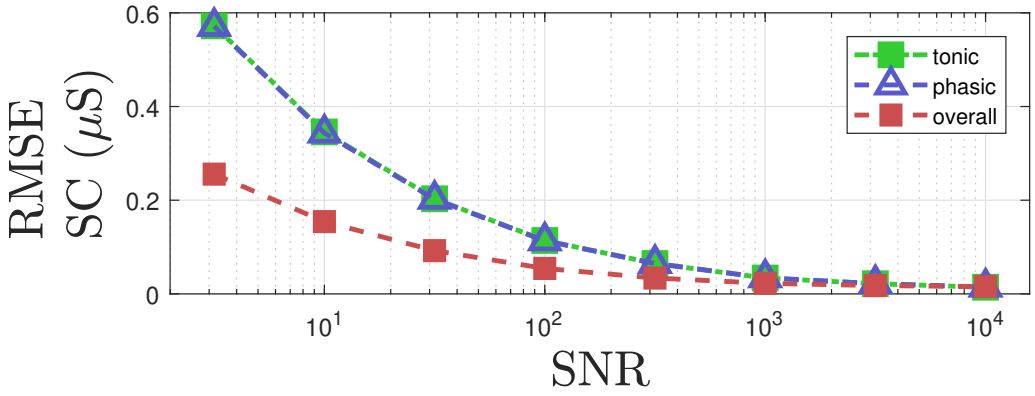

Figure 45: **Root Mean Square Error (RMSE) of the Reconstruction for SC signal and Corresponding Components with Respect to the Ground Truth.**

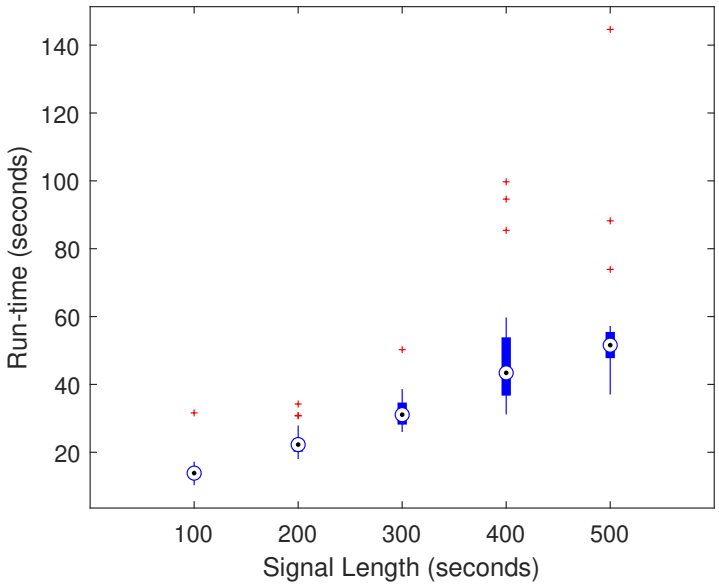

Figure 46: **Run-time vs Signal Length.**

ability between the event related and non-event related SCRs among the ones those are only detected by each methods. However, there is a possibility that an algorithm have over sparsified the solution and missed many smaller but event related SCRs. Therefore, we further calculate for how many of auditory stimulation no SCR was detected. Figure 34-C shows, our spline previous approach is missing most of the auditory stimulation (53) and sparsEDA [24] is missing second most number of the auditory stimulation (46). On the other hand, LedaLab-CDA [29], LedaLab-DDA [21], and cvxEDA [23] are not missing any of the auditory stimulation. One should note that sometimes a participant might not show any SCR in response to an auditory stimulus. Therefore, a fraction of the number of the undetected auditory stimulation can be attributed to the participants physiology and rest of it can be attributed to the algorithm itself. Which means LedaLab-CDA, LedaLab-DDA, and cvxEDA detect noise spikes as SCRs in the places where the participants does not have an SCR response. From our visual investigation, we see that some of the participants does not have any SCR in response to the auditory simulation. Please see experimental results for Female participant 7, 8, 10, 11, 13 and Male participant 8 in Figure 30 and 32. Our

approach is not detecting total of 24 auditory stimuli and most of them can be attributed to no SCR response from the participant. On the other hand, sparsEDA and our spline based approach have missed 46 and 53 number of stimuli, respectively, resulting in an overly sparse solution.

The presence of noise may lead to inaccurate estimates of ANS activations. Although we have incorporated a GCV based approach, the noise filtration also depends on the selected observation noise variance, σ_ν^2. For the experimental study, we have selected $\sigma_\nu^2 = 1 \times 10^{-8}$. This value is working well along with the GCV for balancing between discarding the noise and capturing the process. We have kept the value of σ_ν^2 for the simulated study. Our results show that it is capturing more spikes than the ground truth for heavy noise level. As pointed out in [105], increasing the noise variance σ_ν^2 will lead to a much smoother estimate with a lower number of spikes. For most of the cases, GCV could discard most of the spikes related to noise. Because, the corresponding selected σ_ν^2 are within the reasonable range for GCV to obtain a balance. Therefore, for GCV to balance the noise spike, a reasonable choice of σ_ν^2 is required. However, for some cases it is challenging to find such a reasonable value for GCV. Higher values of σ_ν^2 may result in some of the SCRs undetected. Therefore, we select a relatively small value of σ_ν^2 such that none of the SCRs remain undetected. As most of the detected noise spikes are relatively smaller than the spikes related to the SCRs, application tailored post-processing (e. g. hard/soft thresholding) can remove most of the noise spikes.

The computational complexity of the deconvolution approach is $\mathcal{O}(K)$ as shown in [105]. Furthermore, our empirical investigation also shows run time scales linearly with the number of sample as shown in Figure 46. These shows the feasibility of implementing such approaches in the low power wearable medical devices for edge computation. This scalable implementation has been possible with the proposed comprehensive state-space model. Further optimization can be performed by obtaining the physiological system parameters for a smaller segment and perform the E-step for the longer segments. During a day of recording,

parameters can be updated a few times by running the EM, and these parameters can be used to estimate the ANS activation using only E-step. A real-time implementation can be done with only running the Kalman filter in iterative manner in the FIS after estimating the system parameters for a shorter segment. As Kalman filters are very cheap in terms of computation power, the proposed approach opens up the possibility of performing ANS activity inference in the edge device instead of running it in the cloud facilitating low network traffic and user privacy.

The obtained ANS activities from the single channel SC recording can be used to track the cognitive arousal state of an individual [10, 44, 106]. One of the future goal is to extend this approach for multi-channel SC recording and the nonlinearity of the model for more robust inference in presence of noise which will lead to more reliable inference of individual arousal level similar to our previous study in [54]. For further accurate estimation of emotional arousal, we intend to utilize the inferred ANS activity from SC recording with our approach and to combine with other physiological signals similar to [107, 108, 109, 110, 47, 111, 112]. The proposed new model as well as the scalable ANS inference approach has enabled us to design a scalable control architecture to regulate the arousal level similar to the proposed framework in [113, 114, 115, 116].

6 Evaluation of Adaptive and Bayesian Filters for Artifact Removal from Electrodermal Activity Leveraging Noise Source Reference

6.1 Overview of Electrodermal Activity and Importance of Motion Artifact Reduction

The phrase "electrodermal activity" (EDA) was introduced in 1966 for designating any electrical activity that is measured from the skin electrically [41, 9]. Since its first observation in the 1880s [9], EDA has been widely used in physiology and psychophysiology studies as the information it contains has a relationship with sympathetic nervous system (SNS) activation. As a part of the autonomic nervous system (ANS), SNS is responsible for the fight-or-flight response mechanism in response to a stimulus that the human brain categorizes as a threat to survival. When such an emotional stress stimulus is perceived, the brain stimulates sweat glands via ANS depending on the psychological and physiological demands. Consequent secretions of salty sweat glands increase the skin conductance (SC)–a measure of EDA–by increasing the number of electrical charge carrier ions. SC measurements contain rich information regarding SNS activation. Therefore, evaluation of SC will lead to effective monitoring of emotional arousal fluctuations [10].

Efficient EDA analysis along with SNS activation inference has a wide range of applications including major depression detection [117], pain detection [118], cognitive stress tracking [10], tracking wakefulness [119], etc. Furthermore, abnormal regulation of EDA seems to be a reliable feature of depression and a valid marker of suicidal risk measurement [120]. Azgomi et al. [121] proposed a closed-loop wearable machine interface architecture to regulate arousal utilizing electrodermal activity as the observation. The proposed method comprises of identification of ANS activation utilizing EDA deconvolution [53, 52, 54], the emotional stress estimation [10, 44, 83], and finally closing the loop [113, 113] to maintain

the corresponding emotional state within a desired range. However, in ambulatory settings, the recordings can have artifacts due to motion or other noise sources. For effective implementation of such a regulation scheme, such artifact reduction is a prerequisite.

The noninvasive nature of many biomedical sensors has led to many measurement technologies for ambulatory health monitoring. The most popular modality of biomedical sensors that are currently being deployed in many consumer devices along with wearable devices includes cardiac sensors (e.g., electrocardiogram (ECG) electrodes and photoplethysmogram (PPG) optodes), skin temperature (SKT) sensors, muscle activity sensors (e.g. electromyogram (EMG) electrodes), etc. [11, 12]. Additionally, many low-power inertial sensors such as accelerometers, gyroscopes, and magnetometers are also deployed in wearable devices to monitor user activity [122]. In the past few decades, numerous research efforts have led to the successful implementation of PPG signal analysis for wearable implementation, with the goal of continuous cardiac health monitoring. This effort has led to applications ranging from daily heart rate monitoring [123] to efficient detection of atrial fibrillation to prevent heart stroke [124]. As motion can corrupt signal recordings by PPG, to endeavor a successful day-to-day monitoring, many researchers worked on the prerequisite signal processing pipelines for motion artifact removal [124]. In other contexts, there are many studies proposing various signal processing techniques to remove motion artifacts from other biomedical signals such as ECG [125, 126], electroencephalogram (EEG) [127], functional near-infrared spectroscopy (fNIRS) etc. The motion artifact removal scheme is not only important for deploying sensors in consumer devices but also it is an important preprocessing step for analysis in scientific research. Among the popular approaches, inertial sensor measurement-based motion reference has been extensively utilized to monitor activity.

Adaptive filters have been extensively studied to remove motion artifacts from various biomedical signals, including ECG [125, 126], PPG [128, 129], EEG [130, 131], fNIRS [132], etc. However, to the best of our knowledge, there has not been any study yet that evaluates adaptive filters for motion artifact removal from electrodermal activity utilizing reference

information from inertial sensors. Despite the fact that EDA is one of the most important potential candidates for next-generation wearable health monitoring [13], the amount of research performed on EDA signals is relatively limited compared to cardiac signals. Especially, very little research has been carried out to reduce the artifacts in electrodermal activity. There are a few works that investigate different methods for artifact detection, including semisupervised [133] and unsupervised [134] machine learning approaches. Moreover, supervised machine learning-based [135] as well as wavelet-based heuristic [136] techniques are investigated to correct artifacts. However, the fact that the artifact can be represented as the linear/nonlinear transformation of the accelerometer information and the possibility of modeling such transformation with adaptive filters is yet to be investigated. Additionally, some of the fluctuations that are present in the SC are related to respiration and may not be directly related to ANS activation. In 2003, Schneider et al. [137] reported the evidence of misinterpretation of experimental observations because of irregular respiration-related SC activation. Hence, they proposed a rule-based approach to identify such cases. Later in 2019, Lee *et al.* [138] utilized a similar rule-based approach to detect and later remove the respiration-related noise from SC data based on PPG derived respiration reference signal. However, a more systematic approach is required to identify and isolate such activations, which can be referred to as respiration-related noise.

Therefore, in this study, we evaluate linear adaptive filters as well as nonlinear Volterra adaptive filters that take the three accelerometers as the reference signal to model the artifacts in a multirate manner. We utilize a publicly available dataset and simulated artifacts to evaluate four types of adaptive filters. Furthermore, we perform experiments for inducing motion artifacts during SC data collection while recording the motion information with a three-axis accelerometer sensor. We evaluate the adaptive filtering performance of removing motion artifacts utilizing the experimental data. We also collect respiration reference signals for the identification of respiration-induced noise.

6.2 Methods

6.2.1 Experiment

In this study, we experimented to collect motion artifact corrupted SC signals with the noise reference. This project has been reviewed and approved by the University of Houston Institutional Review Board (IRB). We have collected data from two participants with multiple trials for each participant. Participants were familiar with all the signals and sensors that are considered in the experiment. In the first scenario of data collection, the participants were suggested to observe the SC signals on the monitor in real-time, those will be collected and suggested to perform 'hand waving' as they want so that some motion artifact is generated in the observed signal. In the second scenario, the participants were suggested to do 'in-place jogging' while also observing the recorded signal in real-time. We perform the data collection with the Biopac MP160 system. We measure the SC signal between the proximal phalanx of the index finger and the ring finger of the nondominant hand. For measuring data from the fingers, we used two Shimmer reusable SC electrodes. We have also attached Biopac SC wet electrode to the thenar eminence and hypothenar eminence for SC data collection. Both dry and wet electrodes are then attached to Biopac BioNomadix wireless BN-PPGED amplifiers/transmitters with BN-EDA-LEAD2 leads. For the motion reference collection, we placed the Biopac TSD109C3 three-axis accelerometer on the ring finger SC electrode. Customization of the TSD109C3 accelerometer is performed to be able to use two Biopac BN-GONIO wireless transmitters for three-axis wireless data acquisition. The customization is carried out by Biopac Inc. Furthermore, a photoplethysmogram (PPG) sensor has been placed on the distal phalanx of the ring finger in the nondominant hand. Additionally, we collected the three-lead electrocardiogram (ECG) signals and the respiration signal with the Biopac BioNomadix wireless BN-RSPEC amplifier/transmitter. We record all signals at 2 kHz sampling frequency. Figure 47 shows a brief overview of the sensor placements. Figure 47 shows (a) a participant is wearing a respiration belt as well

as the ECG leads connected to the electrodes; (b) and SC sensor, accelerometer, and PPG sensor placements on the participants nondominant hand.

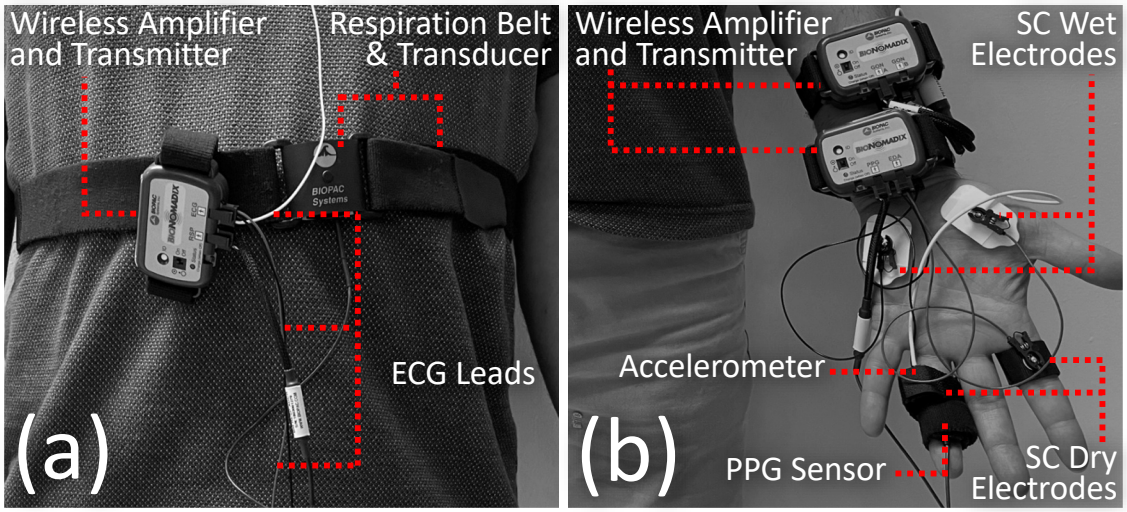

Figure 47: **An Overview of the Experimental Setup.**

6.2.2 Additional Publicly Available Dataset

In addition to the experimental dataset, we also use the dataset including the SCRs related to loud sounds [57] with some simulated noise. Bach *et al.* [30] designed this experiment for modelling event-related SCRs. The dataset includes SC data measurements from the thenar/hypothenar of the nondominant hand, the middle phalanx of the dominant second and third finger, and the medial plantar surface of the nondominant foot for each of the 26 participants. Here we only utilize the SC recordings from the thenar/hypothenar of the nondominant hand participants for single channel analysis. The details of the experiments and the dataset are provided in [30].

6.2.3 Wiener Filter

We briefly discuss the basics of adaptive filters that we utilize for the evaluation of artifact removal performance. In this study, we consider the *finite impulse response* (FIR) adaptive filters. First we describe the ideal case of the filtering and then from there we will

derive different adaptive filters with appropriate assumptions for practical implementation. The most ideal case is known as *Wiener filter* (WF). A WF has two inputs, a desired signal $d[k]$ and noise reference signal $n[k']$ [139]. Here, we assume that the $d[k]$ and $n[k']$ can have different sampling frequency for multi-rate formulation and the sampling frequency of the noise source $n[k']$ is higher than the desired signal $d[k]$. Let the sampling frequencies are F_d and F_n, respectively. We also assume that the sampling ratio $M = F_n/F_d$ is an integer. If the filter at k^{th} is defined with the vector $\mathbf{w}[k]$ where $w[k, k']$ is the k'^{th} element in the filter at k^{th} time step, then the filter output $z[k]$ can be written as follows,

$$z[k] = \mathbf{w}[k]^\top \mathbf{x}[k],$$

where $\mathbf{x}[k] = [\, n[Mk - L + 1]\ n[Mk - L + 2]\ \cdots\ n[Mk - 1]\ n[Mk]\,]^\top$. Here, L is the length of the FIR filter. The error vector can be represented as

$$e[k] = d[k] - z[k]. \tag{84}$$

The objective function in adaptive filtering is the mean square error (MSE) is represented as follows,

$$\begin{aligned} J_{\mathbf{w}} &= \mathbb{E}\{(e^2[k])\} \\ &= \mathbb{E}\{(d[k] - z[k])^\top (d[k] - z[k])\} \\ &= \mathbb{E}\{d^2[k]\} - 2\mathbf{w}[k]^\top \mathbb{E}\{d[k]\mathbf{x}[k]\} \\ &\qquad + \mathbf{w}[k]^\top \mathbb{E}\{\mathbf{x}[k]\mathbf{x}[k]^\top\}\mathbf{w}[k]) \\ &= \mathbb{E}\{d^2[k]\} - 2\mathbf{w}[k]^\top \mathbf{p}[k] + \mathbf{w}[k]^\top \mathbf{R}[k]\mathbf{w}[k]. \end{aligned} \tag{85}$$

Here $\mathbf{p}[k]$, and $\mathbf{R}[k]$ represent the cross-correlation $\mathbb{E}\{d[k]\mathbf{x}[k]\}$ and auto-correlation of $\mathbb{E}\{\mathbf{x}[k]^\top \mathbf{x}[k]\}$, respectively. For WF, $\mathbf{w}[k]$, $\mathbf{p}[k]$, and $\mathbf{R}[k]$ are considered as constant for all k time points with the assumption that $d[k]$ and $\mathbf{x}[k]$ are jointly wide-sense stationary

(WSS). Therefore, the sample indexed k can be dropped for the case of WF and can be written as $\mathbf{w}$, $\mathbf{p}$, and $\mathbf{R}$. In order to minimize the MSE, we need to find the minima of the function in (85). Therefore, we take the derivative with respect to $\mathbf{w}$ and set it to zero to obtain the optimum filter coefficient vector $\mathbf{w}_o$,

$$\begin{aligned} \nabla_{\mathbf{w}} J_{\mathbf{w}} &= -2\mathbf{p} + 2\mathbf{R}\mathbf{w} = 0 \\ \Rightarrow \mathbf{w}_o &= \mathbf{R}^{-1}\mathbf{p}. \end{aligned} \tag{86}$$

However, in practical settings, $\mathbf{R}$ and $\mathbf{p}$ are not known. Therefore, some approximation or good estimates of $\mathbf{R}$ and $\mathbf{p}$ is required. Mostly, different approximations of these lead to different types of adaptive filters which we will discuss in later sections.

6.2.4 Least Mean Squares (LMS) Adaptive Filter

For the least mean square (LMS) filter, at k^{th} the approximations are carried out as follows,

$$\begin{aligned} \hat{\mathbf{R}}[k] &= \mathbf{x}[k]\mathbf{x}[k]^\top \\ \text{and } \hat{\mathbf{p}}[k] &= d[k]\mathbf{x}[k]. \end{aligned}$$

We plug in these approximations in (85) to obtain the approximation of MSE for k^{th} sample, $J_{\mathbf{w}}$,

$$\hat{J}_{\mathbf{w}}[k] = d^2[k] - 2\mathbf{w}[k]\hat{\mathbf{p}}[k] + \mathbf{w}[k]^\top \hat{\mathbf{R}}[k]\mathbf{w}[k]$$

Utilizing this, the filter update equation for k^{th} time stamp is as follows,

$$\mathbf{w}[k+1] = \mathbf{w}[k] - \alpha \nabla_{\mathbf{w}} \hat{J}_{\mathbf{w}}[k]. \tag{87}$$

Here α corresponds to the step size. After simplification, the final equation becomes as follows,

$$\mathbf{w}[k+1] = \mathbf{w}[k] + \alpha e[k]\mathbf{x}[k]. \tag{88}$$

6.2.5 Recursive Least Square (RLS) Adaptive Filter

For the recursive least squares (RLS) filter, at k^{th} the approximations are carried out as follows,

$$\hat{\mathbf{R}}[k] = \sum_{i=0}^{k} \gamma^{(k-i)} \mathbf{x}[i]\mathbf{x}[i]^\top$$
$$\text{and } \hat{\mathbf{p}}[k] = \sum_{i=0}^{k} \gamma^{(k-i)} d[k], \mathbf{x}[k],$$

where γ is called forgetting factor and usually selected between $0 \leq \gamma \leq 1$. If we set $\gamma = 0$, then the corresponding RLS filter is as same as the LMS filter. We plug in these approximations in (85) to obtain the approximation of MSE, $J_{\mathbf{w}}$,

$$\hat{J}_{\mathbf{w}}[k] = d^2[k] - 2\mathbf{w}[k]\hat{\mathbf{p}}[k] + \mathbf{w}[k]^\top \hat{\mathbf{R}}[k]\mathbf{w}[k].$$

We set the derivative $\nabla_{\mathbf{w}[k]} \hat{J}_{\mathbf{w}}[k] = 0$ and find the filter update equation for k^{th} is as follows,

$$\mathbf{w}[k] = \hat{\mathbf{R}}^{-1}[k]\hat{\mathbf{p}}[k] \tag{89}$$

However, this equation is computationally expensive. An iterative update can be done based utilizing the weights calculated in the last step. After simplification, the update equation can be written as follows [139],

$$\mathbf{w}[k+1] = \mathbf{w}[k] + e[k]\mathbf{S}_D[k]\mathbf{x}[k], \tag{90}$$

where,

$$\begin{aligned}\boldsymbol{\psi}[k] &= \mathbf{S}_D[k-1]\mathbf{x}[k],\\ \boldsymbol{\phi}[k] &= \frac{\boldsymbol{\psi}[k]}{\lambda + \boldsymbol{\psi}[k]},\\ \text{and } \mathbf{S}_D[k] &= \frac{1}{\lambda}\left[\mathbf{S}_D[k-1] - \boldsymbol{\psi}[k]\boldsymbol{\phi}[k]^T\right].\end{aligned}$$

During the initialization, set $\mathbf{S}_D(0) = \delta\mathbb{I}$ where δ can be the inverse of an estimate of the input signal power. $\mathbf{x}(0) = \mathbf{w}(0) = [0\ 0 \cdots 0]$, and evaluate.

6.2.6 Second Order Volterra Adaptive Filters (LMS and RLS)

For obtaining a n^{th} order volterra LMS/RLS filter, we need to just merely need to populate the reference signal vector with the non-linear terms for each iterations and update the adaptive filter coefficient vector length accordingly. For example, for 2^{nd} the reference signal is as follows,

$$\begin{aligned}\mathbf{x}[k] &= [\mathbf{x}_{\text{L}}[k]^\top\ \mathbf{x}_{\text{NL}}[k]^\top]^\top\\ \text{where, } \mathbf{x}_{\text{L}}[k] &= [\,n[Mk-L+1]\ n[Mk-L+2]\ \cdots\ n[Mk]\,]^\top\\ \text{and } \mathbf{x}_{\text{NL}}[k] &= \mathbf{vec}(\mathbf{x}_{\text{L}}[k]\mathbf{x}_{\text{L}}[k]^\top)\end{aligned}$$

Here '**vec**' denotes the matrix to vector conversion operation. Now the corresponding adaptive filter length is $L' = L + L^2$, i.e., there are L' number of elements in vector $\mathbf{w}[k]$ for each time steps. All the other steps of adaptive filter is same as the linear cases. We define $V2-LMS$ and $V2-RLS$ to refer to 2^{nd} order Volterra RLS and LMS filter.

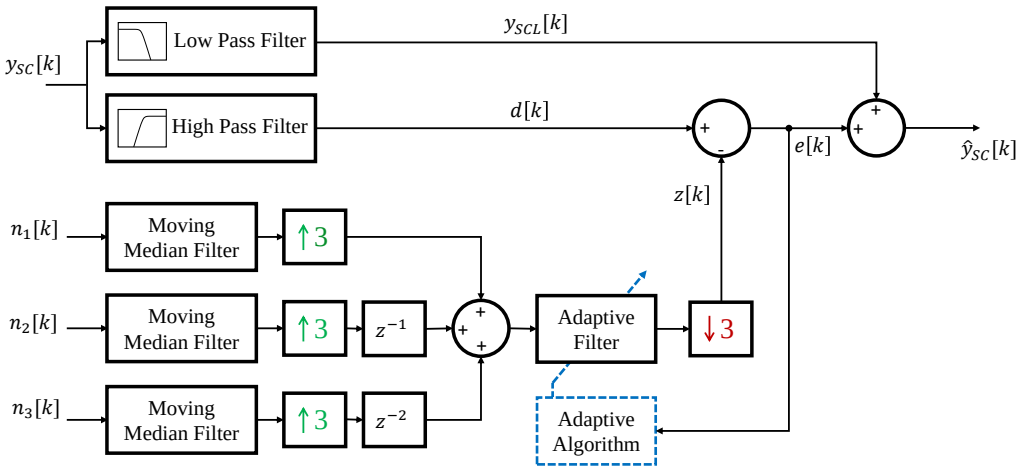

Figure 48: **An overview of Proposed Adaptive Filtering Scheme for Motion Artifact Reduction from SC Recording with Accelerometer Readings as the Noise Source Reference.**

6.2.7 Artifact Reduction from Skin Conductance Signal with Accelerometer As Noise Reference

A part of artifact contamination on the skin conductance signal is related to the movement of the sensors. The motion information can be recorded in many different forms. One of the popular ways is to utilize a three-axis accelerometer. A three-axis accelerometer records data for three different axes. Therefore, we have three different noise reference channels corresponding to three axes. For the discretized recordings, we combine the sample streams from these three signals into one discretized sample stream. Now the new stream has a frequency that is three times the sampling frequency for the single channel. We perform adaptive filtering on the recorded SC signal while considering the accelerometer recording as the noise reference. SC signal, denoted as $y_{SC}(t)$, contains a DC component and some very low frequency components acting as a baseline. We remove these baseline low frequency components so that the mean value of the desired signal is zero. We consider the desired signal as the high pass version of the recorded raw SC signal. We low-pass filter the raw SC signal to obtain the slowly varying component $y_{SCL}(t)$. Then we subtract the

low-pass filtered signal from the raw signal to obtain the high-pass filtered SC signal, which is our desired signal $d[k]$. The noise reference $n[k] = [n_1[k-L+1]\ \ n_2[k-L+1]\ \ n_3[k-L+1]\ \ n_1[k-L+2]\ \ n_2[k-L+2]\ \ n_3[k-L+2]\ \ \cdots\ n_1[k]\ \ n_2[k]\ n_3[k]]$ and set $F_x = 3 \times F_d$ to perform the multi-resolution linear/nonlinear adaptive filtering. Here F_n corresponds to the sampling frequency of the combined noise reference, $n_i[k]$ represent the k^{th} sample of the accelerometer recording for the i^{th} channel representing a spatial axis, $\forall i \in \{1, 2, 3\}$. Before combining all the accelerometer data into one noise vector, we perform a third order moving median filtering to remove any spike noise which has been observed in some of the accelerometer channel data. The reasoning is unknown for this kind of impulse noise, probable reason can be related to internal electronics of the accelerometer. We perform the motion artifact removal on the signal at 100 Hz sampling frequency for $y_{SC}[k]$. Figure 48 shows an overview of the motion artifact removal scheme.

6.2.8 BayesianEDA for Deconvolution of Skin Conductance Response

For obtaining the autonomic nervous system activation from the SC signal, we utilized a deconvolution approach provided in [140]. We utilize the following three-dimensional linearized state-space model to describe the SC fluctuations from [140],

$$\begin{aligned}
\dot{s}_1(t) &= -\frac{1}{\tau_r} s_1(t) + u(t), && \text{(sweat production)} \\
\dot{s}_2(t) &= \frac{\eta s_1(t)}{\tau_r} s_1(t) - \frac{1}{\tau_p} s_2(t), && \text{(pore collapse)} \\
\text{and } \dot{s}_3(t) &= \frac{(1-\eta) s_1(t)}{\tau_r} s_1(t) - \frac{1}{\tau_d} s_3(t), && \text{(slow re-absorption)}
\end{aligned}$$

where $s_1(t)$, $s_2(t)$, and $s_3(t)$ states, respectively, represents the amount of sweat in the sweat ducts, the fraction of sweat in the ducts that are electrically conducted to the surface due to the open pore, and the fraction of sweat that is diffused in the corneum. The parameters τ_p and τ_d represent the faster decay time due to fast reabsorption and slow decay time related

to the slow elimination (due to the cumulative effect of reabsorption, diffusion in the deeper corneum, and evaporation), respectively. The parameter τ_r denotes the SC rise time. The system input $u(t)$ represents the ANS activation. To keep the definition simple, we assume that the ANS activation occurs during the integer multiple of the sampling period. Let T_s be the sampling period. With sparsity assumption as in [18], we represent the ANS activation as $u(t) = \sum_{k=1}^{K} u[k]\delta(t - kT_s)$ where $u[k]$ is the amplitude of the impulse during the ANS activation at time kT_s; here, $u[k]$ is zero if there is no impulse in the stimuli. Here, we set the parameter $\eta = 0.5$ similar to [140]. We represent the continuous state space model as follows,

$$\dot{\mathbf{s}}(t) = \mathbf{A}_c\mathbf{s}(t) + \mathbf{B}_c u(t),$$
$$\text{and } y_{SC}(t) = \mathbf{C}_c\mathbf{s}(t) + \nu(t),$$

where, $\mathbf{s}(t) = \begin{bmatrix} s_1(t) & s_2(t) & s_3(t) \end{bmatrix}^\top$,
$\mathbf{A}_c = \begin{bmatrix} -\frac{1}{\tau_r} & 0 & 0 \\ \frac{\eta}{\tau_r} & -\frac{1}{\tau_p} & 0 \\ \frac{1-\eta}{\tau_r} & 0 & -\frac{1}{\tau_d} \end{bmatrix}$, $\mathbf{B}_c = \begin{bmatrix} 1 \\ 0 \\ 0 \end{bmatrix}$,
and $\boldsymbol{C}_c = \begin{bmatrix} 0 & 1 & 1 \end{bmatrix}$. The phasic and tonic components of the SC can be represented as follows,

$$y_p(t) = \mathbf{C}_{c,s}\mathbf{s}(t) + \nu_s(t)$$
$$\text{and } y_s(t) = \mathbf{C}_{c,p}\mathbf{s}(t) + \nu_p(t),$$

where $\boldsymbol{C}_{c,p} = \begin{bmatrix} 0 & 1 & 0 \end{bmatrix}$, and $\boldsymbol{C}_{c,s} = \begin{bmatrix} 0 & 0 & 1 \end{bmatrix}$. The discretized state-space model is as follows,

$$\mathbf{s}[k] = \mathbf{A}_d \mathbf{s}[k-1] + \mathbf{B}_d u[k] \tag{91}$$

$$\text{and } y_{SC}[k] = \mathbf{C}_d \mathbf{s}[k] + \nu[k], \tag{92}$$

where $\mathbf{s}[k]$, $y[k] \in \mathbb{R}$, $u[k]$, and $\nu[k]$ denote the state vector, the observation, ANS activation, and the measurement error in discrete domain. The vector $\boldsymbol{u} = [u[1] \quad u[2] \quad \cdots \quad u[K]]^\top$ represents the ANS activation over the duration of SC data. Here, $\boldsymbol{A}_d = e^{\boldsymbol{A}_c T_s}$, $\boldsymbol{B}_d = \int_0^{T_s} e^{\boldsymbol{A}_c (T_s - \rho)} B_c d\rho$, and $\boldsymbol{C}_d = \boldsymbol{C}_c$. We further define the tonic and phasic component. Here T_s represents the sampling frequency. With this discrete state-space representation, we perform deconvolution utilizing the scalable iterative re-weighted Bayesian filtering based *expectation-maximization* (EM) approach proposed in [140] to identify $u[k]$, $\forall k \in \{1, 2, 3, \ldots, K\}$, i.e., the discretized version of $u(t)$ as well as the physiological system parameters. We will refer to this deconvolution algorithm as 'bayesianEDA'. The deconvolution is performed on a downsampled clean signal with 4 Hz sampling frequency.

6.2.9 Isolating Respiration Related Skin Conductance Activation

To isolate the respiration related activation of the SC, deep breaths are needed to be detected as only deep breaths are responsible for such SC responses. We have considered two aspects of respiration for the detection of a deep breath. Firstly, the deep breath takes a bit longer time to take. Secondly, the deep breath generates higher stress on the respiration belt, i.e., the corresponding recorded voltage from the transducer will have a higher amplitude. We only considered the respiration signals that are not motion corrupted based on manual eyeballing.

Firstly, we perform a continuous wavelet transform of the respiration signal. From all wavelet coefficients, we keep the ones that relate to $0.05 - 0.25$ Hz frequency components

and perform an inverse wavelet transform to obtain the reconstructed respiration signal. This way we remove any potential high-frequency components related to normal breathing and noise along with any potential DC component related to the baseline shift. Then we perform moving average filtering with a window size of 5 seconds on the absolute value of the respiration signal. Here, the window size is selected to be around the maximum length of a normal breath, which is about 5 seconds. The moving average of the absolute value of the respiration signal will be higher where the respiration belt stress is higher. We use '*movmean*' function from MATLAB [141]. Then we obtain the moving standard deviation of the moving mean signal with a window of 30 seconds. Next, we take the sample-wise ratio of the moving mean signal and the moving standard deviation signal. This ratio standardizes the signal based on the 30 seconds window. The standardization accounts for different levels of fluctuations related to variable tightness levels of the belt. Variability in the belt tightness levels of the transducer belt may originate from changes in the participants' pose or changes in the belt position during the experiment. Next, we subtract the mean from the ratio signal and multiply it by 3. Finally, we perform a sigmoid transformation to map the signal between 0 to 1 to represent probability. We define this probability as $p_1[k]$.

Secondly, we perform peak detection on the wavelet reconstructed respiration signal and peak detection on the negative of it. For peak detection, we use '*findpeaks*' from MATLAB with default settings [141]. We take both peaks from the reconstructed signal and the negative of the reconstructed signals and their locations to perform an spline interpolation. Then we obtain a moving standard deviation of the interpolated signal with a window of 90 seconds. Finally, we take sample-wise ratio of the interpolated signal and the moving standard deviation signal. This ratio standardizes the signal based on the 90 seconds window and accounts for the different level of fluctuations with different tightness levels of the transducer belt because of the change in the participants pose. Finally, we multiply the ratio signal with 10 and perform a sigmoid transformation to map the signal between 0 to 1 to represent probability. We define this probability as $p_2[k]$. We multiply these two

probabilities to obtain one probability signal representing the probability of a deep breath. Lets denote this probability as $p[k]$. Therefore, we can write $p[k] = p_1[k]p_2[k]$. We obtain the probability with 100 Hz sampling frequency and then downsample to match the deconvolution results.

After the deconvolution with BayesianEDA algorithm to obtain the ANS activation, we define the respiration induced activation as $u[k]p[k]$ and the direct ANS activation as $u[k](1 - p[k])$. Here the deconvolution with bayesianEDA algorithm is performed in 4 Hz. Therefore, $p[k]$ is downsampled at same sampling frequency as $u[k]$. Finally, we obtain $u[k]p[k]$ and $u[k](1 - p[k])$ to isolate the respiration induced and direct ANS induced activation, respectively.

6.3 Results

6.3.1 Simulation Study

The objective of the simulation study is to investigate the performance of four different adaptive filters in artifact reduction from SC data. For the simulation study, we first generate a reference noise signal and then perform a nonlinear transformation to add it to the raw signals from the publicly available dataset in [57]. The noise reference is generated by the summation of a sine wave and a square wave where the amplitude and frequencies are randomly varied. For the simulation purposes, the amplitudes of the waves are sampled from a Gaussian distribution every 1 second with the mean of 20% of the standard deviation of the corresponding SC recording. On the other hand, the standard deviation of the random amplitude has been selected to be 5% of the standard deviation of the corresponding SC recording. Similarly, for the frequencies, we sampled every 0.5 seconds randomly from a Gaussian distribution of mean 1 Hz and variance 0.25 Hz. We also generate added zero mean Gaussain noise with 0.2 standard deviation. The sampling frequency for discretization is selected as 100 Hz, which same as the sampling frequency of the dataset. We utilize the

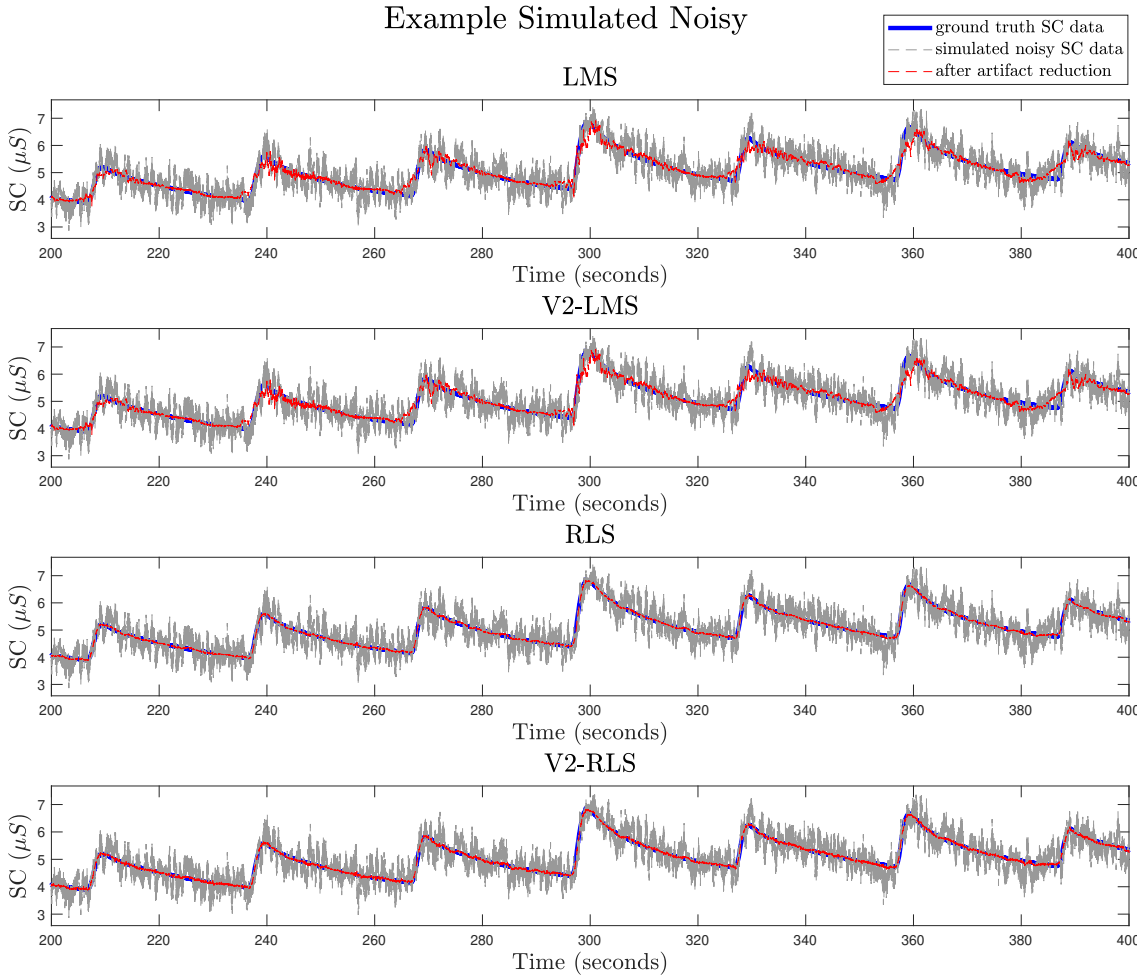

Figure 49: **Examples of Artifact Reduction Results using Simulated Noise Source.**

following transformation for simulating the artifact corrupted SC signal as follows,

$$y_{SC}[k] = y_{SC}^{D}[k] + (h * n)[k] + c_1(n[k])^2 + c_2(n[k])^3. \tag{93}$$

where h is a filter representing the transformation of the noise. We generate it by first by drawing 50 samples from from zero mean Gaussian distributed number to create a vector h_r then normalized by dividing it by its norm to find the filter, i.e. $h = \frac{|h_r|}{||h_r||_2}$. Furthermore, c_1 and c_2 are randomly sampled from Gaussian distributed random variables with standard

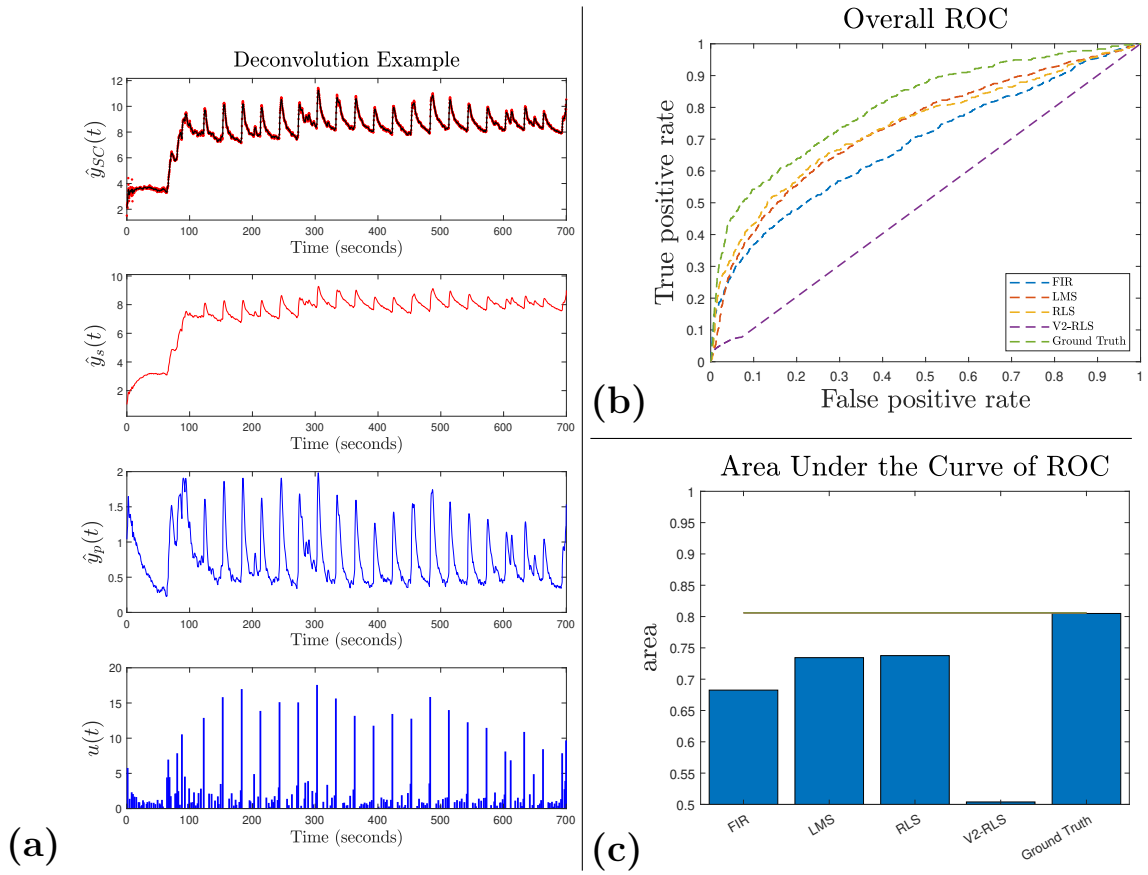

Figure 50: **Inference Performance of ANS Activation After Deconvolution Algorithm After Artifact Removal with Different Filters.**

deviation of 0.1 and 0.01. Here, y_{SC}^{D} represents the SC signals from the publicly available datasets. k denotes the k^{th} sample. We successfully utilized the adaptive filter for artifact removal with parameters $\alpha = 0.02$ and $\lambda = 0.999995$. These values were selected by trial and error and eyeballing results for all 26 simulated data corresponding to the 26 participants in [57]. Figure 49 shows results from LMS, V2-LMS, RLS, and V2-RLS filtering. Subplots from top to bottom in Figure 49 shows the artifact removal performance with LMS filter, V2-LMS, RLS, V2-RLS filter with a single noise reference. The visual depiction shows that the adaptive filters are able to remove most of the simulated noise. The result also shows a qualitative illustration that RLS and V2-RLS are performing better in terms of their ability to follow the ground truth. From our analysis, we observed that for 5 participants, LMS

and V2-LMS filter results became unstable and could not be used for further analysis. On the other hand, the results from RLS and V2-RLS filters were always stable.

Utilizing the stable adaptive filtered results, we deconvolve the artifact reduced SC signal to perform deconvolution with the bayesianEDA algorithm [140]. Figure 50-(a) shows an example deconvolution result showing the inferred ANS activation from the artifact reduced signal. Furthermore, we utilize the estimated ANS activation $u(t)$ in distinguishing between event-related SCRs and non-event-related SCRs. Here the events are hearing loud sound events. First, we label all nonzero elements in estimated $\mathbf{u}[k]$ $\forall k$ as the positive class if they are within 5 seconds after a loud sound event was heard by the participant and other impulses as the negative class. We consider the values of the nonzero elements in $u[k]$ as the score for the classification within the participants for investigating the receiver operating characteristic (ROC) [69, 70]. Figure 50-(b) shows the ROCs obtained from the filtered signal from FIR lowpass filter with 0.5 Hz cut-off, LMS adaptive filter, RLS adaptive filter, and V2-RLS adaptive filter. Figure 50-(c) shows the corresponding area under the curve (AUC) of the ROCs. The result shows that RLS filtered signals yield the highest AUC (≈ 0.738).

6.3.2 Experimental Study

We tried all types of adaptive filters on the experimental data with different settings, however, only RLS filter provided stable results while learning. Therefore, we only present the results of RLS filter for the experimental study. The SC and three-axis accelerometer signals are resampled to 100 Hz. Based on the adaptive filtering scheme shown in Figure 48, the desired signal has a sampling frequency of 100 Hz and the noise reference has a sampling frequency of 300 Hz. The adaptive filter length is also $L = 300$ to consider an 1 second window. For the forgetting factor, we first tried with the value that has been used for the simulated data. Based on the results, we relaxed the forgetting factor to allow the filter to readjust itself for newer data. Based on trial and error, $\lambda = 0.999$ seemed to

work well for our study. Figure 51 shows an example adaptive filtered result utilizing the RLS adaptive filter. In this figure, the first left panel depicts raw (artifact corrupted) and cleaned (artifact reduced) SC data. The first right panel shows the corresponding power spectrum density. The next three panels show three accelerometer channel recordings on the left and their corresponding power spectrum density on the right. Figure 51 also shows that some of the peaks that are seen on the accelerometer captured motion information power spectrum density are also shown in seen in the raw experimental SC signal power spectrum density. RLS adaptive filter could successfully remove those peaks. Figure 51, also depicts that there is a significant amount of energy reduction in the power spectrum density. Additional results for all participants are provided in Section A.4. Figure 52 shows some zoomed in segments from all trials of Participant 1 and 2, where each panel in subplots (a) and (b) denotes the zoomed in plots with different segments from Participant 1 and 2. Black and red lines denote the raw SC data and artifact reduced SC data. The figures provide a qualitative illustration of RLS adaptive filter ability to reduce artifacts utilizing accelerometer information.

Furthermore, we attempt to identify the SCR activation related to deep breath. We only utilized the respiration signal for Trials 1-5 for Participant 1 as other respiration signals seemed to be heavily corrupted with artifacts. First, we successfully detect the respiration based on the method described in Section 6.2.9. Figure 53 represent the results from the deep breath detection. In each panel in Figure 53, the top subplot denotes the raw respiration signal recorded from the respiration belt, the bottom subplot shows the estimated detection probability $p[k]$ (blue lines). The light red and green shaded regions represent the intermediate probabilities $p_1[k]$ and $p_2[k]$, respectively. Next, we deconvolve the motion artifact reduced SC signals and identify the respiration induced SC activation based on the estimated probability $p[k]$. Figure 54 shows results from the identification of respiration induced activation of SCR generation. In each panel in Figure 54, the top subplot denotes the artifact reduced (red stars) and the reconstructed SC (black lines),

the bottom subplot shows the separated respiration induced activation and the pure ANS generated activation.

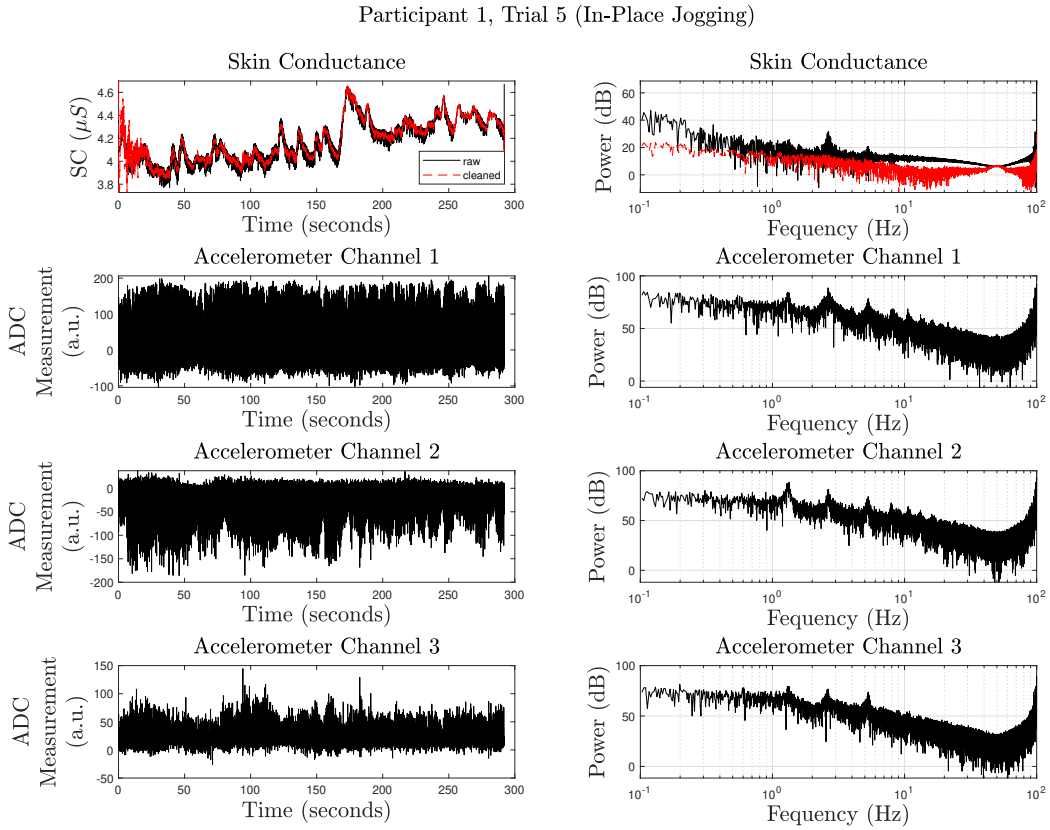

Figure 51: **Example Artifact Reduction Result with Multi-resolution RLS Adaptive Filter from Experimental SC recording Participant 1, Trial 5 During In-Place Jogging.**

6.4 Discussion and Conclusion

From the simulated study with publicly available experimental SC data, we can see that the RLS filter is performing better than other filters in terms of retaining the information about the event-related responses such that the detection of such events is detected. Moreover, the linear RLS filter is has been the most stable one. Although we have considered some nonlinearities in the noise reference transformation, the RLS filter was able to model the transformation in a time-varying piecewise linear fashion. On the other hand, LMS, V2-LMS, and V2-LMS filters suffer from instability and the high number of parameters

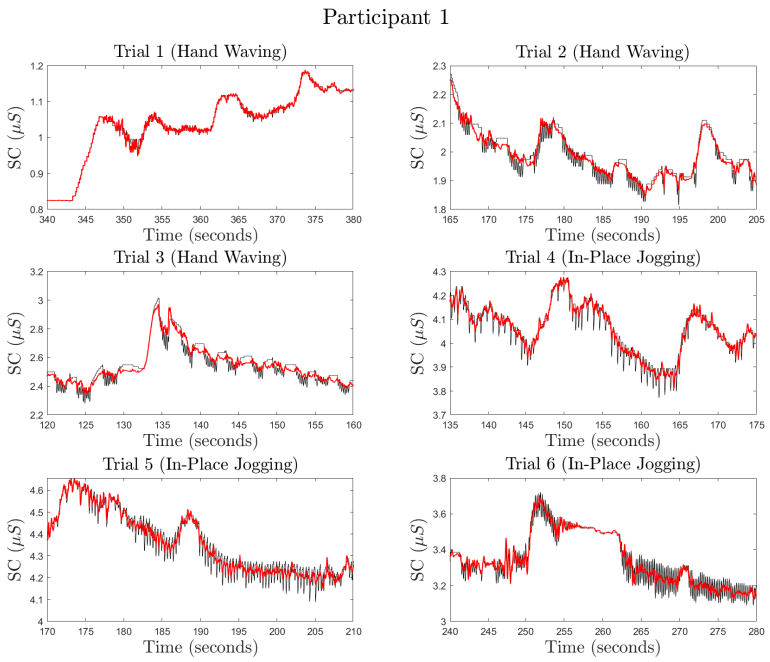

(a)

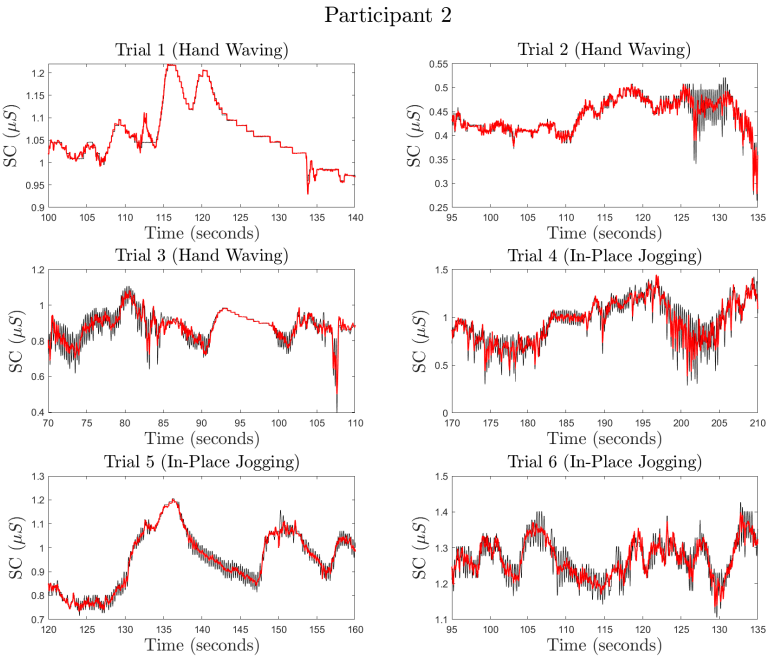

(b)

Figure 52: **Closer View of Different Segments of the Motion Reduced Results for All Trials from Both Participants.**

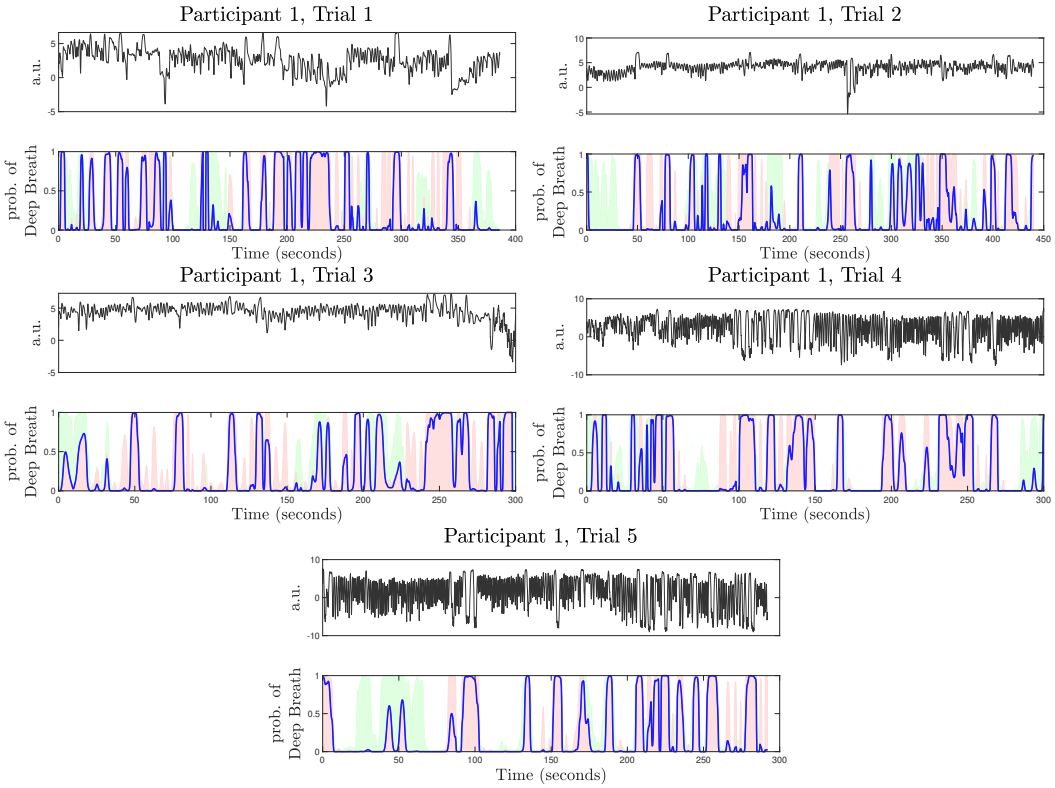

Figure 53: **Deep Breath Detection Results for Five Trials of Participant 1.**

required to update each step compared to the number of observations used during the gradient calculation. Further analysis with deconvolution on artifact-reduced SC data and consequent loud sound detection confirms that the RLS filter is reasonably improving the detection capability of event-related activations for SCR generation.

From the analysis of our experimental study, we see that only the RLS filter was able to achieve stability in terms of reducing the motion artifact. However, none of the other filters were able to achieve stable results. The power spectrum density change also confirms that there is a significant reduction in the spectrum peaks that are generated by motion. We observe some peaks in the accelerometer power spectrum. The similar which are also seen in the power spectrum Raw SC data denoting the artifacts. After artifact removal, these spectrum peaks are not visible anymore. In Figure 52, we also see that how different types of artifacts are reduced. In some cases, we have seen that the RLS filter output becomes

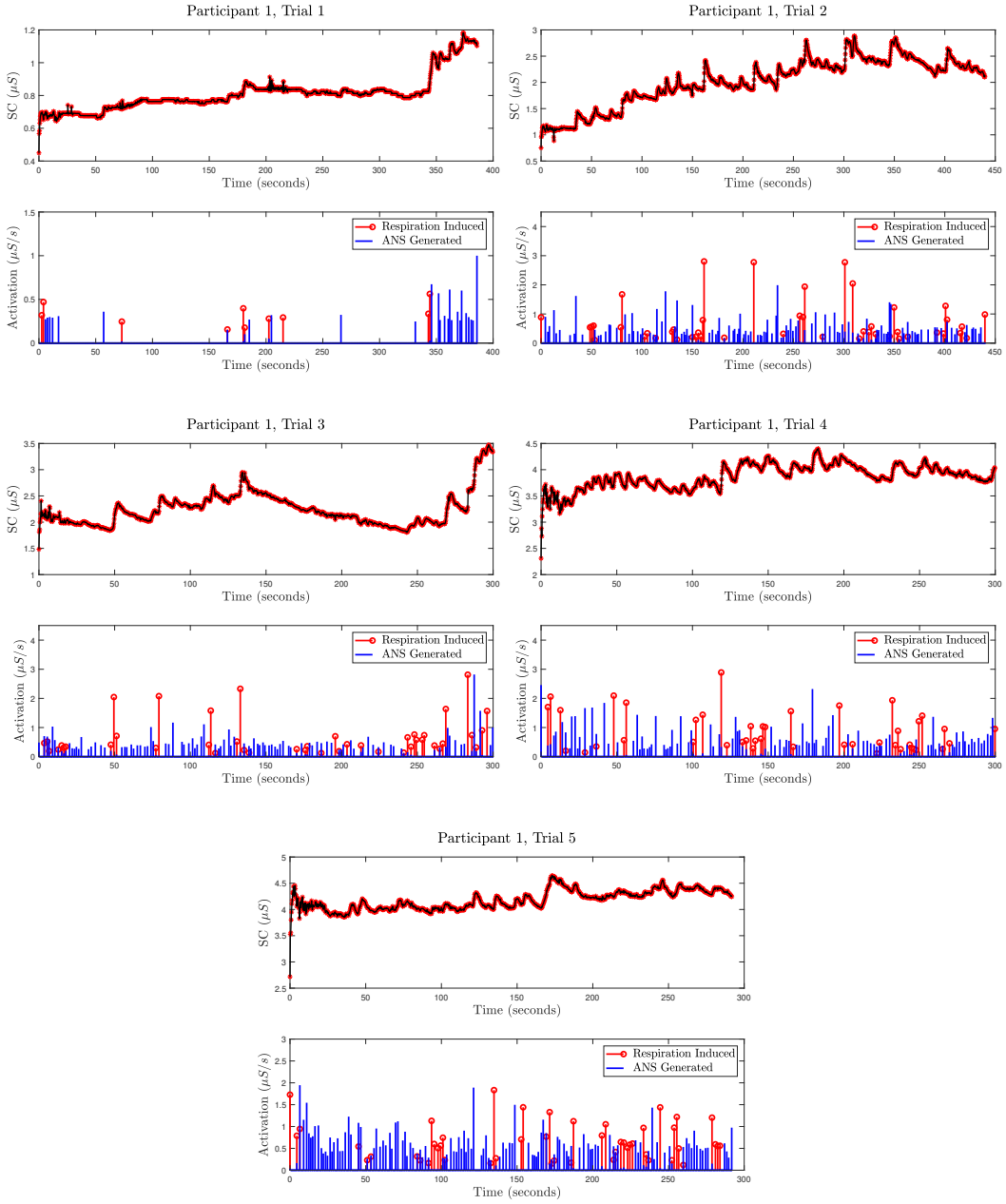

Figure 54: **Separation of Respiration Induced Electrodermal Activity from the Inferred ANS Activation for Five Trials from Participant 1.**

more noise than the input. These scenarios suggest significant changes in the transformation system between the accelerometer data for artifact generation. The RLS filter takes some time to learn the new system and inaccuracy in the artifact reduction can be seen during the learning phase.

Furthermore, we see that the simple heuristic approach can lead to reasonably successful identification of deep breath as well as deep breath related SCR responses. This way, direct ANS activation can be isolated from the respiration related activation. Thus, respiration related alterations of the SC data can be disregarded in some applications of autonomic arousal estimation by modifying the state-space formulations in [10, 106, 44, 83]. However, we have considered some intuition-based heuristic approaches for deep breath detection. The heuristic approach that has been developed for these five trials is just to show the feasibility of such approach. However, the deep breath (specifically, that are responsible for the SCR generation in SC data) detection algorithms can be further improved utilizing data-driven machine learning approach with a large amount of data.

In this study, we have generated simulated noise with some arbitrary settings. Therefore, it might not be capturing the whole space of artifact corruption. However, it has allowed us to obtain an idea of how different the adaptive filter might perform in real-world settings. During the experimental data collection, the participants observed the recordings shown on the screen and tried to generate artifacts by hand waving and in-place jogging on multiple trials, which might be slightly different than the reality. However, this experimental dataset is a stepping stone to evaluate motion artifact contaminated data and corresponding artifact reduction algorithms. In the future, we plan to perform more experiments with different scenarios and different activities such that the dataset approximately represents the real-world motion artifact space. For this study, the experimental study has been beneficial to evaluate adaptive filters in a qualitative manner. One possible future direction would be to perform different physical activities during a loud sound event experiment similar to [57]. We plan to perform the experiment by placing SC sensors and noise reference sensors on different skin locations such as the wrist or foot.

As mentioned in both experimental and simulated study results, there have been many cases of unstable results. RLS filter seems to be more stable for the selected value for both simulated and experimental data. LMS and V2-LMS have shown instability for some

examples of simulated data (5 out of 26 participants) and have been unstable for all experimental datasets that we have analyzed. V2-RLS also show unstable results only for the experimental dataset. For the unstable results, the coefficients of the adaptive filter values are exploding to infinity. To handle stability, we plan to utilize techniques such as regularization in the cost function similar to [142]. Another possible future direction for handling instability is to use techniques such as leaky LMS/RLS algorithms [143, 144].

We have only utilized accelerometer data for the noise reference. We observe that the accelerometer data-based noise reference is helping to reduce a significant amount of artifacts. However, we only placed the accelerometer on one of the electrodes, while the motion artifact could be a resultant of motion on both electrodes on both hands. Therefore, an additional accelerometer on the other electrode can potentially improve the results. Moreover, accelerometers are not good at capturing some types of motion information. For example, if someone bends their finger, resulting in some pressure on the electrodes will lead to an magnitude artifact that might not be captured in the accelerometer reading. Moreover, orientation of the hand might also lead to a change in the sensor placement. Therefore, more noise reference sensors such as gyroscope, magnetometer, and pressure sensors should be investigated in a systematic manner.

From these results, we can see RLS filter has reasonably performed in terms of reducing the motion artifact. As RLS filters are updated in each time step, the resulting filter acts as a piecewise linear transformation of the noise reference $\mathbf{x}[k]$ such that the error signal $e[k]$ is minimized. Thus, the nonlinearity that has been introduced by the RLS filter might not be enough. On the other hand, the Volterra-series based nonlinearity requiring a large number of coefficients might lead to overfitting and instability during learning. One potential future direction of this study is to investigate neural network-based [145] or functional link-based [146] adaptive filters to better realize the nonlinear transformation with lower number of coefficients.

7 Conclusion and Future Directions

7.1 Conclusion

The current state-of-the-art lacks a physiology-motivated approach for scalable and robust identification of brain activation (ANS activation). In this thesis, we study physiology-motivated state-space models and the corresponding robust and scalable methodology for the inference of brain activation.

7.1.1 Identification of Sympathetic Nervous System Activation from Skin Conductance: A Sparse Decomposition Approach with Physiological Priors

In Chapter 2, we proposed an approach to decompose SC recordings into their constituents to accurately identify the SNS-generated neural stimuli to sweat glands and the physiological system parameters. We propose a GCV and coordinate descent-based deconvolution algorithm for simultaneously estimating the tonic component, neural stimuli, and the physiological system parameters by automatically balancing the smoothness of the tonic component, the sparsity of neural stimuli, and the residual error. Analyzing the experimental and simulated data, we showed that our approach successfully uncovers the neural stimuli due to the known auditory stimulation times. We have performed comparisons with six widely used previous approaches and have qualitatively shown that our approach outperforms previous approaches in terms of balancing between discarding noise spikes and capturing significant neural impulses.

7.1.2 Robust Inference of Autonomic Nervous System Activation using Skin Conductance Measurements: A Multi-Channel Sparse System Identification Approach

In Chapter 3, we proposed a physiological state-space model for multichannel SC recordings from different regions of skin. Moreover, we proposed a concurrent deconvolution algorithm for simultaneously collecting multichannel SC data. Analysis on experimental and simulated data showed that the algorithm successfully recovers the neural stimuli due to the known auditory stimulation times. Our proposed method and algorithm results in integrating multiple simultaneously collected SC data to recover the ANS stimuli robustly in the presence of noise and different artifacts. Moreover, we applied our approach to concurrently deconvolve simultaneously recorded signals from multiple skin regions in real-world driving stress conditions. Using the concurrently deconvolved driver's stress data, we were able to achieve a better estimate of stress states than the previous study. The state-space model formulation and deconvolution algorithm successfully recover the stimuli.

7.1.3 Sparse Deconvolution of Electrodermal Activity via Continuous-Time System Identification

In Chapter 4, we present a sparse deconvolution approach utilizing continuous-time system identification to account for the challenge of nonconvex cost function for system identification. We use cvxEDA to separate the phasic component of SC data and then perform deconvolution to recover the underlying neural stimuli. We model the phasic component of the signal using a state-space model similar to the models in [42, 18, 19]. [18, 19]. Then, we propose a two-step coordinate descent deconvolution scheme to identify the system parameters and the underlying neural stimuli. We use a system identification approach that recovers the system parameters and neural stimuli in the HMF domain. We incorporate an adaptive band selection scheme in HMF domain to have the best possible estimate. We also use GCV-FOCUSS+ to solve the inverse problem and find the neural stimuli in

HMF domain. We apply our algorithm to analyze the SC data collected from subjects who were performing tasks involving 'cognitive stress'. Finally, to validate our algorithm, we simulate noisy data based on the results obtained from the deconvolution of experimental data. We illustrate that our algorithms successfully deconvolve noisy simulated data. We also compare the performance of our method with cvxEDA [23] and LedaLab [21] algorithms. Our algorithm outperforms both these algorithms in finding the stimuli while balancing the sparsity and filtering out the noise. Moreover, our algorithm estimates the system parameters while the other two algorithms assume fixed known system parameters.

7.1.4 Physiological Characterization of Electrodermal Activity Enables Scalable Near Real-Time Autonomic Nervous System Activation Inference

In Chapter 5, we have proposed a comprehensive physiological state-space model for a complete understanding of the SC recording fluctuations. Our proposed comprehensive model enables us to design a scalable autonomic nervous system activation inference leveraging Bayesian filters. We utilize an *expectation-maximization* framework for deconvolution where the expectation step is carried out via iterative reweighted Bayesian filtering and smoothing-based sparse recovery. Furthermore, we utilized generalized cross-validation for tuning the sparsity level of ANS activation. With simulated and experimental studies, we show the scalability of our approach. Comparison with other previous approaches reveals that our approach outperforms all previous approaches in terms of the detection of event-related SCRs. The proposed new model unlocks a whole new perspective on the analysis of EDA. The scalable deconvolution framework will lead to real-world deployment of the autonomic nervous system inference activation algorithm with SC measurement.

7.1.5 Evaluation of Adaptive and Bayesian Filters for Artifact Removal from Electrodermal Activity Leveraging Noise Source Reference

In Chapter 6, we have investigated linear and nonlinear adaptive filters in terms of artifact reduction performance. We have utilized the scalable Bayesian filter-based deconvolution algorithm to deconvolve the SC data to identify the activations. We utilized simulated data utilizing publicly available datasets to quantitatively and qualitatively investigate different filters. Furthermore, we perform an experimental study to qualitatively investigate different filters in terms of reducing real-world motion artifacts. The results show that the linear recursive least-squares filter is performing best in terms of reducing motion artifact as well as the stability during the filter coefficient learning. We further show that deep breath detection and scalable deconvolution can be utilized to identify the deep breath-related activations and corresponding SCRs. The study is an important step towards deploying SC signal-based ANS activation detection [53, 54, 52, 140], arousal estimation [10, 44, 83, 106], and corresponding control design for an effective wearable brain-machine interfacing architecture for emotional stress management [113, 114].

7.2 Future Directions

The thesis opens up many future directions that can potentially disrupt the current practices. The future direction ranges from further development of novel algorithms to the implementation of these algorithms for closing the loop with appropriate control for mental well-being.

7.2.1 Utilization of Different Sparse Recovery Algorithms

Within the proposed framework, we have only IRLS based sparse recovery algorithms. One of the potential directions is to leverage the orthogonal matching pursuit (OMP) based greedy approaches [147]. In some applications, OMP might provide faster results. Furthermore, other sparse recovery algorithms can be explored to evaluate their performance.

Moreover, there are many ways to impose the sparsity priors during the sparse deconvolution. Another future direction is to carry out thorough investigations of different sparsity priors within the proposed deconvolution framework for different applications [148]. Furthermore, the utilization of the recent development of deep-learning-based sparse recovery approaches can also be carried out to remove some of the hurdles within the proposed framework [149, 150, 151].

7.2.2 Extention of Proposed Methods for Scalable Mutli-channel Concurrent and Nonlinear Implementation

In this thesis, we have proposed how to model both tonic and phasic components along with the decomposition algorithms by adaptively finding the regularizing parameters for smoothness and sparsity [8, 41]. On the other hand, we also have shown how to combine multichannel phasic components for concurrent deconvolution [53, 54]. In the future, a combination of these two approaches can be carried out to concurrently decompose the tonic and phasic components from multichannel SC data and infer the common ANS activation. Concurrent deconvolution with concurrent tonic-phasic decomposition will lead to a more reliable inference of individual arousal level, similar to our previous study in [54]. Furthermore, we have proposed a new physiological model that has the ability to comprehensively describe the SC dynamics. One of the future goals is to extend this approach for multichannel SC recording [53, 54]. We have proposed a nonlinear state-space model to explain the physiology and then linearized it for a scalable implementation. A potential future direction is to design a proper extended Kalman filter/smoother or particle filter/smoother that can be designed to consider the nonlinearity. Finally, neural networks can be utilized similar to the work in [152] to represent the generalized nonlinear state-transition matrix for extending this work to learn any dynamical system with many states that have a sparse innovation term as the input.

7.2.3 Concurrent Artifact Removal and Deconvolution with Unified Bayesian Filter

In this thesis, we have evaluated different adaptive filters for motion artifact removal. One of the future directions would be to evaluate Kalman filter-based adaptive filter for motion artifact reduction for SC data similar to [153]. On the other hand, we have proposed a Bayesian filtering and smoothing approach for deconvolution. The ideal future direction would be to combine the deconvolution filter and the Kalman filter-based adaptive filter for the concurrent deconvolution and motion artifact framework.

7.2.4 Deep-Learning for Deconvolution and Artifact Reduction

As a future direction, physiology-informed deep neural net-based architecture can be utilized for the deconvolution problem similar to physics-informed deep learning approaches [154]. In this case, the physiological dynamics can be described with the state-space model and can be integrated into the loss function during the training of the deep neural net. This way, an infinite resolution of the timing of the activation can be obtained. On the other hand, we have evaluated nonlinear Volterra series adaptive filters in our study, however, the Volterra series suffer from a high number of parameters and they become unstable during training. An alternative future direction to the Volterra series is to train shallow neural networks to capture the non-linearity [155]. Furthermore, experimental data with and without motion artifacts can be utilized to train Generative Adversarial Networks to remove artifacts [156].

7.2.5 Experimental Design for Real-World Implementation

One of the future directions of this thesis is to design experimental studies that resemble different real-world scenarios. Rigorous experiments with healthy and patient populations will lead to the identification of the bottlenecks of the proposed algorithms. Studies may include experiments with event-related stimuli [57], tasks requiring continuous cognitive or

emotional stress [95], and data collection in real-world settings [157]. The experimental study should consider both laboratory and ambulatory settings. An example of the experiment with event-related stimuli would be to play loud sounds (e.g., 1-second long Gaussian noise burst with 85 dB of loudness level) or provide sudden electric shocks while participants are performing work-related or learning-related real-world tasks. Such tasks include using computer applications to carry out office work, doing homework, taking part in sports, and doing physical activity. Experiments with event-related stimuli can also be carried out on patients (e.g., patients with diabetic neuropathy) to compare them with a healthy population. Statistical analysis on the multichannel deconvolution results from such experimental data may lead to system theoretic understandings of corresponding diseases similar to [55]. Other examples of the experiment may include participants listening to arousing or calming music while taking part in physical exercise. One of the current limitations in current datasets is that the number of participants is very low. This potentially prevents us from leveraging deep-learning-based generalized inference methods. Furthermore, experimental studies with a reasonable number of participants and trials will lead to better fine-tuning of the current algorithms and future directions for reliable estimation.

7.2.6 Close-loop Control and Other applications

The obtained ANS activities from the single/multi-channel SC recording can be used to track the cognitive arousal state of an individual [10, 44, 106]. For further accurate estimation of emotional arousal, one of the future directions is to utilize the inferred ANS activity from SC recording with our approach and to combine with other physiological signals similar to [107, 108, 109, 110, 47, 111, 112]. The proposed new model as well as the scalable ANS inference approach has enabled us to design a scalable control architecture to regulate the arousal level similar to the proposed framework in [113, 114, 115, 116]. Finally, the proposed sparse deconvolution approach has applicability in different fields such as calcium deconvolution, EEG sleep spindle detection [105], hormone deconvolution

[56, 55, 158], etc.

References

[1] Mario C Raviglione, Dixie E Snider, and Arata Kochi. Global epidemiology of tuberculosis: morbidity and mortality of a worldwide epidemic. *Jama*, 273(3):220–226, 1995.

[2] Robert V Tauxe, Eric D Mintz, and Robert E Quick. Epidemic cholera in the new world: translating field epidemiology into new prevention strategies. *Emerging Infectious Diseases*, 1(4):141, 1995.

[3] Dileep V Mavalankar. Indian'plague'epidemic: unanswered questions and key lessons. *Journal of the Royal Society of Medicine*, 88(10):547, 1995.

[4] Richard J Coker, Rifat A Atun, and Martin McKee. Health-care system frailties and public health control of communicable disease on the european union's new eastern border. *The Lancet*, 363(9418):1389–1392, 2004.

[5] Diana D Jeffery, Lakmini Bulathsinhala, Michelle Kroc, and Joseph Dorris. Prevalence, health care utilization, and costs of fibromyalgia, irritable bowel, and chronic fatigue syndromes in the military health system, 2006–2010. *Military medicine*, 179(9):1021–1029, 2014.

[6] Robyn McDermott, Kevin G Rowley, Kerin O'Dea, Amanda J Lee, and Sabina Knight. Increase in prevalence of obesity and diabetes and decrease in plasma cholesterol in a central australian aboriginal community. *Medical Journal of Australia*, 172(10):480–484, 2000.

[7] Claudia Newbegin. The stress epidemic. *InnovAiT*, 8(1):36–40, 2015.

[8] Md Rafiul Amin and Rose T Faghih. Tonic and phasic decomposition of skin conductance data: A generalized-cross-validation-based block coordinate descent approach. In *2019 41st Annual International Conference of the IEEE Engineering in Medicine and Biology Society (EMBC)*, pages 745–749. IEEE, 2019.

[9] Wolfram Boucsein. *Electrodermal activity*. Springer Science & Business Media, 2012.

[10] Dilranjan S. Wickramasuriya, C Qi, and Rose T. Faghih. A state-space approach for detecting stress from electrodermal activity. In *Annual International Conference of the IEEE Engineering in Medicine and Biology Society. IEEE Engineering in Medicine and Biology Society. Annual Conference*, volume 2018, pages 3562–3567, 2018.

[11] Ya-Li Zheng, Xiao-Rong Ding, Carmen Chung Yan Poon, Benny Ping Lai Lo, Heye Zhang, Xiao-Lin Zhou, Guang-Zhong Yang, Ni Zhao, and Yuan-Ting Zhang. Unobtrusive sensing and wearable devices for health informatics. *IEEE Transactions on Biomedical Engineering*, 61(5):1538–1554, 2014.

[12] Yao Guo, Xiangyu Liu, Shun Peng, Xinyu Jiang, Ke Xu, Chen Chen, Zeyu Wang, Chenyun Dai, and Wei Chen. A review of wearable and unobtrusive sensing technologies for chronic disease management. *Computers in Biology and Medicine*, page 104163, 2020.

[13] Kristina T Johnson and Rosalind W Picard. Advancing neuroscience through wearable devices. *Neuron*, 108(1):8–12, 2020.

[14] Sandya Subramanian, Riccardo Barbieri, and Emery N Brown. Point process temporal structure characterizes electrodermal activity. *Proceedings of the National Academy*

of Sciences, 117(42):26422–26428, 2020.

[15] Vaughan G Macefield, Cheree James, and Luke A Henderson. Identification of sites of sympathetic outflow at rest and during emotional arousal: concurrent recordings of sympathetic nerve activity and fMRI of the brain. *International Journal of Psychophysiology*, 89(3):451–459, 2013.

[16] Monica Bomba, Fabiola Corbetta, Alessandro Gambera, Franco Nicosia, Luisa Bonini, Francesca Neri, Lucio Tremolizzo, and Renata Nacinovich. Heart rate variability in adolescents with functional hypothalamic amenorrhea and anorexia nervosa. *Psychiatry research*, 215(2):406–409, 2014.

[17] Ping Jack Soh, Guy AE Vandenbosch, Marco Mercuri, and Dominique MM-P Schreurs. Wearable wireless health monitoring: Current developments, challenges, and future trends. *IEEE Microwave Magazine*, 16(4):55–70, 2015.

[18] Rose T Faghih, Patrick A Stokes, Marie-France Marin, Rachel G Zsido, Sam Zorowitz, Blake L Rosenbaum, Huijin Song, Mohammed R Milad, Darin D Dougherty, Emad N Eskandar, and A.S. Widge. Characterization of fear conditioning and fear extinction by analysis of electrodermal activity. In *Engineering in Medicine and Biology Society (EMBC), 2015 37th Annual International Conference of the IEEE*, pages 7814–7818. IEEE, 2015.

[19] Rose T Faghih, Munther A Dahleh, Gail K Adler, Elizabeth B Klerman, and Emery N Brown. Deconvolution of serum cortisol levels by using compressed sensing. *PloS one*, 9(1):e85204, 2014.

[20] Rose T Faghih, Munther A Dahleh, Gail K Adler, Elizabeth B Klerman, and Emery N Brown. Quantifying pituitary-adrenal dynamics and deconvolution of concurrent cortisol and adrenocorticotropic hormone data by compressed sensing. *IEEE Transactions on Biomedical Engineering*, 62(10):2379–2388, 2015.

[21] Mathias Benedek and Christian Kaernbach. Decomposition of skin conductance data by means of nonnegative deconvolution. *Psychophysiology*, 47(4):647–658, 2010.

[22] Dominik R Bach, Jean Daunizeau, Karl J Friston, and Raymond J Dolan. Dynamic causal modelling of anticipatory skin conductance responses. *Biological psychology*, 85(1):163–170, 2010.

[23] Alberto Greco, Gaetano Valenza, Antonio Lanata, Enzo Pasquale Scilingo, and Luca Citi. cvxEDA: A convex optimization approach to electrodermal activity processing. *IEEE Transactions on Biomedical Engineering*, 63(4):797–804, 2016.

[24] Francisco Hernando-Gallego, David Luengo, and Antonio Artés-Rodríguez. Feature extraction of galvanic skin responses by non-negative sparse deconvolution. *IEEE Journal of Biomedical and Health Informatics*, 2017.

[25] Rose Taj Faghih. *System identification of cortisol secretion: Characterizing pulsatile dynamics*. PhD thesis, Massachusetts Institute of Technology, 2014.

[26] Rose T Faghih. From physiological signals to pulsatile dynamics: a sparse system identification approach. In *Dynamic Neuroscience*, pages 239–265. Springer, 2018.

[27] Irina F Gorodnitsky and Bhaskar D Rao. Sparse signal reconstruction from limited data using FOCUSS: A re-weighted minimum norm algorithm. *IEEE Transactions on signal processing*, 45(3):600–616, 1997.

[28] Robert Edelberg. Electrodermal mechanisms: A critique of the two-effector hypothesis and a proposed replacement. In *Progress in electrodermal research*, pages 7–29. Springer, 1993.

[29] Mathias Benedek and Christian Kaernbach. A continuous measure of phasic electrodermal activity. *Journal of neuroscience methods*, 190(1):80–91, 2010.

[30] Dominik R Bach, Guillaume Flandin, Karl J Friston, and Raymond J Dolan. Modelling event-related skin conductance responses. *International Journal of Psychophysiology*, 75(3):349–356, 2010.

[31] Elizabeth Reisinger Walker, Robin E McGee, and Benjamin G Druss. Mortality in mental disorders and global disease burden implications: a systematic review and meta-analysis. *JAMA psychiatry*, 72(4):334–341, 2015.

[32] Lay San Too, Matthew J Spittal, Lyndal Bugeja, Lennart Reifels, Peter Butterworth, and Jane Pirkis. The association between mental disorders and suicide: A systematic review and meta-analysis of record linkage studies. *Journal of affective disorders*, 2019.

[33] Sherry L Murphy, Jiaquan Xu, Kenneth D Kochanek, and Elizabeth Arias. Mortality in the united states, 2017. 2018.

[34] Donald S Shepard, Deborah Gurewich, Aung K Lwin, Gerald A Reed Jr, and Morton M Silverman. Suicide and suicidal attempts in the united states: costs and policy implications. *Suicide and Life-Threatening Behavior*, 46(3):352–362, 2016.

[35] James J Gross and Hooria Jazaieri. Emotion, emotion regulation, and psychopathology: An affective science perspective. *Clinical Psychological Science*, 2(4):387–401, 2014.

[36] Brian C Callaghan, Hsinlin T Cheng, Catherine L Stables, Andrea L Smith, and Eva L Feldman. Diabetic neuropathy: clinical manifestations and current treatments. *The lancet NEUROLOGY*, 11(6):521–534, 2012.

[37] Barry I Freedman, Donald W Bowden, Susan Carrie Smith, Jianzhao Xu, and Jasmin Divers. Relationships between electrochemical skin conductance and kidney disease in type 2 diabetes. *Journal of Diabetes and its Complications*, 28(1):56–60, 2014.

[38] Barry I Freedman, Susan Carrie Smith, Benjamin M Bagwell, Jianzhao Xu, Donald W Bowden, and Jasmin Divers. Electrochemical skin conductance in diabetic kidney disease. *American journal of nephrology*, 41(6):438–447, 2015.

[39] Tianyi He, Chuan Wang, Anju Zuo, Pan Liu, Ruxing Zhao, Wenjuan Li, Li Chen, and Xinguo Hou. Electrochemical skin conductance may be used to screen for diabetic cardiac autonomic neuropathy in a chinese population with diabetes. *Journal of diabetes research*, 2017, 2017.

[40] Nicola Gerrett, Katy Griggs, Bernard Redortier, Thomas Voelcker, Narihiko Kondo, and George Havenith. Sweat from gland to skin surface: production, transport, and

skin absorption. *Journal of Applied Physiology*, 125(2):459–469, 2018.

[41] Md Rafiul Amin and Rose T Faghih. Identification of sympathetic nervous system activation from skin conductance: A sparse decomposition approach with physiological priors. *IEEE Transactions on Biomedical Engineering*, 68(5):1726–1736, 2020.

[42] David M Alexander, Chris Trengove, P Johnston, Tim Cooper, JP August, and Evian Gordon. Separating individual skin conductance responses in a short interstimulus-interval paradigm. *Journal of neuroscience methods*, 146(1):116–123, 2005.

[43] Jason J Braithwaite, Derrick G Watson, Robert Jones, and Mickey Rowe. A guide for analysing electrodermal activity (EDA) & skin conductance responses (SCRs) for psychological experiments. *Psychophysiology*, 49(1):1017–1034, 2013.

[44] Dilranjan S Wickramasuriya and Rose T Faghih. A bayesian filtering approach for tracking arousal from binary and continuous skin conductance features. *IEEE Transactions on Biomedical Engineering*, 2019.

[45] Swayambhoo Jain, Urvashi Oswal, Kevin Shuai Xu, Brian Eriksson, and Jarvis Haupt. A compressed sensing based decomposition of electrodermal activity signals. *IEEE Transactions on Biomedical Engineering*, 64(9):2142–2151, 2017.

[46] Noura Howell, Laura Devendorf, Rundong Kevin Tian, Tomás Vega Galvez, Nan-Wei Gong, Ivan Poupyrev, Eric Paulos, and Kimiko Ryokai. Biosignals as social cues: Ambiguity and emotional interpretation in social displays of skin conductance. In *Proceedings of the 2016 ACM Conference on Designing Interactive Systems*, pages 865–870. ACM, 2016.

[47] Srinidhi Parshi, Rafiul Amin, Hamid Fekri Azgomi, and Rose T Faghih. Mental workload classification via hierarchical latent dictionary learning: A functional near infrared spectroscopy study. In *2019 IEEE EMBS International Conference on Biomedical & Health Informatics (BHI)*, pages 1–4. IEEE, 2019.

[48] Zhong Yin, Mengyuan Zhao, Yongxiong Wang, Jingdong Yang, and Jianhua Zhang. Recognition of emotions using multimodal physiological signals and an ensemble deep learning model. *Computer methods and programs in biomedicine*, 140:93–110, 2017.

[49] Hugo F Posada-Quintero and Ki H Chon. Innovations in electrodermal activity data collection and signal processing: A systematic review. *Sensors*, 20(2):479, 2020.

[50] Dominik R Bach and Matthias Staib. A matching pursuit algorithm for inferring tonic sympathetic arousal from spontaneous skin conductance fluctuations. *Psychophysiology*, 52(8):1106–1112, 2015.

[51] Dominik R Bach. A head-to-head comparison of SCRalyze and Ledalab, two model-based methods for skin conductance analysis. *Biological psychology*, 103:63–68, 2014.

[52] Md Rafiul Amin and Rose T Faghih. Sparse deconvolution of electrodermal activity via continuous-time system identification. *IEEE Transactions on Biomedical Engineering*, 66(9):2585–2595, 2019.

[53] Md Rafiul Amin and Rose T Faghih. Inferring autonomic nervous system stimulation from hand and foot skin conductance measurements. In *2018 52nd Asilomar Conference on Signals, Systems, and Computers*, pages 655–660. IEEE, 2018.

[54] MD Rafiul Amin and Rose T Faghih. Robust inference of autonomic nervous system activation using skin conductance measurements: A multi-channel sparse system identification approach. *IEEE Access*, 7:173419–173437, 2019.

[55] Divesh Deepak Pednekar, Md Rafiul Amin, Hamid Fekri Azgomi, Kirstin Aschbacher, Leslie J Crofford, and Rose T Faghih. Characterization of cortisol dysregulation in fibromyalgia and chronic fatigue syndromes: A state-space approach. *IEEE Transactions on Biomedical Engineering*, 2020.

[56] Divesh Deepak Pednekar, Md Rafiul Amin, Hamid Fekri Azgomi, Kirstin Aschbacher, Leslie J Crofford, and Rose T Faghih. A system theoretic investigation of cortisol dysregulation in fibromyalgia patients with chronic fatigue. In *2019 41st Annual International Conference of the IEEE Engineering in Medicine and Biology Society (EMBC)*, pages 6896–6901. IEEE, 2019.

[57] Dominik R. Bach, Guillaume Flandin, Karl J. Friston, and Raymond J. Dolan. PsPM-SCRV10: Skin conductance responses to loud sounds, simultanously recorded from palm, fingers and foot, February 2017.

[58] Dominik R. Bach, Guillaume Flandin, Karl J. Friston, and Raymond J. Dolan. PsPM-SCRV5: Skin conductance responses to auditory oddballs, February 2017.

[59] Dominik R. Bach, Guillaume Flandin, Karl J. Friston, and Raymond J. Dolan. PsPM-SCRV6: Skin conductance responses to pain by electric stimulation, February 2017.

[60] Dominik R. Bach, Guillaume Flandin, Karl J. Friston, and Raymond J. Dolan. PsPM-SCRV7: Skin conductance responses to white noise sounds in quick succession, February 2017.

[61] Dominik R. Bach, Guillaume Flandin, Karl J. Friston, and Raymond J. Dolan. PsPM-SCRV9: Skin conductance responses to visual targets, February 2017.

[62] Hartmut Prautzsch, Wolfgang Boehm, and Marco Paluszny. *Bézier and B-spline techniques*. Springer Science & Business Media, 2013.

[63] Dominik R Bach, Karl J Friston, and Raymond J Dolan. An improved algorithm for model-based analysis of evoked skin conductance responses. *Biological psychology*, 94(3):490–497, 2013.

[64] Zahra Ghasemi, Jong Chan Lee, Chang-Sei Kim, Hao-Min Cheng, Shih-Hsien Sung, Chen-Huan Chen, Ramakrishna Mukkamala, and Jin-Oh Hahn. Estimation of cardiovascular risk predictors from non-invasively measured diametric pulse volume waveforms via multiple measurement information fusion. *Scientific reports*, 8(1):1–11, 2018.

[65] Akane Sano, Andrew J Phillips, Z Yu Amy, Andrew W McHill, Sara Taylor, Natasha Jaques, Charles A Czeisler, Elizabeth B Klerman, and Rosalind W Picard. Recognizing academic performance, sleep quality, stress level, and mental health using personality traits, wearable sensors and mobile phones. In *Wearable and Implantable Body Sensor Networks (BSN), 2015 IEEE 12th International Conference on*, pages 1–6. IEEE, 2015.

[66] Joseph F Murray. *Visual recognition, inference and coding using learned sparse overcomplete representations*. PhD thesis, University of California, San Diego, 2005.

[67] Gene H Golub, Michael Heath, and Grace Wahba. Generalized cross-validation as a method for choosing a good ridge parameter. *Technometrics*, 21(2):215–223, 1979.

[68] Rafal Zdunek and Andrzej Cichocki. Improved M-FOCUSS algorithm with overlapping blocks for locally smooth sparse signals. *IEEE Transactions on Signal Processing*, 56(10):4752–4761, 2008.

[69] Neil A Macmillan and C Douglas Creelman. *Detection theory: A user's guide*. Psychology press, 2004.

[70] Chaya S Moskowitz and Margaret S Pepe. Quantifying and comparing the predictive accuracy of continuous prognostic factors for binary outcomes. *Biostatistics*, 5(1):113–127, 2004.

[71] Vaughan G Macefield and B Gunnar Wallin. The discharge behaviour of single sympathetic neurones supplying human sweat glands. *Journal of the autonomic nervous system*, 61(3):277–286, 1996.

[72] Dominik R Bach, Giuseppe Castegnetti, Christoph W Korn, Samuel Gerster, Filip Melinscak, and Tobias Moser. Psychophysiological modeling: Current state and future directions. *Psychophysiology*, 55(11):e13214, 2018.

[73] John L Andreassi. *Psychophysiology: Human behavior & physiological response*. Psychology Press, 2013.

[74] Michael E Dawson, Anne M Schell, and Diane L Filion. The electrodermal system. *Handbook of psychophysiology*, 2:200–223, 2007.

[75] Hugo D Critchley. Electrodermal responses: what happens in the brain. *The Neuroscientist*, 8(2):132–142, 2002.

[76] Don C Fowles, Margaret J Christie, Robert Edelberg, William W Grings, David T Lykken, and Peter H Venables. Publication recommendations for electrodermal measurements. *Psychophysiology*, 18(3):232–239, 1981.

[77] Jacqueline Wijsman, Bernard Grundlehner, Hao Liu, Hermie Hermens, and Julien Penders. Towards mental stress detection using wearable physiological sensors. In *Engineering in Medicine and Biology Society, EMBC, 2011 Annual International Conference of the IEEE*, pages 1798–1801. IEEE, 2011.

[78] Dawei Zhou, Jiebo Luo, Vincent MB Silenzio, Yun Zhou, Jile Hu, Glenn Currier, and Henry A Kautz. Tackling mental health by integrating unobtrusive multimodal sensing. In *AAAI*, pages 1401–1409, 2015.

[79] Ivan Vargas, Alexandros N Vgontzas, James L Abelson, Rose T Faghih, Knashawn H Morales, and Michael L Perlis. Altered ultradian cortisol rhythmicity as a potential neurobiologic substrate for chronic insomnia. *Sleep medicine reviews*, 41:234–243, 2018.

[80] Akane Sano, Sara Taylor, Andrew W McHill, Andrew JK Phillips, Laura K Barger, Elizabeth Klerman, and Rosalind Picard. Identifying objective physiological markers

and modifiable behaviors for self-reported stress and mental health status using wearable sensors and mobile phones: Observational study. *Journal of medical Internet research*, 20(6):e210, 2018.

[81] Asma Ghandeharioun, Szymon Fedor, Lisa Sangermano, Dawn Ionescu, Jonathan Alpert, Chelsea Dale, David Sontag, and Rosalind Picard. Objective assessment of depressive symptoms with machine learning and wearable sensors data. In *Affective Computing and Intelligent Interaction (ACII), 2017 Seventh International Conference on*, pages 325–332. IEEE, 2017.

[82] D.S. Wickramasuriya, Chaoxian Qi, and Rose T Faghih. A state-space approach for detecting stress from electrodermal activity. In *Engineering in Medicine and Biology Society (EMBC), 2018 40th Annual International Conference of the IEEE*. IEEE, 2018.

[83] Dilranjan S Wickramasuriya, Md Amin, and Rose T Faghih. Skin conductance as a viable alternative for closing the deep brain stimulation loop in neuropsychiatric disorders. *Frontiers in neuroscience*, 13:780, 2019.

[84] M. R. Amin, D. S. Wickramasuriya, and R. T. Faghih. Wearable-machine interface architectures for mental stress. In *Engineering in Medicine and Biology Society (EMBC), 2019 41st Annual International Conference of the IEEE*.

[85] Jennifer A Healey and Rosalind W Picard. Detecting stress during real-world driving tasks using physiological sensors. *IEEE Trans. Intell. Transp. Syst.*, 6(2):156–166, 2005.

[86] Anne C Smith, Loren M Frank, Sylvia Wirth, Marianna Yanike, Dan Hu, Yasuo Kubota, Ann M Graybiel, Wendy A Suzuki, and Emery N Brown. Dynamic analysis of learning in behavioral experiments. *J. Neuroscience*, 24(2):447–461, 2004.

[87] Nynke A Groenewold, Esther M Opmeer, Peter de Jonge, André Aleman, and Sergi G Costafreda. Emotional valence modulates brain functional abnormalities in depression: evidence from a meta-analysis of fMRI studies. *Neuroscience & Biobehavioral Reviews*, 37(2):152–163, 2013.

[88] Keith Hawton, Carolina Casañas i Comabella, Camilla Haw, and Kate Saunders. Risk factors for suicide in individuals with depression: a systematic review. *Journal of affective disorders*, 147(1):17–28, 2013.

[89] Massimiliano Beghi, Jerrold F Rosenbaum, Cesare Cerri, and Cesare M Cornaggia. Risk factors for fatal and nonfatal repetition of suicide attempts: a literature review. *Neuropsychiatric disease and treatment*, 9:1725, 2013.

[90] Maurizio Pompili, Leo Sher, Gianluca Serafini, Alberto Forte, Marco Innamorati, Giovanni Dominici, David Lester, Mario Amore, and Paolo Girardi. Posttraumatic stress disorder and suicide risk among veterans: a literature review. *The Journal of nervous and mental disease*, 201(9):802–812, 2013.

[91] Ken-ichi Yamamoto, Toshikazu Shinba, and Mitsunobu Yoshii. Psychiatric symptoms of noradrenergic dysfunction: a pathophysiological view. *Psychiatry and clinical neurosciences*, 68(1):1–20, 2014.

[92] Kirtland C Peterson, Maurice F Prout, and Robert A Schwarz. *Post-traumatic stress disorder: A clinician's guide*. Springer Science & Business Media, 2013.

[93] Kelly Werner and James J Gross. Emotion regulation and psychopathology: A conceptual framework. 2010.

[94] Ulrich Hegerl, Christian Sander, and Tilman Hensch. Arousal regulation in affective disorders. *Systems neuroscience in depression*, pages 341–370, 2016.

[95] Javad Birjandtalab, Diana Cogan, Maziyar Baran Pouyan, and Mehrdad Nourani. A non-EEG biosignals dataset for assessment and visualization of neurological status. In *Signal Processing Systems (SiPS), 2016 IEEE International Workshop on*, pages 110–114. IEEE, 2016.

[96] HA Preisig and DWT Rippin. Theory and application of the modulating function method—i. review and theory of the method and theory of the spline-type modulating functions. *Computers & chemical engineering*, 17(1):1–16, 1993.

[97] GP Rao and H Unbehauen. Identification of continuous-time systems. *IEE Proceedings-Control theory and applications*, 153(2):185–220, 2006.

[98] AMIT PATRA and HEINZ UNBEHAUEN. Identification of a class of nonlinear continuous-time systems using hartley modulating functions. *International Journal of Control*, 62(6):1431–1451, 1995.

[99] H Unbehauen and P Rao. Identification of continuous-time systems: A tutorial. *IFAC Proceedings Volumes*, 30(11):973–999, 1997.

[100] Square Daniel-Berhe and Heinz Unbehauen. Bilinear continuous-time systems identification via hartley-based modulating functions. *Automatica*, 34(4):499–503, 1998.

[101] Ronald N Bracewell. *The hartley transform*. Oxford University Press, Inc., 1986.

[102] Hugues Garnier, MICHEL Mensler, and ALAIN Richard. Continuous-time model identification from sampled data: implementation issues and performance evaluation. *International journal of Control*, 76(13):1337–1357, 2003.

[103] AE Pearson. Explicit parameter identification for a class of nonlinear input/output differential operator models. In *Decision and Control, 1992., Proceedings of the 31st IEEE Conference on*, pages 3656–3660. IEEE, 1992.

[104] Chong L Lim, Chris Rennie, Robert J Barry, Homayoun Bahramali, Ilario Lazzaro, Barry Manor, and Evian Gordon. Decomposing skin conductance into tonic and phasic components. *International Journal of Psychophysiology*, 25(2):97–109, 1997.

[105] Abbas Kazemipour, Ji Liu, Krystyna Solarana, Daniel A Nagode, Patrick O Kanold, Min Wu, and Behtash Babadi. Fast and stable signal deconvolution via compressible state-space models. *IEEE Transactions on Biomedical Engineering*, 65(1):74–86, 2017.

[106] Dilranjan S Wickramasuriya and Rose T Faghih. A marked point process filtering approach for tracking sympathetic arousal from skin conductance. *IEEE Access*, 2020.

[107] Dilranjan S Wickramasuriya and Rose T Faghih. A novel filter for tracking real-world cognitive stress using multi-time-scale point process observations. In *2019 41st Annual International Conference of the IEEE Engineering in Medicine and Biology Society (EMBC)*, pages 599–602. IEEE, 2019.

[108] Dilranjan S Wickramasuriya and Rose T Faghih. A cortisol-based energy decoder for investigation of fatigue in hypercortisolism. In *2019 41st Annual International Conference of the IEEE Engineering in Medicine and Biology Society (EMBC)*, pages 11–14. IEEE, 2019.

[109] Dilranjan S Wickramasuriya and Rose T Faghih. Online and offline anger detection via electromyography analysis. In *2017 IEEE Healthcare Innovations and Point of Care Technologies (HI-POCT)*, pages 52–55. IEEE, 2017.

[110] D. S. Wickramasuriya and R.T. Faghih. A mixed-filter algorithm for arousal tracking from galvanic skin response and heart rate measurements. In *IEEE-EMBS Iternational Conference on Biomedical and Health Informatics*, May 2019.

[111] Mohammad Badri Ahmadi, Alexander Craik, Hamid Fekri Azgomi, Joseph T Francis, Jose L Contreras-Vidal, and Rose T Faghih. Real-time seizure state tracking using two channels: A mixed-filter approach. In *2019 53rd Asilomar Conference on Signals, Systems, and Computers*, pages 2033–2039. IEEE, 2019.

[112] Akshay Sujatha Ravindran, Sho Nakagome, Dilranjan S Wickramasuriya, Jose L Contreras-Vidal, and Rose T Faghih. Emotion recognition by point process characterization of heartbeat dynamics. In *2019 IEEE Healthcare Innovations and Point of Care Technologies,(HI-POCT)*, pages 13–16. IEEE, 2019.

[113] Hamid Fekri Azgomi, Dilranjan S Wickramasuriya, and Rose T Faghih. State-space modeling and fuzzy feedback control of cognitive stress. In *2019 41st Annual International Conference of the IEEE Engineering in Medicine and Biology Society (EMBC)*, pages 6327–6330. IEEE, 2019.

[114] Hamid Fekri Azgomi and Rose T Faghih. A wearable brain machine interface architecture for regulation of energy in hypercortisolism. In *2019 53rd Asilomar Conference on Signals, Systems, and Computers*, pages 254–258. IEEE, 2019.

[115] Rose Taj Faghih, Munther A Dahleh, and Emery N Brown. An optimization formulation for characterization of pulsatile cortisol secretion. *Frontiers in neuroscience*, 9:228, 2015.

[116] Manuel S Seet, Md Rafiul Amin, Nida I Abbasi, Junji Hamano, Anumita Chaudhury, Anastasios Bezerianos, Rose T Faghih, Nitish V Thakor, and Andrei Dragomir. Olfactory-induced positive affect and autonomic response as a function of hedonic and intensity attributes of fragrances. In *2020 42nd Annual International Conference of the IEEE Engineering in Medicine & Biology Society (EMBC)*, pages 3170–3173. IEEE, 2020.

[117] Ah Young Kim, Eun Hye Jang, Seunghwan Kim, Kwan Woo Choi, Hong Jin Jeon, Han Young Yu, and Sangwon Byun. Automatic detection of major depressive disorder using electrodermal activity. *Scientific reports*, 8(1):1–9, 2018.

[118] Youngsun Kong, Hugo F Posada-Quintero, and Ki H Chon. Pain detection using a smartphone in real time. In *2020 42nd Annual International Conference of the IEEE Engineering in Medicine & Biology Society (EMBC)*, pages 4526–4529. IEEE, 2020.

[119] Hugo F Posada-Quintero, Jeffrey B Bolkhovsky, Michael Qin, and Ki H Chon. Human performance deterioration due to prolonged wakefulness can be accurately detected using time-varying spectral analysis of electrodermal activity. *Human factors*, 60(7):1035–1047, 2018.

[120] Marco Sarchiapone, Carla Gramaglia, Miriam Iosue, Vladimir Carli, Laura Mandelli, Alessandro Serretti, Debora Marangon, and Patrizia Zeppegno. The association between electrodermal activity (EDA), depression and suicidal behaviour: A systematic review and narrative synthesis. *BMC psychiatry*, 18(1):1–27, 2018.

[121] Hamid Fekri Azgomi, Iahn Cajigas, and Rose T Faghih. Closed-loop cognitive stress regulation using fuzzy control in wearable-machine interface architectures. *IEEE Access*, 9:106202–106219, 2021.

[122] Gobinath Aroganam, Nadarajah Manivannan, and David Harrison. Review on wearable technology sensors used in consumer sport applications. *Sensors*, 19(9):1983, 2019.

[123] Dwaipayan Biswas, Neide Simões-Capela, Chris Van Hoof, and Nick Van Helleputte. Heart rate estimation from wrist-worn photoplethysmography: A review. *IEEE Sensors Journal*, 19(16):6560–6570, 2019.

[124] Tania Pereira, Nate Tran, Kais Gadhoumi, Michele M Pelter, Duc H Do, Randall J Lee, Rene Colorado, Karl Meisel, and Xiao Hu. Photoplethysmography based atrial fibrillation detection: a review. *NPJ digital medicine*, 3(1):1–12, 2020.

[125] Li-Ming Bai, Ming-Hui Fan, Chen-Hui Feng, and Liang-Hung Wang. Using an adaptive filter to remove ECG motion artifact interference. In *2018 IEEE International Conference on Consumer Electronics-Taiwan (ICCE-TW)*, pages 1–2. IEEE, 2018.

[126] Waltenegus Dargie and Jannis Lilienthal. Review of motion artifacts removing techniques for wireless electrocardiograms. In *2020 IEEE 23rd International Conference*

on Information Fusion (FUSION), pages 1–8. IEEE, 2020.

[127] Atilla Kilicarslan and Jose Luis Contreras Vidal. Characterization and real-time removal of motion artifacts from EEG signals. *Journal of neural engineering*, 16(5):056027, 2019.

[128] Yalan Ye, Yunfei Cheng, Wenwen He, Mengshu Hou, and Zhilin Zhang. Combining nonlinear adaptive filtering and signal decomposition for motion artifact removal in wearable photoplethysmography. *IEEE Sensors Journal*, 16(19):7133–7141, 2016.

[129] Sayeed Shafayet Chowdhury, Rakib Hyder, Md Samzid Bin Hafiz, and Mohammad Ariful Haque. Real-time robust heart rate estimation from wrist-type PPG signals using multiple reference adaptive noise cancellation. *IEEE journal of biomedical and health informatics*, 22(2):450–459, 2016.

[130] Chung Song Kim, Jinwei Sun, Dan Liu, Qisong Wang, and Sung Gyun Paek. Removal of ocular artifacts using ica and adaptive filter for motor imagery-based BCI. *IEEE/CAA journal of automatica sinica*, 2017.

[131] Christopher Beach, Mingjie Li, Ertan Balaban, and Alexander J Casson. Motion artefact removal in electroencephalography and electrocardiography by using multichannel inertial measurement units and adaptive filtering. *Healthcare Technology Letters*, 8(5):128, 2021.

[132] Choong-Ki Kim, Seungduk Lee, Dalkwon Koh, and Beop-Min Kim. Development of wireless nirs system with dynamic removal of motion artifacts. *Biomedical Engineering Letters*, 1(4):254–259, 2011.

[133] Sara Taylor, Natasha Jaques, Weixuan Chen, Szymon Fedor, Akane Sano, and Rosalind Picard. Automatic identification of artifacts in electrodermal activity data. In *2015 37th Annual International Conference of the IEEE Engineering in Medicine and Biology Society (EMBC)*, pages 1934–1937. IEEE, 2015.

[134] Yuning Zhang, Maysam Haghdan, and Kevin S Xu. Unsupervised motion artifact detection in wrist-measured electrodermal activity data. In *Proceedings of the 2017 ACM International Symposium on Wearable Computers*, pages 54–57, 2017.

[135] Jose Llanes-Jurado, Lucía Amalia Carrasco-Ribelles, Mariano Alcañiz, and Javier Marín-Morales. Automatic artifact recognition and correction for electrodermal activity in uncontrolled environments. 2021.

[136] Weixuan Chen, Natasha Jaques, Sara Taylor, Akane Sano, Szymon Fedor, and Rosalind W Picard. Wavelet-based motion artifact removal for electrodermal activity. In *2015 37th Annual International Conference of the IEEE Engineering in Medicine and Biology Society (EMBC)*, pages 6223–6226. IEEE, 2015.

[137] Rainer Schneider, Stefan Schmidt, Markus Binder, Florian Schäfer, and Harald Walach. Respiration-related artifacts in eda recordings: introducing a standardized method to overcome multiple interpretations. *Psychological reports*, 93(3):907–920, 2003.

[138] Gaang Lee, Byungjoo Choi, Houtan Jebelli, Changbum Ryan Ahn, and SangHyun Lee. Reference signal-based method to remove respiration noise in electrodermal activity (EDA) collected from the field. In *Computing in civil engineering 2019: Data,*

sensing, and analytics, pages 17–25. American Society of Civil Engineers Reston, VA, 2019.

[139] Paulo SR Diniz. *Adaptive filtering*, volume 4. Springer, 1997.

[140] Md Rafiul Amin and Rose T Faghih. Physiological characterization of electrodermal activity enables scalable near real-time autonomic nervous system activation inference. Manuscript submitted for publication.

[141] The Mathworks, Inc., Natick, Massachusetts. *MATLAB version 9.9.0.1467703 (R2020b)*, 2020.

[142] Jacob Benesty, Constantin Paleologu, and Silviu Ciochina. On regularization in adaptive filtering. *IEEE Transactions on Audio, Speech, and Language Processing*, 19(6):1734–1742, 2010.

[143] Khaled A Mayyas and Tyseer Aboulnasr. Leaky lms: A detailed analysis. In *Proceedings of ISCAS'95-International Symposium on Circuits and Systems*, volume 2, pages 1255–1258. IEEE, 1995.

[144] Eisuke Horita, Keitaro Sumiya, Hiroyuki Urakami, and Satoru Mitsuishi. A leaky RLS algorithm: Its optimality and implementation. *IEEE transactions on signal processing*, 52(10):2924–2936, 2004.

[145] S Selvan and R Srinivasan. Removal of ocular artifacts from EEG using an efficient neural network based adaptive filtering technique. *IEEE Signal Processing Letters*, 6(12):330–332, 1999.

[146] Danilo Comminiello, Michele Scarpiniti, Luis A Azpicueta-Ruiz, Jerónimo Arenas-García, and Aurelio Uncini. Functional link adaptive filters for nonlinear acoustic echo cancellation. *IEEE Transactions on Audio, Speech, and Language Processing*, 21(7):1502–1512, 2013.

[147] Joel A Tropp and Anna C Gilbert. Signal recovery from random measurements via orthogonal matching pursuit. *IEEE Transactions on information theory*, 53(12):4655–4666, 2007.

[148] Shuai Huang and Trac D Tran. Sparse signal recovery via generalized entropy functions minimization. *IEEE Transactions on Signal Processing*, 67(5):1322–1337, 2018.

[149] Ali Mousavi and Richard G Baraniuk. Learning to invert: Signal recovery via deep convolutional networks. In *2017 IEEE international conference on acoustics, speech and signal processing (ICASSP)*, pages 2272–2276. IEEE, 2017.

[150] Youye Xie, Zifan Wang, Weiping Pei, and Gongguo Tang. Fast approximation of non-negative sparse recovery via deep learning. In *2019 IEEE International Conference on Image Processing (ICIP)*, pages 2921–2925. IEEE, 2019.

[151] Scott Wisdom, Thomas Powers, James Pitton, and Les Atlas. Building recurrent networks by unfolding iterative thresholding for sequential sparse recovery. In *2017 IEEE International Conference on Acoustics, Speech and Signal Processing (ICASSP)*, pages 4346–4350. IEEE, 2017.

[152] Rahul Krishnan, Uri Shalit, and David Sontag. Structured inference networks for nonlinear state space models. In *Proceedings of the AAAI Conference on Artificial*

Intelligence, volume 31, 2017.

[153] SSAL Seyedtabaii and L Seyedtabaii. Kalman filter based adaptive reduction of motion artifact from photoplethysmographic signal. *World Acad. Sci. Eng. Technol*, 37:173–176, 2008.

[154] Maziar Raissi, Paris Perdikaris, and George E Karniadakis. Physics-informed neural networks: A deep learning framework for solving forward and inverse problems involving nonlinear partial differential equations. *Journal of Computational Physics*, 378:686–707, 2019.

[155] Olivier Nerrand, Pierre Roussel-Ragot, Léon Personnaz, Gérard Dreyfus, and Sylvie Marcos. Neural networks and nonlinear adaptive filtering: Unifying concepts and new algorithms. *Neural computation*, 5(2):165–199, 1993.

[156] Phattarapong Sawangjai, Manatsanan Trakulruangroj, Chiraphat Boonnag, Maytus Piriyajitakonkij, Rajesh Kumar Tripathy, Thapanun Sudhawiyangkul, and Theerawit Wilaiprasitporn. Eeganet: Removal of ocular artifact from the EEG signal using generative adversarial networks. *IEEE Journal of Biomedical and Health Informatics*, 2021.

[157] Kristin J Heaton, James R Williamson, Adam C Lammert, Katherine R Finkelstein, Caitlin C Haven, Douglas Sturim, Christopher J Smalt, and Thomas F Quatieri. Predicting changes in performance due to cognitive fatigue: A multimodal approach based on speech motor coordination and electrodermal activity. *The Clinical Neuropsychologist*, 34(6):1190–1214, 2020.

[158] Jon Xavier Genty, Md RAFIUL Amin, Natalie D Shaw, Elizabeth Klerman, and Rose Taj Faghih. Sparse deconvolution of pulsatile growth hormone secretion in adolescents. *IEEE/ACM Transactions on Computational Biology and Bioinformatics*, 2021.

A Appendix

A.1 Additional Results for Chapter 2

Figure 55, 56, 57, 58, 59, 60, 61, 62, 63 and 64 shows deconvolution results from all five datasets where in each panel, i) the top sub-panel shows the experimental SC signal (blue stars), the reconstructed SC signal (red curve), the estimated tonic component (green curve), and the timings of the auditory stimulations (gray vertical lines); ii) the bottom sub-panel shows the estimated phasic component (blue curve), estimated neural stimuli timings and amplitudes (black vertical lines) due to SNS activation and the timings of the auditory stimuli (gray vertical lines). The number before the hyphen in the participant ID represents the dataset ID. Table 10 shows the estimated rise times (τ_r), decay times (τ_d), number of SCRs ($||\mathbf{u}||_0$), regularization parameters (λ_1 and λ_2), multiple correlation coefficient (R^2), and deconvolution run-times for all participants from dataset 1. Figure 65 and 66 shows the quantile-quantile plots of the SC model residual errors for all the thirteen female participants and thirteen male participant from dataset 1. Each of the panels in Figure 65 and 66 displays the quantile-quantile plot of the SC model residual errors; the graph shows that the residual errors are Gaussian. Slight deviation from the straight line suggest that there is a scope of improvement in the model. The number before the hyphen in the participant ID represents the dataset ID. The quantile-quantile plots suggests that the model captures the SC dynamics, and the SC residual errors have a white Gaussian structure. However, slight deviations from the straight line also suggest that there is a scope of improvement in the current model.

Figure 67 and 68 shows deconvolution results from simulated phasic SC data for thirteen female and thirteen male participants simulated using the results obtained from experimental data from dataset 1. In each of the panels in Figure 67 and 68, i) the top sub-panel shows the ground truth for SC signal (blue stars), the reconstructed SC signal (red curve), the ground truth for tonic component (red stars), the estimated tonic component (green

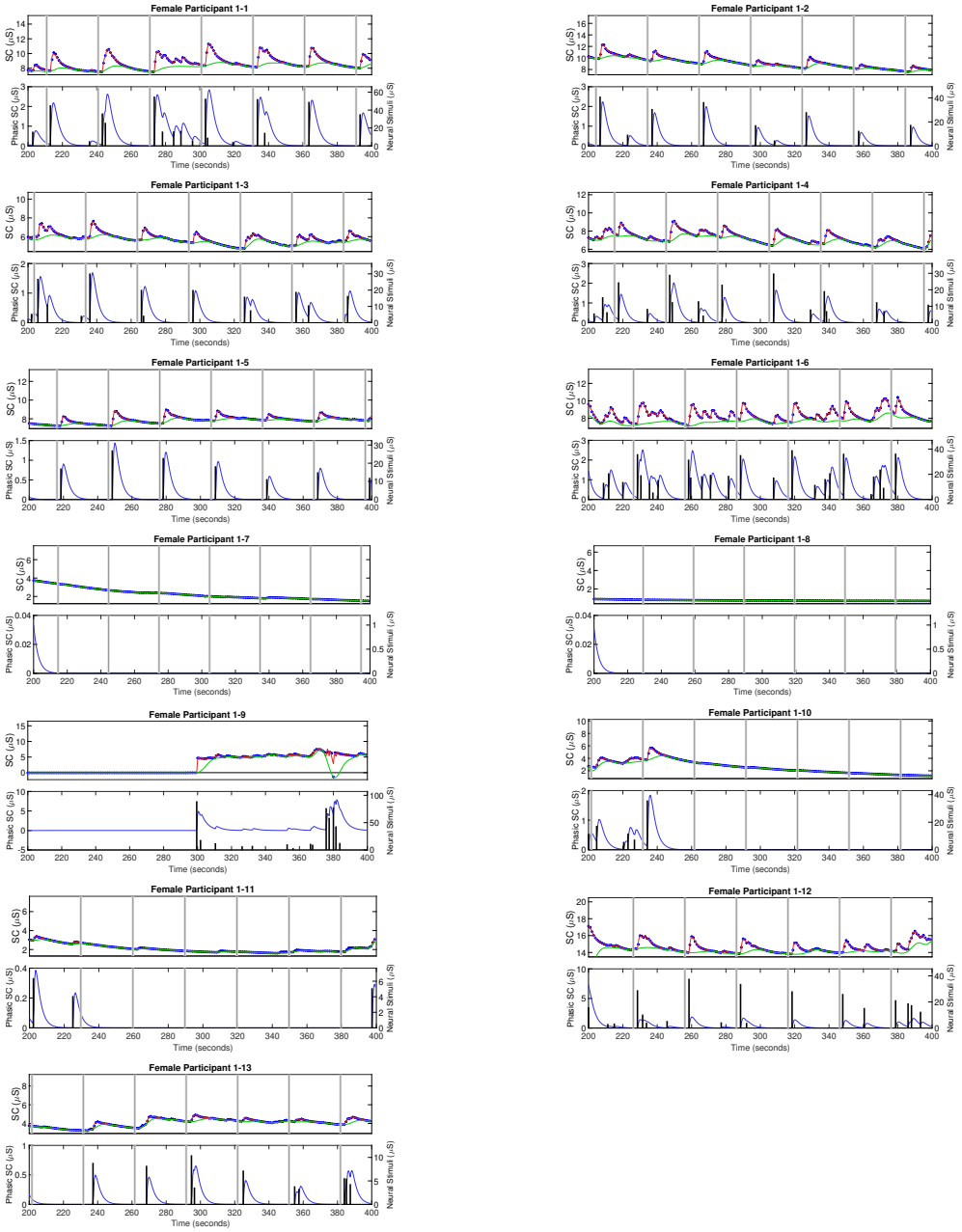

Figure 55: **Estimated Decomposition of the Experimental SC Signals for Thirteen Female Participants from Dataset 1.**

curve), and ground truth for the neural stimuli (pink vertical lines); ii) the bottom sub-panel shows the estimated phasic component (blue curve), estimated neural stimuli timings and amplitudes (black vertical lines) due to SNS activation and the ground truth for the neural stimuli (pink vertical lines). The number before the hyphen in the participant ID

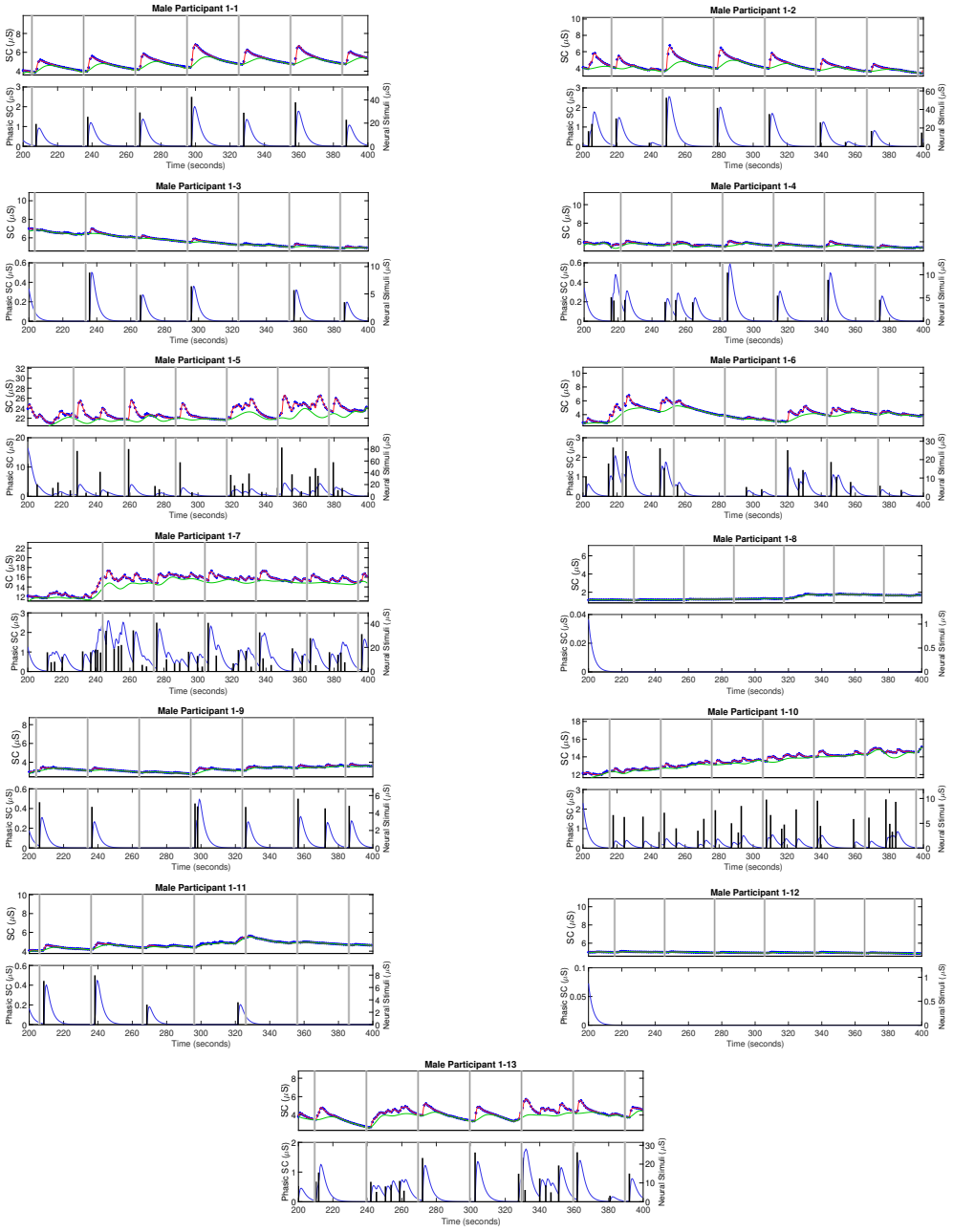

Figure 56: **Estimated Decomposition of the Experimental SC Signals for Thirteen Male Participants from Dataset 1.**

represents the dataset ID. The quantile-quantile plots in Figure 69 and 70 also show that the residuals error follow Gaussian structure. In this two figures, each of the panels displays the quantile-quantile plot of the SC model residual errors; the graph shows that the residual errors are Gaussian. The number before the hyphen in the participant ID represents the

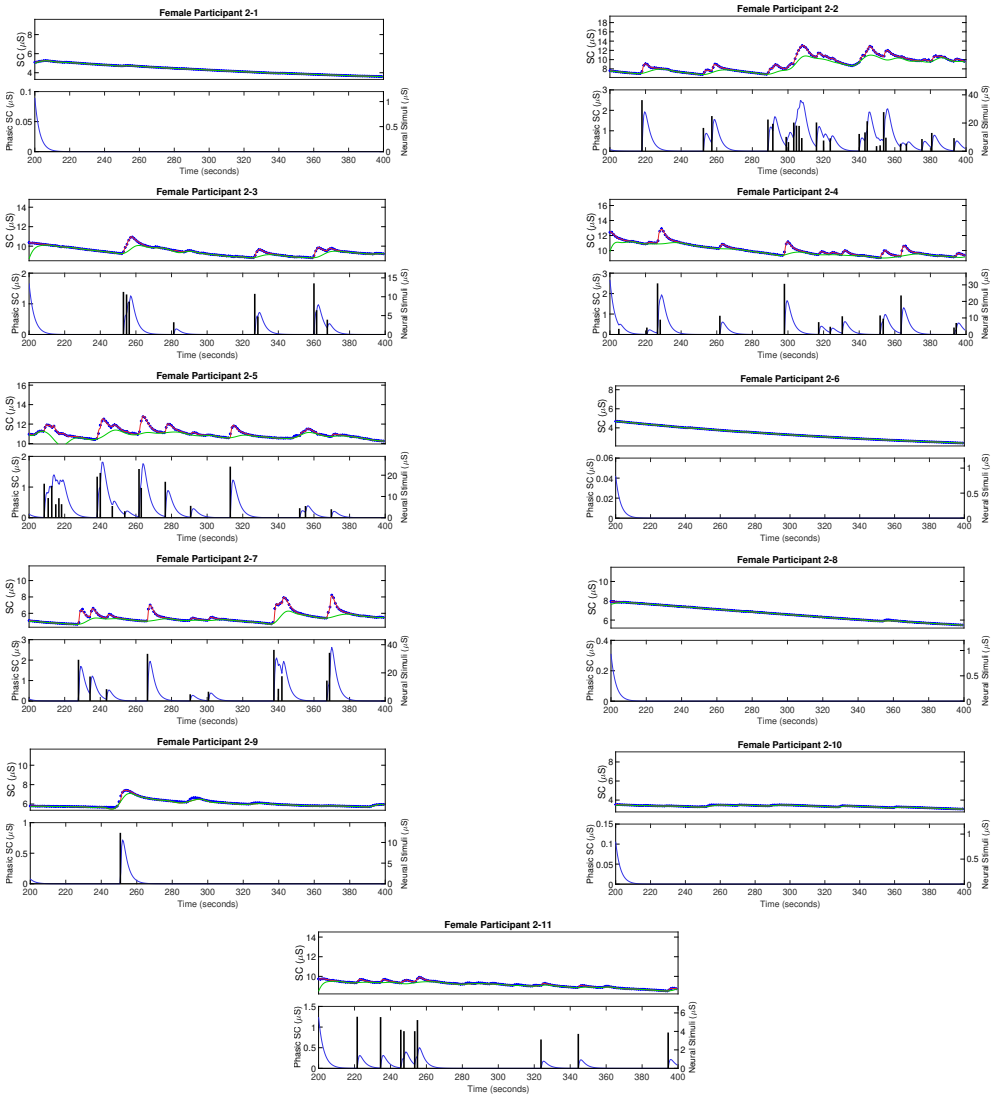

Figure 57: **Estimated Decomposition of the Experimental SC Signals for Thirteen Female from Dataset 2.**

dataset ID. It should also be noted that we have used eight different random initialization values for SCR shape parameters in parallel in eight different CPU cores while solving the optimization problem in (15). The run-time reported in Table 10 only shows run time for the result correspond to the initialization that took maximum time. Table 11, shows the results from simulated data. In Table 11, Here $\hat{\tau}_r$ and $\hat{\tau}_d$ denote the estimated rise time and decay time for the simulated SC data. The SC signal is simulated with 25 dB Gaussian noise.

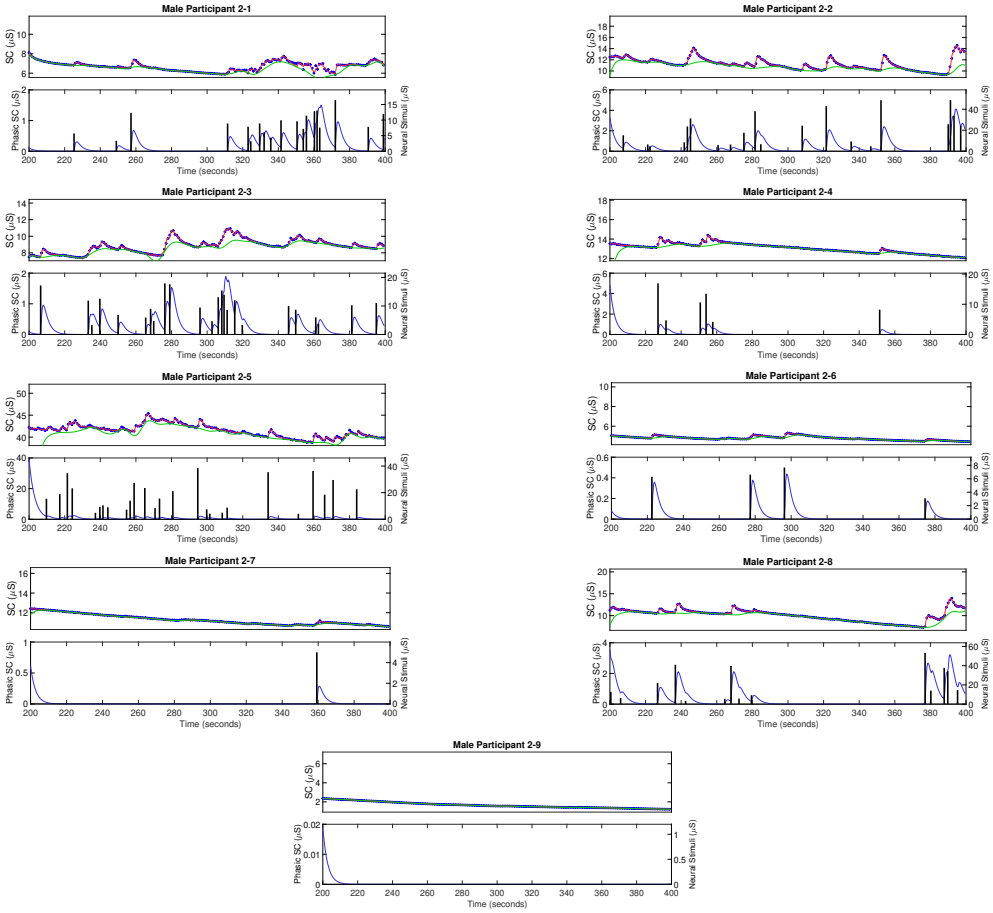

Figure 58: **Estimated Decomposition of the Experimental SC Signals for Thirteen Male from Dataset 2.**

To perform an efficacy analysis of how our algorithm performs in distinguishing between event-related and non-event-related SCRs, we derive receiver operating characteristics (ROC) curves. We label all the SCRs that have been detected within 5 seconds after auditory stimulations as event-related SCRs (positive class). The rest of the detected SCRs are labeled as the non-event-related SCRs (negative class). We consider the amplitudes of the SCRs as the classification scores within the subjects for obtaining the ROC curves [69, 70]. Figure 71 shows the individual ROC curves with the area under the curve (AUC) ranging from 0.5611 to 1 with a median of 0.8636 and a mean of 0.9130. In this figure, each panel shows the ROC curve for each participants in Dataset 1 based on the estimated $\mathbf{u}$ from our approach. The last panel shows the overall ROC obtained by combining all the

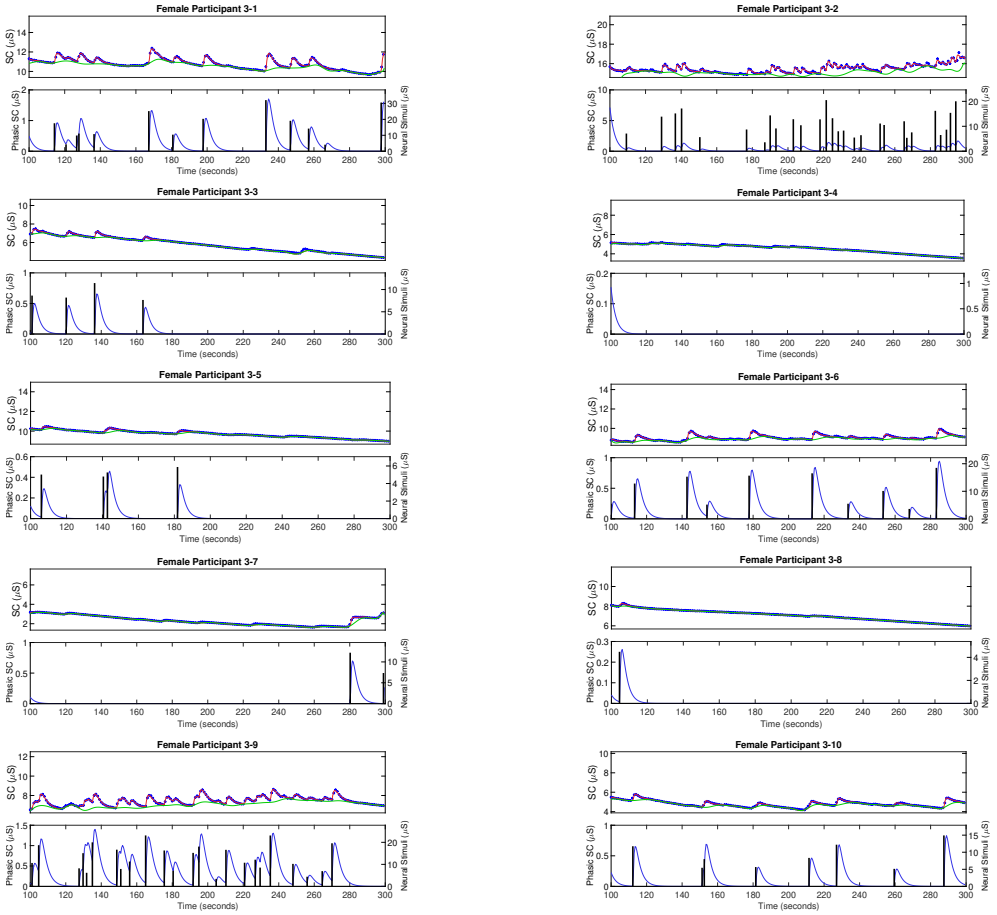

Figure 59: **Estimated Decomposition of the Experimental SC Signals for Thirteen Female from Dataset 3.**

normalized **u** from each of the individual participants. The number before the hyphen in the participant ID represents the dataset ID. The corresponding overall AUC is 0.864 for Dataset 1.

To perform a further comparison between the deconvolution results from different algorithms, we have added noise to the raw experimental data. The noise level is selected in a way that the signal SNR is 25 dB for the corresponding phasic component estimated during deconvolution. In the case of, cvxEDA we have used three configurations, two with fixed parameters within the bound mentioned in [23] and one with optimized parameters obtained from our approach. We performed deconvolution on six participants as an example. Figure 72-77 show the comparative results from each participants. In Figure 72-77,

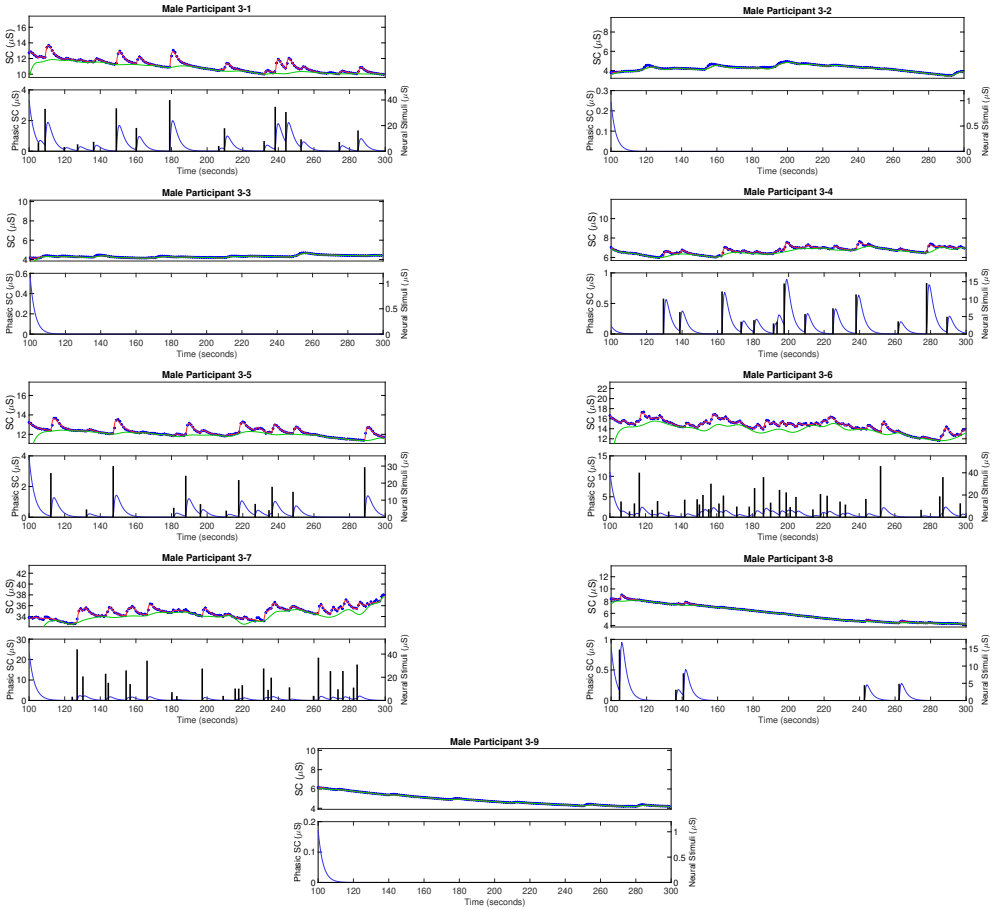

Figure 60: **Estimated Decomposition of the Experimental SC Signals for Thirteen Male from Dataset 3.**

each panel shows the decomposition performance based on Experimental SC signal with 25 dB noise with respect to the corresponding phasic component based on the corresponding deconvolution results. The top to bottom shows the result using CDA - LedaLab [29], DDA - LedaLab [21], DCM - PsPM [22], MP - PsPM [50], cvxEDA with three different configurations [23], sparsEDA [24], and our proposed approach, respectively. In each panel, blue stars represent the simulated data, pink vertical lines represent the ground truth neural stimuli, black vertical lines represent the recovered neural stimuli, the green curve represents the tonic component, the black dotted curve represents the tonic component result obtain with the our previous deconvolution without any noise, and the red curve represents the reconstructed signal. The estimated neural stimuli for all the panels except for the last

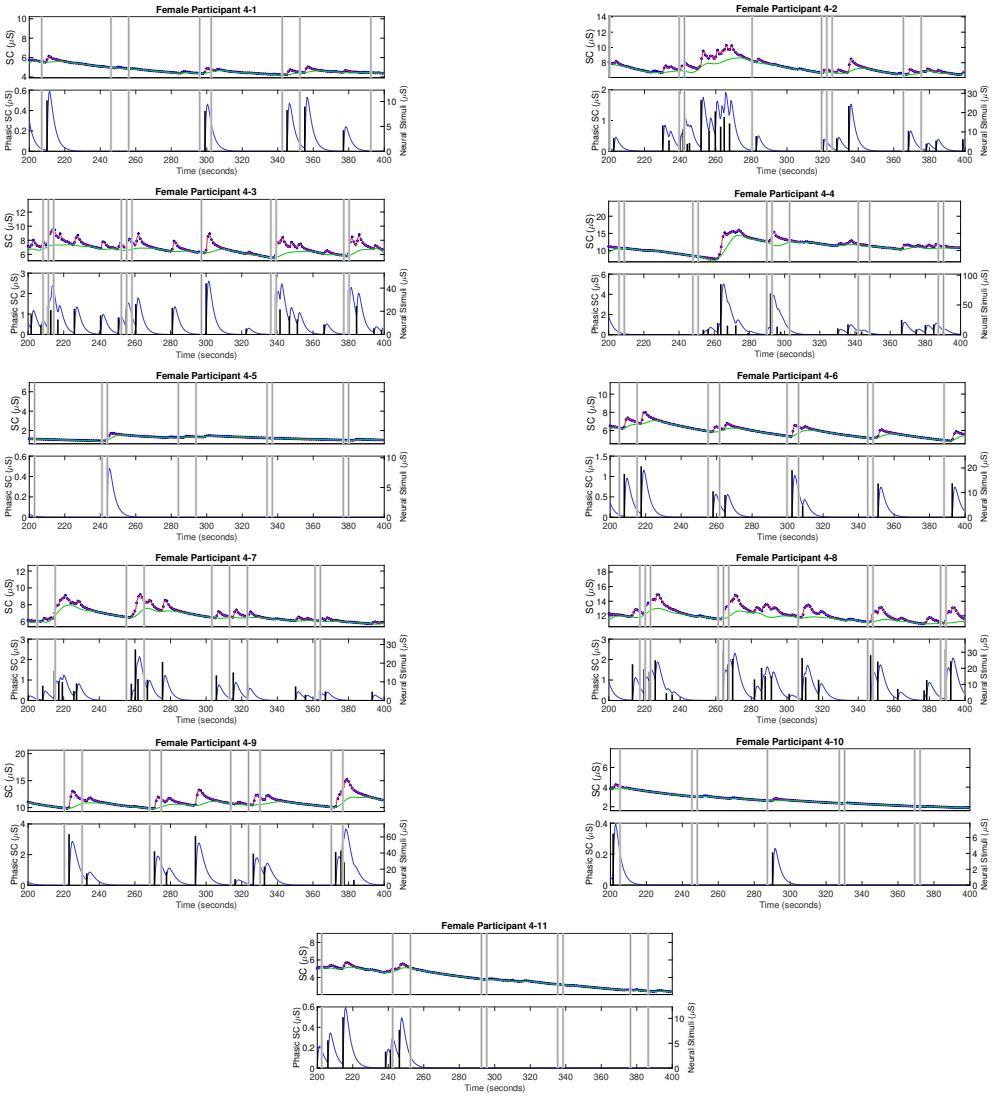

Figure 61: **Estimated Decomposition of the Experimental SC Signals for Eleven Female from Dataset 4.**

one is normalized from zero to one to avoid any amplitude scaling originating from different methods for a fair comparison. Table 12 and 13 show the number of inferred pulses and corresponding multiple correlation coefficients R^2. As sparsEDA does not provide both the phasic and tonic components, we did not calculate the corresponding R^2. R^2 values are almost similar for all the approaches including ours. However, the results show that except for our approach and sparsEDA, other methods detect more numbers of spikes in neural stimuli, and therefore, there are potential chances of overfitting in the results from

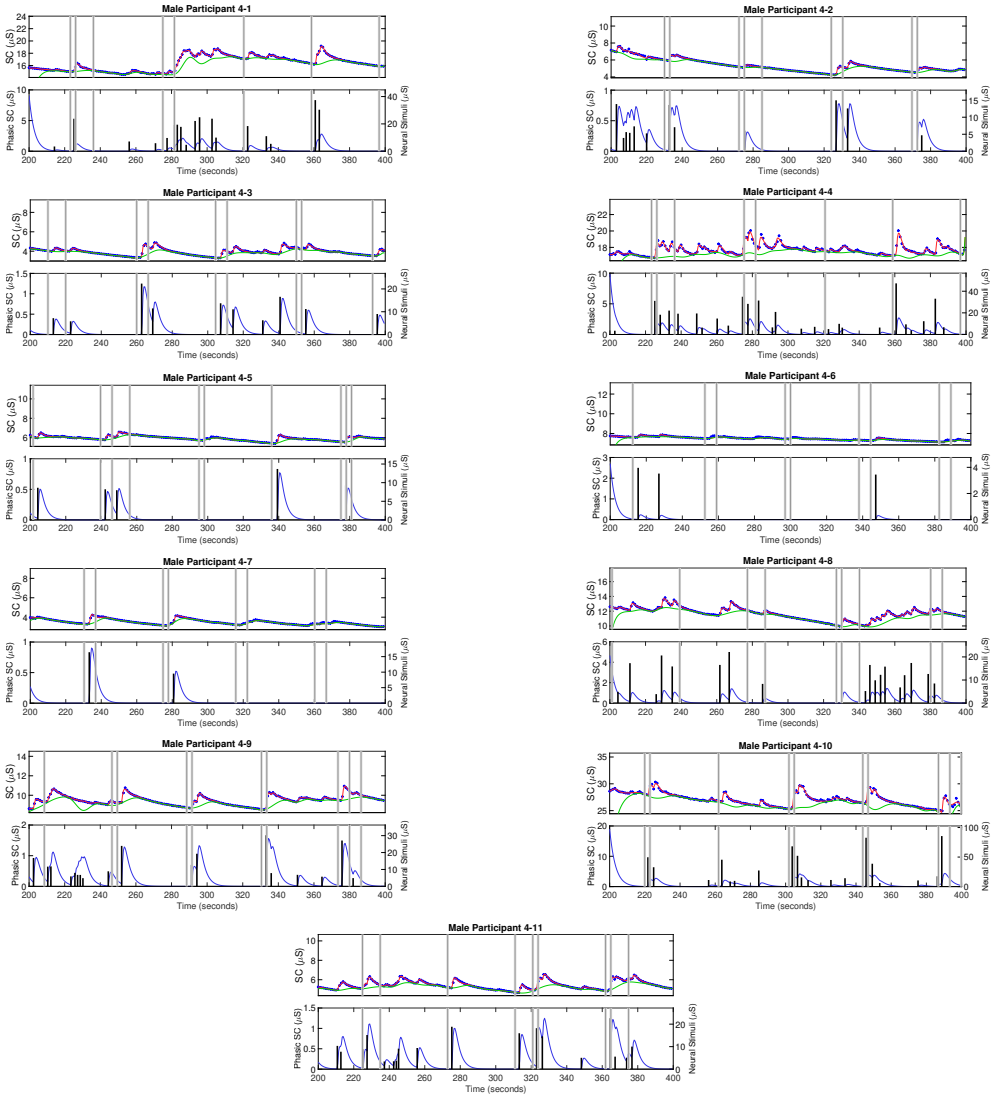

Figure 62: **Estimated Decomposition of the Experimental SC Signals for Eleven Male from Dataset 4.**

other algorithms. From Figure 72-77, we further observe that sparsEDA is missing a lot of obvious pulses. Figure 72-77 also show that with different values of τ_r and τ_d, how cvxEDA performs. The results reveal that the different fixed physiological parameters can lead to a different solution for the neural stimuli. For example in Figure 73 and 75, with the optimized parameters from our approach, the amplitude of the detected impulses reduced after detection of the first neural stimuli impulse after an auditory stimulation compared to the fixed parameters. The solutions have improved when the optimized τ_r and τ_d are used. It

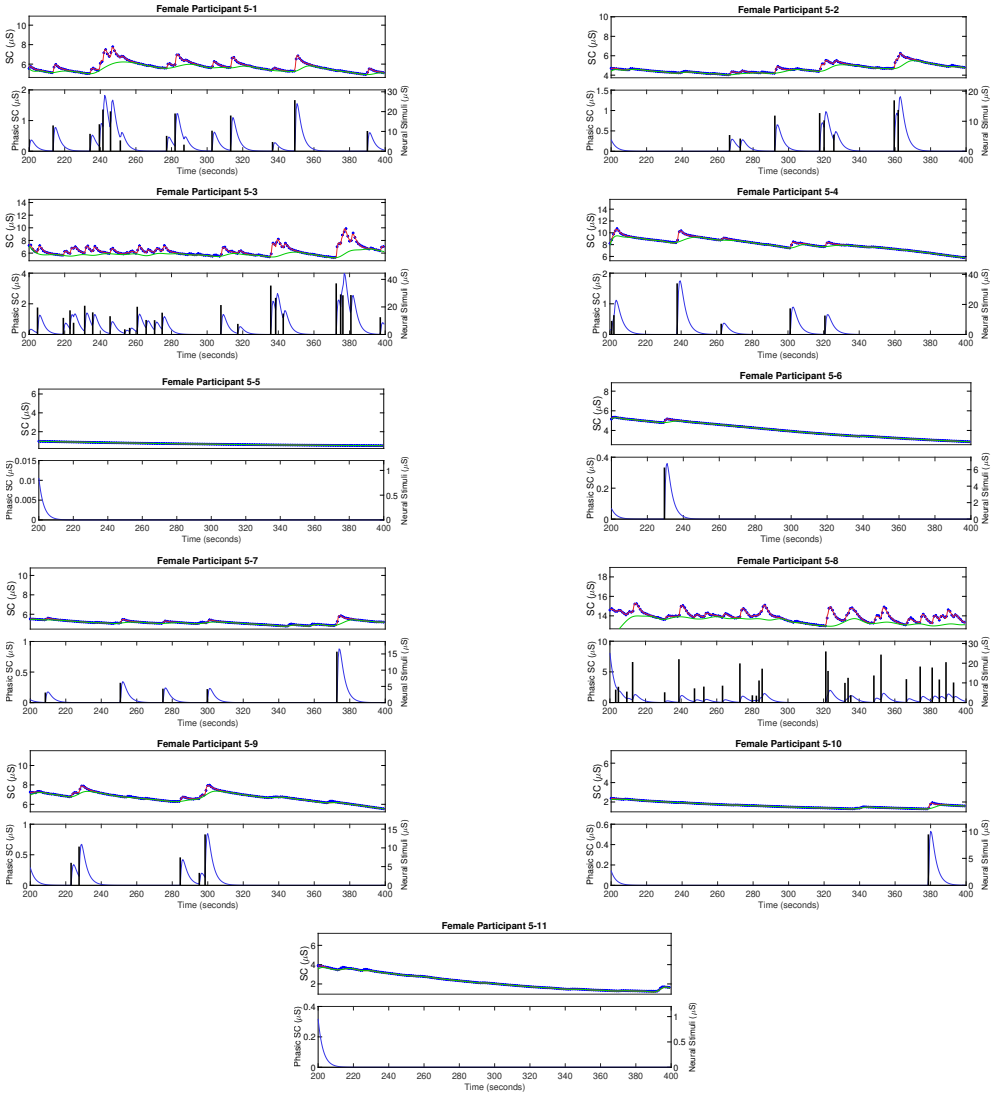

Figure 63: **Estimated Decomposition of the Experimental SC Signals for Eleven Female from Dataset 5.**

can be further improved, if we manually tune the regularization related to the smoothness and sparsity penalization in their optimization formulation.

We have used the same knot size as our approach for the cubic B-spline functions in all the comparisons with cvxEDA. On the other hand, we have kept the regularization parameters in cvxEDA for the sparsity prior on u and energy prior on q to the default value to show how optimizing it is improving in our approach. In the case of sparsEDA, we have relaxed the constraints in a way that produces the least sparse solution as it tends

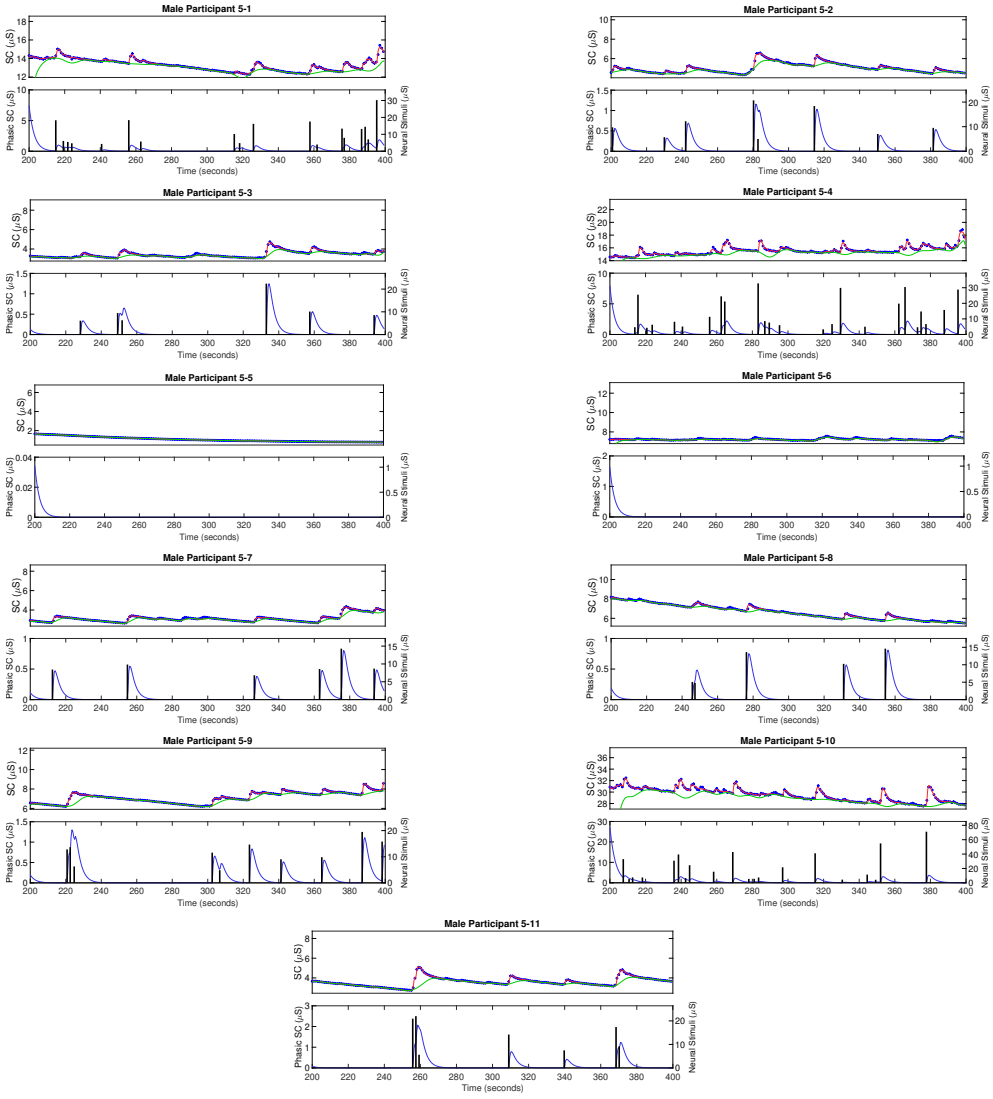

Figure 64: **Estimated Decomposition of the Experimental SC Signals for Eleven Male from Dataset 5.**

to provide an overly sparse solution. For all the other methods, we have considered default parameters. Further, we have used a 4 Hz version of the signal while applying the other algorithms and we compare it against our results obtained from the 2 Hz version signal. This shows that our algorithm is performing better even if we have a lower number of samples (i.e. compressed sensing regime).

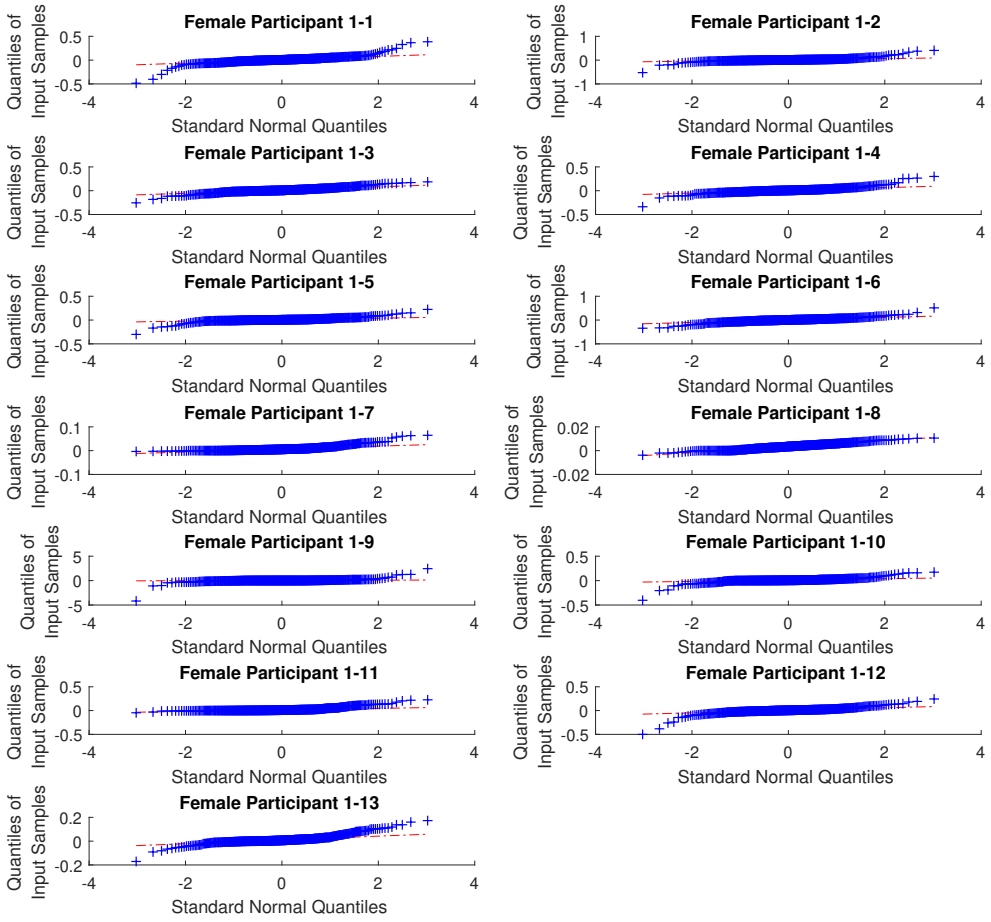

Figure 65: **White Gaussian Structure in the Model Residual Errors for SC Data Collected From Thirteen Female Participants.**

A.2 Additional Results for Chapter 3

Figure 78 and 79 show deconvolution results from six female and six male participants, respectively. In each of the panels in Figure 78 and 79, i) the top subpanel shows the experimental (red stars) and the estimated (green curve) phasic components corresponding to the middle phalanx of the hand; ii) the middle subpanel shows the experimental (blue stars) and estimated (green curve) foot phasic component corresponding to the medial planar surface of foot; and iii) bottom sub-panel shows the timings of the auditory stimuli (gray vertical

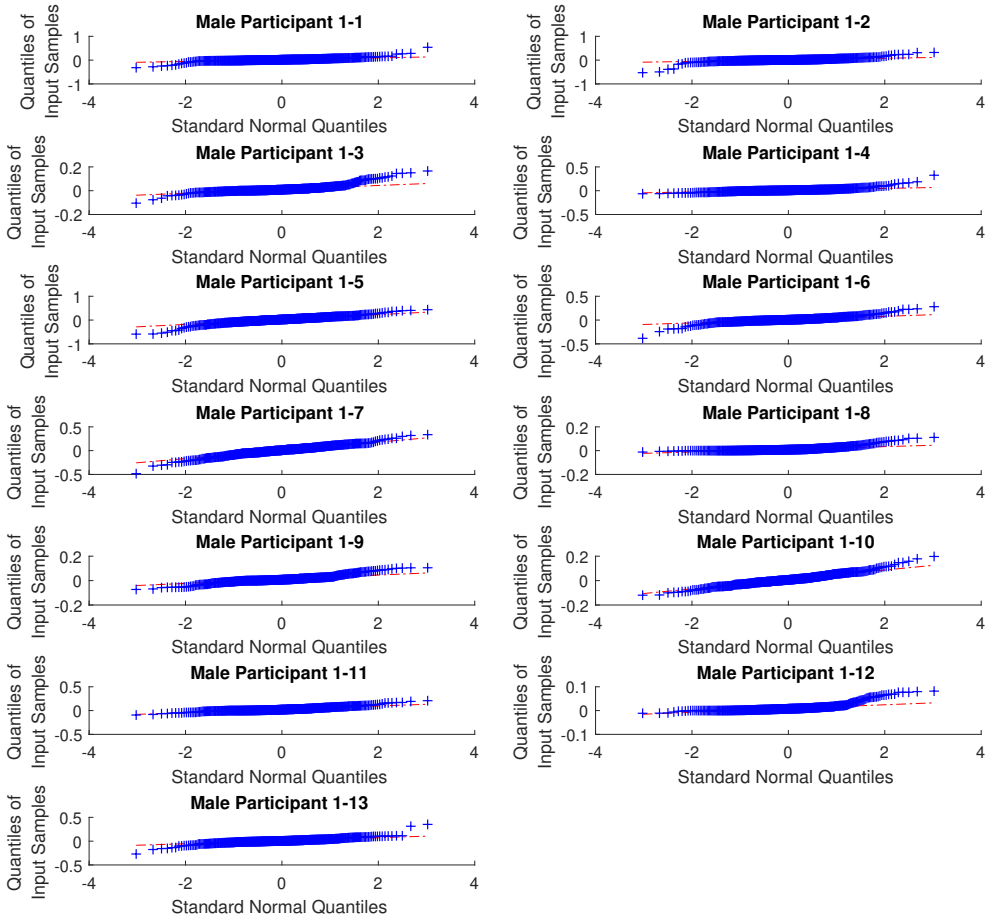

Figure 66: **White Gaussian Structure in the Model Residual Errors for SC Data Collected From Thirteen Male Participants.**

lines) and the estimated ANS activation timings and amplitudes (green vertical lines). Figure 80 and 81 shows the quantile-quantile plots of the phasic SC model residual errors for the 6 female participants and 6 male participants from both channels. In both figures, each of the panels displays the quantile-quantile plot of the Phasic SC model residual errors; the graph shows that the residual errors are Gaussian. The quantile-quantile plot suggests that the model captures the Phasic SC dynamics, and the phasic SC residual errors have a white Gaussian structure. Figure 82 and 83 show deconvolution results from simulated

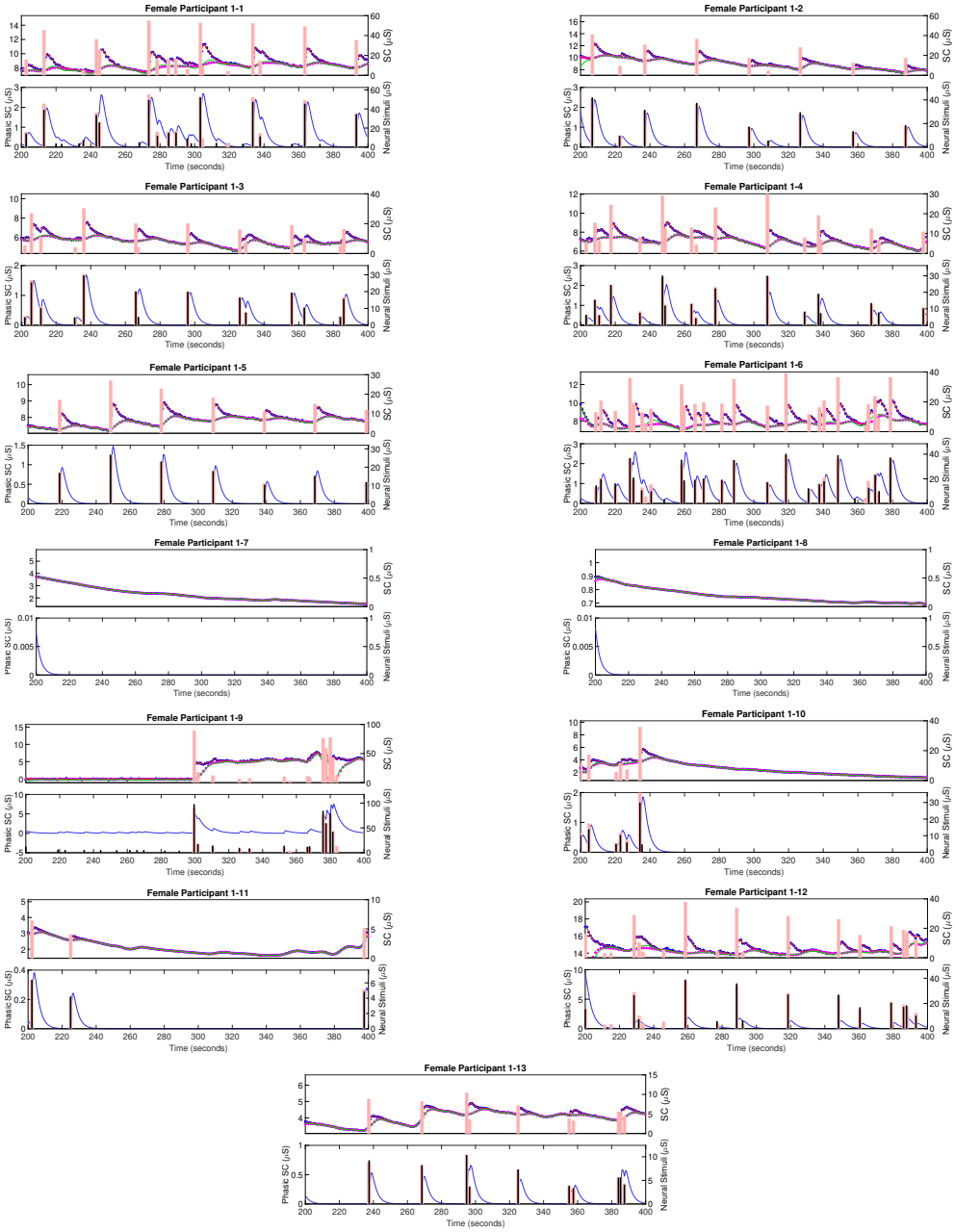

Figure 67: **Estimated Decomposition of the Simulated SC Signals with 25 dB SNR for Thirteen Female Participants from Dataset 1.**

phasic SC data for six female and six male participants, respectively. In both figures, the panels show the deconvolution results on the simulated data for six female participants, respectively. In each panel, i) the top subpanel shows the simulated (blue stars) and the estimated (red curve) phasic component corresponding to the middle phalanx of hand; ii)

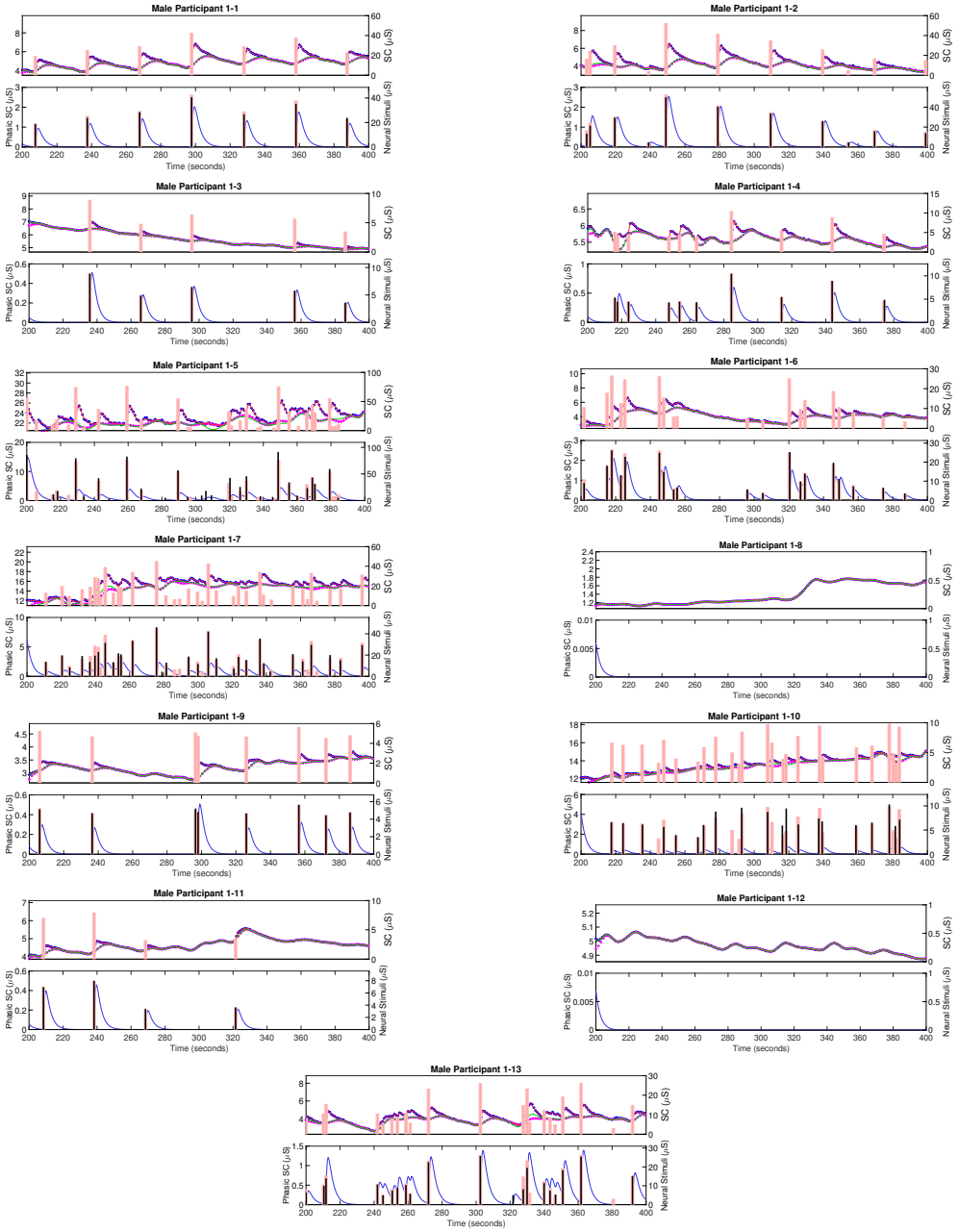

Figure 68: **Estimated Decomposition of the Simulated SC Signals with 25 dB SNR for Thirteen Male Dataset 1.**

middle panel shows the simulated (blue stars) and estimated (red curve) phasic component corresponding to the the medial planar surface of foot; and iii) bottom sub-panel shows the timings of the simulated ANS activation timings and amplitudes (gray line) and the estimated ANS activation timings and amplitudes (red dashed line).

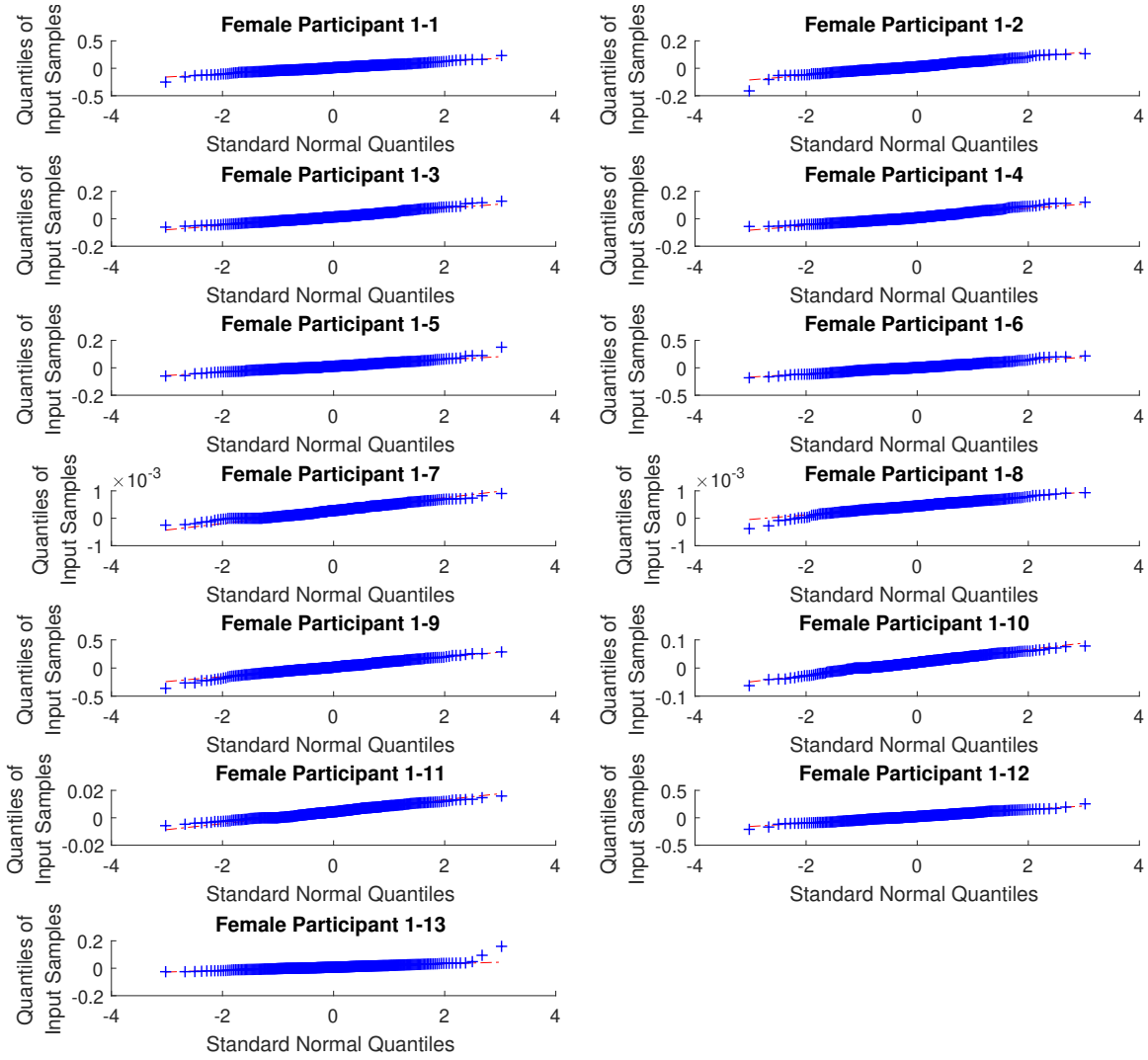

Figure 69: **White Gaussian Structure in the Model Residual Errors of SC Data for the Simulated with the Corresponding Results for Thirteen Female from Dataset 1.**

A.3 Additional Results for Chapter 4

Figure 84 shows the quantile-quantile plots of the phasic SC model residual errors for the six participants, suggesting that the model captures the SC dynamics, and that the phasic SC residual errors have a Gaussian structure and are white. In Figure 84, each of the panels displays the quantile-quantile plot of the SC model residual errors for each of the 6 participants; the graph shows that the residual errors are Gaussian. Figure 85 shows

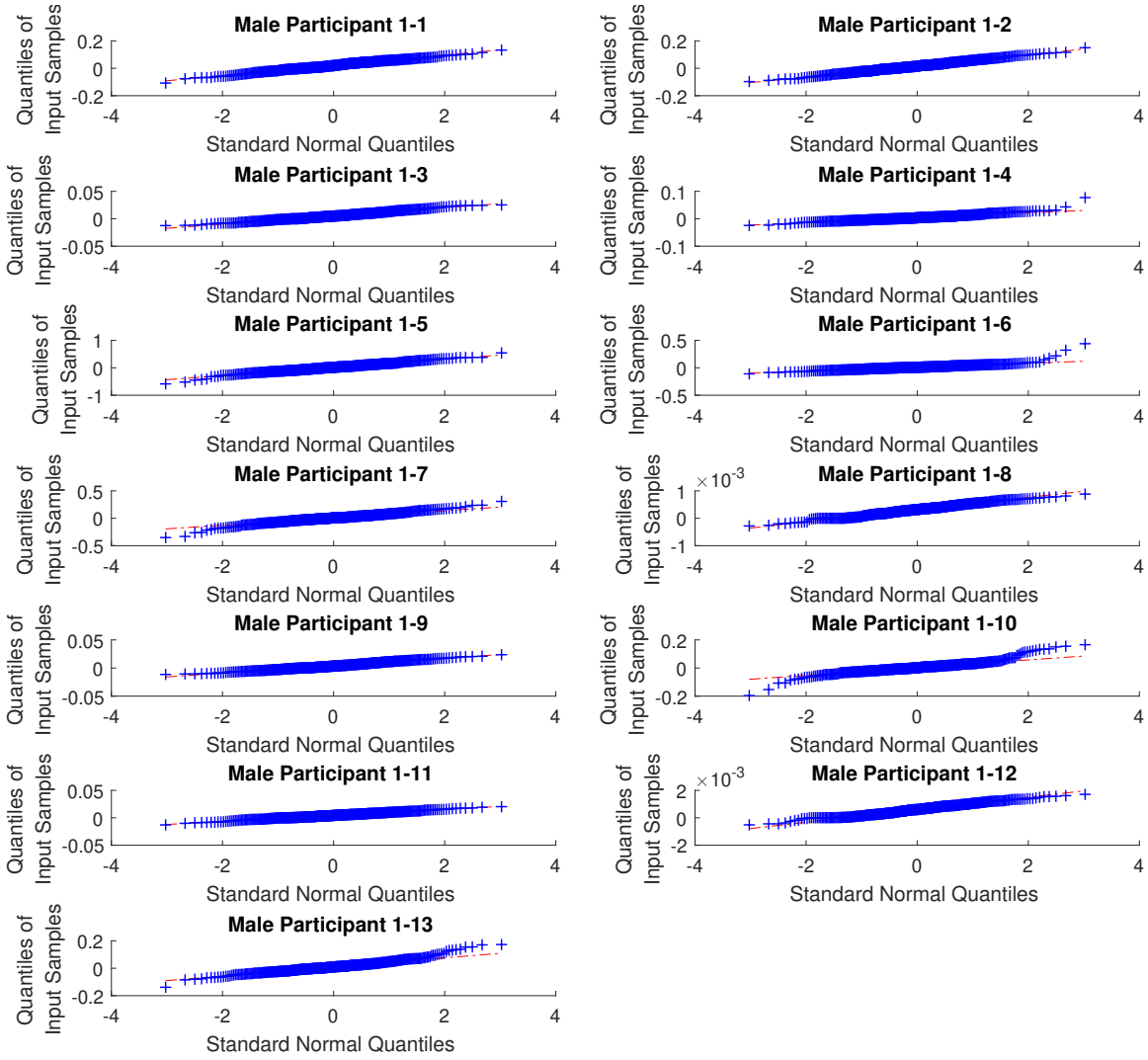

Figure 70: **White Gaussian Structure in the Model Residual Errors of SC Data for the Simulated with the Corresponding Results for Thirteen Male from Dataset 1.**

the reconstructed signal that includes both tonic and phasic components. The value R^2 for this case is higher than 0.95 for all participants. In Figure 85, each panel shows the SC signal (sum of phasic and tonic components) (blue curve), the reconstructed SC signal (sum of phasic and tonic components) (red dashed), the estimated neural stimuli timings and amplitudes (black vertical lines with a circle on top) for each of the participants. The estimation is done on phasic components using the proposed method; then, the previously

Figure 71: **ROC curves for the sensitivity of Our Approach For Distinguishing Between Event-Related vs Non-Event-Related SCRs.**

separated tonic components are added to the estimated phasic components.

A.4 Additional Results for Chapter 6

Figure 86-97 shows the motion artifact reduction results from two participants for all trials. In these figures, the first left panel depicts raw (artifact corrupted) and cleaned

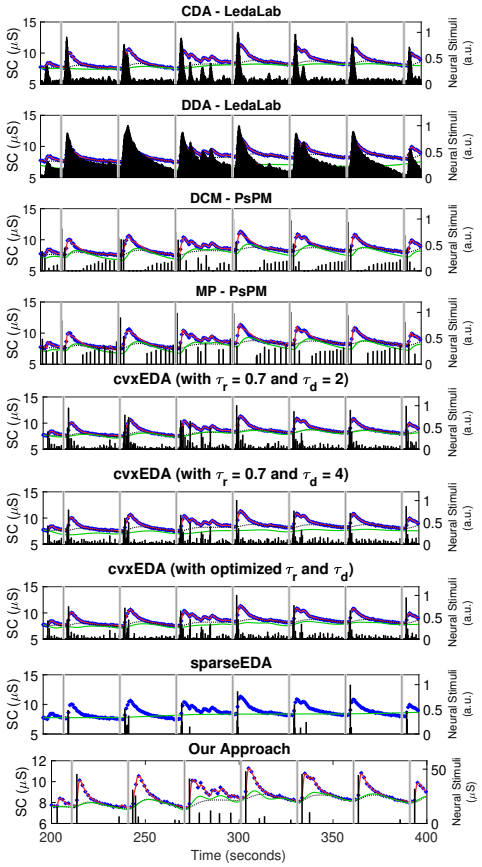

Figure 72: **Performance Comparison of Proposed Approach with Existing Approaches for Noisy Experimental Data from Female Participant 1-1.**

(artifact reduced) SC data; the first right panel shows the corresponding power spectrum density; the next three panels show three accelerometer channel recordings on the left and their corresponding power spectrum density on the right.

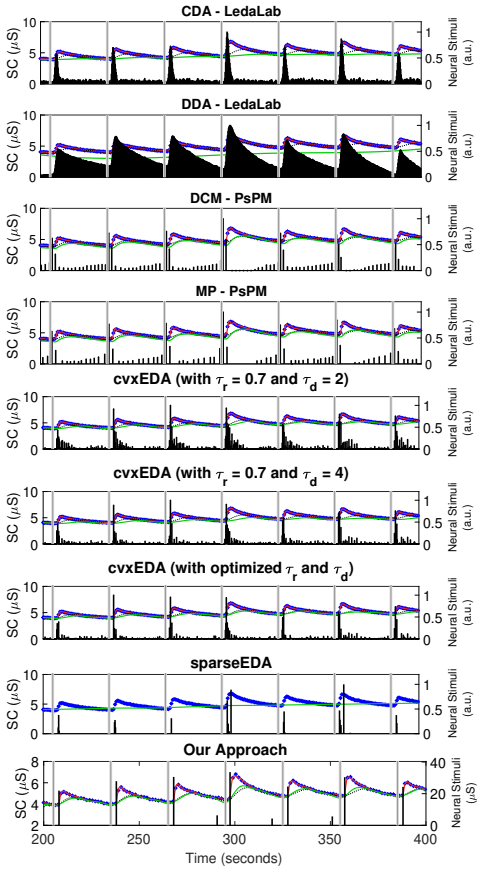

Figure 73: **Performance Comparison of Proposed Approach with Existing Approaches for Noisy Experimental Data from Male Participant 1-1.**

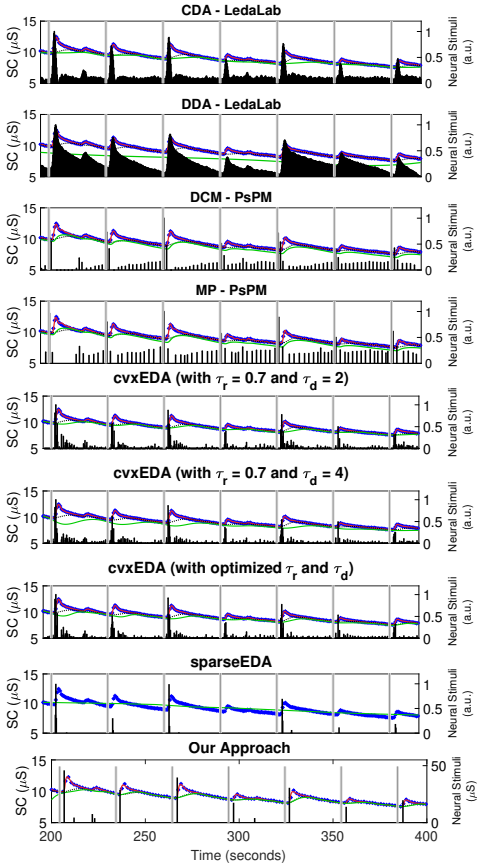

Figure 74: **Performance Comparison of Proposed Approach with Existing Approaches for Noisy Experimental Data from Female Participant 1-2.**

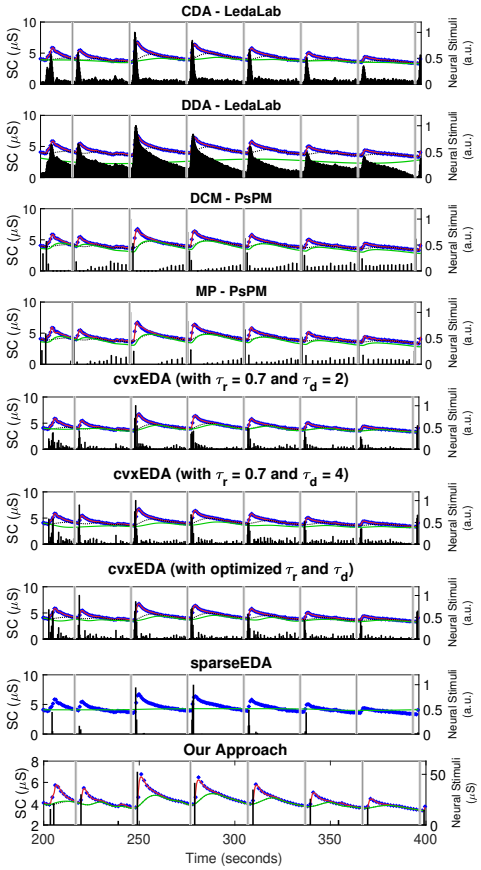

Figure 75: **Performance Comparison of Proposed Approach with Existing Approaches for Noisy Experimental Data from Male Participant 1-2.**

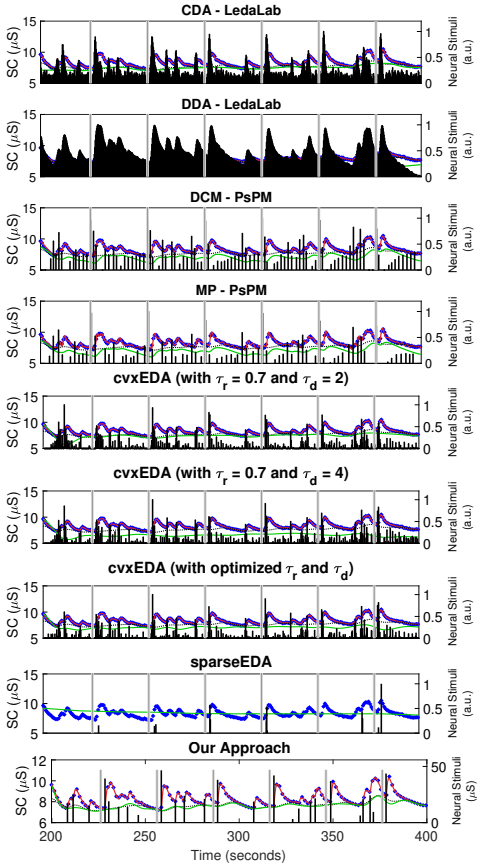

Figure 76: **Performance Comparison of Proposed Approach with Existing Approaches for Noisy Experimental Data from Female Participant 1-2.**

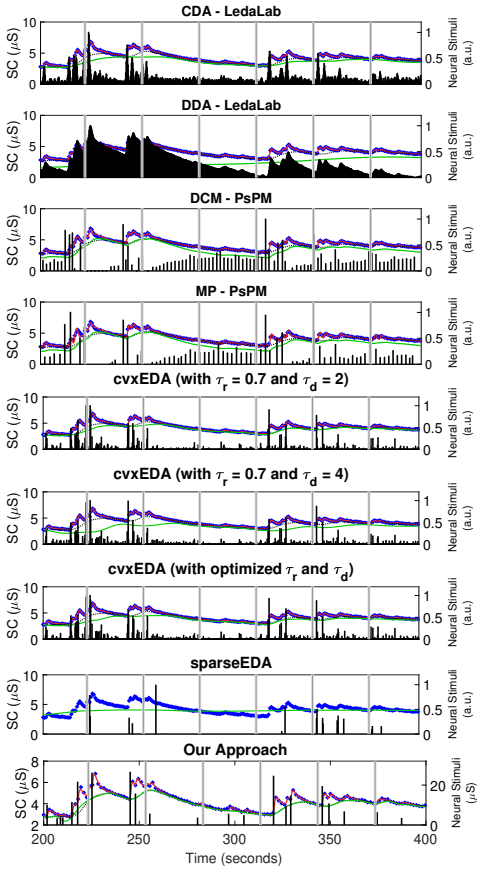

Figure 77: **Performance Comparison of Proposed Approach with Existing Approaches for Noisy Experimental Data from Male Participant 1-6.**

Table 10: The Estimated Model Parameters and the Squares of the Multiple Correlation Coefficients (R^2) for the Fits of the Experimental Skin Conductance Recordings

Female Participant	Subject ID	τ_r (seconds)	τ_d (seconds)	$\|\|\mathbf{u}\|\|_0$	λ_1	λ_2	R^2	Deconvolution Time (seconds)
1-1	12	0.9617	3.1112	17	2.3694	1.03452	0.9936	529
1-2	15	0.7188	2.8759	9	1.4592	3.62286	0.9954	915
1-3	7	0.7622	2.8594	14	1.9086	3.54442	0.9913	214
1-4	18	0.708	2.835	17	1.6896	0.23258	0.9933	640
1-5	21	0.7712	2.9073	7	0.4074	2.45125	0.9894	113
1-6	25	0.8497	2.6488	25	5.0875	3.86205	0.9853	498
1-7	1	0.6506	2.7733	0	9999.9404	0.08108	0.9997	98
1-8	2	0.6506	2.7733	0	9999.9404	0.07918	0.9978	89
1-9	5	0.2927	3.6009	14	46.0459	3.99022	0.989	195
1-10	6	0.8705	3.0454	6	1.133	3.9663	0.9986	218
1-11	14	0.6512	2.7736	3	0.8912	0.47611	0.9925	129
1-12	16	0.9041	3.0213	18	2.2797	0.2407	0.9923	7525
1-13	19	0.6837	2.807	10	1.5347	3.92633	0.9936	86
Male Participant	Subject ID	τ_r (seconds)	τ_d (seconds)	$\|\|\mathbf{u}\|\|_0$	λ_1	λ_2	R^2	Deconvolution Time (seconds)
1-1	11	0.9132	3.2105	7	0.9279	35.1903	0.9895	207
1-2	26	0.8836	3.1121	11	1.6957	38.1157	0.9877	348
1-3	8	0.6688	2.8055	5	0.5012	8.4414	0.9977	71
1-4	10	0.6647	2.8338	10	0.9592	38.5224	0.964	108
1-5	20	0.9871	2.7481	30	16.22	39.0317	0.9882	8637
1-6	23	0.6116	2.7395	19	2.1704	36.5492	0.9948	225
1-7	3	0.9402	2.8816	36	8.0795	39.0272	0.9957	8445
1-8	4	0.6506	2.7734	0	9999.9404	7.1226	0.9945	96
1-9	9	0.6587	2.8043	8	0.5945	18.4884	0.9879	99
1-10	13	0.6855	2.8838	25	2.4387	2.1094	0.997	2590
1-11	17	0.6637	2.8232	4	1.2189	39.4724	0.9846	124
1-12	22	0.6506	2.7738	0	9999.9404	20.2611	0.9902	99
1-13	24	0.8185	2.9402	21	1.9879	35.826	0.9932	324

Table 11: The Estimated Model Parameters, Estimation Errors, and the Squares of the Multiple Correlation Coefficients (R^2) for the Fits of the Simulated Skin Conductance Data

Female Participant	Subject ID	$\hat{\tau}_r$ (seconds)	$\hat{\tau}_d$ (seconds)	$\|\|\hat{\mathbf{u}}\|\|_0$	$\frac{\|\tau_r-\hat{\tau}_r\|}{\tau_r} \times 100\%$	$\frac{\|\tau_d-\hat{\tau}_d\|}{\tau_d} \times 100\%$	$\|\|\|\hat{\mathbf{u}}\|\|_0 - \|\|\mathbf{u}\|\|_0\|$	R^2
1	12	0.8595	3.0526	24	11.8923	1.9218	7	0.9956
2	15	0.7042	2.9227	9	2.0797	1.5984	0	0.9988
3	7	0.7054	2.8544	14	8.0397	0.1740	0	0.9967
4	18	0.6724	2.8546	17	5.2946	0.6862	0	0.9972
5	21	0.7030	2.8636	7	9.7036	1.5271	0	0.9956
6	25	0.7320	2.9086	25	16.0842	8.9343	0	0.9915
7	1	0.6506	2.7733	0	0.0000	0.0024	0	1
8	2	0.6506	2.7733	0	0.0000	0.0025	0	1
9	5	0.1960	4.4068	23	49.3255	18.288	9	0.9989
10	6	0.6849	2.8122	7	27.1048	8.2932	1	0.9996
11	14	0.6502	2.7737	3	0.1555	0.0058	0	0.9999
12	16	0.7839	3.2262	14	15.3389	6.3601	4	0.9901
13	19	0.6440	2.7830	10	6.1551	0.8622	0	0.9988
Male Participant	Subject ID	$\hat{\tau}_r$ (seconds)	$\hat{\tau}_d$ (seconds)	$\|\|\hat{\mathbf{u}}\|\|_0$	$\frac{\|\tau_r-\hat{\tau}_r\|}{\tau_r} \times 100\%$	$\frac{\|\tau_d-\hat{\tau}_d\|}{\tau_d} \times 100\%$	$\|\|\|\hat{\mathbf{u}}\|\|_0 - \|\|\mathbf{u}\|\|_0\|$	R^2
1	11	0.819	3.0863	7	11.5015	4.0221	0	0.9967
2	26	0.8086	3.0400	11	9.2805	2.371	0	0.9962
3	8	0.652	2.7772	5	2.5805	1.0198	0	0.9999
4	10	0.6522	2.7798	10	1.9235	1.9396	0	0.9968
5	20	0.9448	3.4021	26	4.4785	19.2245	4	0.9853
6	23	0.5739	2.7126	19	6.562	0.991	0	0.9969
7	3	0.8983	3.1078	27	4.6655	7.2776	9	0.9971
8	4	0.6506	2.7732	0	0	0.0042	0	1
9	9	0.6517	2.7789	8	1.0875	0.9155	0	0.9993
10	13	0.7079	2.8875	20	3.1634	0.1282	5	0.9978
11	17	0.6533	2.7788	4	1.5901	1.5981	0	0.9997
12	22	0.6506	2.7733	0	0	0.0196	0	0.9999
13	24	0.7380	2.9141	20	10.9133	0.894	1	0.9957

Table 12: The Comparison between Different Algorithms with Noisy Experimental Data in terms of Number of Estimated Pulses

Participant	Our Approach	sparsEDA	cvxEDA with optimized τ_r and τ_d	cvxEDA with $\tau_r = 0.7$ and $\tau_d = 2$	cvxEDA with $\tau_r = 0.7$ and $\tau_d = 4$	CDA LedaLab	DDA LedaLab	DCM PSPM	MP PSPM
Female 1-1	10	29	797	798	798	799	799	99	75
Female 1-2	23	21	798	798	798	799	799	99	74
Female 1-6	11	26	798	798	798	799	799	99	74
Male 1-1	22	30	798	798	799	799	799	99	68
Male 1-2	26	12	798	798	798	799	799	99	74
Male 1-6	11	18	798	798	798	799	799	99	80

Table 13: The Comparison between Different Algorithms with Noisy Experimental Data in terms of Multiple Correlation Coefficient

Participant	Our Approach	sparsEDA	cvxEDA with optimized τ_r and τ_d	cvxEDA with $\tau_r = 0.7$ and $\tau_d = 2$	cvxEDA with $\tau_r = 0.7$ and $\tau_d = 4$	CDA LedaLab	DDA LedaLab	DCM PSPM	MP PSPM
Female 1-1	0.9896	NA	0.9988	0.9989	0.9988	0.9988	0.9988	0.9971	0.9852
Female 1-2	0.9931	NA	0.9991	0.9991	0.9991	0.9987	0.9987	0.9952	0.9742
Female 1-6	0.9877	NA	0.9978	0.9980	0.9980	0.9976	0.9976	0.9943	0.9818
Male 1-1	0.9911	NA	0.9977	0.9978	0.9978	0.9975	0.9975	0.9878	0.9704
Male 1-2	0.9873	NA	0.9963	0.9964	0.9965	0.9960	0.9960	0.9873	0.9419
Male 1-6	0.9942	NA	0.9994	0.9994	0.9994	0.9993	0.9993	0.9970	0.9921

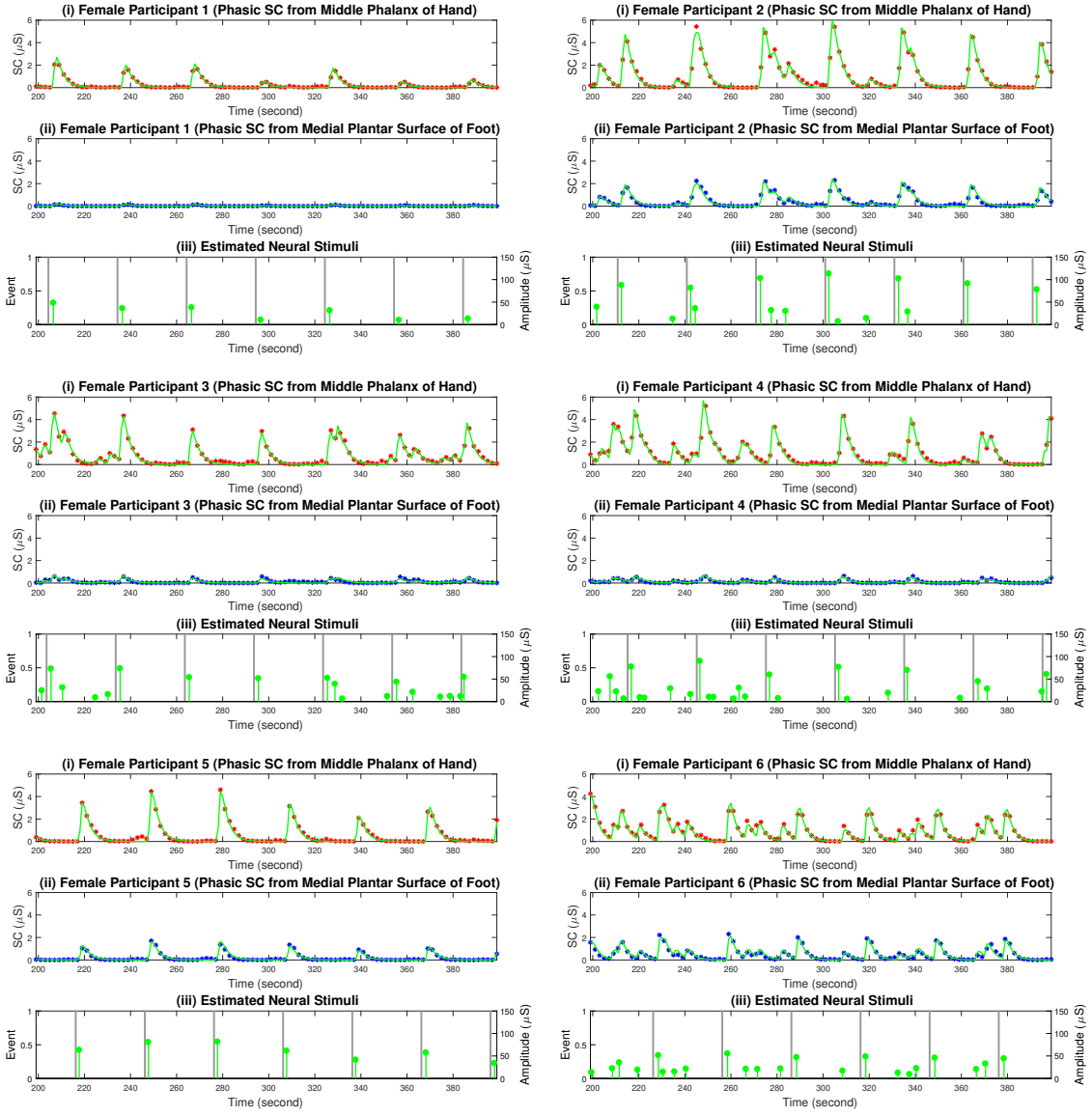

Figure 78: **Estimated Deconvolution of the Experimental Phasic SC Signals Six Female Participants.**

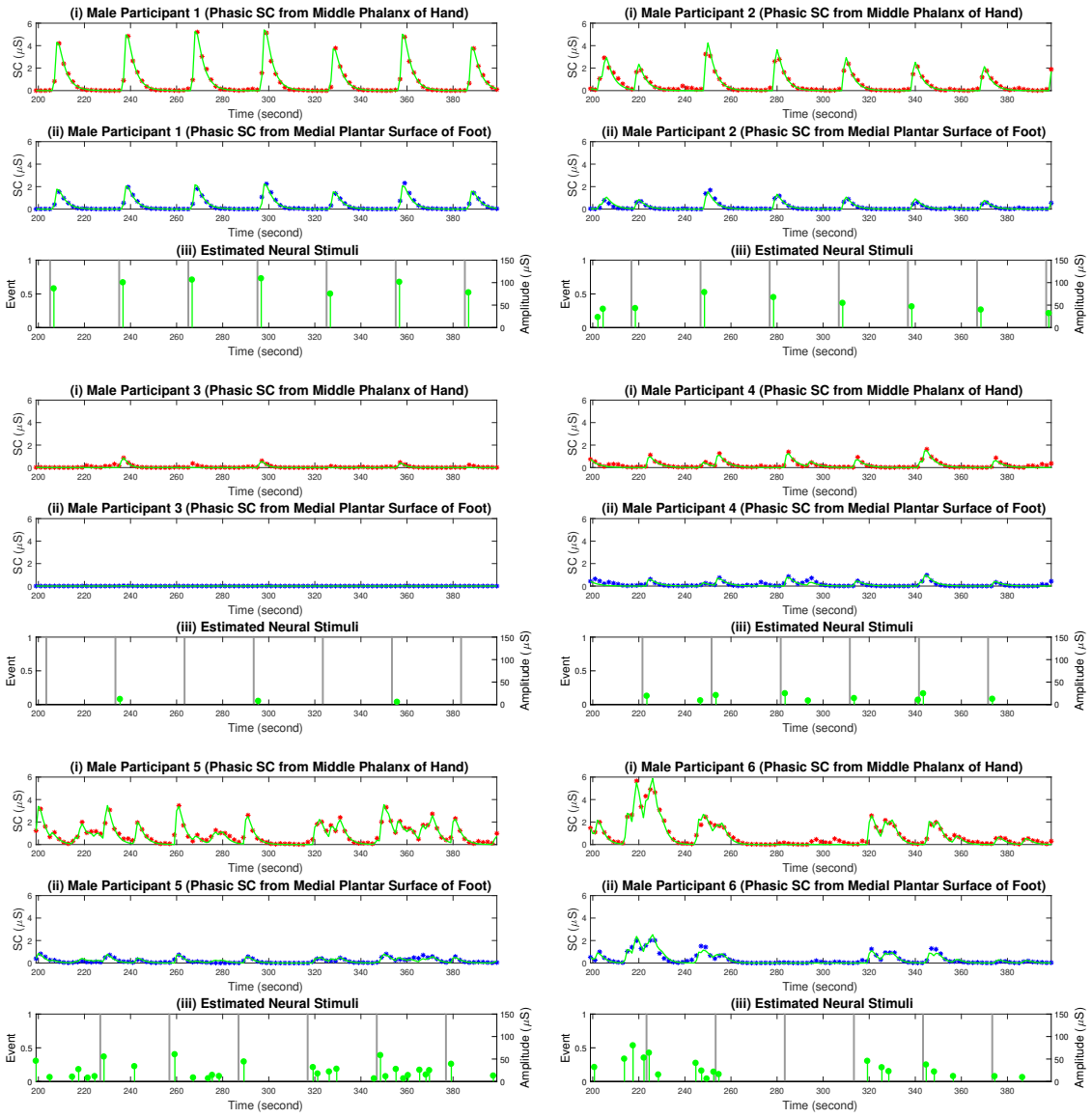

Figure 79: **Estimated Deconvolution of the Experimental Phasic SC Signals Six Male Participants.**

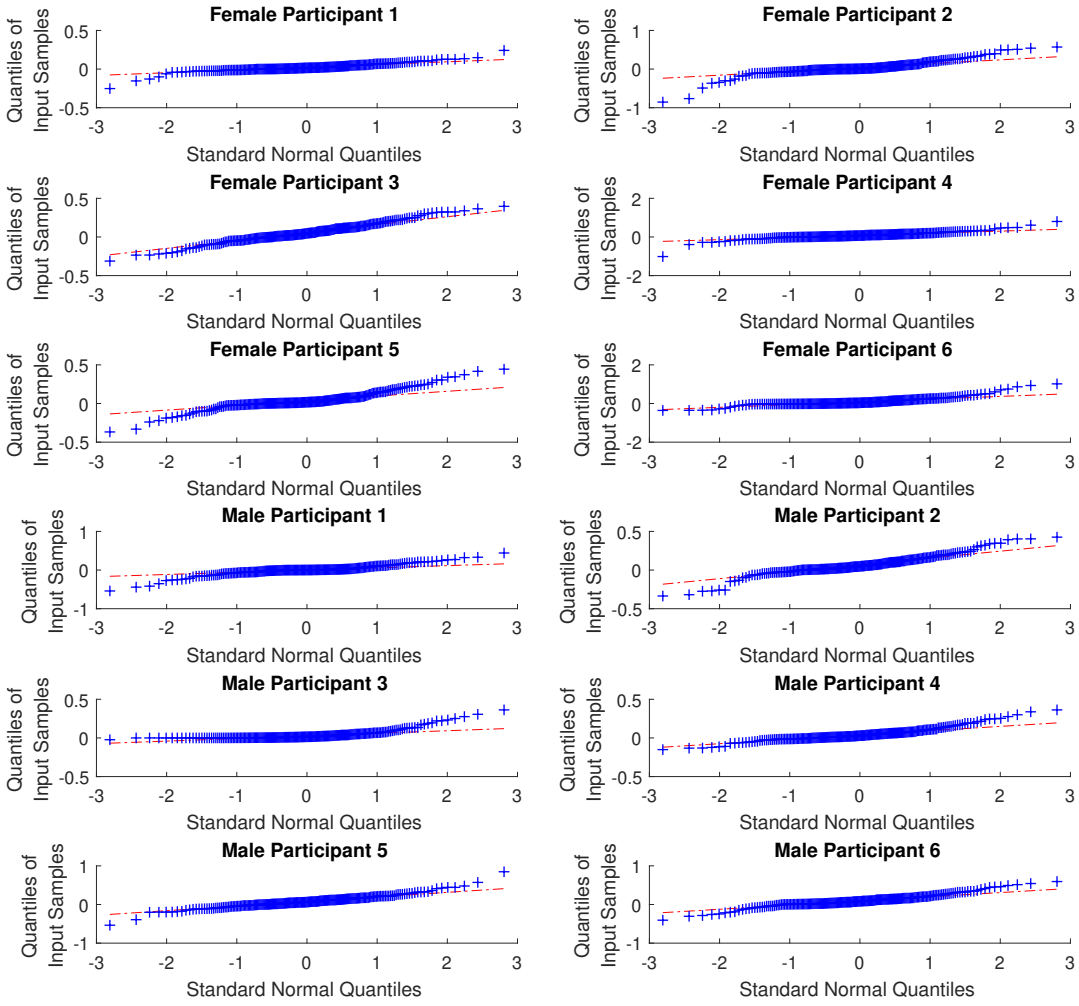

Figure 80: **White Gaussian Structure in the Model Residual Errors of Phasic SC Data of Six Female Participants and Six Male Participants for the Recordings Corresponding to Hand.**

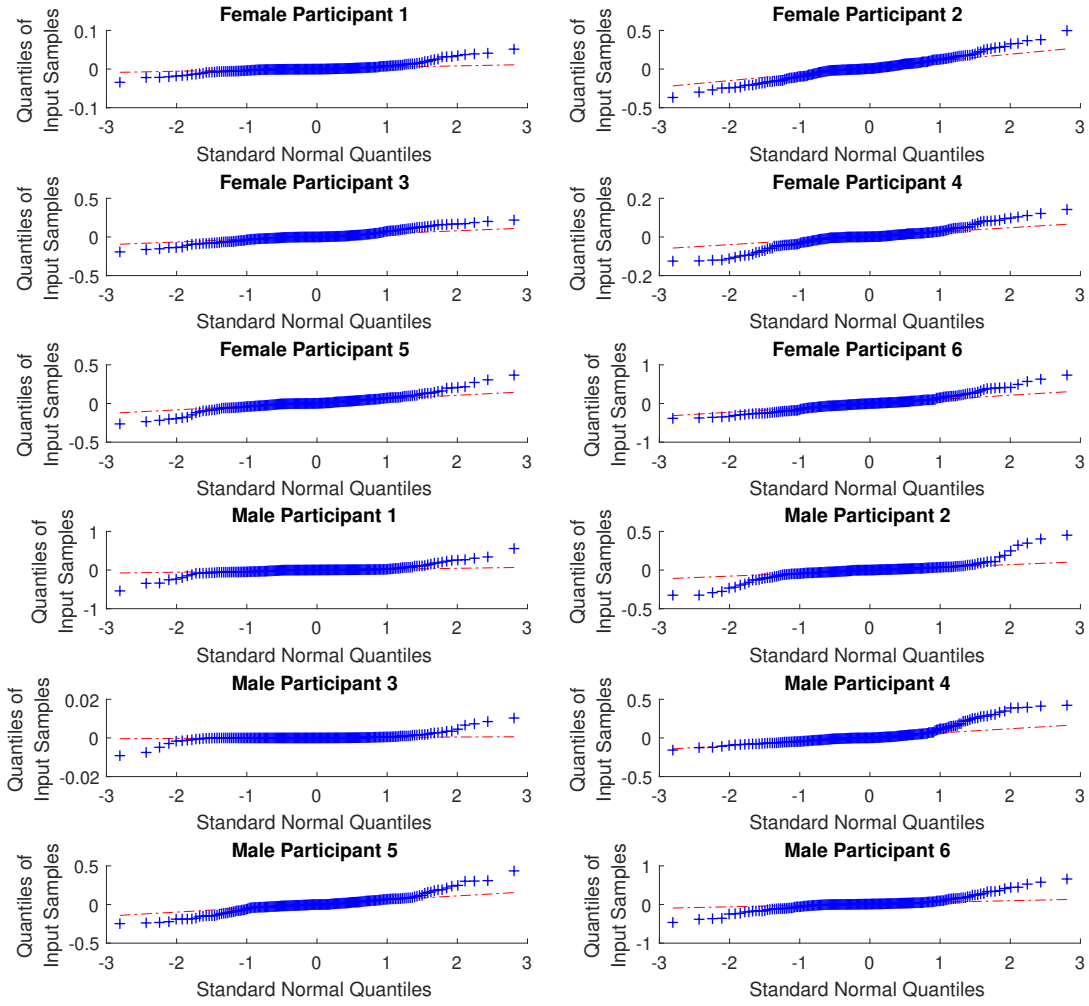

Figure 81: **White Gaussian Structure in the Model Residual Errors of Phasic SC Data of Six Female Participants and Six Male Participants for the Recordings Corresponding to Foot.**

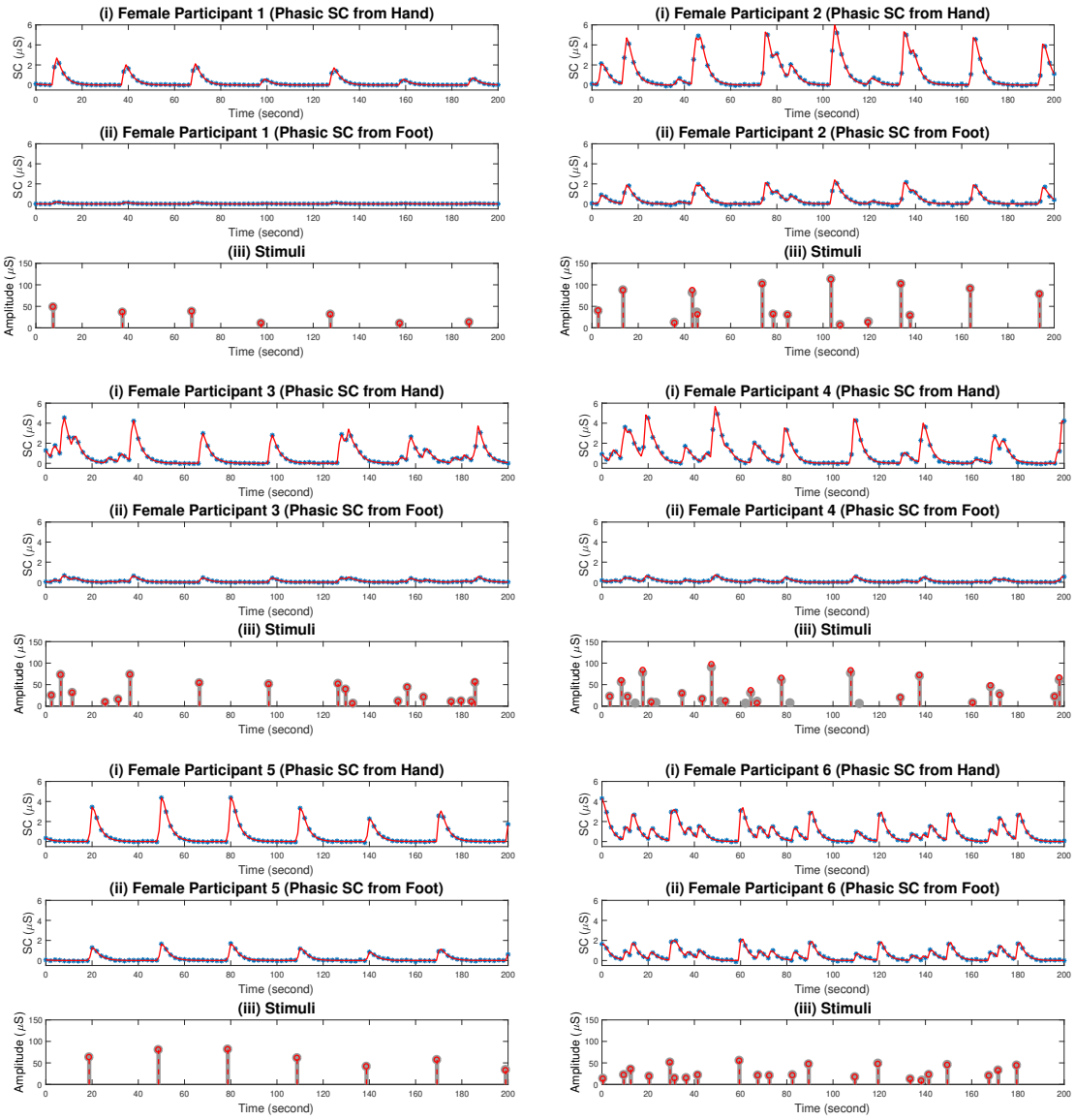

Figure 82: **Estimated Deconvolution of the Simulated Phasic SC Signal.**

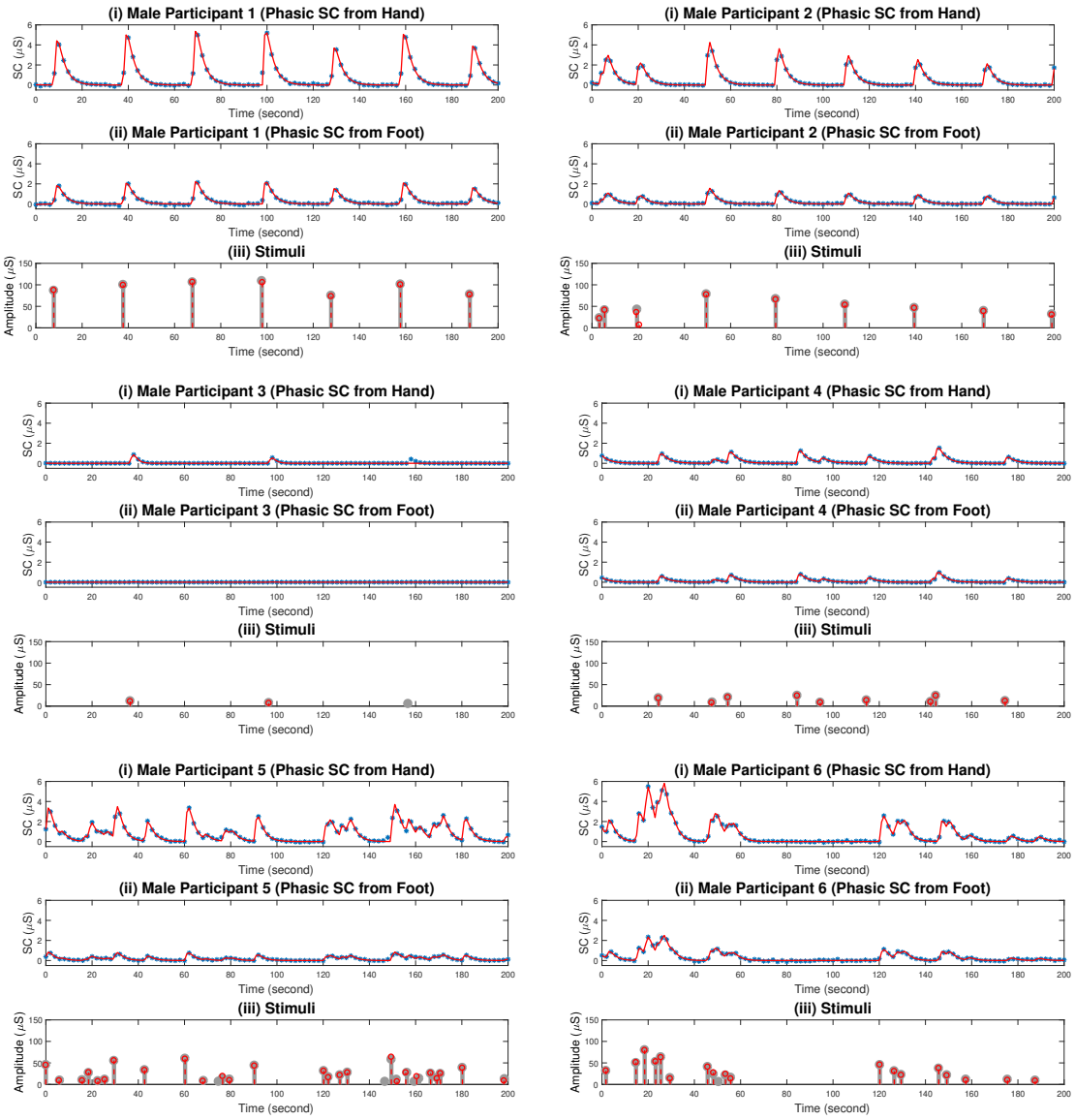

Figure 83: **Estimated Deconvolution of the Simulated Phasic SC Signal.**

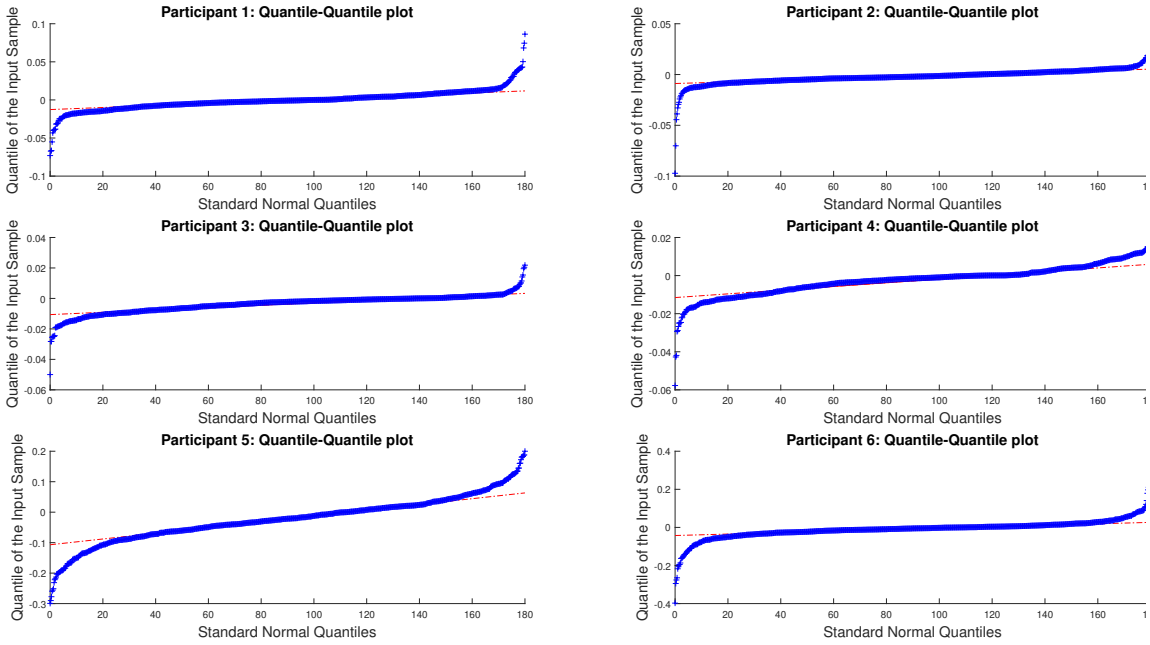

Figure 84: **White Gaussian Structure in the Model Residual Errors of Phasic SC data of 6 Participants.**

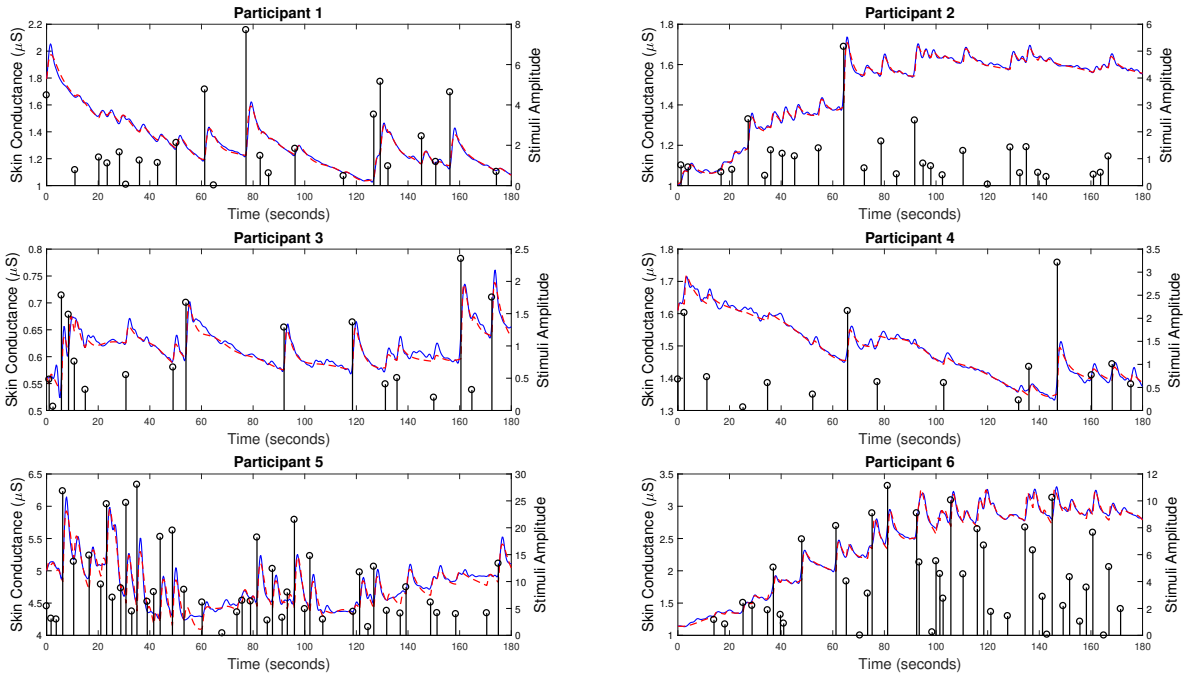

Figure 85: **Estimated Neural Stimuli and Reconstructed Signals of the Experimental SC Data in 6 Participants.**

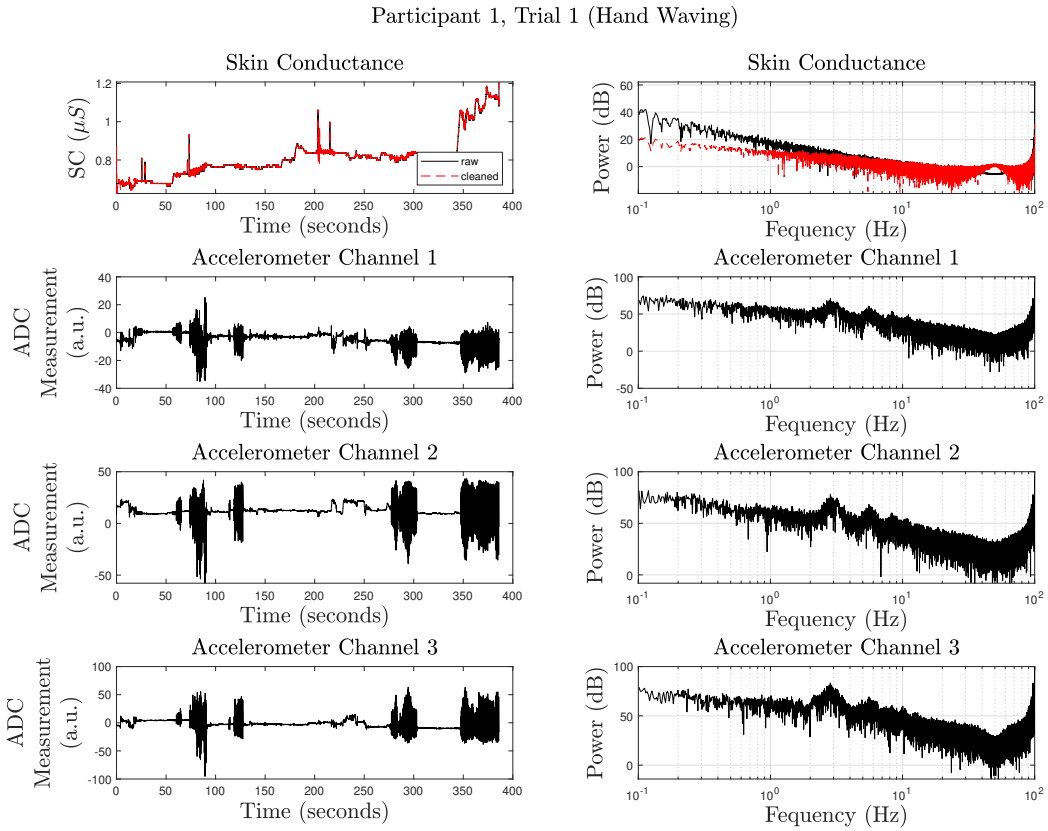

Figure 86: **Example Artifact Reduction Result with Multi-resolution RLS Adaptive Filter from Experimental SC recording Participant 1, Trial 1 During Hand Waving.**

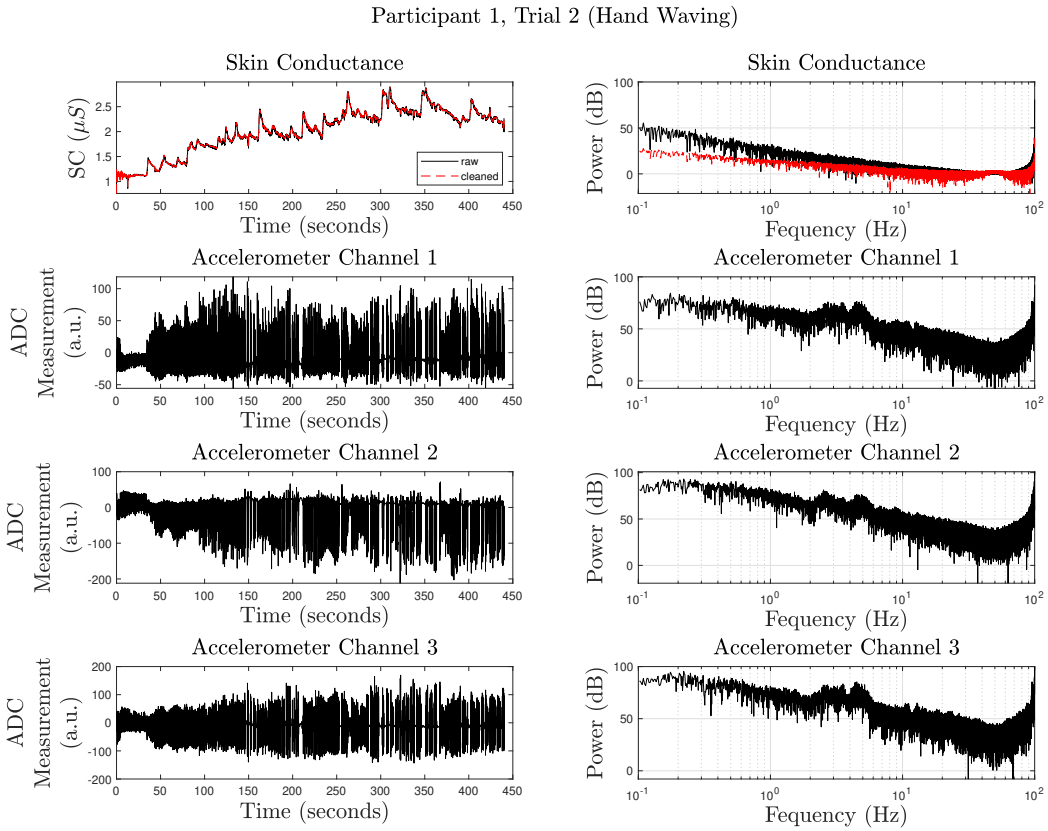

Figure 87: **Example Artifact Reduction Result with Multi-resolution RLS Adaptive Filter from Experimental SC recording Participant 1, Trial 2 During Hand Waving.**

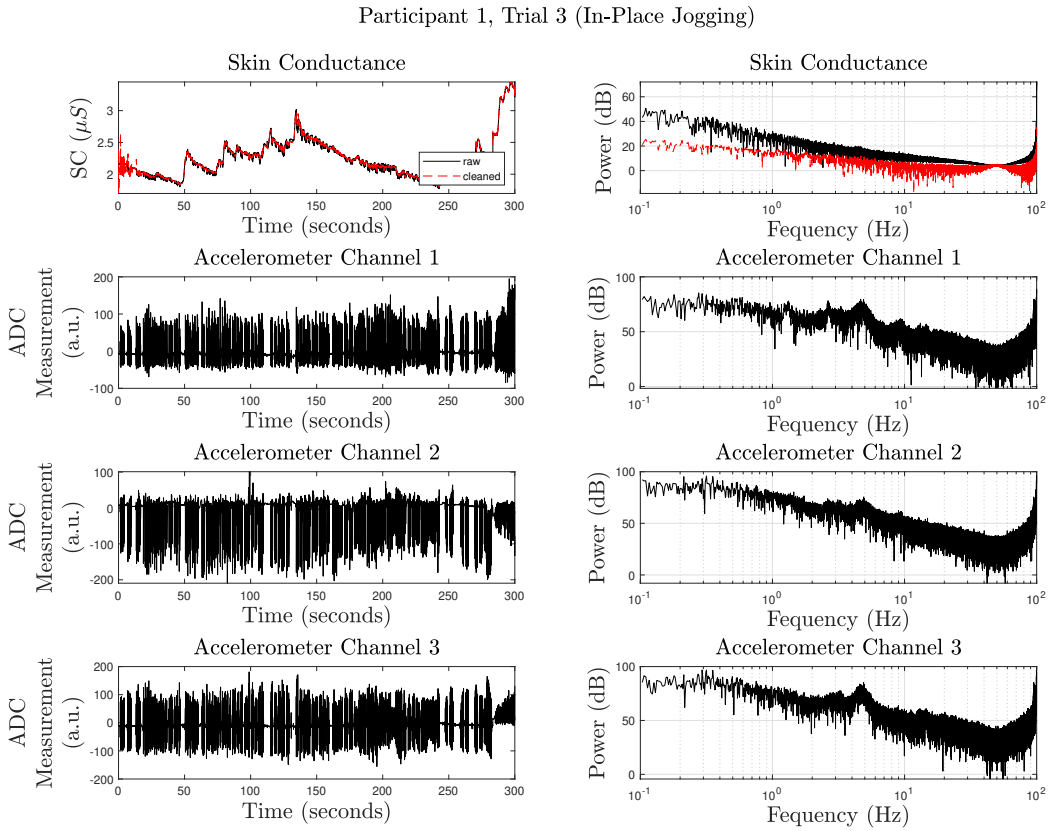

Figure 88: **Example Artifact Reduction Result with Multi-resolution RLS Adaptive Filter from Experimental SC recording Participant 1, Trial 3 During Hand Waving.**

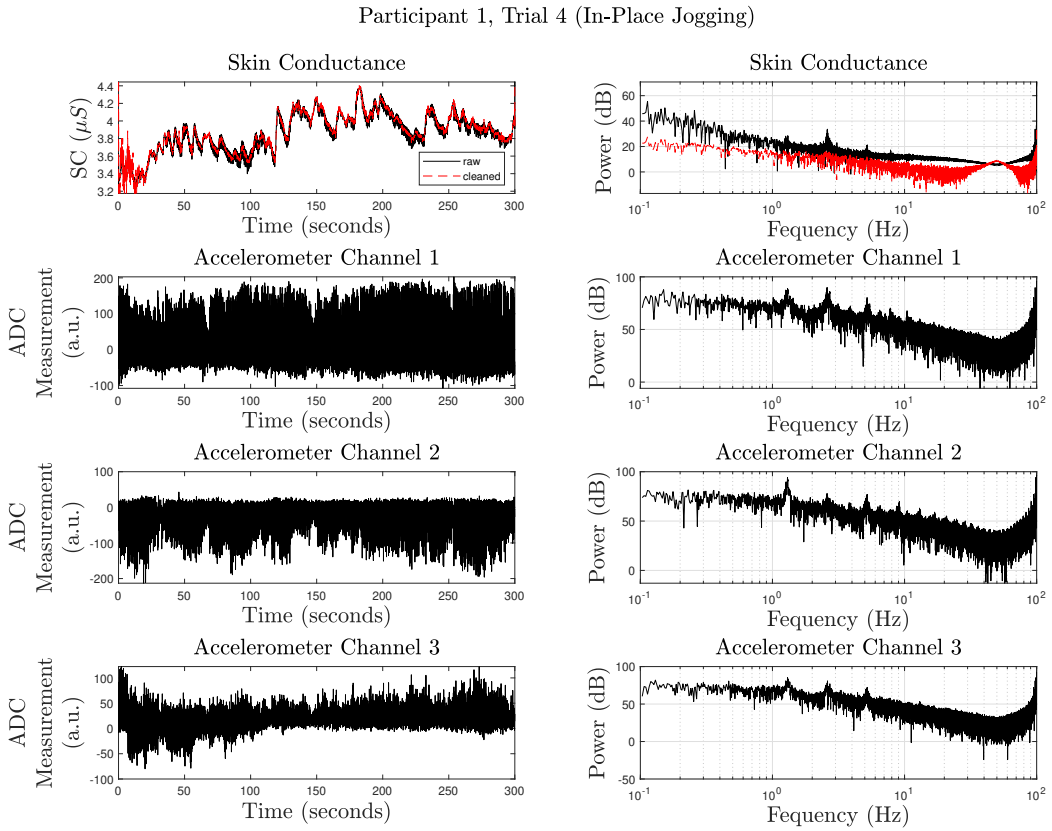

Figure 89: **Example Artifact Reduction Result with Multi-resolution RLS Adaptive Filter from Experimental SC recording Participant 1, Trial 4 During Hand Waving.**

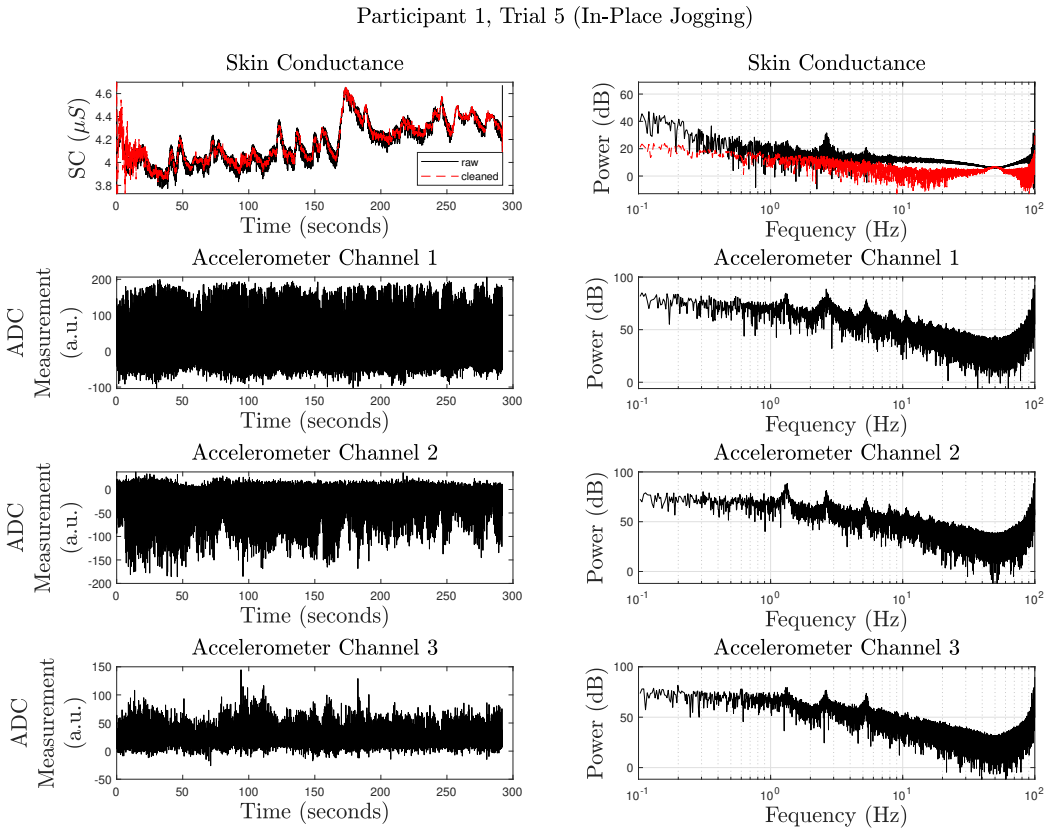

Figure 90: **Example Artifact Reduction Result with Multi-resolution RLS Adaptive Filter from Experimental SC recording Participant 1, Trial 5 During Hand Waving.**

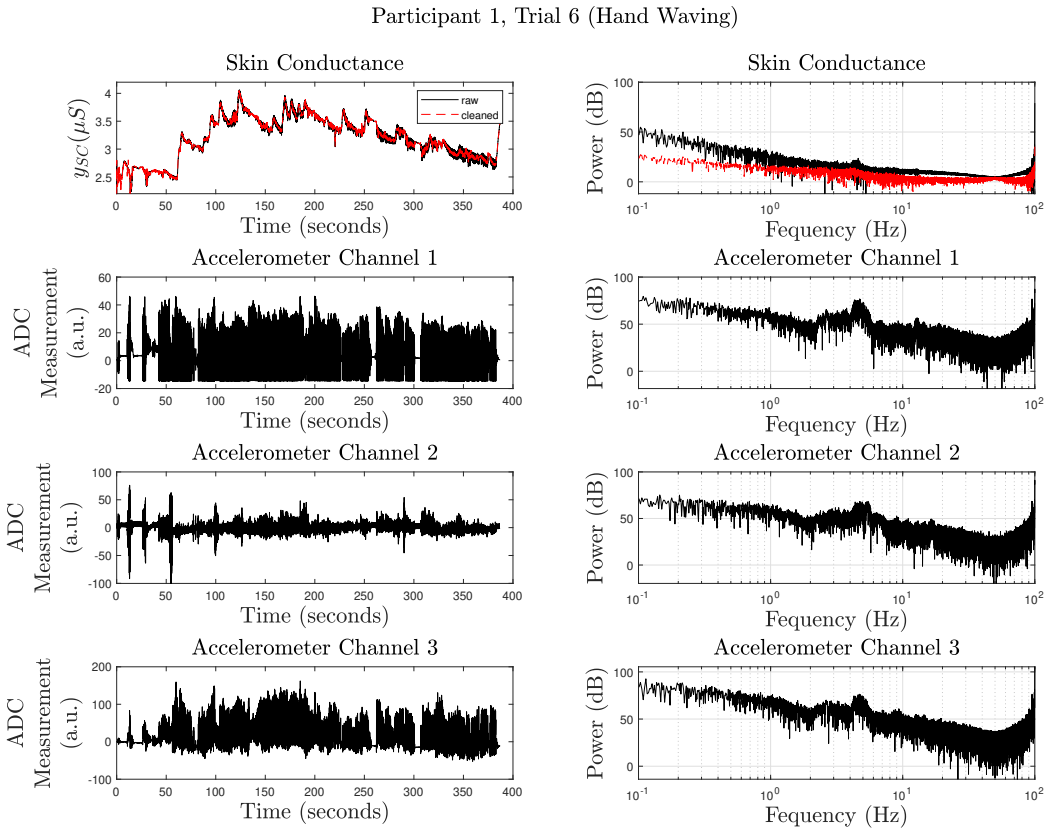

Figure 91: **Example Artifact Reduction Result with Multi-resolution RLS Adaptive Filter from Experimental SC recording Participant 1, Trial 6 During Hand Waving.**

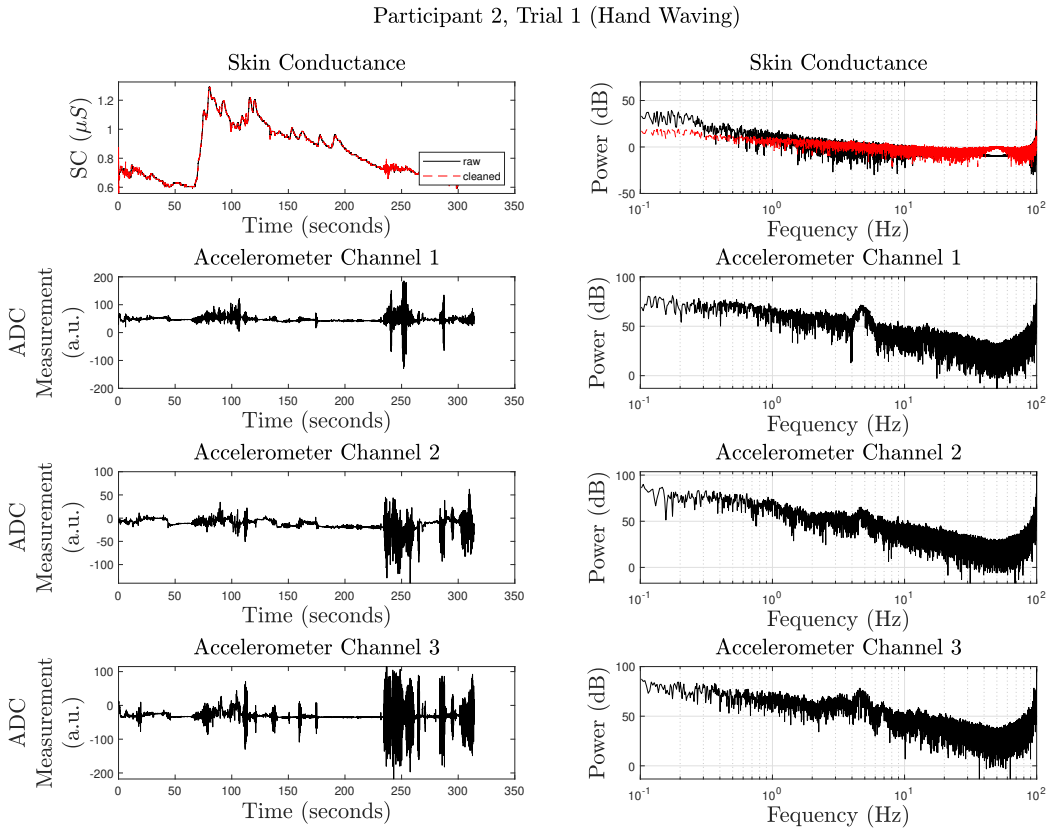

Figure 92: **Example Artifact Reduction Result with Multi-resolution RLS Adaptive Filter from Experimental SC recording Participant 2, Trial 1 During Hand Waving.**

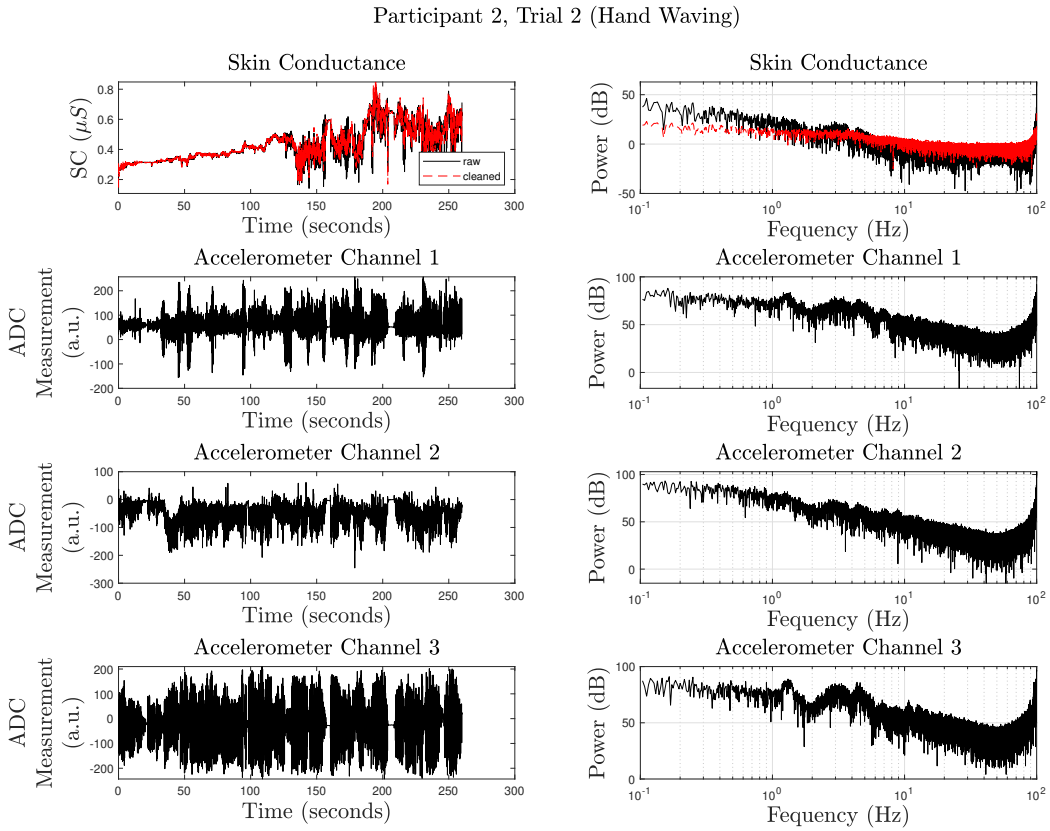

Figure 93: **Example Artifact Reduction Result with Multi-resolution RLS Adaptive Filter from Experimental SC recording Participant 2, Trial 2 During Hand Waving.**

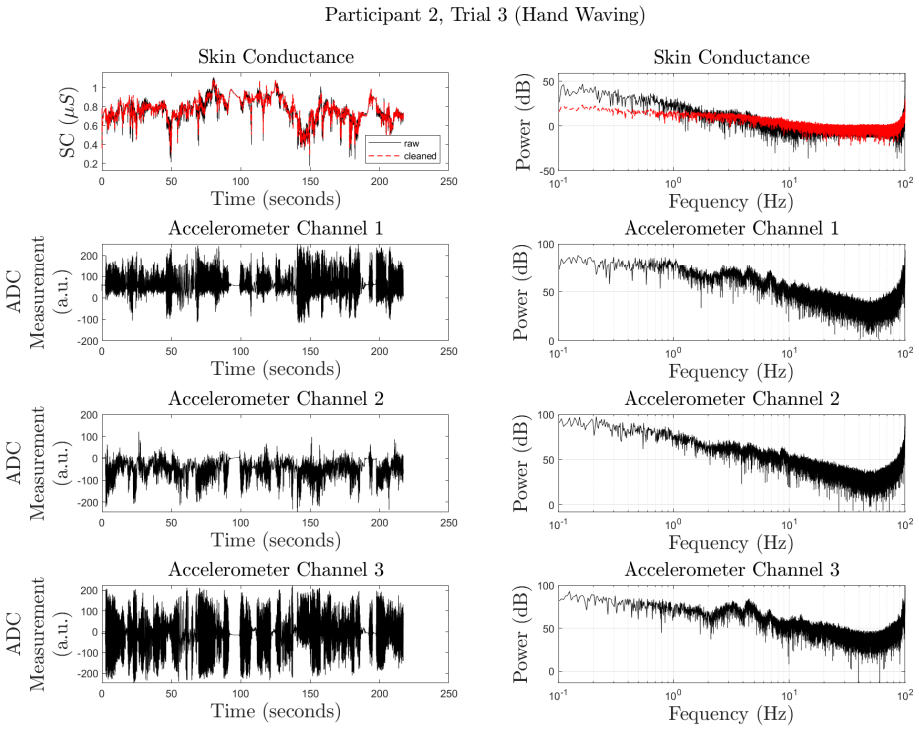

Figure 94: **Example Artifact Reduction Result with Multi-resolution RLS Adaptive Filter from Experimental SC recording Participant 2, Trial 3 During Hand Waving.**

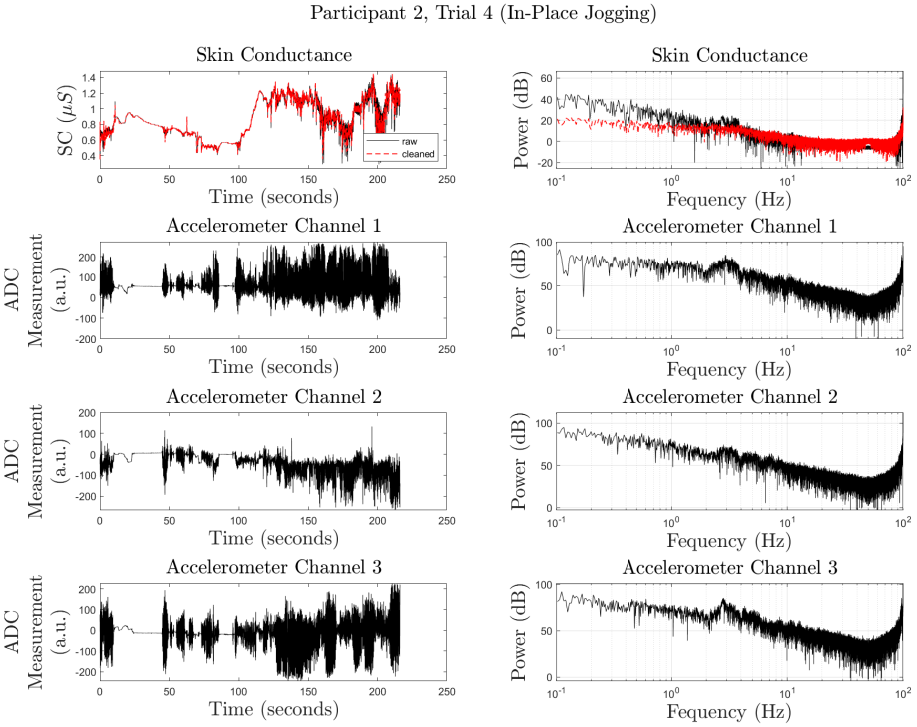

Figure 95: **Example Artifact Reduction Result with Multi-resolution RLS Adaptive Filter from Experimental SC recording Participant 2, Trial 4 During Hand Waving.**

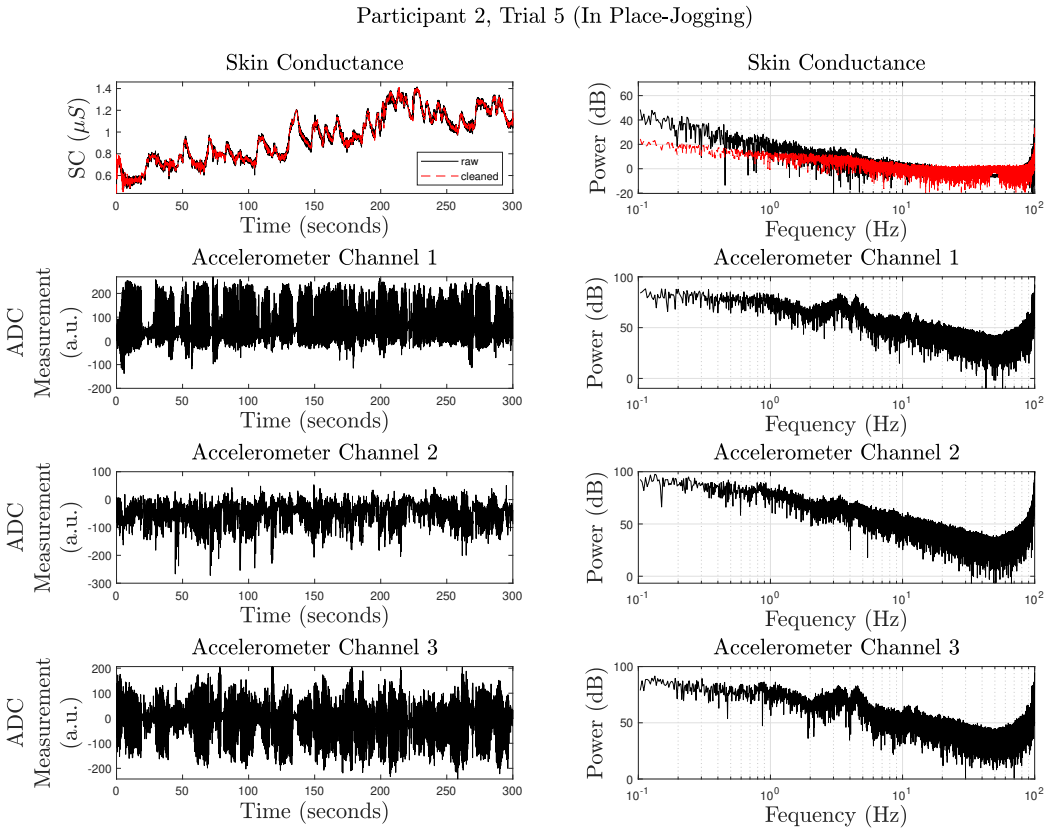

Figure 96: **Example Artifact Reduction Result with Multi-resolution RLS Adaptive Filter from Experimental SC recording Participant 2, Trial 5 During Hand Waving.**

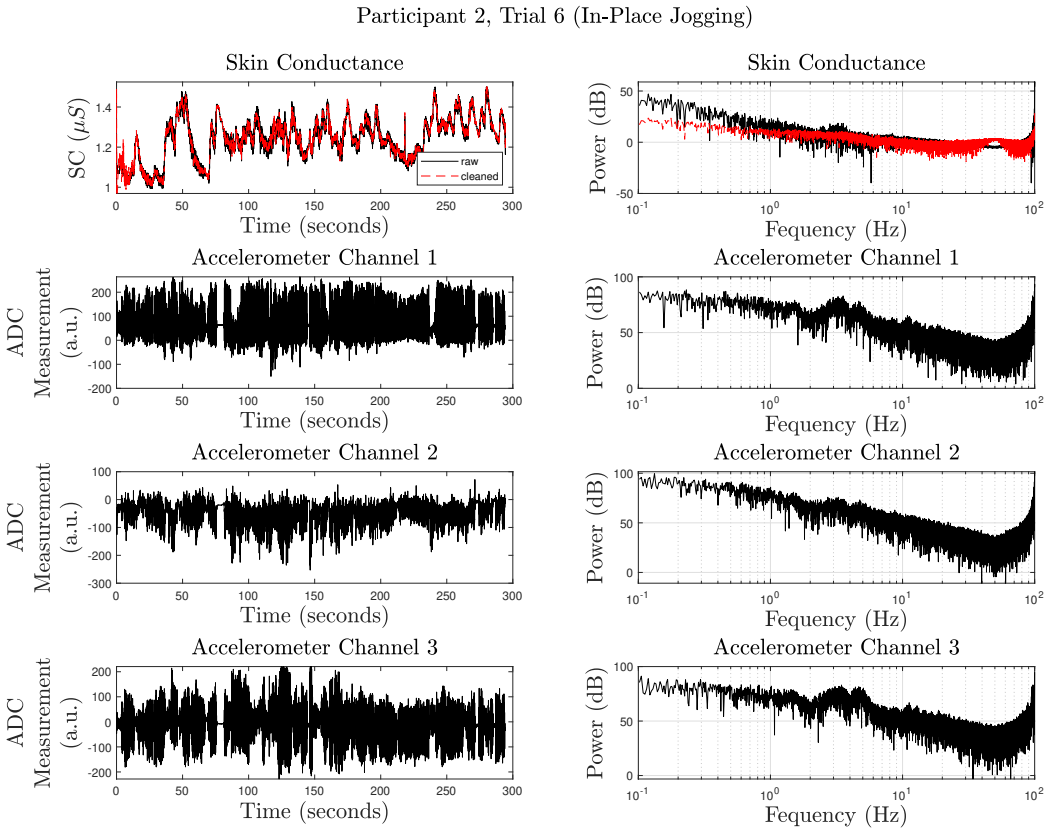

Figure 97: **Example Artifact Reduction Result with Multi-resolution RLS Adaptive Filter from Experimental SC recording Participant 2, Trial 6 During Hand Waving.**